CFD INVESTIGATIONS OF MIXTURE FORMATION, FLOW AND COMBUSTION FOR MULTI-FUEL ROTARY ENGINE

Von der Fakultät für Maschinenbau, Elektrotechnik and Wirtschafts-Ingenieurwesen der Brandenburgischen Technischen Universität Cottbus

zur Erlangung des akademischen Grades eines

Doktor-Ingenieurs (Dr.-Ing.)

genehmigte Dissertation

vorgelegt von

Master of Science

Husni Taher Izweik

Geboren am 15.12.1954 in Zawia, Libyen

Vorsitzender:	Prof. Dr.-Ing. P. Steinberg
Gutachter:	Prof. Dr.-Ing. H.P. Berg
Gutachter:	Prof. Dr. E. Sigmund

Tag der mündlichen Prüfung: 18.11.2009

I dedicate this work to my family, my wife, and my children

Abstract

Powerful, smooth, compact and light combined with multi-fuel capability are the main features of the rotary engine. The Wankel engine superb power-to-weight ratio and reliability make it not only suitable for automobile application, but also particularly well suited to aircraft engine use and it can replace the reciprocating piston engine in many areas of use such as sport cars, motorcycle, boats, and small power generation units etc.

Since the physics that taking place inside Wankel engine combustion chambers are exceedingly complex, a numerical CFD studies were obtained to understand the unsteady, multidimensional fluid flow and fuel-air mixing inside the combustion chamber of the Wankel rotary engine during the intake and compression cycles. The effects of the engine combustion chamber design and operating parameters on fluid flow and fuel-air mixture formation were investigated: engine velocity, direction of fuel injection into the combustion chamber, with emphasize on diesel and hydrogen injection fuels. The injector nozzle size, injected fuel velocity, the position of injector and angle of injection were also investigated.

A well known CFD Code AVL-Fire v7.x and v8.x with its moving mesh capability was used to simulate one rotor side, presenting the intake and compression stroke. The CFD-Code is capable of simulating the complex movement of the rotor and calculates the fluid flow parameters; temperature, pressure, velocity, volume changes and combustion variables. The k-ε model is the most widely used turbulence model in practical engineering applications and was used by the code to calculate the flow variables.

A variety of ignition and combustion models available by this code including: eddy breakup or magnussen model, coherent flame (CFM) model, PDF model, and TFSC model. The fire combustion module enables the calculation of species transport/mixing phenomena and the simulation of combustion in internal combustion engines and technical combustion devices under premixed, partially premixed or a non-premixed conditions. In combination with fire spray model, the combustion module enables the calculation of spray combustion process in direct injection engines; where mixture formation and combustion are simultaneous process exhibiting a significant degree of interaction and interdependence. The droplet breakup models available with suitably adjusted model parameters are highly recommended for this type of application.

In previous work conducted by Fushui Liu [1], in this chair of combustion engines and flight propulsion, at BTU-Cottbus, the fire code has been validated and approved for high velocity gas injection of hydrogen and it helps to choose and adjust the different model variables for hydrogen injection. A geometrical data of a new family of compact, lightweight Wankel engine for multi-purpose applications were designed and are currently under an optimization test was used in this research work.

In the first part of this research simulation work, concentration on understanding the flow field inside the combustion chamber is a part of this research work to help understanding engine fuel injection configuration. The engine is capable of burning different kind of liquid and gas fuels. The diesel fuel is the most extreme liquid fuel and more complicated in comparison to the other light liquid fuels regards to its mixture formation and combustion. So, it is important in the second part to consider the diesel fuel injection configuration to study the mixture formation, injector configuration (position, injection angles etc.) and ignition.

The third part is concentrated on hydrogen mixture formation and the best engine configuration to burn hydrogen, as hydrogen is the lightest and extremist gas fuel with regard to its mixture formation and combustion.

The results show that a swirl flow started at early stage of intake and continued just before the end of compression stroke, when the distance between the rotor and the housing become very close. This swirl is advantage for mixture formation of low-pressure direct injection of hydrogen.

The diesel spray results show that the injector with angle between holes of 18º gives better fuel penetration and covers most of the combustion chamber at spray angle of 32º.The spark plug position of 31mm from short axis shows better mixture concentration than the near one (18mm) and hence better ignition chances.

Multi-hole Hydrogen injector and multi-injector gives better fuel distribution and reduces the maximum rail pressure needed to inject the right amount of hydrogen in very limited short time.Low-pressure direct hydrogen injection has simpler installations and gives almost homogeneous mixture at the end of compression stroke and hence better combustion.High-pressure hydrogen direct injection is more sophisticated system, needs a very high injection pressure and complicated pressure instruments installation.

Acknowledgement

First of all and the greatest important, all praises and thanks are due to my ALMIGHTY GOD for all his blessings without which nothing of my work could have been done.

I would like to thank my supervisor Prof. Dr. Ing. Heinz Peter Berg, for his inspiration and encouraging way to guide me to a deeper understanding of my work, and his invaluable comments during the whole work of this dissertation. Without his encouragement and constant guidance, I could not have finished this dissertation. He was always there to meet and discuss about my ideas related to my work and to proofread and make important comments throughout my papers and chapters, and also to ask me important questions that helped me think through my problems. His efforts are very much appreciated.

Also, I would like to thank Wankel Super Tech staff members, especially Dr. Rudolf Klotz, Prof. Dr. Ernst Sigmund, Herr Norman Müller and Herr Dankwart Eiermann for their continuous support including the geometrical engineering drawing supply.

I would like to thank all my colleagues in the Chair for Combustion Engines and Flight Propulsion, Brandenburg University of Technology in Cottbus (BTU Cottbus), Dr. Fushui Liu, for his support and encouragement when I just came to this chair. Dr. Oleksiy Antoshkiv, Thanapol Poojitganont, Axel Himmelberg, Michael Prinzler, with whom I have had and still have a wonderful time. They provided me with a very friendly atmosphere and ensured that working at the department was always fun.

Last, but not the least, I would like to thank my beloved wife, my family, my children for their firm support and patience in the most important period of my life.

Table of Contents

ABSTRACT ..... **I**

ACKNOWLEDGEMENT ..... **III**

TABLE OF CONTENTS ..... **V**

LIST OF FIGURES ..... **IX**

LIST OF TABLES ..... **XV**

CHAPTER 1 INTRODUCTION **1**

1.1 Introduction **1**
1.2 Problem overview **3**
1.3 Multi-fuel engine modeling **6**
1.4 Objectives **6**
1.5 Dissertation overview **7**

CHAPTER 2 WANKEL ROTARY ENGINE AND HYDROGEN APPLICATION **9**

2.1 Rotary Wankel engine **9**
2.1.2 Engine history 10
2.1.3 Wankel rotary engine application 13
2.1.4 Principal of operation 14
2.1.5 Advantages 16
2.1.6 Disadvantages 16
2.1.7 Engine main parts 17

2.2 Hydrogen fuel **27**
2.2.1 Hydrogen economy 27
2.2.2 Hydrogen as fuel of future 27
2.2.3 Hydrogen fuel physical properties 28
2.2.4 Combustion of hydrogen fuel 29
2.2.5 Theoretical thermal efficiency 29

2.3 Hydrogen Fuel mixture strategy **31**
2.3.1 External mixture formation system 31
2.3.2 Direct injection 32

2.4 Power output in comparison to gasoline 35
2.5 Emissions 38
2.6 Summary 39

CHAPTER 3 REVIEW OF PREVIOUS CFD ROTARY ENGINE RESEARCH AND HYDROGEN ENGINE 41

3.1 Introduction 41

3.2 CFD engine modeling 41

3.3 Hydrogen engine 45

3.4 Liquid fuel engine 48

CHAPTER 4 CFD THEORY AND MATHEMATICAL FORMULATION 50

4.1 Introduction 50

4.2 Differential equations in Cartesian coordinates 51
4.2.1 Conservation of mass and momentum 51
4.2.2 Conservation of thermal energy 51
4.2.3 Passive scalar equation 52

4.3 Turbulence models 52
4.3.1 Introduction 52
4.3.2 k-ε model 53

4.4 Species transport 57
4.4.1 Introduction 57
4.4.2 General species transport model equations 58
4.4.3 Standard species transport model equations 59

4.5 Combustion 61
4.5.1 Introduction 61
4.5.2 Basic theoretical background 62

CHAPTER 5 CFD FLOW SIMULATION 67

5.1 Introduction 67

5.2 Types of investigation 67
5.2.1 Conceptual investigation 68
5.2.2 Specific investigation 68
5.2.3 Validation investigation 68

5.3 Modeling and simulation tools 68
5.3.1 Moving mesh 69
5.3.2 Dynamic geometry and boundary condition 70
5.3.3 Rezone data sets 72
5.3.4 Ramp 74

5.3.5 Analysis process 74

5.4 Wankel engine simulation 75
5.4.1 Engine geometrical data 78
5.4.2 Geometrical surface preparation 78
5.4.3 Volume grid preparation 83
5.4.4 Simulating differences of various fuel systems 85

5.5 Effects of different variables on flow fields 85
5.5.1 Effect of the rotor recess shape 85
5.5.2 Effect of inlet port surface area 91

5.6 Results 91
5.6.1 Flow velocity analysis 92
5.6.2 Effect of inlet port surface area 106

5.7 Total pressure 108

5.8 Temperature 111

5.9 Model validation 113
5.9.1 CFD models 113
5.9.2 Engine visualization 119

5.10 Discussion and conclusion 121
5.10.1 Discussion 121
5.10.2 Brief summary 123

CHAPTER 6 DIESEL SPRAY AND MIXTURE FORMATION FOR WANKEL ROTARY ENGINE 125

6.1 Introduction 125

6.2 Model preparation 126
6.2.1 Geometrical model 126
6.2.2 Nozzle configuration 126
6.2.3 Boundary condition 128
6.2.4 Initial condition 128
6.2.5 Spray file 130
6.2.6 Nozzle validation 132

6.3 Results 134
6.3.1 Spray angles 134
6.3.2 Spray starting angle 139
6.3.3 Engine speed 143
6.3.3 Injector position 150

6.4 Discussion and summary 156

CHAPTER 7 HYDROGEN INJECTION FOR ROTARY ENGINE AND COMBUSTION 158

7.1 Introduction 158

7.2 General hydrogen injection research 159
7.2.1 Volume grid validation 160
7.2.2 Hydrogen injection validation 162

7.3 Wankel engine hydrogen injection strategies 162
7.3.1 Injection hole size 166
7.3.2 Results 167

7.5 H2 low-pressure injection, real engine models 178
7.5.1 Geometrical surface preparation 178
7.5.2 Results 182
7.5.3 High-pressure injection 186
7.5.4 Results 188

7.6 Hydrogen combustion 192
7.6.1 Results 194
7.6.2 Effect of different initial parameters 197

7.7 Brief summary 208

CHAPTER 8 SUMMARY AND MAIN CONCLUSION 210

8.1 CFD Simulation 210

8.2 Wankel engine 211
8.2.1 Flow inside combustion chamber 211
8.2.2 Diesel mixture formation 211
8.2.3 Hydrogen mixture formation and combustion 212

8.3 General conclusion 213

8.4 Recommendations and future work 214

NOMENCLATURE 215

REFERENCES 218

List of Figures

Fig.1. 1 The world's oil peak with the producing areas 2
Fig.1. 2 The world's oil peak production 2
Fig.2. 3 Wankel engine main components [6] 15
Fig.2. 4 The main engine parts 17
Fig.2. 5 Rotary engine housing 18
Fig.2. 6 Peritrochoid curve of housing 19
Fig.2. 7 Engine rotor 20
Fig.2. 8 Rotor contour 21
Fig.2. 9 Gas sealing with springs 22
Fig.2. 10 Engine output shaft 23
Fig.2. 11 Intake and exhaust ports comparison 24
Fig.2. 12 RENENSIS cut-off seal (courtesy Mazda) 25
Fig.2. 13 Engine timing comparison in terms of degrees. 26
Fig.2. 14 stoichiometric air demand/calorific value for different fuels 29
Fig.2. 15 p-v and T-s diagrams of the Dual Combustion Cycle 30
Fig.2. 16 External mixture formation 32
Fig.2. 17 Low pressure hydrogen injection, 2 injectors per chamber by Mazda [52]. 33
Fig.2. 18 High-pressure direct injection 34
Fig.2. 19 A typical schematic diagram of the high-pressure hydrogen 34
Fig.2. 20 Cylinder charging concept, Gasoline and hydrogen fueled engines. [1] 36
Fig.2. 21 IMEP for different cylinder charging concept, [2] 37
Fig.2. 22 Typical full-load hydrogen combustion, in comparison with gasoline, [2] 38
Fig.2. 23 Typical NO_x emission for a hydrogen engine vs ϕ,(equivalent ratio) [3,18]. 39
Fig.5. 1 Defining moving walls 70
Fig.5. 2 Grid rezone 73
Fig.5. 3 Simulation time 74
Fig.5. 4 Engine test bench, with a single rotor engine (Basic engine). 76
Fig.5. 5 Modular design concept 77
Fig.5. 6 engine trochoid 79

Fig.5. 7 Engine housing surface 80
Fig.5. 8 Engine housing with inlet/outlet ports connected 80
Fig.5. 9 Rotor surface and rotor recess connected. 81
Fig.5. 10 Rotor surface connected to the housing. 82
Fig.5. 11 The rotor three contact points 83
Fig.5. 12 Volume grid at different angle positions 84
Fig.5. 13 Rotor different geometrical recess shapes 87
Fig.5. 14 KKM 407 Rotor recess shape 88
Fig.5. 15 Volume grid (mesh) at the inlet port is just closed. 89
Fig.5. 16 Boundary condition 90
Fig.5. 17 Rectangular and cylindrical inlet ports 91
Fig.5. 18 Velocity vector during inlet cycle (2000 rpm), Re = 53733.6, R_0 = 935.5 95
Fig.5. 19 Flow regions 96
Fig.5. 20 Cross-sectional cut planes 97
Fig.5. 21 Inlet flow velocity during inlet port open (2000 rpm), Re = 53733.6, R_0 = 935.5 97
Fig.5. 22 Comparison of flow velocity vector at [310°], after inlet port closed 99
Fig.5. 23 Flow velocity vector during compression cycle 100
Fig.5. 24 KKM-407 Model during compression 101
Fig.5. 25 Flow velocity vector, TDC-540°, at (2000 rpm) Re = 53733.6, R_0 = 935.5 102
Fig.5. 26 Inlet flow velocity at (6000 rpm), Re = 161200.8, R_0 = 935.5 103
Fig.5. 27 Swirl flow, at (4000 rpm), Re = 107467.2, R_0 = 935.5 104
Fig.5. 28 Maximum Flow velocity vs. Engine speed at TDC, 540° 105
Fig.5. 29 Flow velocity at the end of compression (TDC-540°, (6000 rpm), Re = 161200.8, R_0 = 935.5 106
Fig.5. 30 Velocity vector during inlet cycle at (6000 rpm), Re = 161200.8, R_0 = 935.5 (rectangular port) 107
Fig.5. 31 Flow velocity at TDC, (2000 rpm), Re = 53733.6, R_0 = 935.5 107
Fig.5. 32 Fluid mean total pressure [pa] at (2000 rpm), Re = 53733.6, $R0$ = 935.5 109
Fig.5. 33 Fluid mean total pressure [pa] at (4000 rpm), Re = 107467, R_0=935.5 110
Fig.5. 34 Fluid mean temperature [K] at (2000 rpm) Re= 53733.6, R_0= 935.5 112
Fig.5. 35 Fluid mean Temperature [k] at (4000 rpm) Re= 107467, R_0= 935.5 112

Fig.5. 36 Flow model and boundary condition 113
Fig.5. 37 Velocity vector display of three planes 115
Fig.5.38 Boundary condition 116
Fig.5. 39 Velocity vector display 118
Fig.5. 40 Illustration of the transparent rotary engine for flow visualization, [37] 119
Fig.5. 41 Effect of recess shapes on flow fields, [37] 120
Fig.5. 42 Experimental results [37] and CFD 2D-Model, comparison 121
Fig.6. 1 3-D geometrical surface of rotor No. 5 at 54º BTDC 127
Fig.6. 2 Injector and spark plug configuration 128
Fig.6. 3 Different spray angles at engine TDC 129
Fig.6. 4 Angles between holes possibilities 130
Fig.6. 5 Model boundary condition 131
Fig.6. 6 Spray cone at 18º angle between holes and 32º spray angle 131
Fig.6. 7 Nozzle flow profile comparison 132
Fig.6. 8 Liquid and fuel vapor penetration evaluation; (a) 800 bar injection 133
Fig.6. 9 The plane cut distances from nozzle center 134
Fig.6. 10 Mixture equivalent ratio [-], spray angle 27º 135
Fig.6. 11 Mixture equivalent ratio [-], spray angle 29º 136
Fig.6. 12 Mixture equivalent ratio [-], spray angle 32º 137
Fig.6. 13 Mixture equivalent ratio [-], for different spray angles 27º, 32º, ... 138
Fig.6. 14 Equivalence ratio, spray starts 20º BTDC 140
Fig.6. 15 Equivalence ratio, spray starts 29º BTDC 141
Fig.6. 16 Equivalence ratio, spray starts 39º BTDC 142
Fig.6. 17 Injector and spark plug positions 143
Fig.6. 18 Mixture equivalence ratio at engine speed (300 rpm), Re = 8060, R_0 = 935.5 144
Fig.6. 19 Mixture equivalence ratio at engine speed (2000 rpm), Re = 53733.6, R_0 = 935.5 145
Fig.6. 20 Mixture equivalence ratio at engine speed (4000 rpm), Re = 107467, R_0=935.5 146
Fig.6. 21 Mixture equivalent ratio, [-], at (P1, and P2), for different engine speed 148
Fig.6. 22 Main spray 50 mm^3, for (2000 rpm), Re = 53733.6, R_0 = 935.5 149

Fig.6. 23 Equivalence ratio [-], main spray 50 mm^3, (2000 rpm), Re = 53733.6, R_0 = 935.5 150
Fig.6. 24 Injector, spark plug position and result planes (KKM-407) 151
Fig.6. 25 KKM-407 with injector fitted at 31 mm before short axis, spray angle 32º, (2000 rpm), ... 152
Fig.6. 26 Injector, spark plug position and result planes (KKM-500) 153
Fig.6. 27 KKM-500, spray angle 32º, 31 mm to short axis, (2000 rpm), Re = 53733.6, R_0 = 935.5 154
Fig.6. 28 KKM-500 spray angle 40º,31 mm to short axis, (2000 rpm), Re = 53733.6, R_0 = 935.5 155
Fig.7. 1 Three validation meshes with different smoothness 160
Fig.7. 2 The calculated velocity fields of three meshes comparison, [1] 161
Fig.7. 3 Injection stream penetration and angle comparison to the schlieren capture 162
Fig.7. 4 Simulated and experimental density gradients of one hole injector, [1] 163
Fig.7. 5 Single hole injector, stream penetration comparison 163
Fig.7. 6 Injectors position and direction 164
Fig.7. 7 Low-pressure gas injector installation 165
Fig.7. 8 Effect of injector installation hole 165
Fig.7. 9 Three models with different nozzle-hole size 167
Fig.7. 10 Flow Mach number 169
Fig.7. 11 Flow total pressure 169
Fig.7. 12 H2 mass fraction 170
Fig.7. 13 H2 total mass for different cylinder pressure 170
Fig.7. 14 H2 mass flow rate for different cylinder pressure 171
Fig.7. 15 Maximum total pressure for different cylinder pressure 171
Fig.7. 16 Maximum flow Mach no. for different cylinder pressure 172
Fig.7. 17 H2 total mass for different cylinder pressure 172
Fig.7. 18 H2 mass flow rate for different cylinder pressure 173
Fig.7. 19 Maximum total pressure for different cylinder pressure 173
Fig.7. 20 Maximum flow Mach no. for different cylinder pressure 174
Fig.7. 21 H2 total mass for different cylinder pressure 174

Fig.7. 22 H2 mass flow rate for different cylinder pressure 175
Fig.7. 23 Maximum total pressure for different cylinder pressure 175
Fig.7. 24 Maximum flow Mach no. for different cylinder pressure 176
Fig.7. 25 H2 total mass, (1e+5 pa and 5e+5Pa) 177
Fig.7. 26 H2 total mass, (1e+6pa, 1.5e+6pa and 2e+6pa) 177
Fig.7. 27 Low pressure injector positions 178
Fig.7. 28 A single 3-holes injector, position-1 179
Fig.7. 29 Double, 3-holes injector installation, position-1 180
Fig.7. 30 A single 3-holes injector, position-2 181
Fig.7. 31 Injected hydrogen mass fraction 182
Fig.7. 32 Pressure and temperature display at TDC 183
Fig.7. 33 Mixture equivalence ratio at spark plug position 184
Fig.7. 34 Injected hydrogen mass fraction 185
Fig.7. 35 Pressure and temperature display at TDC 186
Fig.7. 36 Mixture equivalence ratio at spark plug position 186
Fig.7. 37 High-pressure hydrogen injection geometry 188
Fig.7. 38 Injected hydrogen mass fraction 189
Fig.7. 39 1-hole injector equivalence ration at spark plug position 190
Fig.7. 40 3-hole injector equivalence ration at spark plug position 191
Fig.7. 41 Maximum injection total pressure 192
Fig.7. 42 Hydrogen combustion model 193
Fig.7. 43 combustion reaction progress variable at 2ms 194
Fig.7. 44 Pressure and temperature changes 195
Fig.7. 45 Rate of heat release, Tke and dissipation rate changes 196
Fig.7. 46 Mean NO_x mass fraction 197
Fig.7. 47 Effect of initial temperature on end mean pressure, temperature and rate of heat release 198
Fig.7. 48 Effect of initial temperature on NO_x mass fraction 199
Fig.7. 49 Effect of initial pressure on mean temperature, pressure and rate of heat release 200
Fig.7. 50 Effect of initial Pressure on NO_x mass fraction 201

Fig.7. 51 Effect of mixture concentration on mean temperature and pressure 202
Fig.7. 52 Effect of mixture concentration on rate of heat release and accumulated heat released 203
Fig.7. 53 Mixture concentration effect on mean Tke and dissipation rate 204
Fig.7. 54 Mixture concentration effect on mean NO_x mass fration 206
Fig.7. 55 NO_x as a function of mixture concentration 207
Fig.7. 56 Effect of concentration on flame speed at different initial temperature 207
Fig.8. 1 Hydrogen engine load control proposal..... 214

List of Tables

Table 2. 1 Physical properties of hydrogen and gasoline [2] 28
Table.4. 1 Values of model constants 57
Table 5. 1 Setup description 71
Table 5. 2 Setup description 71
Table 5. 3 Grid coordinates and boundary setting 72
Table 5. 4 Engine power data 77
Table 5. 5 Engine geometrical data 78
Table 5. 6 Engine timing data 78
Table 5. 7 fluid initial conditions 90
Table 5. 8 Reynolds No., velocity No. and engine speed result comparison 93
Table 5. 9 Average total pressure [Pa], all rotor geometries, different engine speeds 108
Table 5. 10 Mean fluid temperature [k], all rotor geometries, different engine speeds 111
Table 5. 11 Initial and boundary condition 114
Table 5. 12 Initial and boundary condition 116
Table 6. 1 Models initial condition 129
Table-7. 1 Models initial condition 168
Table-7. 2 Models initial conditions 188
Table-7. 3 Model initial conditions 194

1

Introduction

1.1 Introduction

"*The fifth revolution will come when we have spent the stores of coal and oil that have been accumulating in the earth during hundreds of millions of years... It is to be hoped that before then other sources of energy will have been developed... Whether a convenient substitute for the present fuels is found or not, there can be no doubt that there will have to be a great change in ways of life. This change may justly be called a revolution, but it differs from all the preceding ones in that there is no likelihood of its leading to increases of population, but even perhaps to the reverse.*" Sir Charles Galton Darwin, 1952, [49].

The world's population is expected to increase to ten billion in the 21st century, accompanied by a rapid increase in energy consumption. This will bring about a shortage of oil fuel resources and global warming caused by CO2 emissions.

The world's resources of oil are limited and non-renewable. Therefore production must reach a peak and then decline. About half of our oil reserves have been already consumed, the half that was easiest to produce. The oil field discovery rate has been declining for 40 years despite extensive exploration with advanced technology, and there is uncertainty about the timing of the peak of oil production, but the predictions range are from 2003 to 2020. There is no doubt about the fact that oil production will not meet demand in the near future. When that happens, oil prices will rise substantially and the global economy will be adversely affected.

The basic solution to these problems will be to use energy resources more efficiently and to switch from fossil fuels to some renewable energy resources. Nuclear, solar, wind and water energy are some of the alternative energy sources. Despite of the nuclear energy, all other energy resources are renewable and environmentally friendly to be used in power generation and power plants.

Fig.1.1 and Fig.1.2 show the historical and predicted future of oil production in 2003, by newsletter of Association for the Study of Peak Oil. [50]

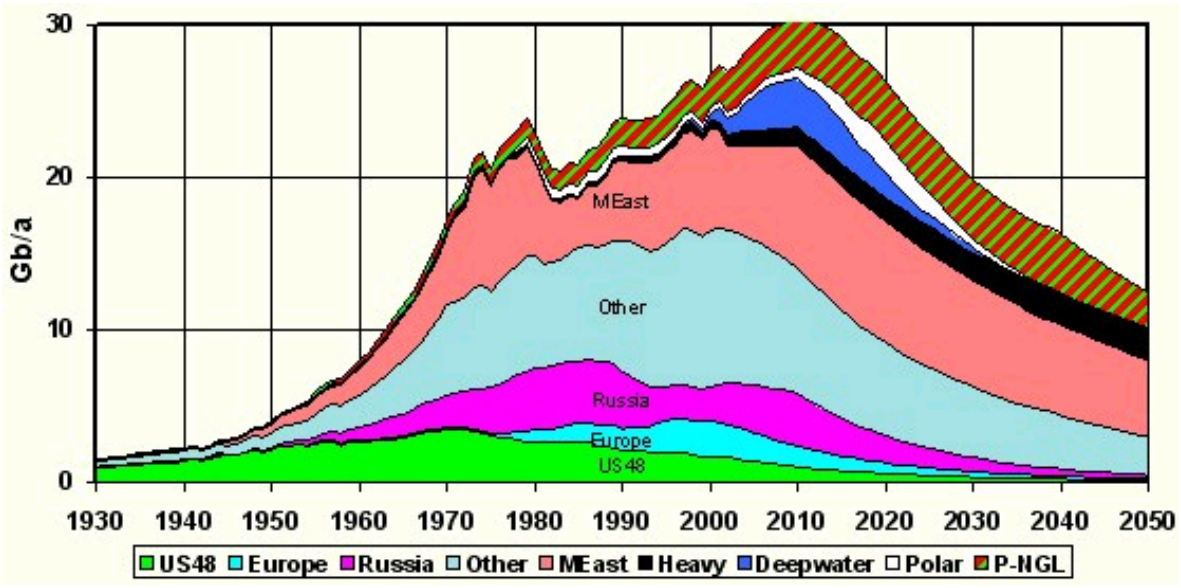

Fig.1. 1 The world's oil peak with the producing areas

Here is the Hubbert curve for the whole Earth, the chart that puts it all together.

The part before 2003 is historical fact, and the part that comes after is extrapolation.

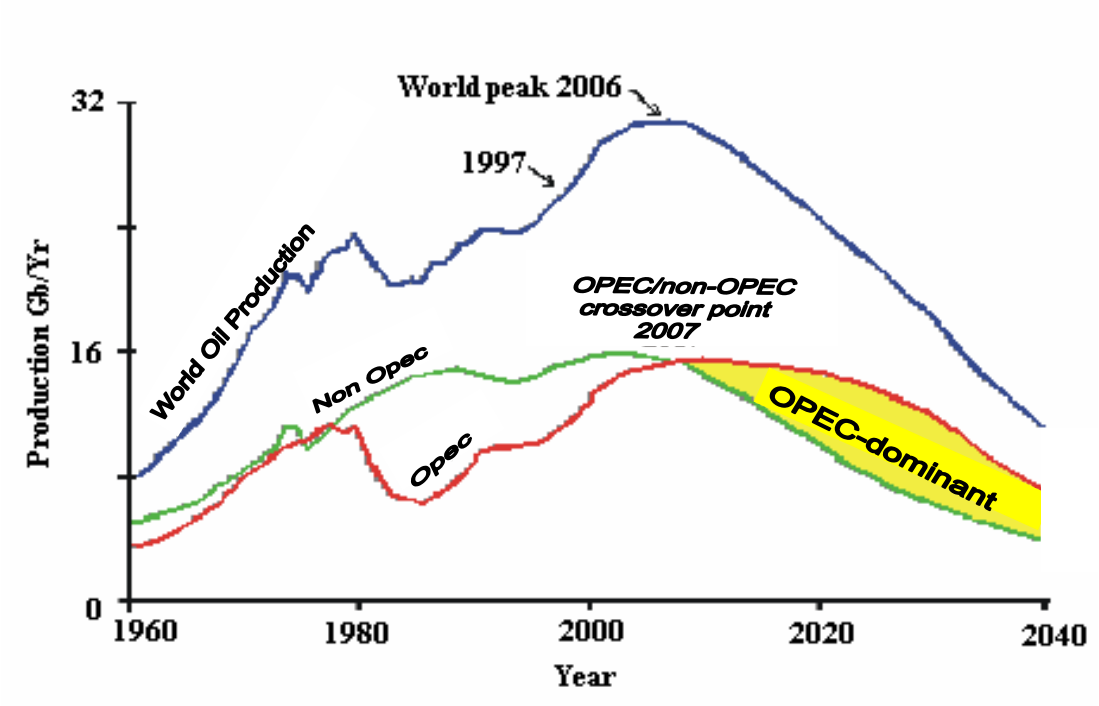

Fig.1. 2 The world's oil peak production

These graphs appeared in the May 2003 newsletter of Association for the Study of Peak Oil. [50]

However, electricity and Hydrogen fuel are more suitable to be used to power the automotive or transportation system as an alternative to the fossil fuels.

Hydrogen is an attractive transportation fuel as it is the least polluting fuel that can be burned in an internal combustion engine, or to be used in fuel cell to produce electricity. Hydrogen is the most abundant element in the universe and one of the most abundant on earth, but it does not occur free in nature in useful quantities and it has to be made normally, by steam reforming of natural gas or by splitting water H_2O to get hydrogen.

Many researchers have stated that Wankel rotary engine is better suited for multi-fuel including hydrogen than the reciprocating engine. In rotary engine, the intake of the fuel/air mixture occurs in a different location from the place where hot exhaust gases are expelled. This creates a cold zone and a hot zone within the engine, preventing any pre-ignition or backfire possibilities during the intake or compression stroke, which is normally occurred in the reciprocating engine. Also, the small quenching distance of hydrogen fuels lets the fuel to be burned near the wall and through the long and narrow combustion chamber of the Wankel engine.

A major task of the future research work is concentrated on the development of an advanced hydrogen internal combustion engine with absolute and specific power and torque characteristics exceeding those of today's gasoline or diesel engines with emphasis on efficiency and emission aspects.

1.2 Problem overview

The transportation system is very important to the entire world today. Nowadays, this system is dependent on engines that burn mainly gasoline or diesel fuels in an internal combustion engines. Therefore, concerns about atmospheric pollution and new strict environment legislations, oil limited resources and production prices, continue to stimulate research on new, clean and fuel efficient vehicle technologies.

With this trend in mind, the use of alternative, renewable fuels and innovative vehicle architectures has been a proposed solution to help reduce harmful emissions and to substitute the oil shortage and high prices in the coming near future.

In recent years, activity in alternative fuel research, such as bio-diesel, ethanol, hydrogen, natural gas, and propane has increased rapidly. Except hydrogen and bio-diesel, all other alternative fuels are considered as fossil fuels and are subject to the limited global production resources and, more or less, have its contribution to produce air pollutant emissions. The use of bio-diesel fuel these days has its own contribution on the food crisis in poor countries and the global food higher prices.

In feasible future, the best and unlimited clean alternative energy carrier to fossil fuels is hydrogen to drive our mobility on fuel cell or to be burned in internal combustion engines. Hydrogen has advantages over conventional fuels when used in an internal combustion engine. The characteristics of hydrogen improve engine efficiencies as well as dramatically reduce emissions. It is the most abundant element on the plant, and it is the cleanest burning fuel in comparison with fuels, that bases of carbon atoms. It also has the potential of producing only water when reacting with oxygen. Carbon emissions (CO_2, CO, and HC) from hydrogen engine are virtually nonexistent. The primary emissions are nitrous oxides (NO_x). A lean hydrogen mixture has an equivalent octane rating of 140, [67]. The higher octane rating allows higher compression ratio than conventional gasoline engines. This property alone adds a potential 15-25% increase in engine efficiency.

Electric vehicles have long held the promise of zero emissions vehicles. However, battery powered electric vehicles have not been accepted by general public, in large part, because of their very limited range and its long charging time.

The fuel cell vehicles are thought to be more of far-term reality. The major obstacles in the way of use fuel cells are their high cost and low reliability. Compared with using fuel cell as a power source, the hydrogen engine achieves economic feasibility because it is based on existing engine design.

However, the normal piston hydrogen engine with homogeneous charge has suffered from a series of pre-ignition and back fire caused mainly by hot surfaces like exhaust valves, spark plug electrodes and deposits on combustion walls, [66]. Most of these combustion difficulties can be minimized in rotary engine, mainly because of its combustion chamber design differences, and no hot surfaces reported because of airflow cooling effect and there are no exhaust valves in rotary engine.

Furthermore, many researchers have stated that Wankel rotary engine is better suited for multi-fuel usage and hydrogen than the normal piston reciprocating engine, basically because the rotary engine intake of the fuel/air mixture occurs in a different location from the place where hot exhaust gases are expelled. This creates a cold zone and a hot zone within the engine, preventing any pre-ignition or backfire possibilities during the intake or compression stroke, which is normally occurred in the reciprocating engine.

The hydrogen flame speed is much higher than that of conventional fuels, causing engine knock due to its sudden heat release in normal piston engine. The long combustion chamber of Wankel rotary engine makes the flame front travels longer which reduces the sudden heat release and hence eliminates engine knock.

Also, the small quenching distance of hydrogen fuels lets the fuel to be burned near the wall and through the long and narrow combustion chamber ends of the Wankel engine.

However, one of limitation of hydrogen vehicle to be widespread is the limitation of on board storage. Because of its low density requires considerably higher volume and higher storage system mass than the existing liquid fuel vehicles. The use of lightweight compact rotary hydrogen engine can compensate for the larger size and greater weight of hydrogen storage systems and hence increases the overall vehicle efficiency, [66].

Also, the hydrogen engine vehicles development has suffered from the lack of hydrogen infrastructure and filling stations. To solve such problems of hydrogen availability, several countries throughout the world are investing in hydrogen production and to build new filling stations, but it is still far to produce and build enough filling stations and handling networks.

During this transition period from 100% fossil fuels to some share (or 100%) of hydrogen vehicle use, it is necessary to run the vehicle engine on multi-fuel, such as hydrogen when it is available and on diesel or gasoline where hydrogen is not possible to be found.

Based on the above analysis, the best engine reported to be capable of burning most of liquid and gas fuels including hydrogen is the rotary Wankel engine and therefore, the strategy of this research is to develop a new rotary Wankel engine with multi-fuel system to burn diesel and hydrogen. To achieve this goal, it is necessary to understand how the different variables that affecting the combustion process inside this engine including flow and mixture formation in order to reach better combustion with higher engine efficiency and fuel consumption as well as lower pollutants.

However, a major task of today and future research work is always concentrated on the development of an advanced hydrogen internal combustion engine with absolute and specific power and torque characteristics exceeding those of today's gasoline or diesel engines with emphasis on efficiency and emission aspects.

1.3 Multi-fuel engine modeling

Multi-fuel engine is that engine capable of burning liquid and gas fuels. It has been reported that rotary engine has this capability of running on multi fuel, liquid and gas fuels.

Diesel fuel is a heavy fuel and is the most difficult fuel to be simulated and ignited, from point of view of mixture formation, evaporation and combustion, that makes the diesel fuels at the one extreme edge of liquid fuels. It is well known that any engine burns diesel can burn any other liquid fuels. Therefore, in this research, only diesel fuel mixture formation was simulated and can present most of liquid fuels.

On the other extreme side Hydrogen gas has the lowest density in comparison to the other gas fuels, that means a huge volume of gas should be injected to the engine cylinder makes the injection velocity to be very high.

Hydrogen injection and mixture formation models simulation is the most difficult simulation work that needs finer grids and consumes more time, clearly because of hydrogen injection supersonic speed and high injection pressure. Therefore, any model used in this research for hydrogen injection can be simply used also for any other gas fuel.

In this research investigation, the diesel fuel is presented on liquid fuels and hydrogen presented on gas fuels as both fuels are the extremist in their categories.

1.4 Objectives

Based on the above discussion, the time of hydrogen use in world's mobility is coming soon, and may be it is not too late for researchers and scientist to develop and prepare the right technology before it is too late. The main objectives of this work are concentrated on diesel and hydrogen mixture formation inside Wankel rotary engine, in order to develop an engine can be run on diesel and in the same time can be switched to hydrogen.

To achieve this objective the engine can be fitted with two injectors, one for diesel injection and the other for hydrogen. But, it is necessary to understand the flow behavior inside the engine combustion chamber, in order to optimize the injection position and direction of fuel spray. Therefore, the objectives of this research will be as follows:

- Investigation and analysis of flow behavior inside different combustion chamber shapes of rotary Wankel engine, to understand the effect of recess shape and size on flow patterns inside the combustion chamber.
- Investigation and analysis of diesel mixture formation, including injector position and spray angles.
- Investigation and analysis of hydrogen mixture formation and its combustion.

All these investigations will be carried out with the help of AVL-Fire 7.3/8.31 and validation of these models, either by using simple models or from literature when it is possible.

1.5 Dissertation overview

This thesis documents and details of work carried out to develop and design a better multi-fuel Wankel rotary engine by concentrating on optimization of mixture formation and injection strategies that leading to better engine combustion and hence better engine efficiency.

The next chapter (chapter 2) will deal in more details with the Wankel rotary engine history, engine main components and the principals of engine operation. Also, it will describe in more details the hydrogen economy and hydrogen fuel characteristics.

The third chapter will preview some of literature works concerning the hydrogen fuel and the Wankel rotary engine. Lack of CFD simulation work on Wankel engine in literature, especially when hydrogen is concerned, makes this chapter to be limited to some of engine simulation and to experimental flow visualization work.

The forth chapter will introduce in summary the governing equations of motion for compressible reactive flow, heat transfer, species transport, spray and combustion models, in its form that used by the AVL-Fire main-program, and for more details refer to the program manual, theory part.

In chapter 5, investigations of flow patterns inside different combustion chambers that fitted with different rotor recess shapes. The results and conclusion of this part is also presented.
The sixth and seventh chapters presented the mixture formation and combustion work of diesel and hydrogen respectively.
Chapter eight presented the general conclusion and recommendations of future work.

2

Wankel Rotary Engine and Hydrogen Application

2.1 Rotary Wankel engine

The highly advanced Wankel rotary engine is a promising engine for use in general aviation aircraft and suitable for various stationary and mobile applications. Advantages of the Wankel rotary engine over conventional reciprocating piston engine for use in general aviation aircraft and mobile applications include a higher power-to-weight ratio, larger specific power output from higher allowable speed operations, simpler and more compact due to fewer moving parts; multi-fuel capability and lower noise and vibration levels, due to non-reciprocating parts.

On the other hand, Wankel rotary engine has some drawbacks in using liquid fuels, such as gasoline and diesel fuels. However, the long and narrow combustion chamber makes the flame travels to long and cannot reach the far ends of the combustion chamber. Also, low flame speed and relatively high quenching distance of liquid fuels, gasoline and diesel, preventing the flame from reaching the very narrow distance at the rotor ends during combustion. As a result, high fuel consumption and high hydrocarbon pollutant emissions are the main drawbacks of Wankel engine burning fossil liquid fuels, since it was firstly come to application. When comes to hydrogen fuels, reciprocating hydrogen engines have serious problems of a pre-ignition and backfire still to be solved.

However, it was believed that the best choice for Wankel engine is hydrogen fuel and the best choice for hydrogen fuel is Wankel engine

In fact, the rotary Wankel engine is better suited for hydrogen than the reciprocating engine. In rotary engine, the intake of fuel-air mixture occurs in a different location from the place where hot exhaust gases are expelled. This creates a cold zone and a hot zone within the engine, preventing any pre-ignition or backfire possibilities during the intake or compression stroke, which is normally occurred in the reciprocating engine. Also, the small quenching

distance of hydrogen fuels lets the fuel to be burned near the wall and through the long and narrow combustion chamber of Wankel engine. In hydrogen-fueled engine the flame velocity of hydrogen is much higher than any other fuel, which gives better thermodynamic efficiency as the heat release almost takes place at constant volume. However, unlike conventional SI engine fuels, hydrogen has wide flammability limits allowing the engine to run at extremely lean mixture. This is favorable as varying the strength of the charge rather than the quantity can control the engine. This allows the hydrogen-fuelled engine to run without throttling of the air supplied and just varying the fuel flow rate can vary the power output, and only at low load conditions can apply a little throttling for better combustion stability, [35].

In addition, the Wankel rotary engine is inherently suited for direct-injection, stratified charge operation. Successful direct injection operation will reduce the engine's brake specific fuel consumption by allowing for leaner operations.

The direct injection stratified-charge engine combines the operation principals of diesel and spark ignition engine, with a thermal efficiency close to that of diesel engine. The direct injection stratified charge has also demonstrated a wide fuel tolerance without a loss in performance.

The disadvantage of conventional fuel DI stratified charge engine is the high level of unburned hydrocarbons at light load operation. Research efforts are directed towards decreasing the level of unburned hydrocarbons at light load operation due to improvements of the combustion chamber geometrical parameters (swirl, tumble etc.), to improve the turbulent combustion inside the chamber.

Direct injection together with turbo-charger engine technology is the most promising future of Wankel engine enhancing its power to weight ratio and reduces the hydrocarbon emersions.

2.1.2 Engine history

Soon after the invention of the conventional internal combustion engine, engineers realized that a tremendous savings in both weight and energy could be realized if the combustion of gasoline could be used to produce rotary motion directly instead of via the reciprocating action of the typical piston engine. The engineer who transformed this idea into a working

rotary engine was a German inventor Felix Wankel, beginning with drawings and prototypes in the 1920s. His first patent for a rotary piston engine was granted in 1936. He worked through the 1940s and 1950s to improve the design, when Wankel began collaboration with German car and motorcycle manufacturer NSU, that the Wankel rotary was developed to the point of actually being useable in a motor vehicle.

Early Wankel engines were of a design called ``Drehkolbenmaschine'' (DKM) in which an inner rotating housing and rotor move around a fixed central shaft. It was remarkably smooth in operation, and could run at fantastic speeds, but the engine need to be disassembled in order to change the spark plugs, this was not a good characteristic for a production power plant. So the ``Kreiskolbenmotor'' (KKM) was developed. In the KKM, the rotor and output shaft rotate inside a fixed housing. Spark plugs are easily accessible on the housing. Intake and exhaust are by ports on the housing, similar in principle to a two-stroke piston engine.

In Britain, Norton Motorcycles developed a Wankel rotary engine for motorcycles, which was included in their Commander; Suzuki also produced a production motorcycle with a Wankel engine, the RE-5. John Deere Inc, in the US, had a major research effort in rotary engines and designed a version, which was capable of using a variety of fuels without changing the engine. The design was proposed as the power source for several US Marine combat vehicles in the late 1980s.

After occasional use in automobiles, for instance by NSU with their RO-80 model, Citroen with the M35 and GS using engines produced by Comotor. Also, there are extensive attempts by General Motors and Mercedes Benz to design Wankel engine automobiles.

The most extensive automotive use of the Wankel engine has been by the Japanese company Mazda. After years of development, Mazda's first Wankel engine car was in the 1967 Mazda Cosmo. However they had the very bad luck of being released in the middle of efforts to decrease emissions and increase fuel economy. But the company continued using the Wankel rotary engine in their RX-7 sports car until 2002.

In the racing world, Mazda has had substantial success with two-rotor, three-rotor, and four-rotor cars, and private racers have also had considerable success with stock and modified Mazda Wankel-engine cars.

The refined Mazda HR-X... is a concept car that runs on pure, renewable hydrogen**,** and emits primarily only water vapor. Mazda engineers have improved the performance and fuel

efficiency of this engine, since its original debut in 1991. After many years of development Mazda re-launched the rotary engine called RENESIS with the new RX-8 sports car. RENESIS was awarded "The international engine of the year 2003" and already meets EURO-4 emissions. The Mazda vehicle shows that hydrogen can be safely used as a fuel with very high engine performance. [7]

Direct injection stratified charge rotary engine development began at Curtiss-wright during the mid 60's. Two prototype stratified charge military engines were designed and developed to the operational test stand phase. These engines displayed multi-fuel capability. However, neither engines matched the fuel economy of reciprocating spark ignition carbureted engine at that time. In 70's, research in the stratified rotary combustion engine continued. The curtiss-wright RC1-60, 60 cubic inch displacement, test engine was developed in 1974. Research efforts continued, analyzing the effects of nozzle configuration, increased rotor and housing temperature and increased compression ratio on specific fuel consumption with favorable results.

The development department of Mercedes-Benz in 1970 eventually succeeds in solving the engineering-design problems in their rotary direct injection wankel engine, fitted in C111-I and C111-II. The base engine was 600 cc, in three and four rotor, developing 280 hp and 350 hp. However, Mercedes-Benz discontinued work on this type of engine in 1971, in spite of its impressively smooth running characteristics and compact size.

Advantages of the stratified charge rotary engine include: high specific power density, multi-fuel capability, and no balancing problems due to lack of reciprocating parts and low NOx emissions. The main problem arises with the premixed spark-ignition Wankel engine, is its low fuel economy. Despite the encouraging results on the fuel economy, the direct injection rotary Wankel engine is not yet widely commercially produced.

In order to realize fully these attractive features of the Wankel rotary engine, it is necessary to have a good understanding of how engine design and operating parameters affect the unsteady, multidimensional fluid flow, fuel-air mixing process, and combustion inside the engine's combustion chambers.

2.1.3 Wankel rotary engine application

The Wankel engine superb power-to-weight ratio and reliability make it not only suitable for automobile application, but also particularly well suited to aircraft engine use. There was intense interest in them in this role in the 1950s when the design was first becoming well known, but it was at this same time that almost the entire industry was moving to the jet engine, which many believed would be the only engine in use within a decade. The Wankel suffered from a lack of interest, and when it later became clear that the jet engine was far too expensive for all roles, the general aviation world had already shrunk so much that there was little money for new engine designs. Nevertheless, interest in them for small aircraft has continued. [41]. A typical compact two-rotor engine used in small aircraft is shown in Fig.2.1.

The rotary Wankel engine can replace the reciprocating piston engine in many areas of use such as sport cars, motorcycle, bouts, and small power generation units etc.

The simplicity of the Wankel makes it ideal for mini, micro engine designs. The Micro Electro Mechanical Systems (MEMS) Rotary Engine Lab at the University of California at Berkeley has been developing Wankel engines approximately the size of an American penny (4-5 mm in diameter), displacing 0.0775 cc, Fig.2.2.

The goal is to eventually develop an internal combustion engine that will deliver 0.10 watts of electrical power; the engine itself will serve as the rotor of the generator, with magnets built into the engine rotor itself.

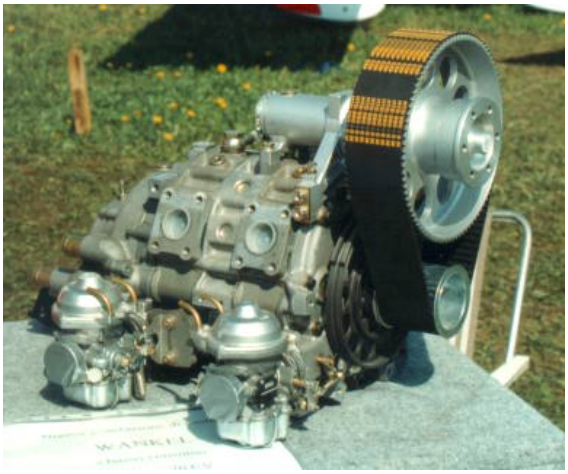

Fig.2. 1 Aircraft two rotor engine (Courtesy Flavio Giacosa)

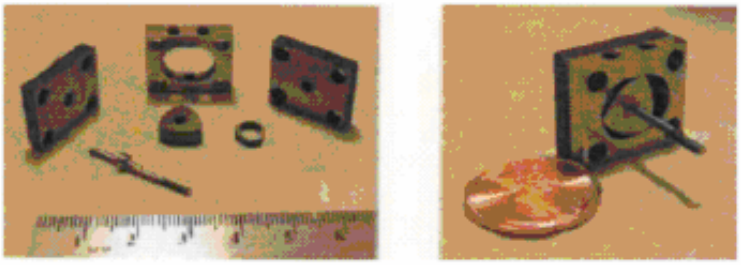

Fig.2. 2 MN30 Mini-Rotary engine [6]

The largest Wankel engine was built by Ingersoll-Rand, available in 550 horsepower one rotor and 1100 horsepower two rotor versions, displacing 41 liters per rotor with a rotor approximately one meter in diameter, it was available between 1975 and 1985. It was derived from a previous, unsuccessful, Curtiss-Wright design, which failed because of a well-known problem with all internal combustion engines; the fixed speed at which the flame front travels, limits the distance combustion can travel from the point of ignition in a given time, and thereby the maximum size of the cylinder or rotor chamber which can be used. This problem was solved by limiting the engine speed to only 1200 rpm and use of natural gas as fuel, this was particularly well chosen, as one of the major uses of the engine was to drive pumps on natural gas pipelines.

Aside from being used for internal combustion engines, the basic Wankel design has also been utilized for air compressors, and superchargers for internal combustion engines.

2.1.4 Principal of operation

The Wankel engine is four-stroke engine of a typical Otto cycle (intake, compression, expansion and exhaust strokes). The strokes are arranged sequentially around an epitrochoid (housing), unlike the reciprocating and oscillating motion of a piston engine. In the basic single rotor Wankel engine, a single (epitrochoid) housing surrounds a three-sided rotor (a triangle shape), which turns and moves within the housing. The sides of the rotor seal against the sides of the housing, and the corners of the rotor seal against the inner periphery of the housing, dividing it into three combustion chambers. Fig.2.3 shows the main engine parts.

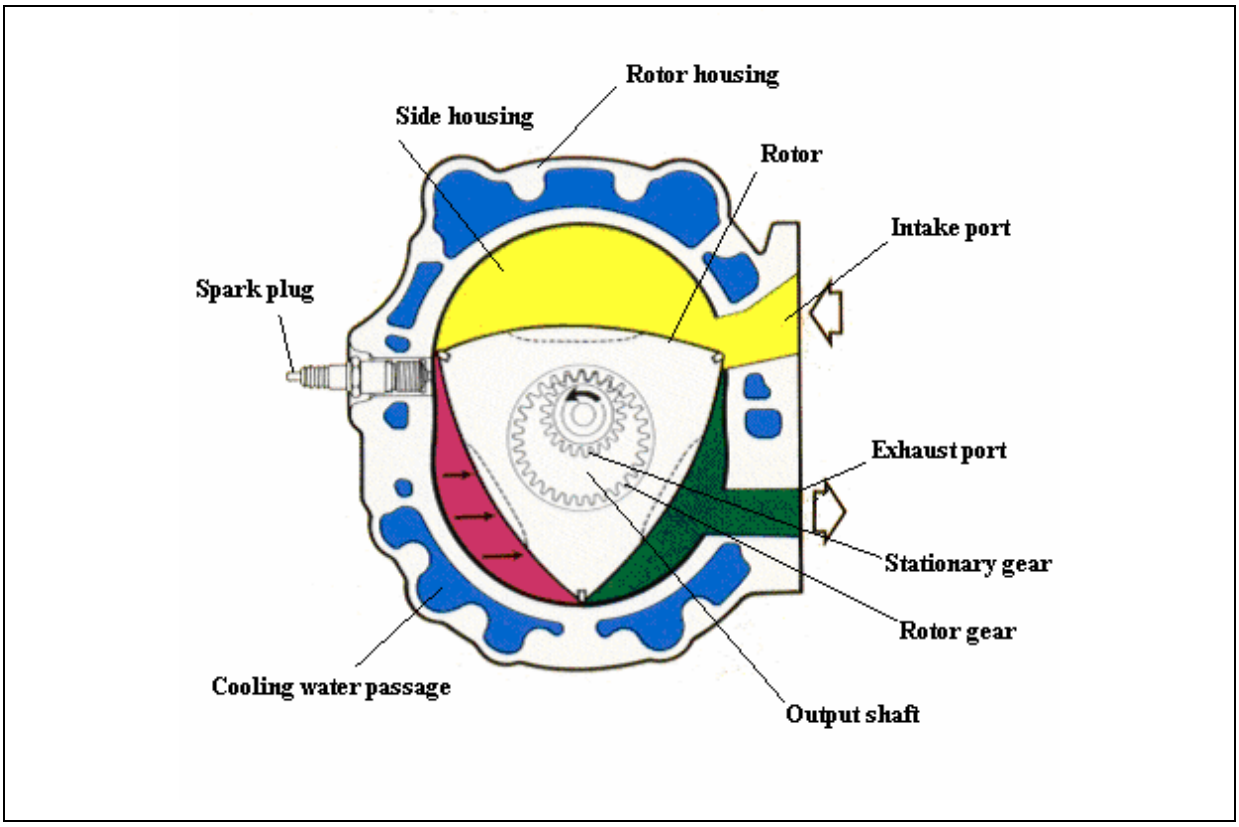

Fig.2. 3 Wankel engine main components [6]

As the rotor turns, each side of the rotor get closer and farther from the wall of the housing, compressing and expanding the combustion chamber similarly to the "strokes" in a reciprocating engine.

However, whereas a normal four-stroke engine produces one combustion stroke per cylinder for every two revolutions, the Wankel engine produces one combustion stroke every one revolution of the output shaft or three combustion strokes every one revolution of the rotor.

Since the Wankel output shaft is geared to spin at three times the rotor speed, this becomes one combustion stroke per output shaft revolution for one rotor engine, twice as many as the four-stroke piston engine, and similar to the output of a two-stroke engine. Thus, power output of a Wankel engine is generally higher than that of a four-stroke piston engine of similar engine displacement in a similar state of tune, and higher than that of a four-stroke piston of similar physical dimensions and weight.

2.1.5 Advantages

Wankel engines have several major advantages over reciprocating piston designs, in addition to having higher output for similar displacement and physical size:

1. Wankel engines are considerably simpler and contain far fewer moving parts. The simplicity of design and smaller size allow for a savings in construction costs, compared to piston engines of comparable power output.
2. Very compact engine in comparison to the conventional reciprocating engine with equivalent power.
3. There are no valves and its complex valve train, which makes the engine to be simpler and reduces the total engine weight.
4. There is no any reciprocating parts such as connecting rods and conventional crankshaft, only the rotor geared directly to the output shaft, which makes the engine lighter, smoother, 100% balanced and can run at higher rpm.
5. The rotary engine generating power with each rotation of eccentric output shaft resulting in extremely low torque oscillations and vibration.
6. Higher power to weight ratio. Rotary Wankel engine makes high power for their size because of their high volumetric efficiency; obviously more air going in means more fuel and thus more power.
7. Multi fuel capability. The Separation of combustion region from intake region prevent localized hot spots from forming, thereby allowing the use of fuel of very low octane number without pre-ignition or detonation, a particular advantage for Hydrogen engine.
8. The engine rotor has 1/3 of the output shaft speed giving more time for mixture formation.

2.1.6 Disadvantages

However, the Wankel rotary engine has some disadvantages, despite of sealing problems, which can be solved by the improved material technology.

1. Higher fuel consumption.
2. Low thermal efficiency, due to the high surface to volume ratio of the combustion chamber. The engine's long and narrow combustion chamber makes the flame to

be travel longer. All production rotaries made by Mazda use two spark plugs per rotor to ensure that most of the mixture is ignited. However, Mazda has been successful with the RX-7 sports car, where its efficiency and fuel economy is comparable to other cars in its class.

2.1.7 Engine main parts

A single rotor engine consists of very few parts in comparison with the conventional reciprocating engine; Fig.2.4 shows the main parts of the engine. The rotary engine has an ignition system and fuel-delivery system that are similar to those on piston engine.

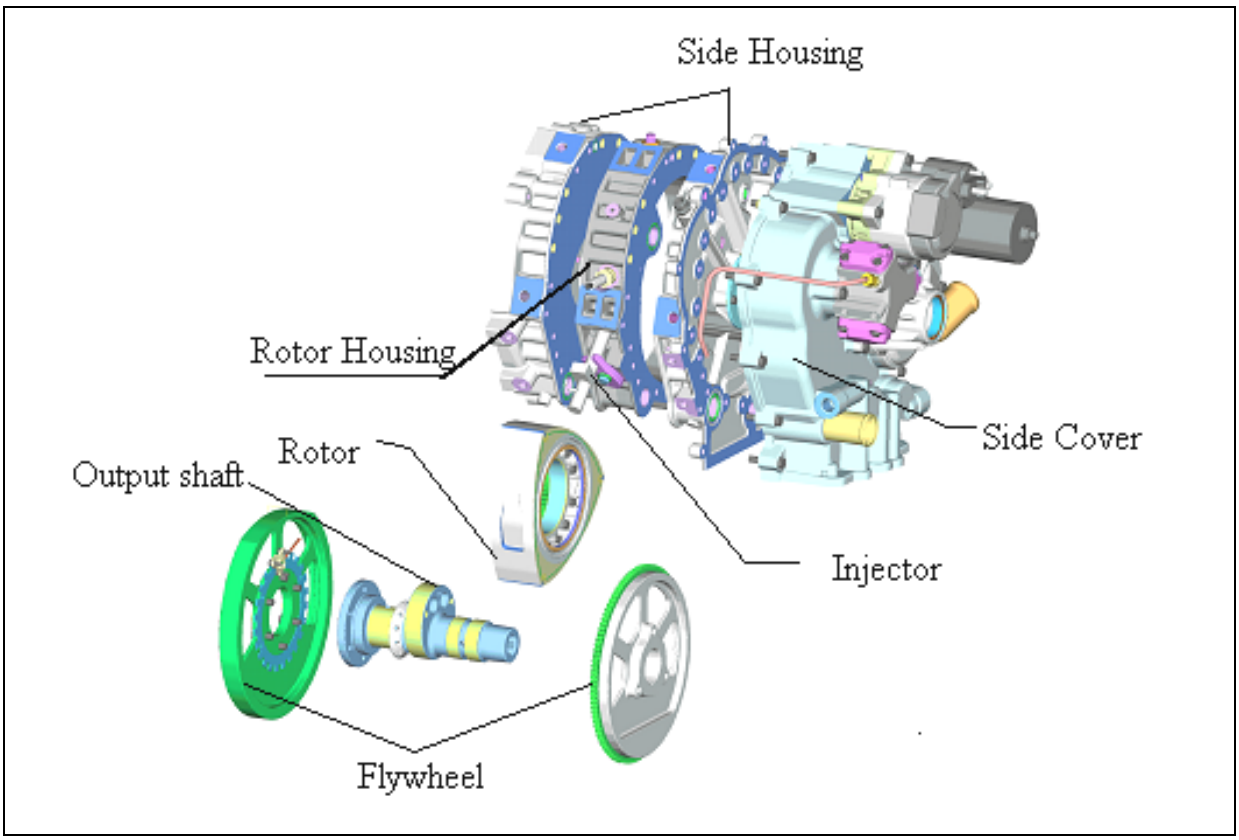

Fig.2. 4 The main engine parts

2.1.7.1 Engine housing

The housing of the rotary Wankel engine consists of two side parts and an epitrochoid. It is similar (in functionality) to the cylinder block and cylinder in piston engine. The shape of the combustion chamber is designed so that the three tips of the rotor will always stay in contact

with the wall of the chamber, forming three sealed volumes of gas. Each part of the housing is dedicated to one part of the combustion process, intake, compression, combustion and exhaust stroke. Fig.2.5 shows the housing parts.

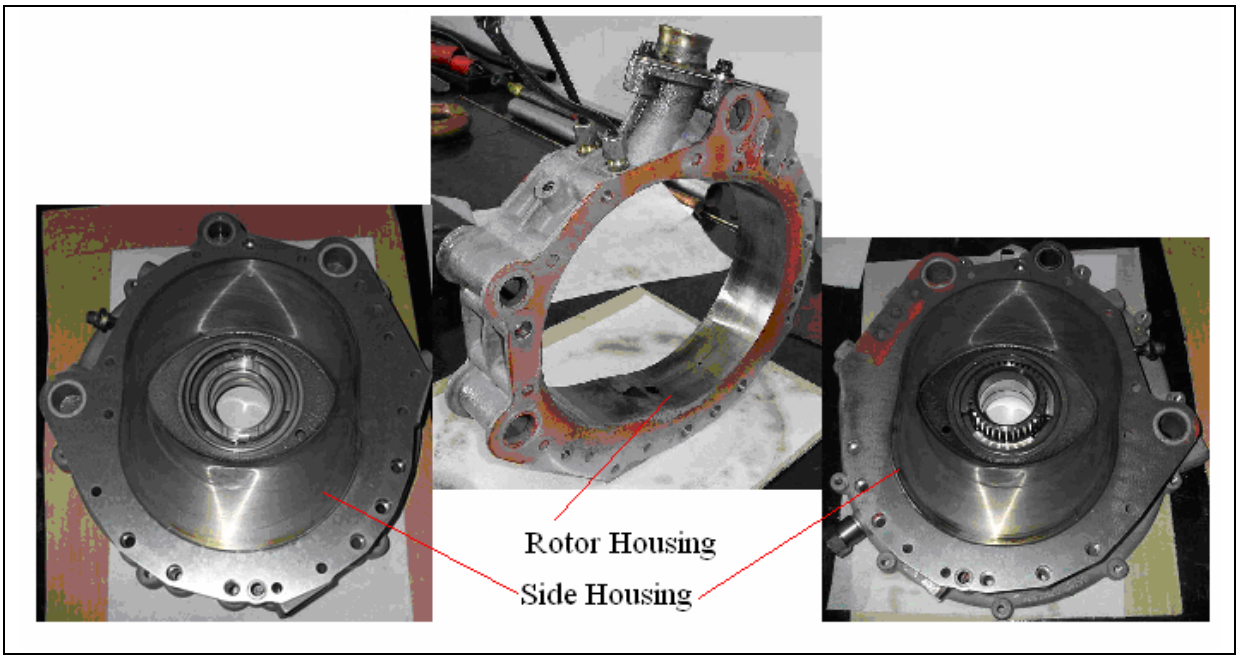

Fig.2. 5 Rotary engine housing

The main bearings of the output shaft are fitted to both side housing parts. One of the side housing is fitted with the rotor fixed gear. The cooling jacket and intake/exhaust ports are shaped in the rotor housing.

In practical, the inner curve of the epitrochoid expressed by the coordinates of point, p (x, y), where it can be seen in equation (2.1).

$$\left.\begin{aligned} x &= e\cos 3\alpha + (R+a)\cos\alpha \\ y &= e\sin 3\alpha + (R+a)\sin\alpha \end{aligned}\right\} \qquad (2.1)$$

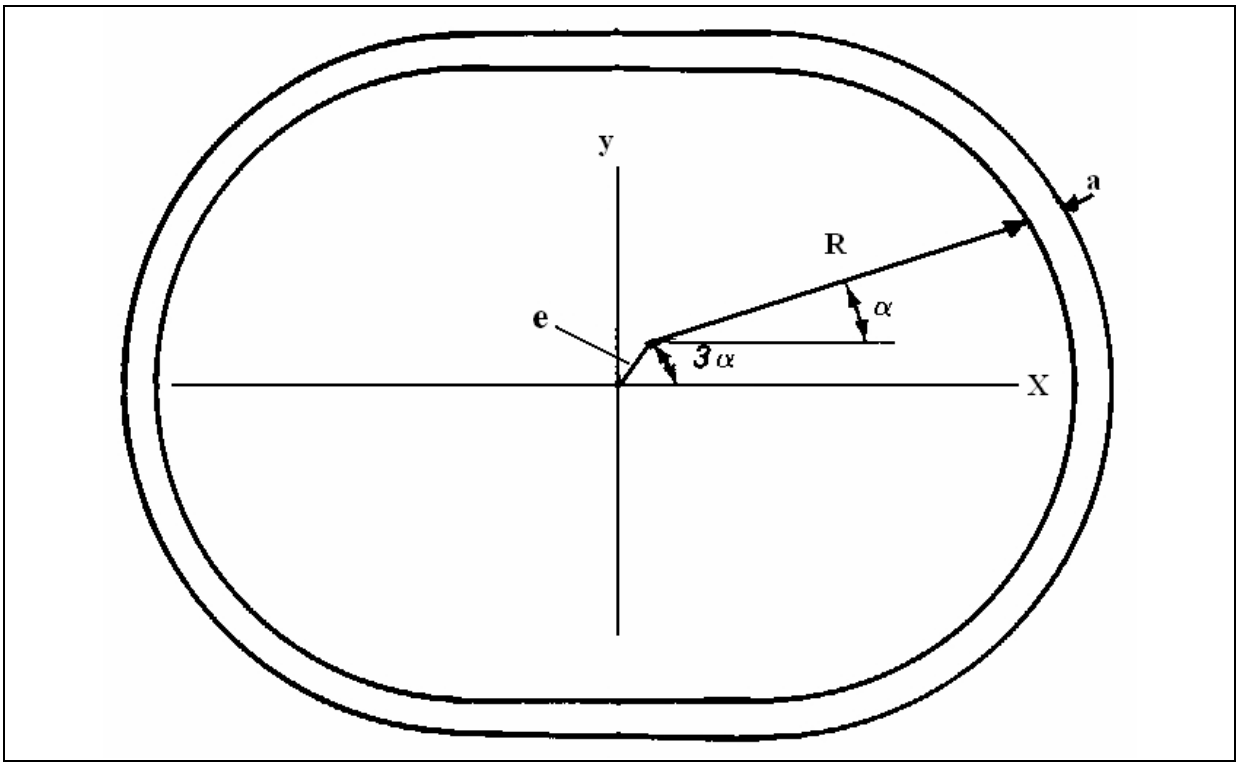

Fig.2. 6 Peritrochoid curve of housing

Where: **e** is the eccentricity,
R is the generating radius, and
a is a clearance distance, or
amount parallel transfer.
For KKM-500, e=15.2mm, R=108mm, and a=3mm

2.1.7.2 Engine rotor

The rotor is a triangular shape, has three convex faces, each of which acts like a piston. Each face of the rotor has a pocket (recess) in it, which increases the displacement of the engine, allowing more space for air/fuel mixture.

The rotor follows a path that keeps each of the three peaks (apexes) of the rotor in contact with the housing, creating three separate volumes of gas. As the rotor moves around the chamber, each of the three volumes of gas alternately expands and contracts.

The expansion and contraction that draws air and fuel into the engine, compresses it and makes useful power as the gases expand, and then expels the exhaust gases. Fig.2.7 shows a typical engine rotor.

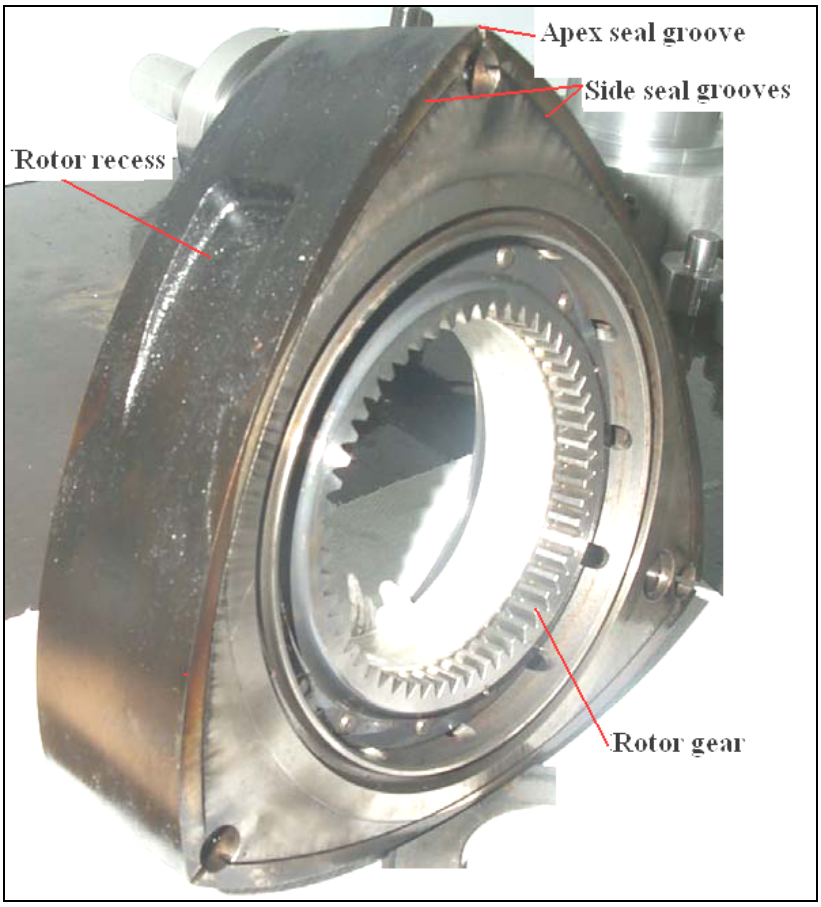

Fig.2. 7 Engine rotor

A groove shaped on the rotor apex to insert the apex sealing, separates the three faces from each other. Also, another groove shaped on the rotor side to insert the side seals preventing any side leakage. In addition to its function as a piston, the rotor is working also as an intake/exhaust valves when it is rotate.

The rotor is coupled to the output shaft eccentric part, applying force on the shaft exerted by the gas expansion to rotate the output shaft. A phasing gear mechanism is also coupled to the rotor, for accurate control of the rotary motion of the rotor.

Coordinates of point, p (x, y) can generate the rotor surface curve as follows [21]:

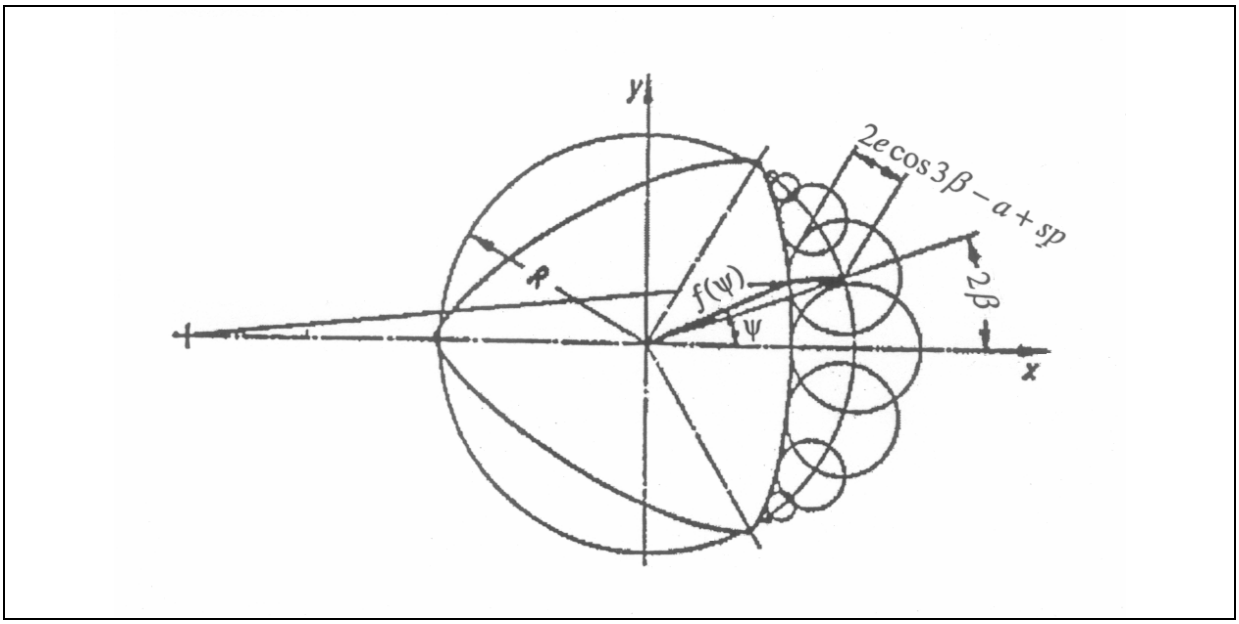

Fig.2. 8 Rotor contour

$$\left.\begin{aligned} x &= R\cos 2\beta + \frac{3e^2}{2R}(\cos 8\beta - \cos 4\beta) - e(\cos 5\beta + \cos\beta)\sqrt{1-\frac{9e^2}{R^2}\sin^2 3\beta} - \\ &- \frac{3}{2}\frac{e(a-sp)}{R}(\cos 5\beta - \cos\beta) + (a-sp)\cos 2\beta\sqrt{1-\frac{9e^2}{R^2}\sin^2 3\beta}, \\ y &= R\sin 2\beta + \frac{3e^2}{2R}(\sin 8\beta + \sin 4\beta) - e(\sin 5\beta - \sin\beta)\sqrt{1-\frac{9e^2}{R^2}\sin^2 3\beta} - \\ &- \frac{3}{2}\frac{e(a-sp)}{R}(\sin 5\beta + \sin\beta) + (a-sp)\sin 2\beta\sqrt{1-\frac{9e^2}{R^2}\sin^2 3\beta}, \end{aligned}\right\} \quad (2.2)$$

$$f(\psi) = \sqrt{x^2 + y^2}\ ,\ \psi = \arctan\frac{y}{x}$$

Where; e, is the distance of eccentricity

R, is the generating radius

β, is the angle of rotation varies from:

π/6 to π/2 for rotor face 1

5π/6 to 7 π/6 for rotor face 2 and

3π/2 to 11π/6 for rotor face 3

a, is a clearance distance, amount of parallel transfer.

sp, is the minimum clearance between rotor and housing.

2.1.7.3 Gas sealing

Gas seal mechanism consists of an apex seal to keep each working chamber gas-tight from its adjacent ones, a side seal with a corner seal used at the junction of each two seals.

One or two springs are provided on the backside of each seal, which will allow the seal to keep close contact with the surface to be sealed even when it is worn.

The function of the gas sealing mechanism of the rotary engine is similar to the compression rings of the piston engine. Fig.2.9 shows the apex gas seal with its springs.

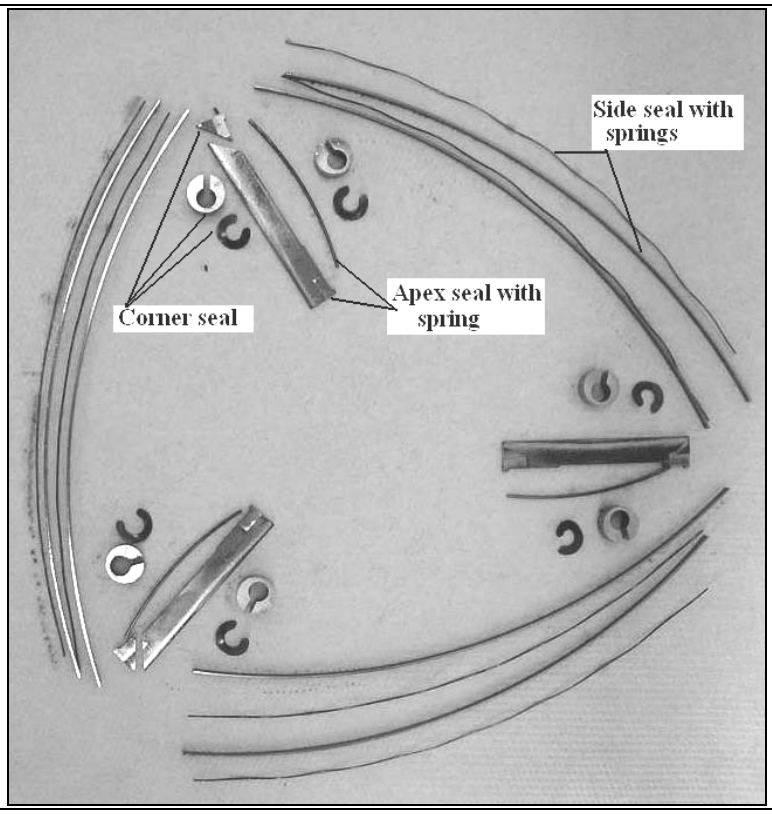

Fig.2. 9 Gas sealing with springs

2.1.7.4 Output shaft

The output shaft of a rotary engine is similar to the crankshaft of the piston engine in its function. It generates the rotating motion by receiving the combustion pressure applied on the rotor journal eccentric to the center of rotation. It rotates three times faster than the rotor. A flywheel and v-belt pulley is fitted to its ends.

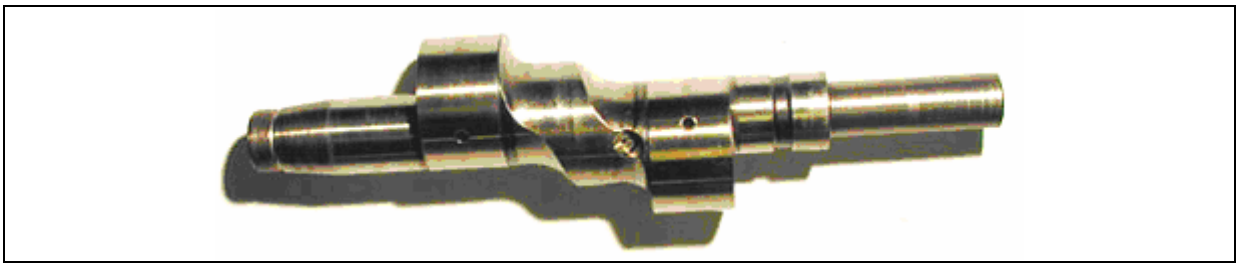

Fig.2. 10 Engine output shaft

2.1.7.5 Intake and exhaust port system

The intake and exhaust ports located in the rotor housing are called peripheral port system. The side ports system, where the ports are located at the side housing of the rotor. The peripheral intake port has a higher charging efficiency at higher engine speed, due to the longer open time and the intake flow has the same direction of the rotor rotation.

However, at lower speed the engine volumetric efficiency is lowered due to the longer over lap time between the intake and exhaust ports where some amount of burned gas is presented in the intake side.

The side intake port has an advantage over the peripheral intake port at lower engine speed due to better swirl and shorter over lap time between intake and exhaust ports. But at higher speed condition, the side intake port has lower engine performance.

Unlike previous rotary engines, which employed a peripheral intake and exhaust port system or side intake peripheral exhaust ports as the side exhaust port system will cause a great amount of leak of high temperature exhaust gas into the rotor side space, RENESIS introduced by Mazda in 2003 (in RX-8), has intake and exhaust ports in the side housings. This configuration eliminates overlap between the opening of the intake and exhaust ports, enhancing combustion efficiency. The intake ports are 30% larger and their timing has been changed to make them open sooner than in previous designs. Moreover, the exhaust ports open later, resulting in a longer power (expansion) stroke and providing radically improved heat efficiency. Fig.2.11 shows the RENESIS port system.

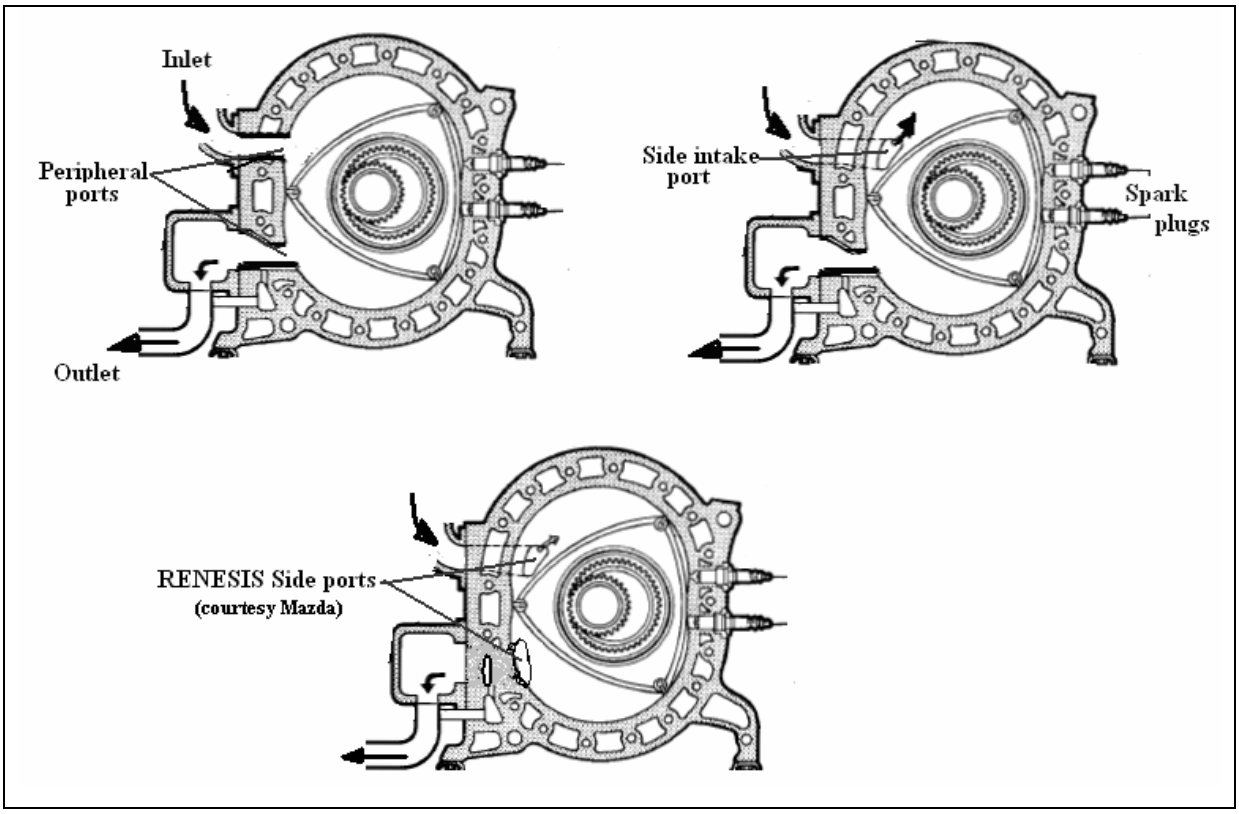

Fig.2. 11 Intake and exhaust ports comparison

The main advantages of the RENESIS can be summarized as follows:

- A bigger intake port means that more time for air to enter and a greater charging volume through the port.
- Less turbulence through the port as well.
- Less overlap gives less dilution of the intake air and a cooler intake charge.
- More available room for incoming air.
- Volumetric efficiency increases.
- Since efficiency goes up, the use of gas gets more efficient. In other words it takes less fuel to do the same amount of work.

RENESIS employs a new cut-off seal located between the rotor's dual oil seal and side seal. This sealing arrangement eliminates blow-by between intake and exhaust ports and prevent carry-over of exhaust gas to the next intake cycle. The seal shape is optimized to remove any carbonization build-up against the side seal. Fig.2.12 shows the cut-off seal arrangement.

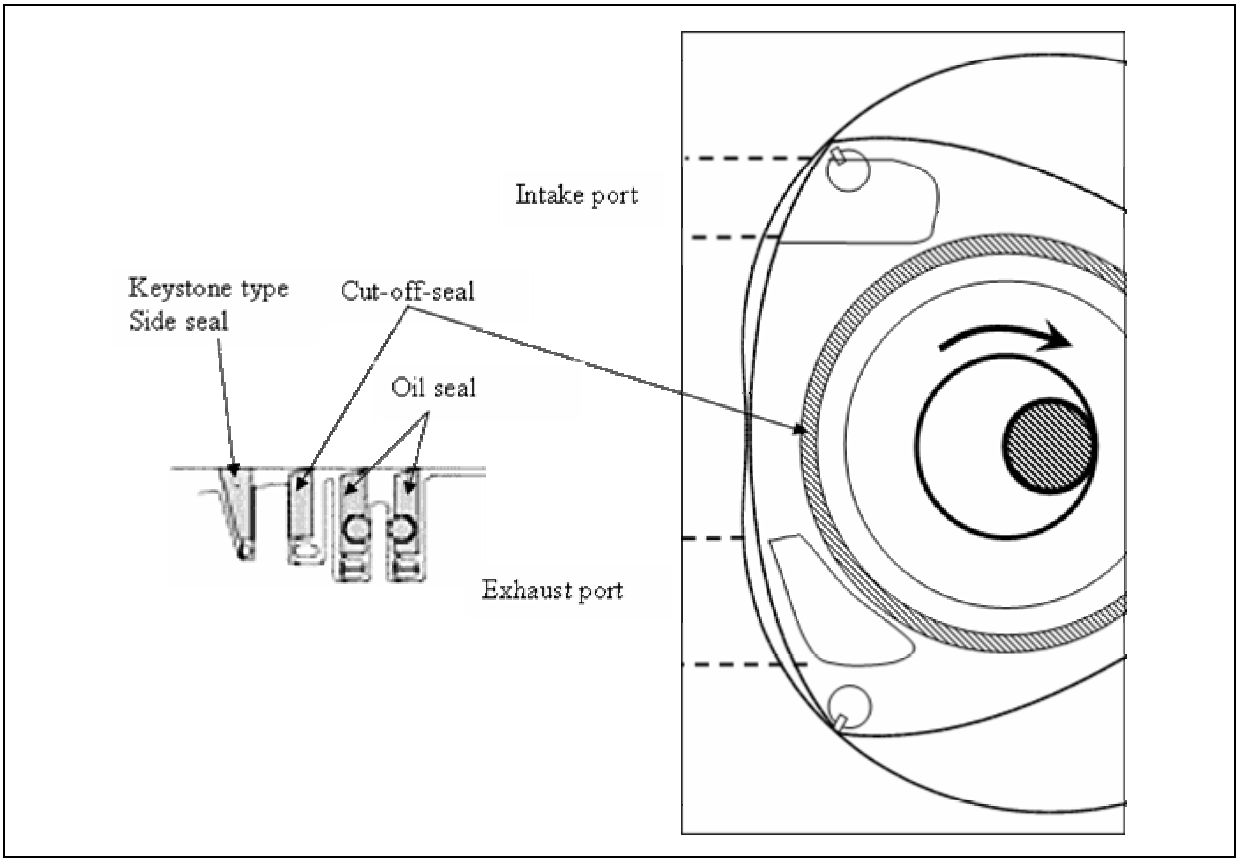

Fig.2. 12 RENENSIS cut-off seal (courtesy Mazda)

2.1.7.6 Volume change of rotary engine compared to 4-stroke piston engine

The Wankel rotary engine works by a volume of a chamber enclosed between the rotor and the rotor housing changing. Intake, Compression, Ignition, Expansion, Exhaust all work as for in a piston engine, but as the rotor has three sides it is all happening at the same time. Despite this, as each rotor gives a power stroke per revolution of the output shaft, it is therefore the same as a two-stroke piston engine. That means, all of the engine's capacity (say 654 cc) is being used for every rotation of the output shaft (as for a two stroke), and therefore the actual volume used is twice that of 4-stroke engine.

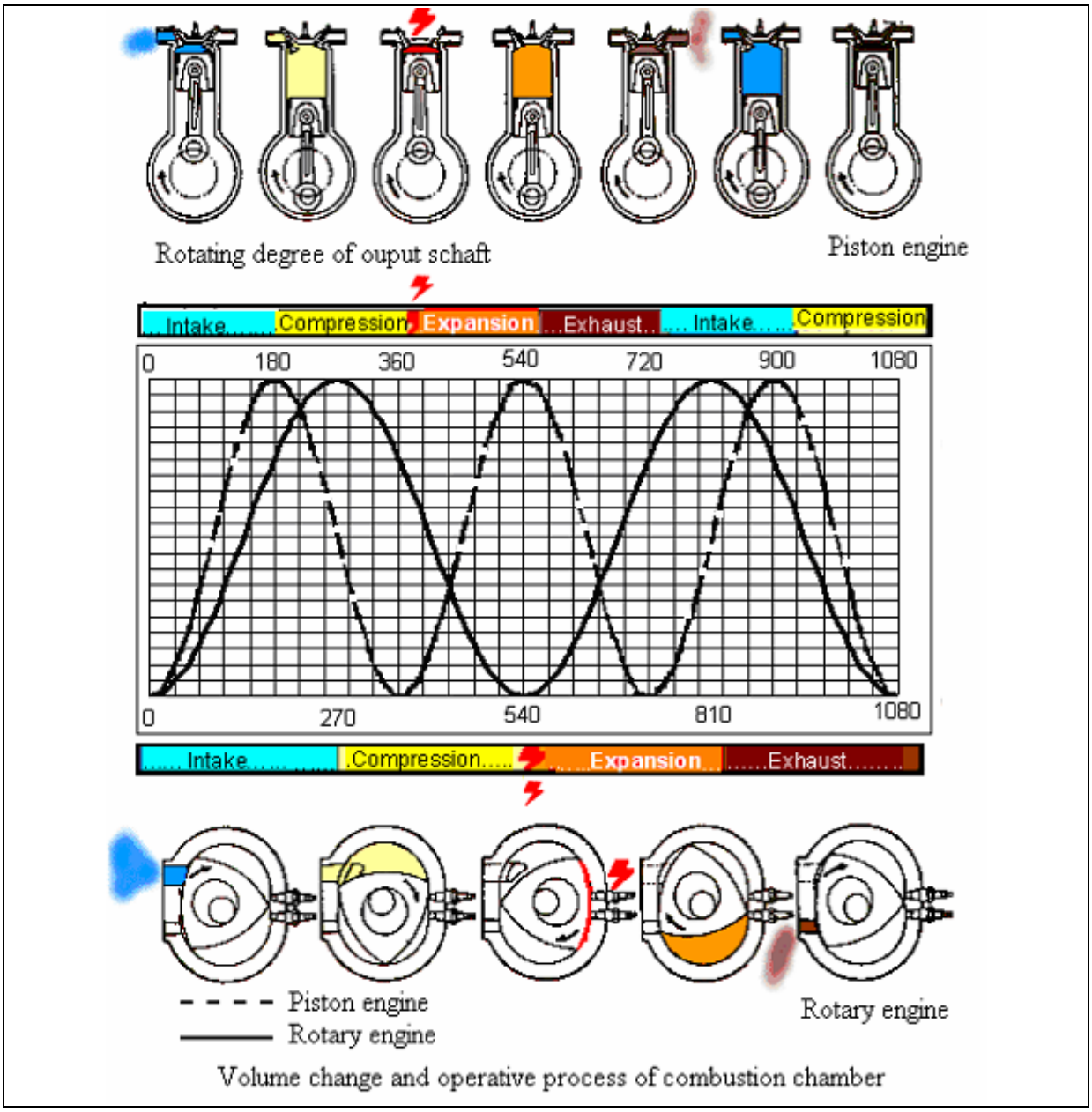

Fig.2. 13 Engine timing comparison in terms of degrees.

In other words, the rotary engine's rotor completes one stroke for every 270º of output shaft rotation that can be seen on fig.2.13.

- Intake 270º of output shaft rotation.
- Compression 540º of output shaft rotation.
- Combustion 810º of output shaft rotation.

- Exhaust 1080º of output shaft rotation.

That means a rotary engine takes 1080º of output shaft rotation to complete an intake, compression, combustion and exhaust cycle, or 3 output shaft rotations per complete cycle.

Piston engine completes one stroke every 180º of crank rotation:

- Intake 180º of crank rotation.
- Compression 360º of crank rotation.
- Combustion 540º of crank rotation.
- Exhaust 720º of crank rotation.

Piston engine requires 720º of crankshaft rotation to complete a cycle. In other words, 2 complete revolutions of the crankshaft.

2.2 Hydrogen fuel

2.2.1 Hydrogen economy

In its molecular form hydrogen can be used directly as a fuel to drive a vehicle, to heat water or indirectly to produce electricity for industrial, transport and domestic use. Unfortunately, hydrogen is only found in nature combined with other elements, and can be extracted from water and biomass as well as from crude oil or natural gas.

Hydrogen has enormous potential to decrease (the non-production countries) dependence on foreign oil imports, and it will be great choice if produced using renewable energy, to eliminate pollutants such as nitrogen oxides, particulates and greenhouse gases such as carbon dioxide. The huge advantage that hydrogen has over other fuels is a non-polluting fuel, and can be produced using renewable non-polluting energy.

2.2.2 Hydrogen as fuel of future

Hydrogen when produced with environmentally friendly energy is expected to have an important role as future energy source. As a fuel, hydrogen reacts with oxygen in the air and produces only water as an emission, despite of NO_x at near stoichiometric mixtures combustion, which should be controlled. Hydrogen can be used as fuel in vehicles and for heat and power production. Also, it is particularly well suited for use in fuel cells where the

hydrogen energy is turned into electricity with relatively high efficiency (non-combustion engines).

2.2.3 Hydrogen fuel physical properties

Hydrogen is a colourless, odour-free, and non-toxic, it is normally gaseous and lighter than air, but the properties that contribute to its use as a combustible fuel are its:

1. Wide range of flammability.
2. Low ignition energy.
3. Small quenching distance.
4. High auto ignition temperature.
5. High flame speed at stoichiometric ratios.
6. High diffusivity.
7. Very low density.
8. Water is the only emission when hydrogen is burned.

Table 2.1, shows the physical properties of hydrogen.

Properties		Hydrogen	Gasoline
Density ρ	[Kg/m^3]	0.09	730 – 780
Ignition limits in air	[Vol.%]	4 -76	1 –7.6
Minimal ignition energy	[mJ]	0.02	0.24
Self ignition temperature	[◦C]	585	>> 350
Laminar flame velocity at λ=1	[m/s]	2.0	0.4 – 0.8
Density of stoichiometric mixture ρ_G	[Kg/m^3]	0.94	1.42
Stoichiometric air demand L_{st}	[-]	34.3	14.7
Lower calorific value H_u	[MJ/kg]	120	43.5
Specific heat ratio	[-]	1.4	1.1
Mixture calorific value H_G	[MJ/m^3]	3.2 (1) 4.5 (2)	3.9 (1) 3.8 (2)

(1) Port injection
(2) Direct injection

Table 2. 1 Physical properties of hydrogen and gasoline [2]

2.2.4 Combustion of hydrogen fuel

Hydrogen burns and combined with oxygen very fast to form water and its energy content is high relative to mass, but its low density means large volume will be injected to the engine chamber. Fig.2.14 shows the stoichiometric air requirement/calorific value for different fuels, and it can be seen that hydrogen has low energy concentration in comparison to other gas and liquid fuels for stoichiometric combustion.

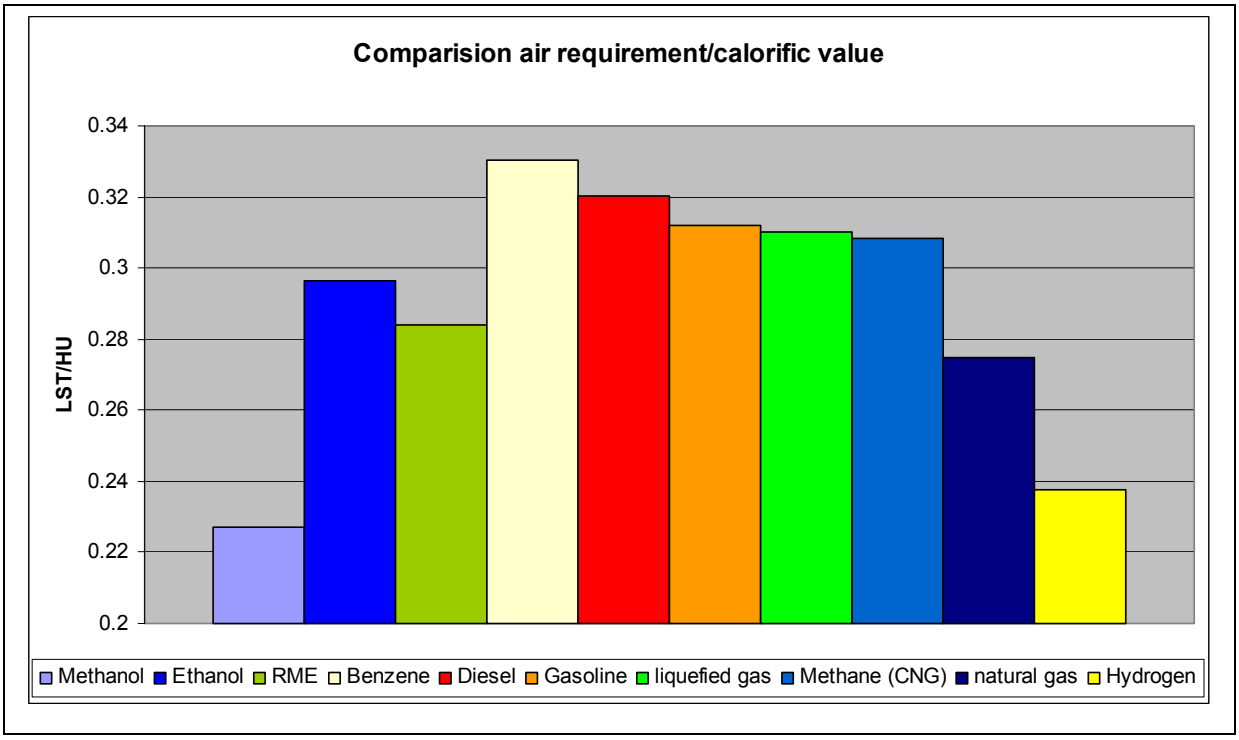

Fig.2. 14 stoichiometric air demand/calorific value for different fuels

Theoretically or stoichiometric combustion of hydrogen and oxygen in air is given as:

The A/F ratio (stoichiometric) = 2.4:1 or 29.6% H_2 by volume.

And by mass as:

The A/F ratio (stoichiometric) = 34.5:1, i.e. 2.8% H_2.

2.2.5 Theoretical thermal efficiency

The high-speed diesel engine is normally followed the dual combustion cycle. In this cycle, part of the fuel burns very close to constant volume followed by the remainder of the fuel

burning very close to constant pressure. The cycle is shown on p-v and T-s diagrams in fig.2.15.

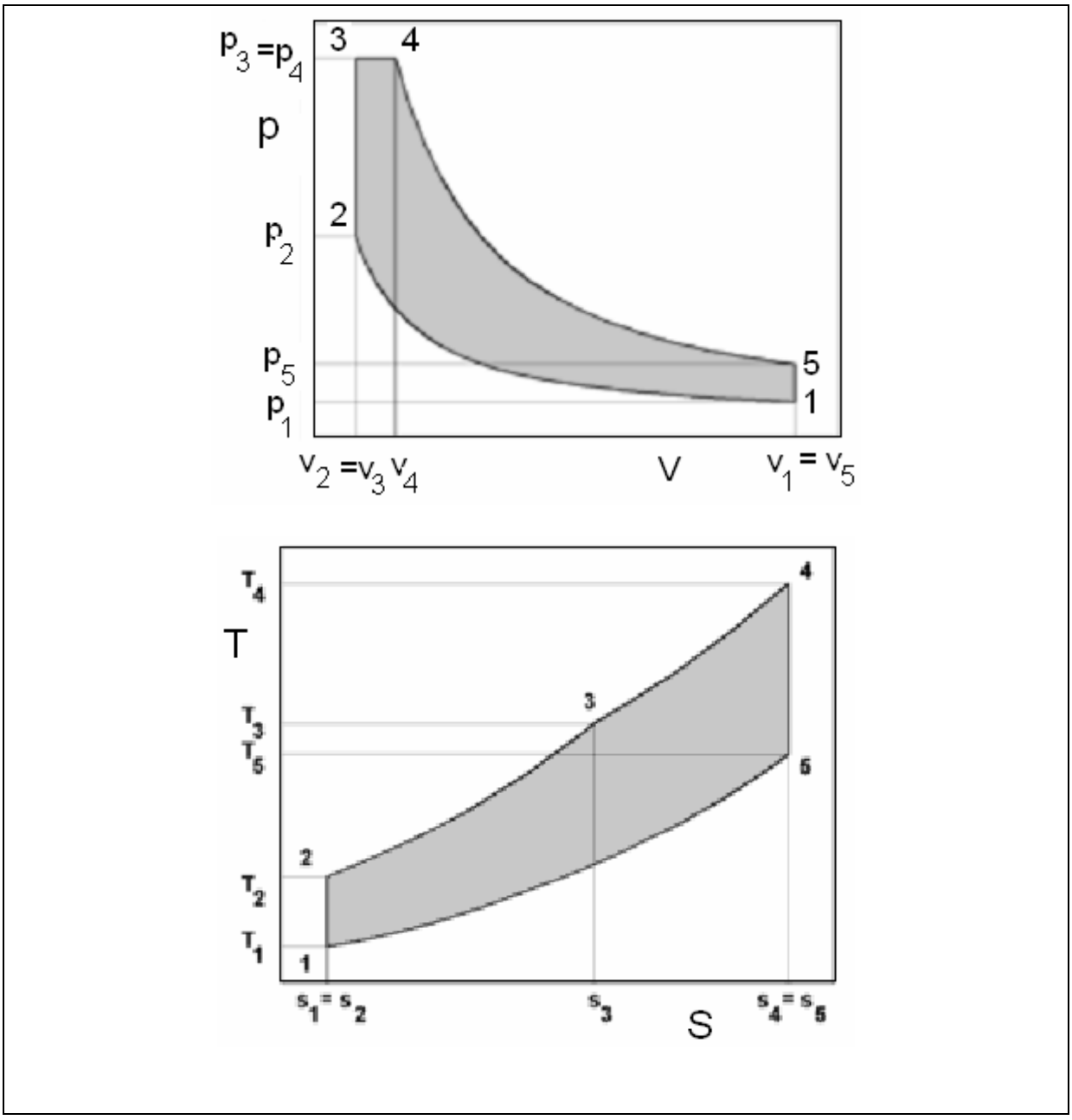

Fig.2. 15 p-v and T-s diagrams of the Dual Combustion Cycle

The theoretical thermal efficiency η_{th} is expressed in terms of the compression ratio $r=v_1/v_2$; the ratio of pressure (constant volume heat addition pressure ratio) $k=p_3/p_2$; the ratio of volumes (constant pressure heat addition cut-off ratio) $\beta=v_4/v_3$; and the specific heat ratio γ.

Then the thermal efficiency is expressed as:

$$\eta_{th} = 1 - \frac{k\beta^{\gamma} - 1}{[(k-1) + \gamma\, k(\beta - 1)]\, r^{\gamma-1}} \qquad (2.3)$$

The efficiency of the dual combustion cycle depends not only on the compression ratio but also on the relative amount of heat supplied at constant volume and at constant pressure. When $k=1$ *(i.e.* $P_3=P_2$*)* in equation (2.3), reduces the cycle efficiency to the constant pressure diesel cycle thermal efficiency.

2.3 Hydrogen Fuel mixture strategy

In general, getting an internal combustion engine to run on hydrogen is not difficult, however, running the engine well is more challenge. To be able to run a hydrogen engine, the mixture formation of fuel and air should be precisely controlled, and highly dependent on the way of introducing the hydrogen fuel to the engine.

The hydrogen fuel delivery system can be divided into two main systems; each system has some advantages over the other. [36].

2.3.1 External mixture formation system

In this method, the fuel and air are mixed externally in the intake manifold either by simple gas carburetor (venturi type) or continuous central injection, Fig.2.15 shows simple engine external mixture configuration. However, such a system when first implemented on a test engine, a complete control of combustion process was not possible. [19]. Better injection system allowing a complete control of the combustion process is obtained by injecting the hydrogen fuel just before the intake valve in each cylinder manifold (port injection), controlled by means of electronic system similar to that used in gasoline engine. [19,25].

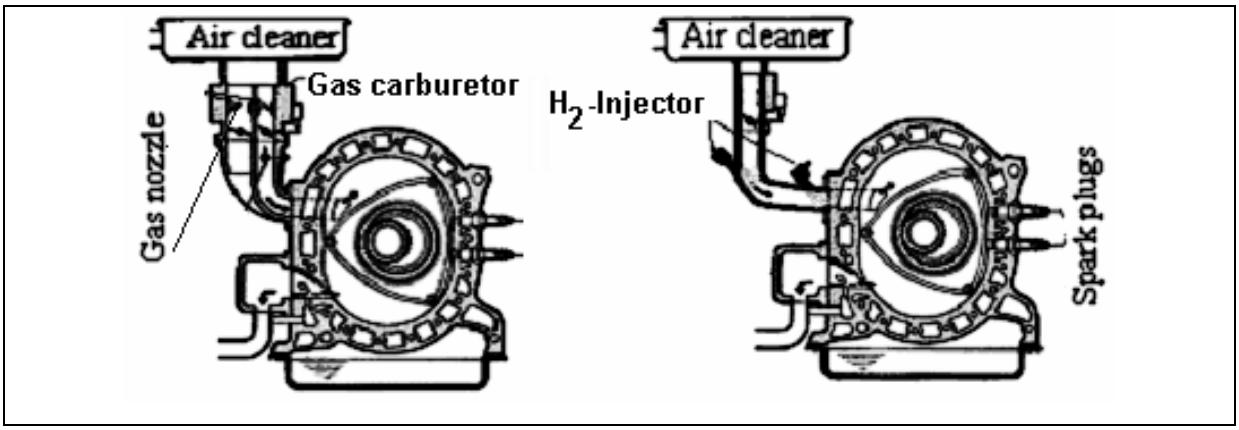

Fig.2. 16 External mixture formation

On one hand, the advantages of this method of mixture formation including its simplicity, low pressure fuel injection and better thermal efficiency due to better homogenous mixture formation. On the other hand, pre-ignition and backfire in certain engine operating conditions are the main disadvantages of this system. Also, the low density of hydrogen compared to other fuels will limit the engine power output to about 82% of comparable gasoline engine, this because of the fact that about 30% of the engine cylinder volume displaced by hydrogen at a stoichiometric mixture, compared to about 1 to 2% for gasoline. [18].

2.3.2 Direct injection

More sophisticated engines use direct injection into the combustion chamber. In this method the hydrogen fuel is injected directly to the combustion chamber in two ways:

2.3.2.1 Low-pressure injection (early injection)

In low-pressure direct injection, the hydrogen fuel is injected to the combustion chamber directly after the intake port closed and before the cylinder pressure becomes very high. A good mixture formation can be achieved due to enough time for the mixture before ignition, and hence better thermal efficiency. Backfire can be eliminated in low-pressure direct injection system, clearly because there is no ignitable mixture in the intake manifold, only air. While the low-pressure direct injection system solves the problem of pre-ignition or backfire in the intake manifold, it does not prevent the pre-ignition within the combustion chamber. [18]. The pre-ignition inside the combustion chamber at several operating

conditions can be a serious problem causing engine knock and reducing engine power output due to the negative work necessary for the compression stroke.

Figure 2.16, shows the principal of low-pressure hydrogen injection developed by Mazda in its RENESIS hydrogen rotary engine applying two injectors in each combustion chamber of two rotor engine, to inject the necessary amount of hydrogen in very short time for better mixture formation.

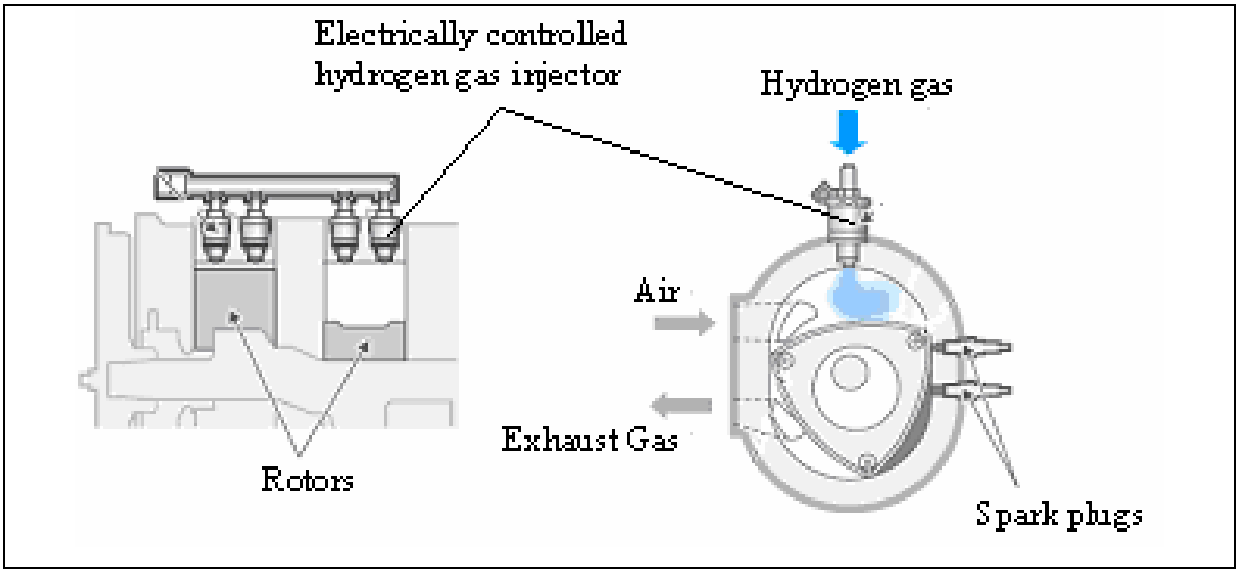

Fig.2. 17 Low pressure hydrogen injection, 2 injectors per chamber by Mazda [52].

2.3.2.2 High pressure direct injection (late injection)

A precise amount of hydrogen fuel is injected at the end of compression stroke just few degrees before ignition process started. The combustion chamber high pressure needs the hydrogen injection pressure to be as high as 80-100 bars. [1].

Ultra lean combustion can be achieved, pre-ignition and backfire can be eliminated in highly sophisticated high-pressure injection system. The combustion process is much similar to the diesel engine, but the use of ignition source is necessary even in a high compression ratio engines due to higher auto-ignition temperature of hydrogen.

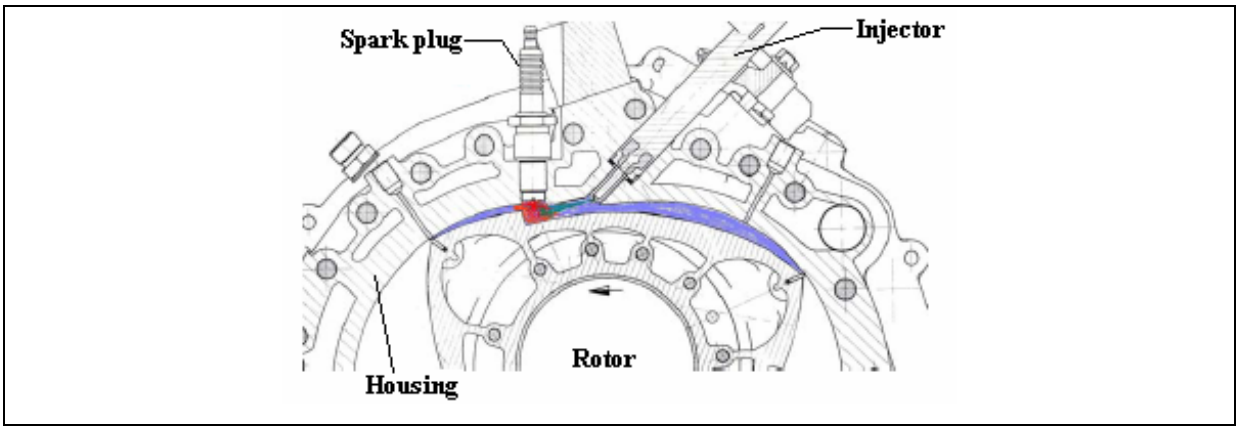

Fig.2. 18 High-pressure direct injection

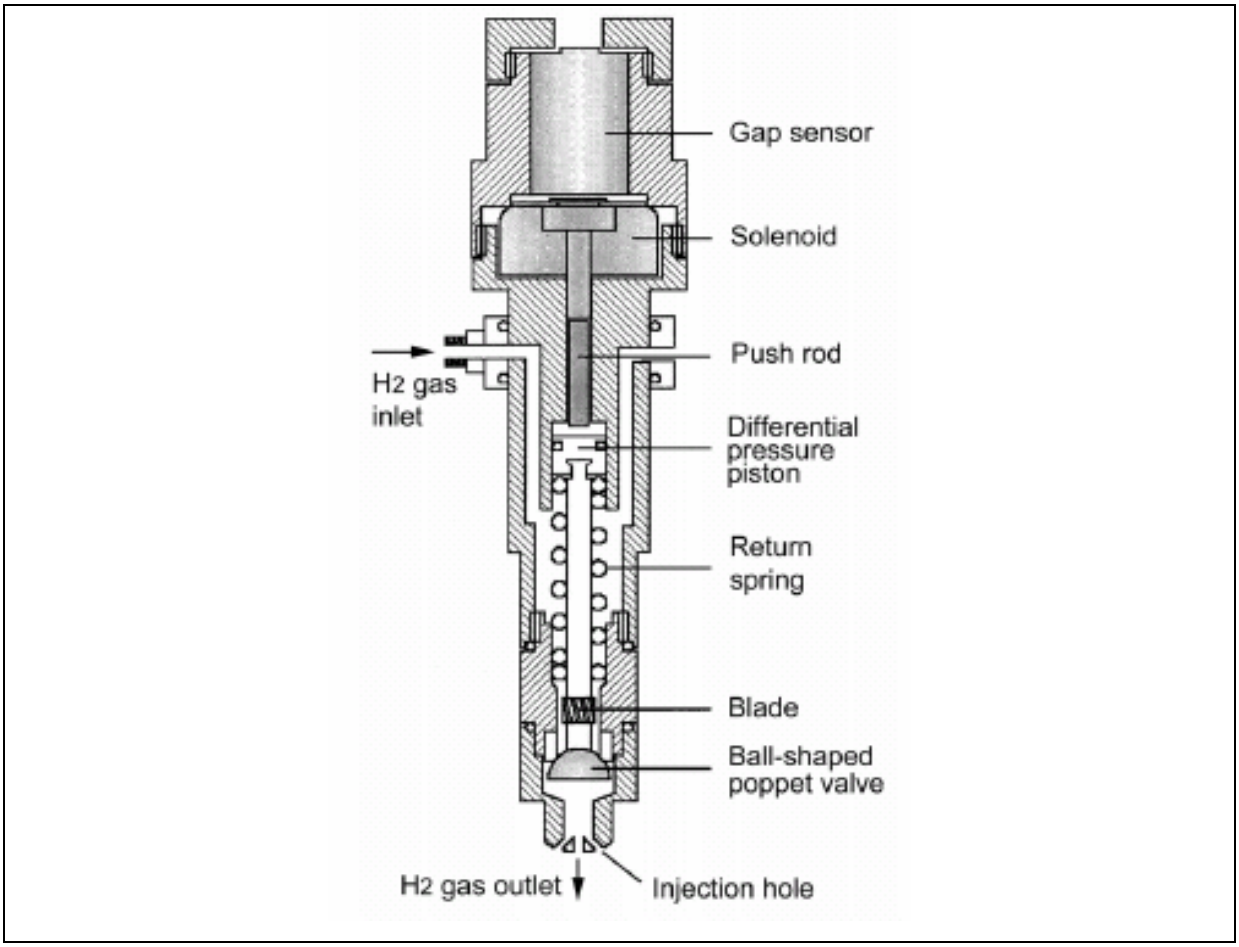

Fig.2. 19 A typical schematic diagram of the high-pressure hydrogen injector of ball valve type with solenoid actuator. [38].

2.4 Power output in comparison to gasoline

When focusing on the actually available (bi-fuel) hydrogen internal combustion engine technology, with about 30% power output less, when compared to the gasoline operation mode; it must be questioned in how far this penalty can be compensated in the scope of an advanced hydrogen engine design. A first evaluation can be derived from the basic equation:

$$P_i = \lambda_a H_G \eta_i \qquad (2.12)$$

This allows the indicated mean effective pressure *Pi* in the cylinder to be determined as a function of the volumetric efficiency λa, the indicated efficiency ηi and the mixture calorific value H_G, which is defined as:

$$H_G = \frac{H_u \rho_G}{\lambda L_{st} + 1} \quad \approx \quad \frac{H_u \rho_G}{\lambda L_{st}} \quad (for\ \lambda\lambda \geq 1;\ L_{st} >> 1 \qquad (2.13)$$

in the case mixture-aspiration engines (port injection/external mixture formation), or:

$$H_G = \frac{H_u \rho_a}{\lambda L_{st}} \qquad (2.14)$$

for air-aspiration engines (direct injection/internal mixture formation).

In equations 2.13 and 2.14 ρ_G denotes the density of the stoichiometric mixture, ρ_a the density of air, H_U the lower calorific value of fuel, L_{St} the stoichiometric air demand and λ the relative air/fuel ratio.

To better understand the overall situation, it is worthwhile to have a close look at the physical properties of the new fuel being formed by gaseous hydrogen. As can be taken from table 2.1, there are significant differences in the properties of gaseous hydrogen when compared to gasoline. Even though the comparison of the ratio between lower calorific value H_U and the stoichiometric air demand L_{St} shows an advantage for hydrogen, the data indicates about 18% lower mixture calorific value in hydrogen mode when compared to the gasoline situation. This effect has to be primarily attributed to the enormously low density of gaseous hydrogen, which entails a lower density of the air/fuel mixture $\rho_{G,}$ and thus a lower mixture calorific value H_G.

The physical properties of hydrogen were presented in Table 2.1.

The internal mixture formation yields of about 17% higher mixture calorific value for hydrogen when compared to gasoline. In the internal mixture case the low density of

hydrogen is not relevant since the pressurized hydrogen is fed to the chamber by a direct injection system at a time when the intake port is already closed. Figure 2.20 shows this comparison with reference to gasoline engine.

According to equation 2.12, the engine power can be further increased by external supercharging which yields larger number for λ_a. But experimental investigations have shown that there is a limitation to supercharging in the external mixture formation method due to the occurrence of combustion anomalies similar to those known from naturally aspirating hydrogen engines operated close to λ =1, [18]. This further underlines the advantageous power potential of H_2-DI internal combustion engines in comparison to mixture aspirating engines.

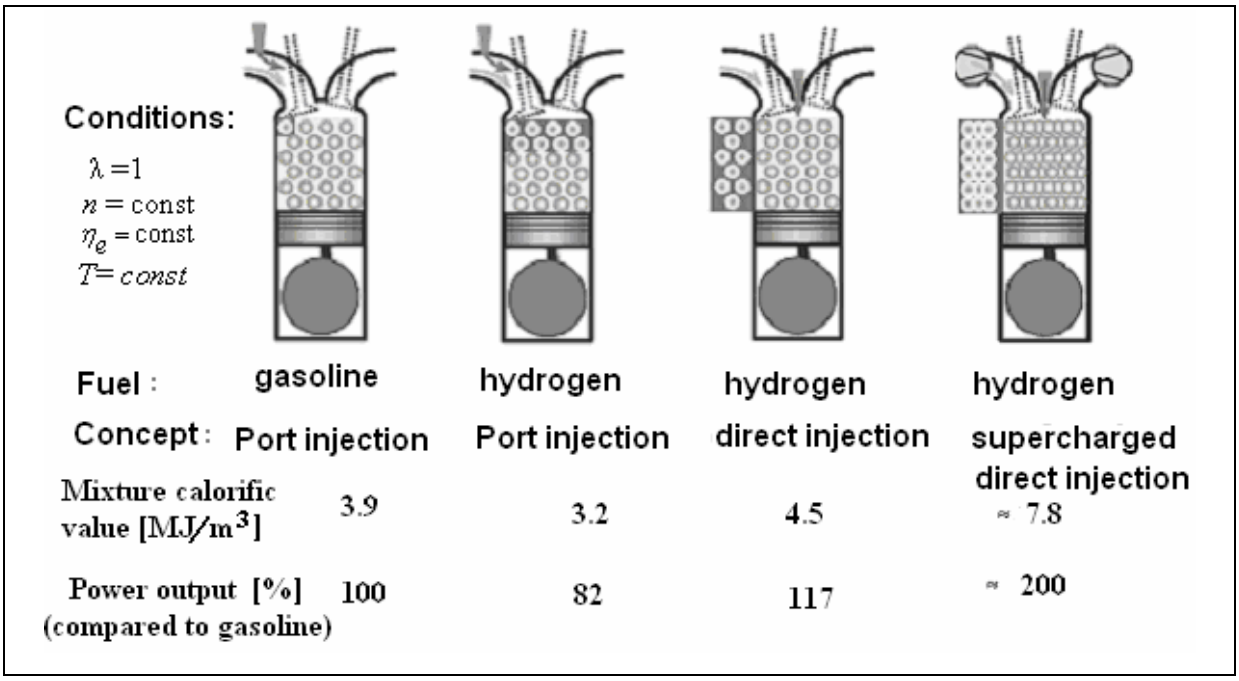

Fig.2. 20 Cylinder charging concept, Gasoline and hydrogen fueled engines. [1]

Figure 2.21 shows the indicated mean effective pressure (IMEP) for different cylinder charging concept.

Therefore from the above illustration, depending on how the fuel is entering the combustion chamber, the maximum output for hydrogen engine can be either 17% higher or 18% less than that of gasoline if a stoichiometric A/F ratio is used.

Moreover, hydrogen typical property related to its ignition capabilities within a wide range of A/F ratios that allows the engine to be operated in a quality controlled mode even with a completely homogeneous mixture at extremely low fuel equivalence ratio, (4-76% by volume). The un-throttled mode of operation is beneficial to the engine's overall efficiency at part load conditions due to the avoidance of throttling losses, and the increase of efficiency by leaner combustion. [2,18]

Also, the high flame propagation velocity of air/hydrogen mixtures at full-load, (stoichiometric), means that the hydrogen engines can more closely approach the thermodynamically ideal engine cycle. The comparison in Fig.2.22 clearly indicates the significantly shorter combustion periods in the full-load range, which are typical for hydrogen engines.

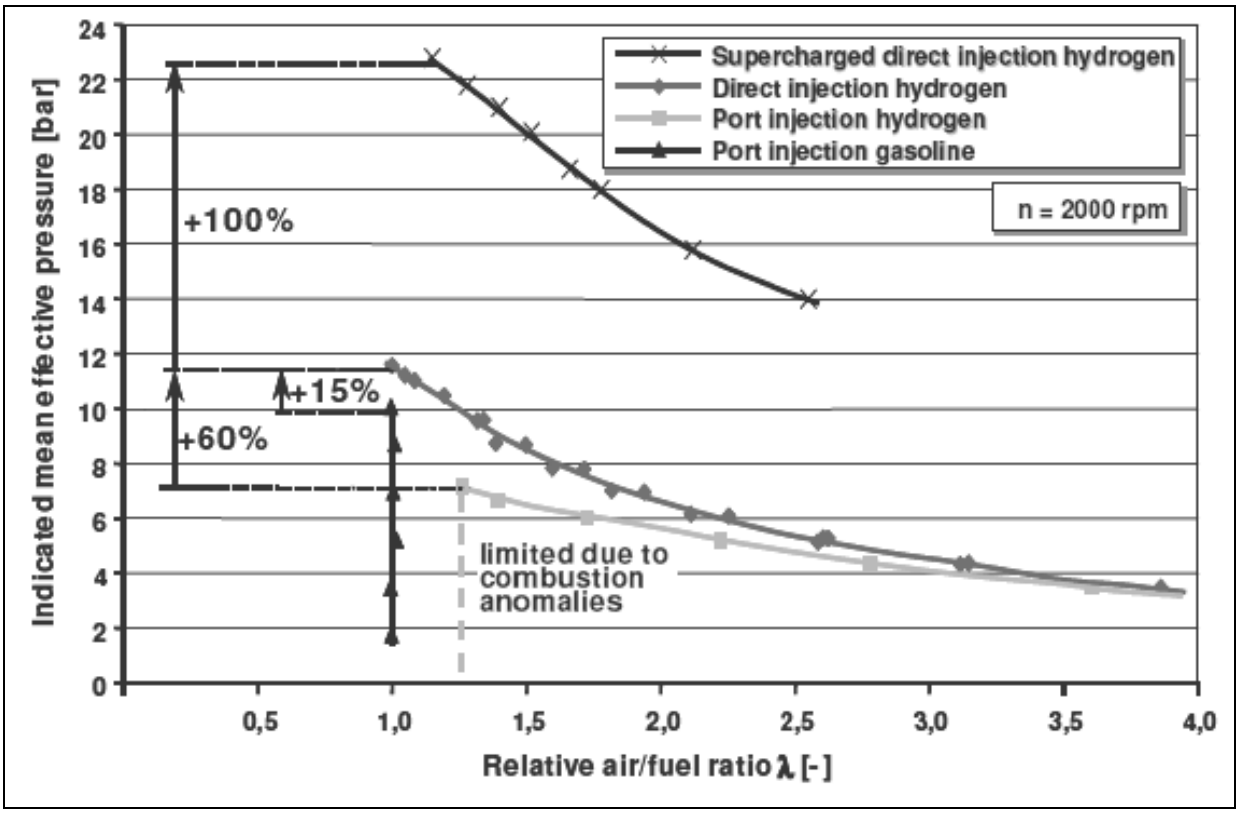

Fig.2. 21 IMEP for different cylinder charging concept, [2]

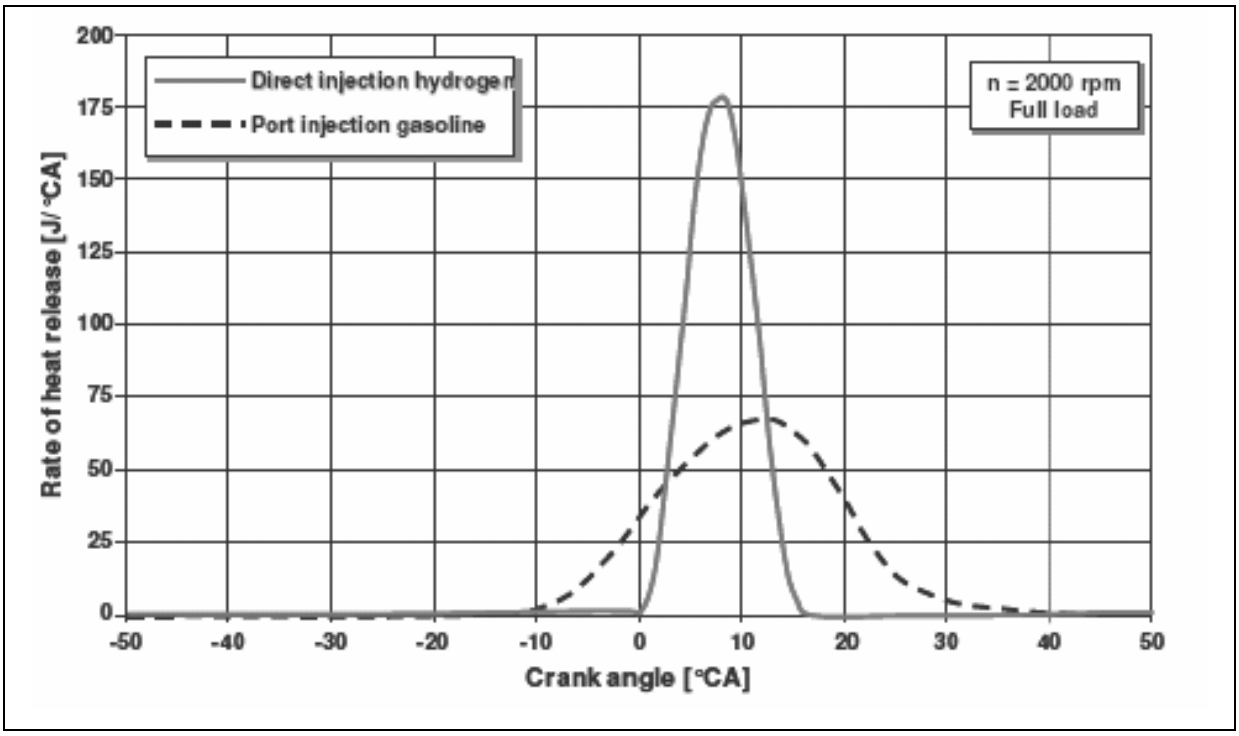

Fig.2. 22 Typical full-load hydrogen combustion, in comparison with gasoline, [2]

2.5 Emissions

The combustion of hydrogen in air produces no HC, CO, or CO2 emissions, due to the lack of carbon in hydrogen fuels despite of small traces produced by the combustion of small amount of engine lubricating oils. However, at a near stoichiometric air-fuel ratio, the combustion temperature is very high and as a result it will form a considerable amount of nitrogen oxides (NO_x). The amount of NO_x formed depends on:

- A/F ratio
- Engine compression ratio
- Engine speed
- Ignition timing

Fig.2.23 shows an intensive testing done by several researchers, [2,3,18]. The work of these researchers has indicated that operating hydrogen combustion engine in a lean mode, at equivalent ratio ϕ-values less than 0.5, does not produce any NO_x. At ϕ-values 0.5 to 0.7, small amount of nitrogen oxides are formed and at higher hydrogen fuel concentration, a large amount of nitrogen oxides are formed, then it is reduced dramatically at equivalent ratio of ϕ=1.

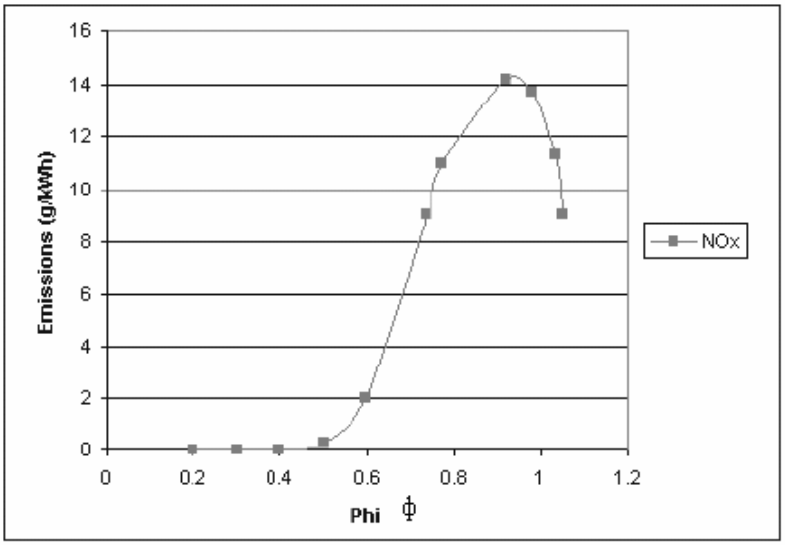

Fig.2. 23 Typical NO_x emission for a hydrogen engine vs ϕ,(equivalent ratio) [3,18].

Since one of the reasons for using hydrogen is low exhaust emissions, hydrogen engines are not normally designed to run at a stoichiometric air-fuel ratio. Typically, hydrogen engines are designed to use about twice as much air as theoretically required for complete combustion. At this air-fuel ratio, the formation of NO_x is reduced to near zero. Therefore, to keep the engine output high compared to similar size of gasoline engine, the hydrogen engines are usually equipped with turbochargers or superchargers.

Two meaningful steps have identified, that allow the engine to be operated at full load without producing unacceptable amount of NO_x, [18]. First, it was experimentally determined that, at high engine loads, a late start of injection is beneficial for the avoidance of NO_x formation in the engine. Second, operating the hydrogen engine at full load with $\phi=1$ (stoichiometric mixture) allows an almost complete catalytic conversion of the NO_x and H_2 to N_2 and H_2O by means of a simple catalytic converter.

2.6 Summary

- Hydrogen may become the "energy carrier of the future". Most schemes for generating hydrogen should base on the splitting of water using renewable energy directly, or indirectly via electricity. Hydrogen would then be used as a substitute for

natural gas. Although the technical feasibility of water splitting on a large scale has yet to be established, a "hydrogen economy" remains at least a distant possibility.

- Hydrogen allows a smooth and gradual transition from 100% fossil to 100% renewable fuel. Simply, because the engine can run on a liquid fuel and switches to hydrogen when it is available.
- Hydrogen is great in energy content (by mass), but its low-density makes the hydrogen needs more storage space on vehicle.
- The direct injection system is more suitable for hydrogen injection into the engine cylinder than the external injection into the inlet manifold. The direct injection can produce about 35% higher power output than the external injection, but it needs up to 40-50 bar injection pressure.
- The rotary Wankel engine is the best choice for the hydrogen internal combustion engine simply because the different strokes occur in different locations with high surface/volume ratios, giving adequate cooling possibilities to prevent backfiring or pre-ignition.
- Wankel engine is very simple in its component with very high volumetric efficiency and it has a very high power to weight ratio makes it a very compact engine.
- The developed technology introduced by Mazda in its RENESIS (RX-8) model has proved that the Wankel engine is the engine of future and suits the hydrogen fuel very well.

The next chapter will preview some of literature works concerning the hydrogen fuel and the Wankel rotary engine. Lack of CFD simulation work on Wankel engine in literature, especially when hydrogen is concerned, makes the next chapter to be limited to some of engine simulation and to experimental flow visualization work.

3

Review of Previous CFD Rotary Engine Research and Hydrogen Engine

3.1 Introduction

This section reviews the existing literature on CFD modeling of rotary Wankel engine as well as some of experimental work to visualize the flow inside the combustion chamber, in an effort to place the current work in the context of what has been previously done.
This chapter divided into two parts; the first part deals with CFD engine modeling, the second part deals with hydrogen engine.

3.2 CFD engine modeling

Computational fluid dynamics modeling has come a long way since its entrance into engineering industry over 20 years ago. Increases in the power of computer hardware, together with decreasing of hardware costs, have allowed CFD software tools to be developed to offer the high-tech capabilities we see today.
Computational fluid dynamics (CFD) is now routinely applied to design processes in all manner of industries where the ability to use simulation to visualize the flow physics, heat transfer and associated phenomena. Such as chemical reaction for various design scenarios, where saved time and reduced costs.
The advantages of CFD over the experimental analysis can be summarized as:

- Reduce time and cost.
- Can simulate and analyze hazardous conditions and the experimentally difficult systems.
- Unlimited optimization models and results.

- Quickly identify the most promising design candidates for further development.

However, CFD will never replace theoretical or experimental approach. But, only helps to interpret and understand the results of theory and experiment and vice versa.

Early modeling efforts on the Wankel engine were based on thermodynamic models [4,8], and also on one-dimensional modeling of premixed-charge combustion, [9]. Multidimensional models of the Wankel engine are of more recent origin. Grasso et al. [10], presented the earliest three-dimensional computation of a stratified charge rotary engine (SCRE) during the early stage of flame propagation.

Subsequent computations performed by Abraham and Bracco [15,16], led to some important design changes in the rotary engine development at Deere and co., especially in the fuel injector configuration. Their code, REC-3D-FSC-86, is a modified version of KIVA code developed at Los Alamos National laboratory [11], for the modeling of reciprocating engines. KIVA makes use of a conditionally stable logarithm; the stability of KIVA scheme is improved by making use of an acoustic sub cycling step in order to alleviate the stiffness problems arising from compressibility effects. They concluded that non-uniformity of mixing of fuel and air is attributed to the large fluid acceleration caused by the motion of the rotor. There appears to be a considerable room for improvement in the code, since it neglects the spatial gradients whenever the grid spacing becomes smaller than some predefined value and also requires excessive CPU time when engine speed becomes small. In another work, Abraham and Bracco [12], with concentration on ignition strategies in stratified charge RE engine; they concluded that the use of two spark plugs would increase the engine efficiency by 7-10%. Also they find that the modification of the rotor pocket located towards the leading edge of the rotor would produce re-circulation results in faster fuel combustion, leads to better engine efficiency.

Shih et al. [13], presented the earliest two-dimensional computations of a motored wankel engine in the absence of combustion. Their code, LEWIS-2D, is based on the beam-warming type of alternating-direction implicit (ADI) method. Their computations were subsequently extended to three-dimensions in Steinthorsson et al. [14]. Linear stability analysis has shown that the ADI method is unconditionally stable in two-dimensions but it is unstable in three-

dimensions. Li et al. [17], modified their LEWIS-3D code based on upwind schemes together with the incorporation of a k-ϵ turbulence model for better stability.

Recently, Raju et al. [25], sponsored by NASA has developed a new computer code to analyze the chemically reactive flow and spray combustion processes occurring inside a stratified-charge rotary engine. The authors described the mathematical and numerical details of their new code. They presented their results at limited operating conditions for code validation process. Typical results include, pressure and temperature, torque generated by the non-uniform pressure distribution within the chamber, energy release rates and various flow related phenomenon were reported and compared with other predictions reported in literature. They concluded that the non-uniform pressure is higher near the trailing apex region than the leading apex region and mostly the rotor-induced fluid motion determines it. The code appears to be potentially efficient compared with other schemes used in modeling wankel engines; even its turbulence model needs to be improved.

In 2003, Fushui Liu, [1] has conducted a research work for BMW, to investigate the mixture formation of direct injection of hydrogen, inside the combustion chamber of normal reciprocating engine. The research was conducted at the chair of combustion engines and flight propulsion, BTU-Cottbus. AVL-FIRE Code, V7.x and V8.x were used for this study. Great effort has been put on verification and validation of these two Codes. The codes were optimized for hydrogen injection including the different variables adjustment and have been proved that the Codes are capable of simulating the sonic speed velocities of hydrogen injection. The moving mesh tool applied by these codes makes the results more reliable.

Liu has proved that the multi-hole injector gives better mixture formation and better fuel concentration at the spark plug. All combustion models available in these codes were tested for there suitability to simulate hydrogen combustion. The Turbulent Flame Speed Closure Combustion Model (TFSCM) is the best model available FIRE-V8.11-V8.3 to simulate the laminar combustion of hydrogen and can reflect a good temperature performance, in the range of $0.5<\Phi\leq 1$.

In 2004, Padmarajan et al. [6], at Cranfield University and with the help of Fluent-6.1 dynamic mesh, have developed a new 2-D model of rotated Wankel engine. The 2-D model simulating the three combustion chambers on the rotor faces with no combustion.

The aim of this work is to study the flow fields inside the combustion chambers and to detect the rotor apex leakage between the chambers. The inlet and outlet ports were not simulated, and their effects were not reported.

Lack of experimental results reported by the authors, limited this work to be validated.

Also, simulating the rotary engine without inlet port, omitting the inlet flow effects on the overall field inside the combustion chamber, limits the flow field to be affected only by the rotor movement. However, the inlet flow is very important for the mixture formation and has a great effect on the flow inside the engine chamber even after inlet port closed.

The authors noticed the effect of inlet flow is important and recommended that in future work.

Also, the optical visualization inside the engine chamber is very important for comparison and validation of computed flow field patterns inside the combustion chamber.

Hamady et al., 1989 [24], realized the importance of flow behavior on mixture formation inside the combustion chamber of a stratified charge rotary engine. They developed a high-speed flow visualization and Laser Doppler Velocimetry (LDV) system, to study the fuel-air mixing and flow characteristics inside a combustion chamber of a motored rotary engine. Mazda 12A base housing, with a modified Plexiglas window to the side housing was used. This provides optical access for LDV measurements and flow visualization inside the combustion chamber by a high-speed camera.

For the fist time, the high-speed camera captured a roll-up vortex during the compression stroke, and it has an important effect on the level of turbulence inside the engine combustion during the initial combustion period. This roll-up vortex has not been observed numerically at that time.

In 1993, Yasuaki et al. [37], have conducted an experimental investigation on air-fuel mixture formation inside a low-pressure direct injection stratified charge rotary engine, using similar technique of visualization. The visible zone covers about three quarter of a peripheral inlet ported (side inlet port) engine, allowing continuous observation of the flow inside the combustion chamber during intake-expansion strokes. An arched quartz glass window was installed at the top of the rotor housing to introduce a laser light sheet into the combustion chamber. A high-speed video camera was used to capture images of flow field during intake-expansion strokes at 500 rpm.

A little effect of the rotor recess shape on the flow field patterns were observed for five shapes of rotor recess tested.

3.3 Hydrogen engine

The use of hydrogen to fuel an engine was reported since N.A. Otto, (the inventor of Otto cycle, 1860s and 1870s), works with combustion engines. [18]. During his work with combustion engines reportedly used a synthetic producer gas for fuel with hydrogen content of over 50%. Otto also experimented with gasoline, but found it dangerous to work with, promoting him to return to using gaseous fuels, until the carburetor was developed to use gasoline practically and safely, where the interest in other fuels subsided.

Liquid hydrogen is extensively used in space program, with its best energy-to-weight ratio of any other fuel, considered to be the best choice for rocket engines.

In recent years, the concern for cleaner air, the stricter air pollution regulation and the reduction of the fossil fuels dependency have raised the interest in hydrogen as an auto engine fuel.

A comprehensive research work conducted by researchers and automakers to produce a hydrogen auto applying a fuel cell or internal combustion engine, with engine performance near to gasoline and diesel engine.

BMW, Ford Motor Company, Nissan Motors, Mazda and some other research institutions are exploring hydrogen fueled IC engines for the near-term use and to compute with fuel cells.

An intensive research effort has been carried out by BMW since 1979 on port fuel injection of hydrogen engines. BMW found that with external mixture formation, at stoichiometric air/fuel ratio operation, the hydrogen displaces approximately 30% of the aspirated air. Therefore, BMW suggests that a direct supply of hydrogen to combustion chamber will allow the engine to have the best power density. [43]. The investigation of BMW shows that the fuel injection should be ended before ignition started. The latest possible injection point with increased load moved from 40˚ to 60˚ crank angle BTDC. It also shows that direct injection of hydrogen was able to achieve an indicated mean effective pressure greater than gasoline. The research efforts from BMW indicated that hydrogen fueled engines are a promising

option for future automobiles. Based on these studies, direct injection of hydrogen into the combustion chamber may provide a means to increase engine efficiency and decrease emissions while maintaining an optimal level of power output. . [42,43,44].

Ford Motor Company began research and development of a hydrogen fueled IC engine in 1997, which was a Ford 2.0L Zetec engine. Many modifications were made to the engine to improve combustion. Test results indicated that hydrogen as a fuel for an IC engine has unique properties such as low carbon related emissions and high fuel economy due to high equivalent octane number rating, [45]. Backfire which can be described as the up normal ignition of the fresh charge before the intake valve closes, is one of the most harmful phenomena of a hydrogen engine. However, pre-ignition of the fresh charge after the intake valve closes, is another harmful phenomena in hydrogen engine. It imposes a limit on maximum torque output that is primarily a function of maximum mixture richness Φ capability, compression ratio and spark timing, charge density and engine speed. Ford's testing indicated that, relative to gasoline, pre-ignition reduced torque output of the engine by 35% at low and mid speeds and 50% at high speed. The best specific fuel consumption occurred at Φ=0.25, while unburned exhaust hydrogen increases drastically when operating leaner than Φ=0.25. The NO_x emissions are primarily a function of equivalence ratio. The NOx concentration increases dramatically at Φ>0.6. As hydrogen has a very broad flammability and burn rate range, Ford suggests that the hydrogen can be controlled in a manner similar to a gasoline engine, where fuel/air ratio is constant and desired torque is a function of both fuel and air flow. To improve performance, the hydrogen engine was installed with a supercharger, which boosted air into the engine to enrich the fuel/air mixture. Tests showed a torque deficit of 28% compared to gasoline and a deficit of 7% utilizing an air-to-air intercooler. [45,46,47,48].

Nissan Motors and Musashi Institute of Technology also have determined that adding boost pressure to a hydrogen-fueled engine will help to achieve higher efficiency, power, and lower NO_x emissions. [51].

When it comes to rotary engine, Mazda Motors is the leader in Wankel rotary engine development and has introduced its RENESIS rotary engine running on hydrogen in 2003 after years of research and development. The engine was fitted to Mazda RX-8 and proved a high power output for a naturally aspirated engine of its size and demonstrates significantly

improved fuel economy and reduced emissions compared with previous generation of rotary engines. [52]. The RENESIS hydrogen rotary engine incorporates an electronically controlled hydrogen injector system, (the hydrogen is injected in a gaseous state). The engine uses a side port system and dual hydrogen injectors in each of the engine's twin rotor housing to directly inject hydrogen into the combustion chambers.

Mazda RX-8. By virtue of its smooth performance, compact size and unique driving characteristics, RENESIS was named international engine of the year in June 2003.

In an experimental study of hydrogen fueled engine, Sierens et al. [20], have modified a V-8 engine with a compression ratio of 8.5:1, to burn hydrogen. For a complete control of the combustion process and to increase the resistance to backfire, a sequential timed multipoint injection of hydrogen and electronic management system were applied. The engine power output was controlled, firstly by varying the A/F ratio (WOT, widely open throttle, like diesel engine), then the power was controlled by fixing the A/R and varying the air flow, (using air throttle, like normal gasoline engine), and both results were compared.

The results show that, when the engine power was controlled without throttle, the greatest benefit is a better engine efficiency due to the reduction of flow losses around the throttle valve, and hence the reduction of the negative pumping work. The engine instability and exhaust hydrogen content, were the main disadvantages when the engine is running at low idling speed. A slight engine throttling was necessary to keep the engine running at low idling speed and to reduce the hydrogen content in exhaust gases.

Lee et al. [36], have investigated the cause of pre-ignition and backfire in hydrogen engine using an external fuel mixture. In addition to hot spots, that suspected to be the main cause of pre-ignition and backfire, similar to gasoline engine, during high temperature engine operation. The hydrogen fuel ultra lean limits of flammability and short quenching distances, makes hydrogen to be burn very slowly in small and narrow volumes where other fuels such as gasoline may not be able to burn. This means that the slow burning process of hydrogen fuel inside the crevice volumes (such as the crevice volume between the piston and cylinder and around the spark plug electrode) could continue up to and during the intake process. During the intake process, the hot burning gases could flow out of crevice volumes and ignite the intake charge thus causing backfire.

3.4 Liquid fuel engine

Most of the Wankel engines, produced in 70's and 80's from the last century were operated on gasoline (petrol) with a simple external mixture system. However, to be able to burn fuels having a higher flash point than gasoline, then the simple carbureted or external injection would not be the preferred system. Adaptation to burn a single fuel such diesel would satisfy some civil requirements but a multi-fuel capability is desired for military use and some other application.

The combustion characteristics of the Wankel engine are favorable to such developments and it has proved possible, in the work at Curtiss-Wright and elsewhere, to run engines successfully on kerosene and diesel type fuels by using spark ignition in combination with fuel injection or ultrasonic atomization system. Wankel engine designs using compression ignition were being developed at Rolls-Royce and elsewhere. The choice of engine type and fuel system for eventual multi-fuel use will depend on the range of fuel considered.

With charge stratification, efficiency and emission improvements are possible and can reach an acceptable level with relatively minor modifications.

The advantage of the fuel injection system over the carburetor system is the possibility of controlling the amount and timing of fuel supply more freely and accurately [21]. The development of the fuel injection system for the rotary engine is under way for the purposes of improvement of performance and fuel economy, purification of exhaust emission, etc.

Early efforts at Curtiss-Wright to develop the stratified combustion concept involved the use of a multi-hole nozzle with one of its sprays directed toward the spark plug [76]. The primary difficulty was one of maintaining the correct fuel/air ratio in the vicinity of the spark plug. Under specific operating conditions, the amount of fuel from the injector spray would be 'just right', and the engine ran fine, having the smoothness, and fuel economy desired. Once the spray penetration characteristics changed as the amount of fuel injected changed, either increased or decreased, the optimum conditions for ignition of the fuel spray that existed by the spark plug changed, resulting in poorer combustion characteristics.

Development progress of the direct injected stratified charge rotary engine program at Curtiss-Wright in detailed basic configurations were described and compared to both reciprocating stratified charge engines and the carbureted rotary engine, by Loyd et al. [72].

Data and theoretical analyses were presented for progressive developments from initial feasibility testing in 1962 through to the latest engine configurations on test in 1975. Loyd et al. has concluded that the stratified charge rotary engine research efforts to date have demonstrated potential for an efficient, light weight, compact, economic power plant capable of broad range operations justifying further research efforts.

Mount et al. 1989 [73] discusses the design and performance of stratified-charge rotary engines developed for commercial aviation propulsion and APU (auxiliary power unit) application as well as for marine, industrial, and military requirements. Mount et al. has introduced a direct fuel injection configuration that has performed well under a wide range of speed, load, and environmental conditions and with a variety of liquid fuels. He reports a lack of octane and cetane sensitivities, so that diesel, gasoline, and jet fuel can all be used with this configuration.

As air in the rotor recess passes below, the spark plug ignites a locally rich pilot stream that in turn ignites the fuel from the main injector. The net fuel-air ratio is lean, resulting in improved fuel economy over normal carburetion.

Jones et al. [74] has introduced a rotary combustion engine designed for operation as a stratified charge engine in which the fuel-air mixture supplied to the engine working chambers during their intake phase is very lean. Additional fuel is injected into the working chambers after there has been substantial compression of the initial lean mixture. The additional fuel being ignited as it is injected into the engine working chambers and the resulting combustion of this additional fuel is effective to ignite the rest lean combustion mixture.

Ryoji K. et al. [75] have a study of a direct-injection stratified-charge system, as applied to a rotary engine for motor vehicle usage undertaken. The goals of this study were improved fuel consumption and reduced exhaust emissions. Stable ignition and ideal stratification system were developed by means numerical calculation, air fuel mixture measurements, and actual engine tests. The use of direct injection stratified-charge resulted in significantly improved fuel consumption and reduced exhaust emissions. The use of an exhaust gas re-circulating system was also studied and found to be beneficial in NO_x reduction.

4

CFD Theory and Mathematical Formulation

4.1 Introduction

In this chapter, governing equations of motion for compressible reactive flow, heat transfer, species transport, spray and combustion models, in its form that used by the AVL-Fire main-program are introduced in summary and for more details refer to the program manual, [63, 64] theory part. Conservation laws of mass, momentum, energy, amount of substance, etc, are governing the fluid flows. It is more common practice in numerical fluid mechanics calculations to compute time or ensemble-averaged values of the variable to be calculated. This is achieved by replacing the instantaneous values of dependent variables (nominated by the symbol $\boldsymbol{\Phi}$) by the sum of an ensemble-averaged value $\overline{\Phi}$ and a variation Φ' about this value.

$$\Phi = \overline{\Phi} + \Phi' \tag{4.1}$$

The replacement of the instantaneous quantities in conservation equations for momentum, continuity and thermal energy, by the average of a mean and fluctuating component, leads to a set of equations in Cartesian tensor notations of mass, momentum and thermal energy conservation, and passive scalar, turbulent kinetic energy and Reynolds stress transport equations.

In flows involving considerable density fluctuation (e.g. due to combustion), the terms of these equations remain the same provided that the velocities and scalars such as species concentrations, turbulence kinetic energy and its viscous dissipation rate, but not density and pressure, are decomposed into a density-weighted mean and fluctuations and then ensemble-averaged.

4.2 Differential equations in Cartesian coordinates

4.2.1 Conservation of mass and momentum

$$\frac{\partial \overline{\rho}}{\partial t} + \frac{\partial}{\partial x_j}\left(\overline{\rho}\,\overline{u}_j\right) = 0 \tag{4.2}$$

And,

$$\frac{\partial}{\partial t}\left(\overline{\rho}\overline{u}_i\right) + \frac{\partial}{\partial x_i}\left(\overline{\rho}\overline{u}_i\,\overline{u}_j + \overline{\rho}\,\overline{u'_i\,u'_j} - \overline{\tau}_{ij}\right) + \frac{\partial p}{\partial x_i} - \overline{\rho} g \frac{x_i}{|x|} = 0 \tag{4.3}$$

In this equation, u_j is the velocity component along the Cartesian coordinate direction x_j, p is pressure, ρ is density, g is the gravity acceleration and the stress tensor component $\boldsymbol{\tau}_{ij}$ have been grouped with certain fluctuation quantities, and will become clear in the next sub-section. Fluctuations in density and in laminar viscosity have been ignored, as these are negligible in non-reacting turbulent flows.

4.2.2 Conservation of thermal energy

Ignoring fluctuation of density, laminar viscosity, thermal conductivity and specific heat, the ensemble-averaged stagnation enthalpy equation is:

$$\frac{\partial}{\partial t}\left(\overline{\rho}h\right) + \frac{\partial}{\partial x_j}\left(\overline{\rho}\,\overline{u}_j\,\overline{h} + \overline{\rho}\,\overline{u'_j h'}\right) - \frac{\partial}{\partial x_j}\left(\frac{\overline{\lambda}}{c_p}\frac{\partial \overline{h}}{\partial x_j}\right) - \frac{\partial}{\partial x_j}\left(\tau_{ij}u_i\right) - \frac{\partial \overline{p}}{\partial t} - S_h = 0 \tag{4.4}$$

Where:

$$\overline{h} = \overline{c}_p\,\overline{T} + \frac{1}{2}\overline{u}_i^{\,2} \tag{4.5}$$

And S_h is the heat release of the chemical reaction.

4.2.3 Passive scalar equation

Air purity is a quantity used to characterize the mixing process between two chemically inert gases (with masses $\mathbf{m}_1$ and $\mathbf{m}_2$ respectively), e.g. hot gases and fresh air. It is defined as:

$$f = \frac{m_1}{m_1 + m_2} \tag{4.6}$$

Its conservation equation in the following form:

$$\frac{\partial}{\partial t}(\bar{\rho}\bar{f}) + \frac{\partial}{\partial x_j}\left(\bar{\rho}\bar{u}_j\bar{f} + \bar{\rho}\overline{u'_j f'}\right) - \frac{\partial}{\partial x_j}\left(D\frac{\partial \bar{f}}{\partial x_j}\right) = 0 \tag{4.7}$$

Terms relating to fluctuations in the molecular diffusion coefficient D have been ignored.
A part from the simplification mentioned above, equations (4.2) to (4.7) are as complete and exact as their counterparts for instantaneous quantities. They are insoluble because the averaging process has given rise to new unknowns like $\rho u_1' u_2'$. Before a solution can be carried out, further equations for these unknowns must be obtained to form a closed set. The process of formulating equations for these unknown correlations is termed turbulence modeling and will clarify in the next section.

4.3 Turbulence models

4.3.1 Introduction

As indicated in the previous subsection, the instantaneous value of some dependent variables of the flow, denoted $\mathbf{\Phi}$, can be represented mathematically by an average value, $\overline{\Phi}$, upon which a fluctuating component, Φ', has been superimposed, i.e.:

$$\Phi = \overline{\Phi} + \Phi' \tag{4.8}$$

For a statistically stationary or "steady" flow, it is usual to define $\overline{\Phi}$ as being a time-averaged value as:

$$\bar{\phi}(x_0,t) = \underset{t_0 \to \infty}{\text{Limit}} \frac{1}{2t_0} \int_{t=-t_0}^{t=t_0} \phi(x_0,t)dt \tag{4.9}$$

If the flow is non-stationary or unsteady, an ensemble-averaged value is defined as:

$$\bar{\phi}(x_0,t) = \underset{m\to\infty}{\text{Limit}} \frac{1}{2m+1} \sum_{n=-m}^{n=m} \phi(x_0, nt_0 + t) \tag{4.10}$$

If the flow is not temporally cyclically repetitive, n stands for the number of identical experimental repetitions. If the flow is cyclically repetitive, then n is the number of cycles; t is the time after the start of each experiment or cycle of period $\mathbf{t}_0$, and $\mathbf{x}_0$ is some fixed point in space.

A variety of models exist for the incorporation of the effects of turbulence into flow calculations. In AVL-Fire Code, the standard model of turbulence is the k-ε model and the Reynolds-stress model can also be used, depending on the flow case some parameters, for more details refer to [38],

4.3.2 k-ε model

The k-ε model is the most widely used turbulence model in practical engineering applications. This model was originally proposed by Harlow and Nakayama, [63] and developed further by a number of researchers. The k-ε model employs additional partial differential equations for the turbulence kinetic energy *k* defined by:

$$k = \frac{\overline{u'_i{}^2}}{2} \tag{4.11}$$

And its dissipation:

$$\varepsilon = C_\mu^{3/4} \frac{k^{3/2}}{l_t} \tag{4.12}$$

Where: l_t is the turbulence scale and C_μ is an empirical coefficient.

4.3.2.1 Turbulent kinetic energy

Multiplying the momentum equation for u_i; with its respective fluctuating component u_i'; summing i, and ensemble-averaging can derive a differential equation for the conservation of turbulence kinetic energy and the result is as follows:

$$\underbrace{\frac{\partial}{\partial t}(\bar{\rho}k)}_{\text{I}}+\underbrace{\frac{\partial}{\partial x_j}(\bar{\rho}\,\bar{u}_j k)}_{\text{II}}+\underbrace{\frac{\partial}{\partial x_j}\left[\bar{\rho}\,\overline{u'_j\left(k+\frac{p'}{\bar{\rho}}\right)}\right]}_{\text{III}}+\underbrace{\bar{\rho}\overline{u'_i u'_j}\frac{\partial \bar{u}_j}{\partial x_i}}_{\text{IV}}+\underbrace{\mu\overline{\left(\frac{\partial u'_j}{\partial x i}\right)^2}}_{\text{V}}-\underbrace{\frac{\partial}{\partial x_j}\left(\mu\frac{\partial k}{\partial x_j}\right)}_{\text{VI}}=0 \qquad (4.13)$$

Terms I, and II represent the rate of change and convection of k by the mean flow respectively. Term III, describes the transport of k by the fluctuating velocities, which has been assumed by Prandtl, Kolmogorov, and others to be a diffusion process.

Term III is modeled as:

$$\text{Term III} = -\frac{\partial}{\partial x_j}\left(\frac{\mu_t}{\text{Pr}}\frac{\partial k}{\partial x_j}\right) \qquad (4.14)$$

Where, Pr is a turbulent Prandtl number.

Term IV consists of products of stresses and mean strain rates and represents the generation rate of turbulence energy. A general form of the Boussinesq hypothesis for a compressible flow may be used to express the stress component in terms of the mean strain rate:

$$-\bar{\rho}\overline{u'_i u'_j} = 2\mu_t\left(\frac{\partial \bar{u}_i}{\partial x_i}\right)-\frac{2}{3}\left(\bar{\rho}k+\mu_t\frac{\partial \bar{u}_m}{\partial x_m}\right) \qquad (4.15)$$

And:

$$-\bar{\rho}\overline{u'_i u'_j} = \mu_t\left(\frac{\partial \bar{u}_j}{\partial x_i}+\frac{\partial \bar{u}_i}{\partial x_j}\right) \qquad (4.16)$$

Using these expressions, the generation rate may be written as:

$$G_t = \frac{\partial \bar{u}_j}{\partial x_i}\left(\frac{\partial \bar{u}_j}{\partial x_i} + \frac{\partial \bar{u}_i}{\partial x_j}\right) \tag{4.17}$$

Term V represents the dissipation of turbulent energy and is replaced by $\rho\varepsilon$, this being the dependent variable of its own transport equation as mentioned earlier.

Noting that $k^{1/2}$ and $k^{2/3}/\boldsymbol{\varepsilon}$ are a characteristic velocity and length scale of the turbulent field respectively, dimensional analysis yields the following relation for turbulent viscosity.

$$\mu_t = C_\mu \bar{\rho} \frac{k^2}{\varepsilon} \tag{4.18}$$

Where, C_μ is an empirical coefficient, usually ascribed a constant value.

Term VI represents the transport of k by molecular diffusion and may be combined with the modeled form of the term III to give:

$$-\frac{\partial}{\partial x_j}\left(\frac{\mu_{eff}}{Pr}\frac{\partial k}{\partial x_j}\right) \tag{4.19}$$

Where the effective viscosity, $\boldsymbol{\mu}_{eff}$ is the sum of the turbulent and laminar viscosity, i.e.:

$$\mu_{eff} = \mu_t + \mu \tag{4.20}$$

The final equation of the k equation may be written as:

$$\frac{\partial}{\partial t}(\bar{\rho}k) + \frac{\partial}{\partial x_j}(\bar{\rho}\bar{u}_j k) = \frac{\partial}{\partial x_j}\left(\frac{\mu_{eff}}{\sigma_k}\frac{\partial k}{\partial x_j}\right) + \mu_{eff} G_t - \frac{2}{3}\frac{\partial \bar{u}_m}{\partial x_m}\left(\mu_{eff}\frac{\partial \bar{u}_m}{\partial x_m} + \bar{\rho}k\right) - \bar{\rho}\varepsilon \tag{4.21}$$

4.3.2.2 Dissipation equation

An exact equation for $\boldsymbol{\varepsilon}$ can be derived by taking a derivative of u_i' with respect to x_1, multiplying by the term in equation (4.22), and ensemble averaging.

$$2\mu\left(\frac{\partial u'_j}{\partial x_1}\right) \tag{4.22}$$

The result in general form is:

$$\underbrace{\frac{\partial}{\partial t}(\bar{\rho}\varepsilon)}_{\text{I}}+\underbrace{\frac{\partial}{\partial x_j}\left(\bar{\rho}\,\bar{u}_j.\varepsilon\right)}_{\text{II}}+\underbrace{\frac{\partial}{\partial x_j}\left(\bar{\rho}\overline{u'_j\varepsilon}\right)}_{\text{III}}+\underbrace{2\mu\left\{\frac{\partial \bar{u}_j}{\partial x_l}\,\overline{\frac{\partial u'_i}{\partial x_l}\frac{\partial u'_i}{\partial x_j}}+\frac{\partial \bar{u}_i}{\partial x_j}\,\overline{\left(\frac{\partial u'_i}{\partial x_l}\frac{\partial u'_i}{\partial x_l}\right)}\right\}}_{\text{IV}}$$

$$\underbrace{+2\mu\left\{\overline{\frac{\partial u'_i}{\partial x_l}\frac{\partial u'_j}{\partial x_l}\frac{\partial u'_i}{\partial x_j}}+\frac{\mu}{\rho}\overline{\left(\frac{\partial^2 u'_i}{\partial x_j\partial x_l}\right)^2}\right\}}_{\text{V}}\underbrace{-2\bar{\rho}\varepsilon\overline{\frac{\partial u'_j}{\partial x_j}}}_{\text{VI}}\underbrace{-\bar{\rho}\varepsilon\frac{\partial \bar{u}_l}{\partial x_l}}_{\text{VII}}\underbrace{+2\mu\frac{\partial^2 \bar{u}_i}{\partial x_l\partial x_j}\overline{u'_j\frac{\partial u'_i}{\partial x_l}}}_{\text{VIII}}-S_\mu=0 \tag{4.23}$$

Where, S_μ contains terms involving gradients of molecular viscosity and mean density.
Term III describes the transport of ε by the fluctuating velocities and is modeled in the same way as the similar term in the k equation:

$$-\frac{\partial}{\partial x_j}\mu_{eff}\frac{\partial \varepsilon}{\partial x_j} \tag{4.24}$$

Term IV expresses the augmentation of the dissipation rate by the mean motion, which is usually modeled as the following:

$$-C_1\frac{\varepsilon}{k}\bar{\rho}.\overline{u'_i u'_j}\frac{\partial \bar{u}_i}{\partial x_j} \tag{4.25}$$

Term V represents the decay of the dissipation rate and is assumed to be proportional to the dissipation rate itself divided by the decay time scale of the turbulence, k/ε, thus:

$$C_2\bar{\rho}\frac{\varepsilon^2}{k} \tag{4.26}$$

Term VI contains the product of dissipation rate and the divergence of the fluctuating velocity and term VII the divergence of the mean velocity. The former is assumed negligible and is neglected while the latter is retained.

Term VIII contains unknown correlations of gradients of fluctuating velocity; these, together with the remaining terms in S_{μ} are neglected for high Reynolds number flows.

The final form of the **ε**–equation is then:

$$\frac{\partial}{\partial t}(\bar{\rho}\varepsilon)+\frac{\partial}{\partial x_j}\left(\bar{\rho}\,\bar{u}_j\,\varepsilon\right)=\frac{\partial}{\partial x_j}\left(\frac{\mu_{eff}}{\sigma_\varepsilon}\frac{\partial\varepsilon}{\partial x_j}\right)+\frac{\varepsilon}{k}\left\{C_1\mu_{eff}G_t-\frac{2}{3}C_1\frac{\partial\bar{u}_m}{\partial x_m}\left(\mu_{eff}\frac{\partial\bar{u}_m}{\partial x_m}+\bar{\rho}k\right)\right\}$$
$$-\ C_2\frac{\bar{\rho}\,\varepsilon^2}{k}+C_3\bar{\rho}\varepsilon\frac{\partial\bar{u}_m}{\partial x_m} \qquad (4.27)$$

The values assigned to the various empirical constants that appear in the turbulence equations are given in table (4.1).

$C\mu$	C_1	C_2	C_3	k	E	σ_k	σ_ε	σ_h	σ_l	σ_f
0.09	1.44	1.92	-0.373	0.41	8.432	1	1.2174	0.9	0.7	1

Table.4. 1 Values of model constants

4.4 Species transport

4.4.1 Introduction

The species transport module provides the necessary transport equations for gas and phase chemical species in computational domain. Several options are available for the calculation of the physical properties of the chemical species and the mixture of gases.

Depending on the application, Fire offers two main options:

1. Standard species transport model, for all combustion, spray and wall film applications.

2. General species transport model, for catalyst applications or user defined reacting systems.

4.4.2 General species transport model equations

According to the Fire CFD solver manual, the transport equation can be expressed in general form:

$$\frac{\partial}{\partial t}(\rho\, y_k)+\frac{\partial}{\partial x_i}\left(\rho(u_i-u\,\delta_i)y_k\right)=\frac{\partial}{\partial x_i}\left(\Gamma^{ii}_{y_k}\frac{\partial y_k}{\partial x_i}\right)+S_{y_k} \qquad k=1....k_{gas}\text{, [71]} \qquad (4.28)$$

With, y_k represents the mass fraction of an individual chemical species *k*. k_{gas} is the total number of chemical species.

In the case of the species transport equation Γy_k is defined as:

$$\Gamma_{y_k}=\left(\rho\, D_{k,m}+\frac{\mu_t}{Sc_t}\right) \qquad (4.29)$$

Where, Sc_t [-] is the turbulent Schmidt number and $D_{k,m}$ [m^2/s] is the diffusion coefficient of species k in mixture.

The mass source is defined as:

$$S_{yk}=\dot{r}_k \cdot M_k \cdot V_{Cell} \qquad (4.30)$$

Where, $\dot{r}_k$ [kmol/(m^3s)] is the reaction rate of species k and M_k [kmol/kg] is the molecular weight of species k and V_{Cell} [m^3] is the volume of the computational cell.

4.4.3 Standard species transport model equations

In order to reduce the number of equations to be solved, dimensionless quantities are introduced to express the reactive system. The fuel mass fraction y_{fu} can be expressed as:

$$y_{fu} = \frac{m_{fu,u}}{m_{tot}} = \frac{mass\ of\ unburned\ fuel}{mixture\ total\ mass} \tag{4.31}$$

Where, $m_{fu,u}$ and m_{tot} are the unburned fuel mass and the total mixture mass respectively, and the mixture fraction f is defined as:

$$f = \frac{m_{fu,u} + m_{fu,b}}{m_{tot}} \tag{4.32}$$

Where, $m_{fu,b}$ is the mass of burned fuel.

In order to account for the presence of fully reacted residual gases, combustible mixture dilution is simulated; introducing the quantity of residual gas mass fraction g_f is given by the residual gas mass m_{rg} and the oxidizer mass m_{oxid} as:

$$g_f = \frac{m_{rg}}{m_{oxid}} \tag{4.33}$$

The oxidizer mass m_{oxid} is:

$$m_{oxid} = m_{air} + m_{rg} \tag{4.34}$$

The solution of transport equations for the density weighted mean quantities y_{fu}, f, and g as:

$$\frac{\partial}{\partial t}\left(\rho y_{fu}\right) + \frac{\partial}{\partial x_i}\left(\rho U_i y_{fu}\right) = \frac{\partial}{\partial x_i}\left(\Gamma_{fu}\frac{\partial y_{fu}}{\partial x_i}\right) + S_{fu} \tag{4.35}$$

With,

$$S_{fu} = \rho\dot{\rho}_{fu}$$

$$\frac{\partial}{\partial t}\left(\rho_f\right) + \frac{\partial}{\partial x_i}\left(\rho U_i f\right) = \frac{\partial}{\partial x_i}\left(\Gamma_f\frac{\partial f}{\partial x_i}\right) \tag{4.36}$$

$$\frac{\partial}{\partial t}\left(\rho_g\right) + \frac{\partial}{\partial x_i}\left(\rho U_i g\right) = \frac{\partial}{\partial x_i}\left(\Gamma_g\frac{\partial g}{\partial x_i}\right) \tag{4.37}$$

Together with the following algebraic expressions determine the chemically reacting system. This system consists of fuel C_nH_m, oxygen, CO_2, H_2O, and N_2, for simplicity as:

$$\left.\begin{aligned} y_{o2} &= a_1\left[(1-f)-S\left(f-y_{fu}\right)\right] \\ y_{N2} &= (1-a_1)(1-f) \\ y_{p_r} &= 1-y_{fu}-y_{o2}-y_{N2} \\ y_{co2} &= a_2\, y_{pr} \\ y_{H2O} &= a_3\, y_{pr} \end{aligned}\right\} \tag{4.38}$$

In these equations above, y_i (i= O_2, N_2, Pr, CO_2, H_2O) are mass fractions in terms of the total mixture mass. The parameters a_i, are the mass fraction of the species.

Where, a_1, mass fraction of oxygen =0.232, and a_2, is mass fraction of CO_2 in products.

$$a_2 = \frac{n\, M_{co2}}{M_{fu} + M_{O_2}\dfrac{n+\dfrac{m}{4}}{a_1}} \tag{4.39}$$

Mass fraction of H_2O, a_3 is:

$$a_3 = \frac{\dfrac{m}{2} M_{H2O}}{M_{fu} + M_{O_2}\dfrac{n+\dfrac{m}{4}}{a_1}} \tag{4.40}$$

S_{st}, is the stoichiometric air/fuel ratio is:

$$S_{st} = \frac{\left(n+\dfrac{m}{4}\right) M_{O_2}}{a_1 \cdot M_{fu}} \tag{4.41}$$

With *n* and *m* denoting the number of carbon and hydrogen atoms in the fuel molecule. M_{fu}, M_{O2}, M_{CO2}, and M_{H2O} express the molar masses of the individual chemical species.

The determination of the mean reaction rate $\rho \dot{r}_{fu}$ of equation (4.35) is the primary objective of combustion modeling. Some of the combustion models and the description of the proper source terms are introduced in the next sub-section.

4.5 Combustion

4.5.1 Introduction

The determination of mean chemical reaction rates represents a central problem in the numerical simulation of chemical kinetic processes. This is because they appear to be highly non-linear functions of the local values of temperature and species concentrations.

Although it is desirable to use detailed reaction mechanisms, available computational resources are inadequate to manage thousands of elementary reactions with hundreds of participating species. This is due to the fact that for each species considered in the reaction mechanism, an additional conservation equation must be solved.

In Fire, the influence of turbulence on the mean rate of reaction may be treated by five different types of combustion models of different levels of complexity. The choice depends on the application case under consideration and the purpose of the numerical simulation.

1. The first model is called Eddy breakup or Magnussen model, this model is based on the ideas of the eddy dissipation concept, which assumes the mean turbulent reaction rate is determined by the intermixing of cold reactants with hot combustion products.
2. The second model is a Turbulent Flame Speed Closure (TFSC) model, this model determines the mean reaction rate, which is based upon an approach depending on parameters of the turbulence such as turbulence intensity and length scale, and of the flame structure like flame speed and thickness, respectively.
3. The third combustion model is based on the flamelet assumption, i.e. the turbulent flame brush should be composed by an ensemble of laminar flamelets. The length and time scales in the reaction zone are assumed to be smaller than the characteristic turbulent length and time scales, respectively.

4. The fourth model adopts the Probability Density Function (PDF) approach. This approach fully accounts for the simultaneous effects of both finite rate chemistry and turbulence.
5. The fifth model is the Characteristic Timescale Model (CTM), which takes into account a laminar and a turbulent time scale. The laminar time scale considers the slower chemical reaction rates especially at the beginning of the combustion. The turbulent time scale gives the influence of the turbulent motion to the reaction rate.

Thermal NO formation is accounted for by using the extended Zeldovich mechanism and soot formation/oxidation is based on the following individual processes of:

• Particle nucleation
• Surface growth and oxidation to the species concentrations
• Temperature conditions in the flame using suitable reaction rate expressions.

4.5.2 Basic theoretical background

4.5.2.1 Turbulence Controlled Combustion Model

The eddy breakup model is usually called Turbulence Controlled Combustion Model, or Magnussen model. This model assumes that in premixed turbulent flames, the reactants (fuel and oxygen) are contained in the same eddies and are separated from eddies containing hot combustion products. The chemical reactions usually have time scales that are very short compared to the characteristics of the turbulent transport processes. Thus, it can be assumed that the rate of combustion is determined by the rate of intermixing on a molecular scale of eddies containing reactants and those containing hot products, in other words by the rate of dissipation of these eddies.

The mean reaction rate can thus be written as:

$$\overline{\rho \dot{r}_{fu}} = \frac{C_{fu}}{\tau_R} \bar{\rho} \ \min\left(\bar{y}_{fu} \frac{\bar{y}_{ox}}{S} \frac{C_{pr} \bar{y}_{pr}}{1+S} \right) \tag{4.42}$$

Where,

y_{fu}, y_{ox} and y_{pr} are the mass fractions of fuel, Oxygen and products respectively.

C_{fu} and C_{pr} are empirical coefficients; τ_R is the turbulent mixing time scale for reaction.

The first two terms of the "minimum value of" operator "min(...)" simply determine whether fuel or oxygen is present in limiting quantity, and the third term is a reaction probability which ensures that the flame is not spread in the absence of hot products.

4.5.2.2 Turbulent Flame Speed Closure Model (TFSCM)

For the simulation of homogeneously/in-homogeneously premixed combustion processes in SI engines, a turbulent flame speed closure model (TFSCM) is available in Fire. The kernel of this model is the determination of the reaction rate based on an approach depending on parameters of turbulence, i.e. turbulence intensity and turbulent length scale, and of flame structure like the flame thickness and flame speed, respectively. The reaction rate can be determined by two different mechanisms via:

• Auto-ignition and

• Flame propagation scheme

The auto-ignition scheme is described by an Arrhenius approach and the flame propagation mechanism depends mainly on the turbulent flame speed. The larger reaction rate of these two mechanisms is the dominant one. Hence, the fuel reaction rate ω_{fuel} can be described using a maximum operator via:

$$\omega_{fuel} = \max \quad (Auto-ignition\ \omega_{AI}, Flame\ propagation\ \omega_{FP}) \tag{4.43}$$

The first scheme is only constructed for air/fuel equivalence ratios from 1.5 up to 2.0 and for pressure levels between 30 and 120 [bar], respectively. The auto-ignition reaction rate ω_{AI} can be written as:

$$\omega_{AI} = a_1 \rho^{a2}\ y_{fuel}^{a3}\ y_{o2}^{a4}\ T^{a5}\ \exp\left(-\frac{T_a}{T}\right) \tag{4.44}$$

Where a_1 to a_5 are empirical coefficients and T_a is the activation temperature, ρ represents the gas density, y_{fuel} and y_{O2} the fuel and oxygen mass fractions, and T the temperature.

The reaction rate ω_{FP} of the flame propagation mechanism, the second one in this model, can be written as the product of the gas density, the turbulent burning velocity S_T and the fuel mass fraction gradient ∇y_{fuel} via:

$$\omega_{FP} = \rho\ S_T\ \nabla y_{fuel} \tag{4.45}$$

This approach was initially constructed for homogeneously premixed combustion phenomena. In order to apply this model also for inhomogeneous charge processes, changes were made concerning the determination of this reaction rate. In this case, the fuel mass fraction gradient is replaced by the reaction progress variable gradient multiplied by the stoichiometric mixture fraction as follows:

$$\omega_{FP} = \rho \;\; S_T \;\; \nabla_c \;\; f_{st} \tag{4.46}$$

This approach can also be used for homogeneous charge combustion and a near-wall treatment of the reaction rate is considered additionally.

The turbulent Karlovitz number *Ka* describes the ratio of the time scale of the laminar flame ($t_F = \delta_L/S_L$) to the Kolmogorov time scale ($t_K = \sqrt{\nu/\varepsilon}$), with δ_L as the laminar flame thickness, S_L as laminar flame velocity, υ as characteristic kinematic viscosity and ε as dissipation rate, respectively. Hence, the turbulent burning velocity S_T is determined by the following formula dependent on the local Karlovitz number via:

$$k_a = b_1 \;\; \left(\frac{u'}{S_L}\right)^{b_2} \;\; \left(\frac{\delta_L}{l_t}\right)^{b_3} \tag{4.47}$$

$$S_T = \left(S_L + \frac{1}{\sqrt{2}}\alpha \; u'\right) \left(1.0 - k_a^{\,2}\right) \quad for \; 0 < k_a \le 0.5 \tag{4.48}$$

$$S_T = \frac{3}{4} \;\; S_L \left(\frac{\alpha\beta}{2\sqrt{2}} + 1.0\right) \;\; for \;\; 0.5 < k_a \le 1.0 \tag{4.49}$$

$S_T = 0.0 \quad for \; ka > 1.0$

With

$$\alpha = \left(1.0 + \frac{\delta L}{l_t}\right)^{b_4} \quad and \;\; \beta = b5 \;\; \left(\frac{S_L}{u'}\right)^{b_6} \;\; \left(\frac{l_t}{\delta_L}\right)^{b_7} \tag{4.50}$$

Additionally in these expressions, u' represents the turbulence intensity; l_t the turbulent length scale and b_1 to b_7 are constants, respectively. The laminar burning velocity S_L, necessary for the determination of the turbulent burning velocity can be expressed via:

$$S_L = \left(c_1 + c_2\ \lambda + c_3\lambda^2 + c_4\lambda^3 + c_5\lambda^4\right) x \left(c_6 + \frac{c_7}{c_8 + p} + \frac{c_9}{c_{10} + c_{11}\,p + p^2}\right) \exp\left(c_{12} + \frac{c_{13}}{T} + \frac{c_{14}}{T^2}\right) \quad (4.51)$$

Where C_1 to C_{14} are empirical constants, the laminar flame speed S_L and flame thickness δ_L, respectively, depends on the air excess λ, pressure P and temperature T.

The turbulent length scale l_t has to be determined in order to close this model using the following formulation via:

$$l_t = C_\mu^{3/4} \quad \frac{k^{1.5}}{\varepsilon} \quad [m] \quad (4.52)$$

With, k is the turbulence kinetic energy; ε is its dissipation rate and $C\mu$ as constant, respectively.

Within the TFSC model the evaluation of the fresh gas properties, such as pressure and temperature, are required for the determination of the laminar burning velocity S_L.

4.5.2.3 Coherent Flame Model (CFM)

The CFM can be applied for both premixed and non-premixed conditions on the basis of a laminar flamelet concept, whose velocity S_L and thickness δ_L are mean values, integrated along the flame front, only dependent on the pressure, the temperature and the richness in fresh gases. In this model assumes that the reaction takes place within relatively thin layers that separate the fresh unburned gas from the fully burnt gas. Using this assumption the mean turbulent reaction rate $\overline{\dot{w}}$ is computed as the product of the flame surface density Σ and the laminar burning velocity S_L via:

$$\overline{\dot{w}} = \omega_L \quad \Sigma \quad (4.53)$$

ω_L is the mean laminar fuel consumption rate per unit surface along the flame front.

For lean combustion:

$$\omega_L = \rho_{fu,fr}\, S_L \quad with \quad \rho_{fu,fr} = \rho_{fr}\, y_{fu} \quad (4.54)$$

$\rho_{fu,\mathrm{fr}}$ is the partial fuel density of the fresh gas, ρ_{fr} the density of the fresh gas and y_{fu} is the fuel mass fraction in the fresh gas.

4.5.2.4 Probability Density Function (PDF) Model

The simultaneous effect of both finite rate chemistry and turbulence have been taken into account, in this model, and thus obviates the need for any prior assumptions as to whether one of the two processes is limiting the mean rate of reaction.

In this method, the thermo-chemistry of the reactive mixture is expressed in terms of a reaction progress variable c (which is algebraically related to y_{fu}), the mixture fraction f, and the enthalpy in order to account for non-adiabaticity and bulk compression effects on temperature.

The reaction progress variable c is defined as:

$$c = \frac{y_{pr}}{y_{pr,\infty}} \tag{4.55}$$

Where, $y_{Pr,\infty}$ is the maximum product mass fraction to occur, such that either all the fuel or all the oxidant is depleted (or both for stoichiometric mixtures). The variable c is bounded by the values of zero and unity, corresponding to fully unburned and burnt states, regardless of equivalence ratio.

The current method solves a transport equation for the joint probability density function $p(\psi)$ of the mixture fraction f, the reaction progress variable c, and the enthalpy h by means of a Monte Carlo Simulation technique. This enables accurate determination of the chemical sources in terms of the instantaneous thermo-chemical quantities of the reactive system.

All these combustion models were studied and compared by Liu [1], at the chair of combustion engines and flight propulsion, BTU-Cottbus, to find the best suitable model for Hydrogen laminar burning phase of combustion after ignition starts. He concluded that, the TFSC Model is the best model available in Fire to simulate the Hydrogen laminar combustion and reflects a good temperature performance in the range of (Φ=0.5 to 1.0).

5

CFD Flow Simulation

5.1 Introduction

In order to design efficient rotary engines, it is necessary to have a good understanding of how engine design and operating parameters affect the unsteady multidimensional fluid flow, fuel-air mixing and combustion occurring inside rotary engine.

An efficient engine is highly related to the fluid flow inside the combustion chamber (swirl, tumble), and well-designed fuel injection system in order to have better air-fuel mixing and better turbulent combustion. However, the combustion chamber geometry and inlet manifold has a great effect in creation of swirl or tumble flow inside the chamber. The fuel injected to a swirl or tumble chamber has better chance to mix with air and hence complete combustion.

CFD is a better choice to investigate the flow inside the rotary engine combustion chamber. In practical, it is difficult to visualize the fluid flow inside the different designed chambers to be optimized.

In this chapter, the fluid flow behavior inside rotary engine combustion chamber will be investigated in five different chamber designs, and comparison was given.

AVL-FIRE moving mesh tool were used to simulate intake and compression stroke of a rotary Wankel engine. These two strokes are most important for mixture formation and injector position and direction design.

5.2 Types of investigation

The CFD program can be applied to a variety of fluid systems using different approaches, depend on the objectives of the investigation. The objectives of investigation can be divided into the following types of investigation:

5.2.1 Conceptual investigation

The purpose of this investigation is to obtain a general picture of the flow behavior, to test the soundness of a new design idea, or to understand the nature of a previously unexplained behavior. This kind of investigation quickly provides a sense of the dominant flow behaviors and regions of interest when precise detail is not important. Typically, the grid resolution is low to medium and the analysis time is short.

5.2.2 Specific investigation

In specific investigation, the volume grid model is designed to focus on certain flow behaviors in specific regions, such as turbulence near a wall. The design process involves tuning grid resolution to regions of interest and regions of dominant fluid behavior. It also includes tuning the time step increments and output interval to the moments during the simulation when these behaviors are of interest.

5.2.3 Validation investigation

Laboratory measurements provide valuable input data and serve as reference with which to validate analysis results. In addition, analysis results can be helpful in validating laboratory measurements. This type of investigation requires a precise volume grid model using high grid resolutions. Time dependent flows require small time step increments during carefully chosen intervals of the simulation.

5.3 Modeling and simulation tools

AVL-FIRE, V7.x and V8.x are well known general purpose CFD software package. It uses finite volume methods to simulate fluid systems with the following characteristics:

- Time dependent and steady state flows, Compressible and incompressible flows.
- Isothermal and non-isothermal flows, Laminar and turbulent flows.
- Combustion and radiation, Conjugate heat transfer.
- NOx and soot formation, Porous media.
- Sprays, Wall films.

The program consists of three pars:

1- Pre-processor, used to build and prepare a finite volume model of the fluid system for analysis.
2- Fire or Swift analysis program, analyzes the model and initiated by a command at the operating system prompt.
3- Post-processor, Displays the results of analysis using either color graphics to represent flow variables values or by plotting data on graphs.

The k-ε model is the most widely used turbulence model in practical engineering applications. A variety of ignition and combustion models available by this code including: eddy breakup or magnussen model, coherent flame (CFM) model, PDF model, and TFSC model. The fire combustion module enables the calculation of species transport/mixing phenomena and the simulation of combustion in internal combustion engines and technical combustion devices under premixed, partially premixed or a non-premixed conditions. In combination with fire spray model, the combustion module enables the calculation of spray combustion process in direct injection engines. Under these conditions, mixture formation and combustion are simultaneous process exhibiting a significant degree of interaction and interdependence. The droplet breakup models available with suitably adjusted model parameters are highly recommended for this type of application

5.3.1 Moving mesh

The principals of moving meshes are to create two meshes represent the entire range of movement, with one at the start point and the other at end point of movement. The two meshes must have the same number of cells, the same topology and the same link information. To insure the two meshes have the same link information, the use of rearrange option in the pre-processor is necessary. It is necessary to use mesh rezoning when there are unacceptable distorted cells caused by mesh movement or the use of different grid resolution to speed up the simulation. The moving mesh principals will be explained in the next simple example.

5.3.2 Dynamic geometry and boundary condition

The FIRE CFD program allows for dynamic geometry and boundary condition to be defined. This involves a linear interpolation between different geometries and boundaries models saved as separate data sets over a defined number of time steps.

In case of moving geometries, the interpolation is between data sets in the same grid coordinates file (.GEO). In fig. (5.1) a simple example, shows a model of a moving blade A, passing through a fluid towards a fixed blade B.

The first volume grid on the left is stored in data set 1 of the grid coordinate file. The second volume grid on the right is stored in data set 2. Because the topology does not change between data set 1 and 2, the grid arrangement (link information or connectivity of the mesh cells in the .LNK-file) and boundary data set values can be constant.

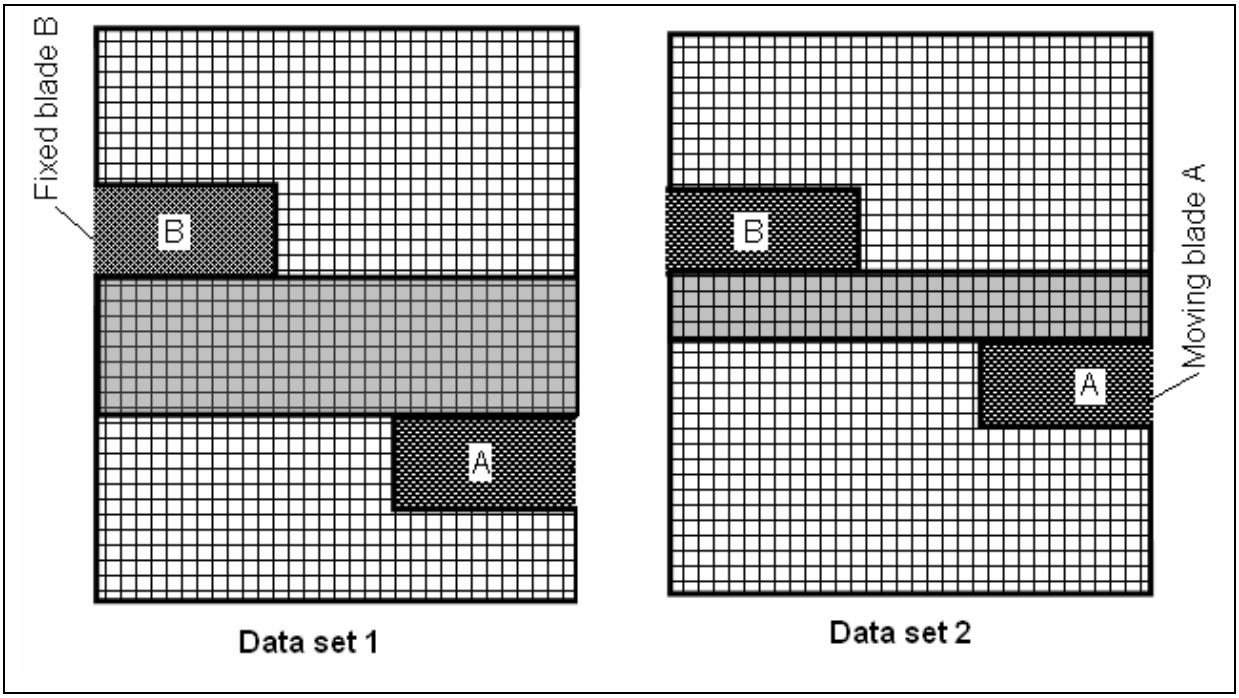

Fig.5. 1 Defining moving walls

After choosing some arbitrary time steps, the grid coordinate interpolation can be defined as follows in table (5.1):

Time Step Range [-]	Starting Data Set	Ending Data Set	Description
0-15	1	1	No motion during the early time steps
16-105	1	2	Blade A in motion, moving equal increments per time step (provided that the time step does not change over the specified range).
106-225	2	2	Blade A reaches the end of its travel and stops.

Table 5. 1 Setup description

In case of boundary properties, the interpolation is between data sets in the same boundary file (.BND). For example if the inlet velocity is changed from 5-10 m/s over a specific period of time. This requires two boundary models, one with an inlet velocity at 5 m/s saved in data set 1, and another with an inlet velocity at 10 m/s saved in data set 2, and every set of data can be loaded at specific time step.

After applying some arbitrary time steps, the interpolation can be defined as follows in table (5.2):

Time Step Range [-]	Starting Data Set	Ending Data Set	Description
0-100	1	1	Inlet velocity is a constant 5m/s from Time step 0 to time step 100.
101-500	1	2	Inlet velocity increases linearly beginning at 5m/s at TS 100 to 10m/s at TS 500. This is a smooth ramping.
501-1000	2	2	Inlet velocity remains at a constant 10m/s through TS 1000.

Table 5. 2 Setup description

The definition of the time steps ranges and associated interpolation ramping are included in the management file.

5.3.3 Rezone data sets

When the previous model involves a moving blade passing near a stationary blade as shown in fig. (5.2). Data set 1 establishes the initial position of blade A. As the analysis program interpolates between data set 1 and data set 2, blade A moves toward blade B compressing the cells between. If blade A were to continue moving with this topology, the cells between the blades would eventually become badly distorted. By rezoning to data set 3 before the cell distortion becomes too great, the integrity of the model can be preserved.

After choosing some arbitrary time steps and assuming a forth data set to continue the motion, the data set interpolation can be specified as follows:

1- **Grid coordinates.**

Time step Range, [-]	Starting Data set	Ending Data set	Description
0-15	1	1	No motion during early steps.
16-105	1	2	Blade A in motion. The rezone occurs at the end of time step 105.
105	2	3	Blade A moves through the rezone. If the ending data set is 3, the blade stops momentarily because the blade position is the same in data sets 2 and 3.
106-225	3.0083	4	Blade A continues moving. Assuming that it requires 120 TS to interpolate from 3 to 4, the increment is 0.0083 (1/120).

2- Boundary.

Time Step Range, [-]	Starting Data Set	Ending Data Set	Description
0-15	1	1	In this case, the boundary properties do not change, and the boundary model data set corresponds to the grid arrangement data set.
16-105	1	1	
105	1	3	During rezone the boundary model data set changed.
106-225	3.0083	3	Unchanged boundary data set.

Table 5. 3 Grid coordinates and boundary setting

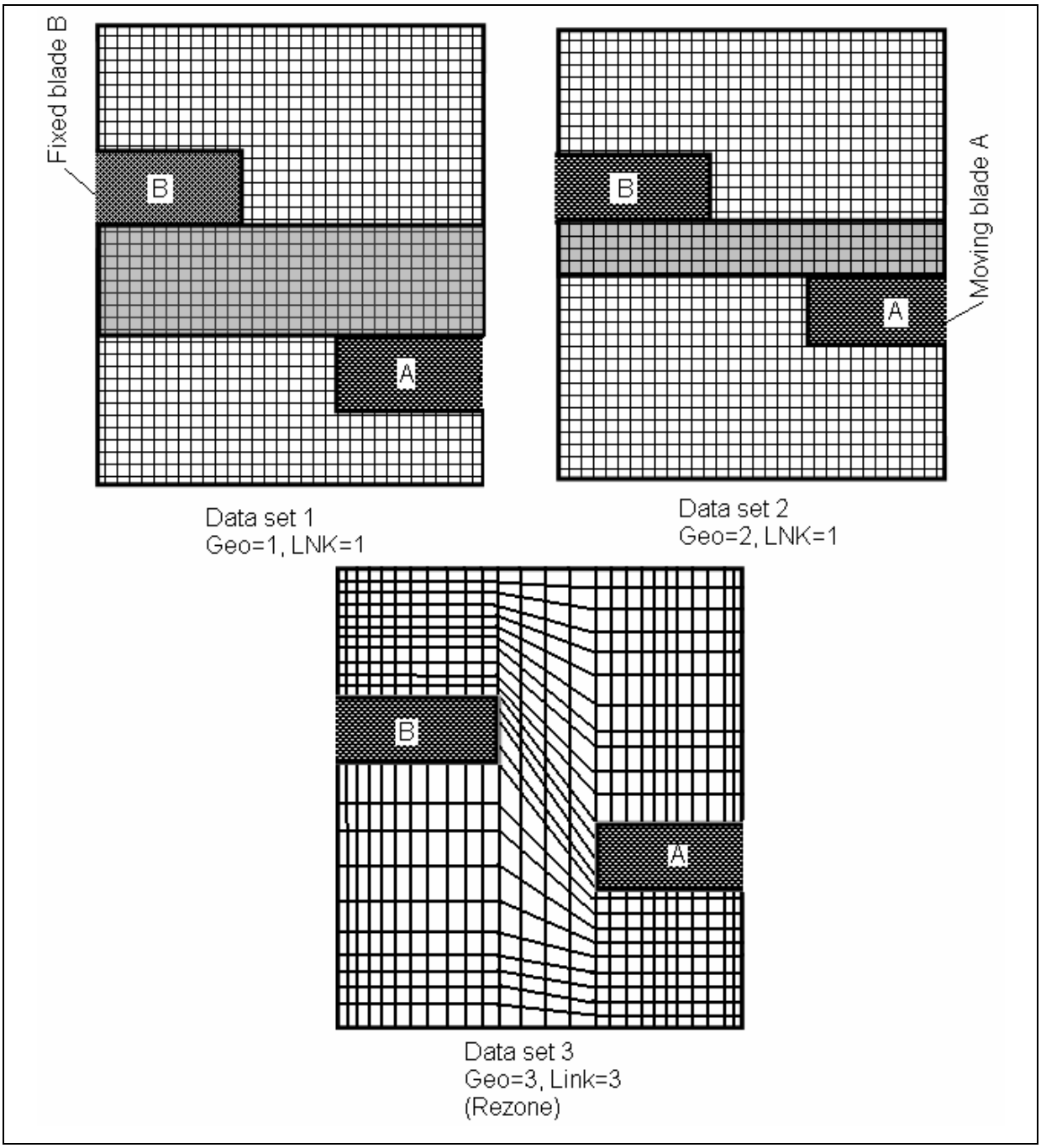

Fig.5. 2 Grid rezone

5.3.4 Ramp

The ramp settings in FIRE-v7.x, allow specifying a dynamic geometry and/or dynamic boundary conditions. For these situations, the changes are defined by specifying a starting condition, an ending condition, and the range of time steps over which this change gradually occurs. The conditions imposed throughout the time step range are linearly interpolated from the defined start and end conditions.

5.3.5 Analysis process

The interest in the fluid system focuses on a specific period called the simulation time. The simulation time may last for a few tenths of a second or several minutes. For calculation purposes, the FIRE program divides the simulation time into units called time steps, as shown in Fig. 5.3. The length of a time step, or time step increment, can vary over the simulation time. The time step increment can be defined in seconds, or for engine application in terms of crank angle.

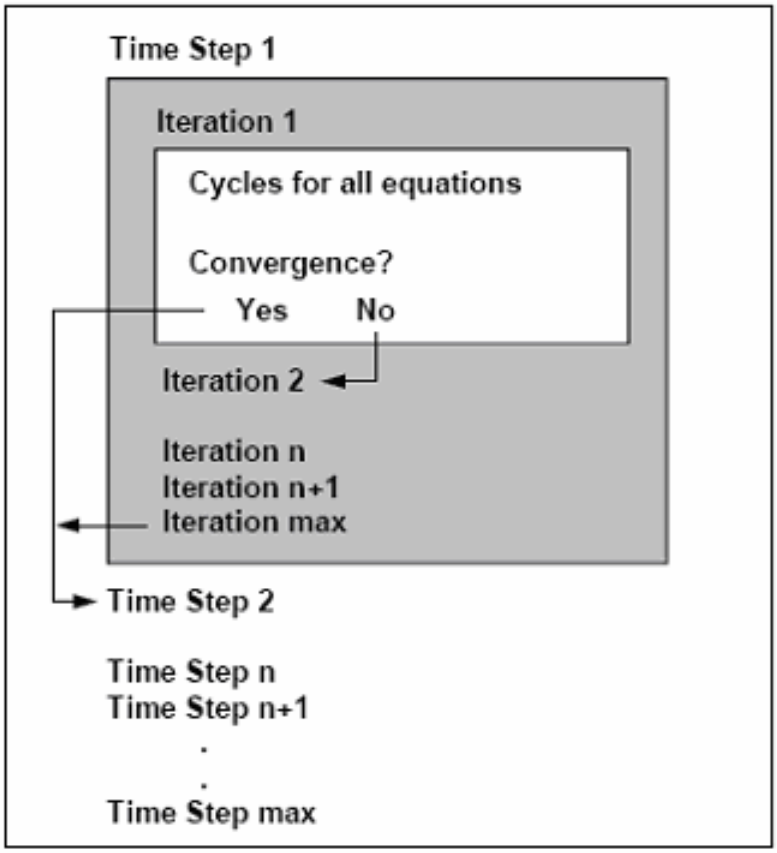

Fig.5. 3 Simulation time

At every time step, the analysis program uses an iterative process to calculate the solution for each flow equation. Each calculation of a particular flow equation is called a cycle.
During each cycle, the program substitutes variable solutions into the flow equation to yield a constant. The program calculates a residual by subtracting this constant from the constant that would be produced by substituting the exact solution. After a sufficient number of cycles, the analysis program compares the pressure correction (mass) residual, averaged over all cells, with a convergence criterion. If the average mass residual is greater than the convergence criterion, the analysis program begins the next iteration. The iterations continue until the convergence criterion is satisfied or until the maximum limit for the number of iterations is reached. Then the analysis program begins the next time step. The analysis program continues processing time steps until the maximum number of time steps is reached.

5.4 Wankel engine simulation

A successful modeling and simulation of Wankel engine flow fields is very important to have a good understanding of the turbulent flow fields inside the combustion chambers of a motored three-dimensional Wankel engine. However, the fuel-air mixture quality is highly dependent on the flow fields inside the combustion chamber and well-optimized fuel injection system. Well understanding of flow behavior inside the combustion chamber leads to answer the important questions of: where to inject the fuel (position and direction), when the fuel should be injected (timing) and how the fuel injected (at once or in several injections).
A geometrical data of a new family of compact lightweight, Wankel engine (KKM-500) for multi-purpose applications are currently under optimization test, were used in this research work. Geometry of five different rotors with different combustion chamber shapes were investigated to find out the effect of combustion chamber shape on the flow fields.
This engine is capable of burning different kind of liquid and gas fuels. The first version of a single rotor, running on diesel fuels is currently fitted to a test bench at BTU-Cottbus for testing and optimization.

The concept basic engine is equipped with a modern Common Rail high-pressure fuel injection system, with a multiple holes injector, as it can be seen in fig. 5.4.

The basic engine is designed to be upgradeable to two, thee or four-rotor engine as a modular design concept and can be seen on fig. 5.5.

Table 5.4 shows the prospect of engine power and power to weight ratio for different sizes of the engine up to four rotors.

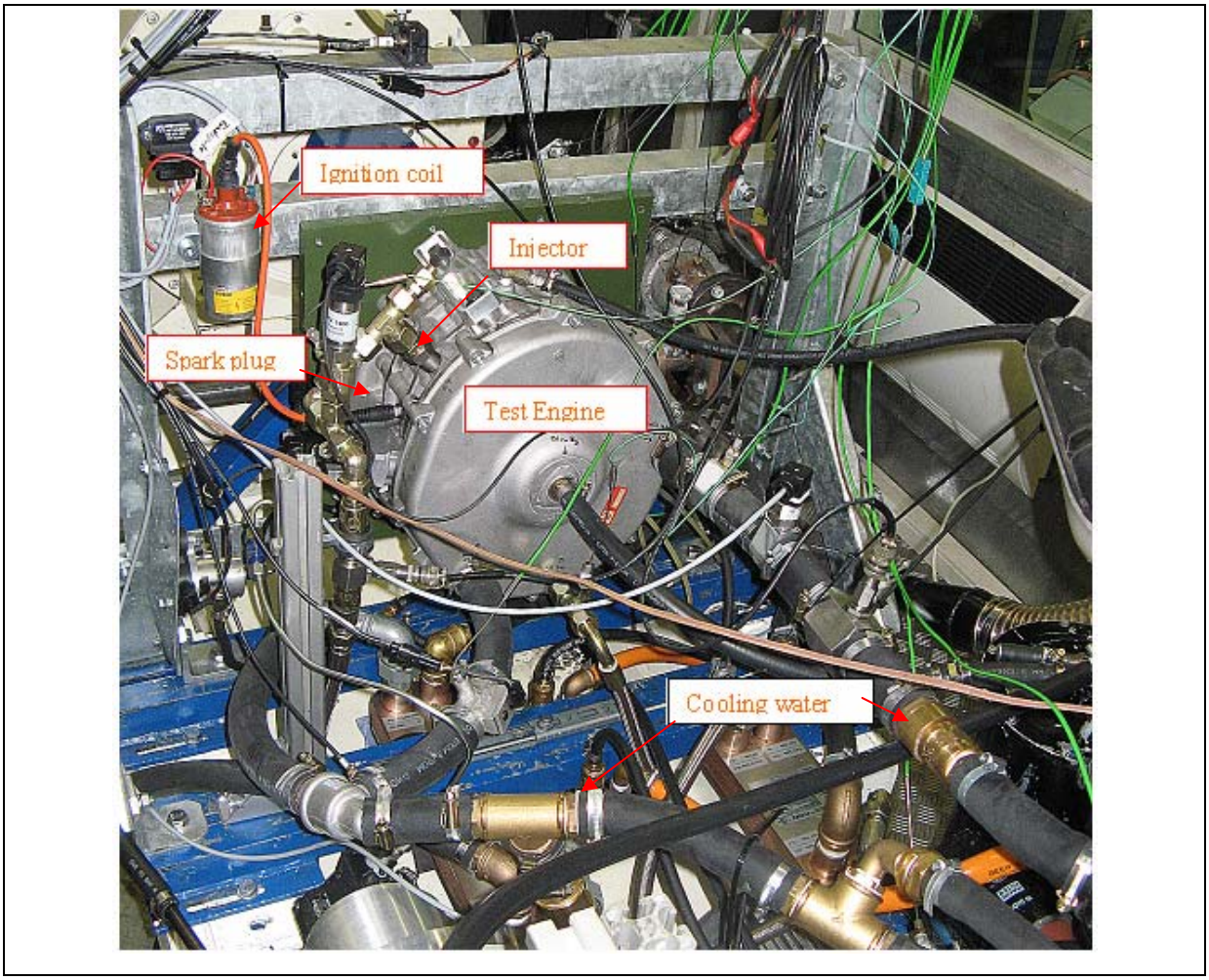

Fig.5. 4 Engine test bench, with a single rotor engine (Basic engine).

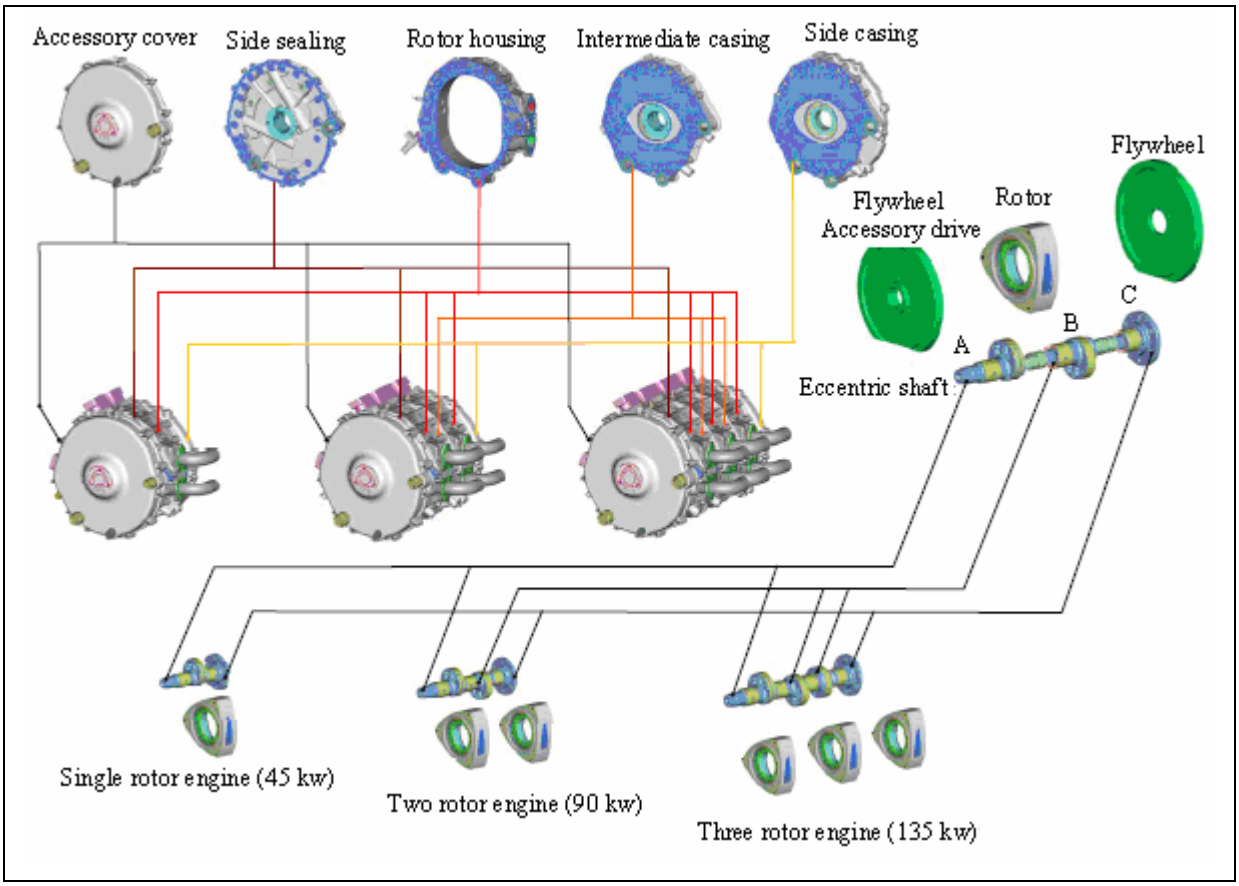

Fig.5. 5 Modular design concept

	KKM-500 1-Rotor	KKM-502 2-Rotor	KKM-503 3-Rotor	KKM-504 4-Rotor
Power, kW (PS)	45 (60)	90 (121)	135 (181)	180 (241)
Engine weight, kg	28	42	56	70
Weight to Power kg/kW(kg/PS)	0.62 (0.47)	0.47 (0.35)	0.41 (0.31)	0.39 (0.29)
Total weight, kg	45	68	92	118
Weight to Power kg/kW(kg/PS)	1.0 (0.75)	0.76 (0.56)	0.68 (0.51)	0.66 (0.51)

Table 5. 4 Engine power data

5.4.1 Engine geometrical data

The KKM-50x engine geometrical data and all engineering drawings were used to create all surfaces and volume girds. Tables [5.5], and Table [5.6], show the engine data and its timing.

Variable	Value	Description
R, [mm]	108	Generating radius
(e), [mm]	15.2	Eccentricity
(a), [mm	3	Clearance distance, amount of parallel transfer
B, [mm]	58	Housing width
Sp, [mm]	0.5	Gap, minimum clearance between rotor and housing
R/e, [-]	7.10526316	Ratio
R+a, [mm]	111	-
L1, [mm]	252.4	Long axis
L2, [mm]	191.6	Short axis
V, [cm^3]	508.483005	Engine capacity volume
Vmax/Vmin, [-]	14	Volume ratio, compression ratio

Table 5. 5 Engine geometrical data

Position	Description		Position	Description
980^o	Inlet opens		0^o	Gas change, TDC i/o
1030^o	Inlet open		270^o	BDC in
270^o	Inlet closes		540^o	TDC ignition
310^o	Inlet closed		720^o	BDC out
780^o	Outlet opens		720^o	Gas change, TDC i/o
810^o	Outlet open		30, [mm]	Spark plug after apex
50^o	Outlet closes		0, [mm]	Origin of injection spray in apex
90^o	Outlet closed		-2, [mm]	Injector behind surface

Table 5. 6 Engine timing data

5.4.2 Geometrical surface preparation

5.4.2.1 Housing

The plane and surface tool available in Fire-v7.x is a good tool to prepare all surfaces necessary from available coordinate points. Firstly, creates a single cross-sectional plane from known coordinate points (x,y). Secondly, creates the required surface by loading several planes and connecting them by B-Spline, to create a 3-D surface.

From table 5.5, the major elements of the rotary engine, the housing and the rotor, can be created. The housing inner surface has a mathematical form known as a trochoid or epitrochoid. The parametric form of the epitrochoid is given by:

$$\left.\begin{aligned} x &= e\cos 3\alpha + (R+a)\cos\alpha \\ y &= e\sin 3\alpha + (R+a)\sin\alpha \end{aligned}\right\} \qquad (5.1)$$

A simple Fortran program was written to solve these equations (from α=0 to α =360), and the points coordinates (x,y) were calculated.

Fig. 5.7 presented the half of the width of the actual housing surface (29mm), as a symmetrical boundary will be used on this model. Then, the inlet and outlet ports were connected, as it can be seen on fig.5.8.

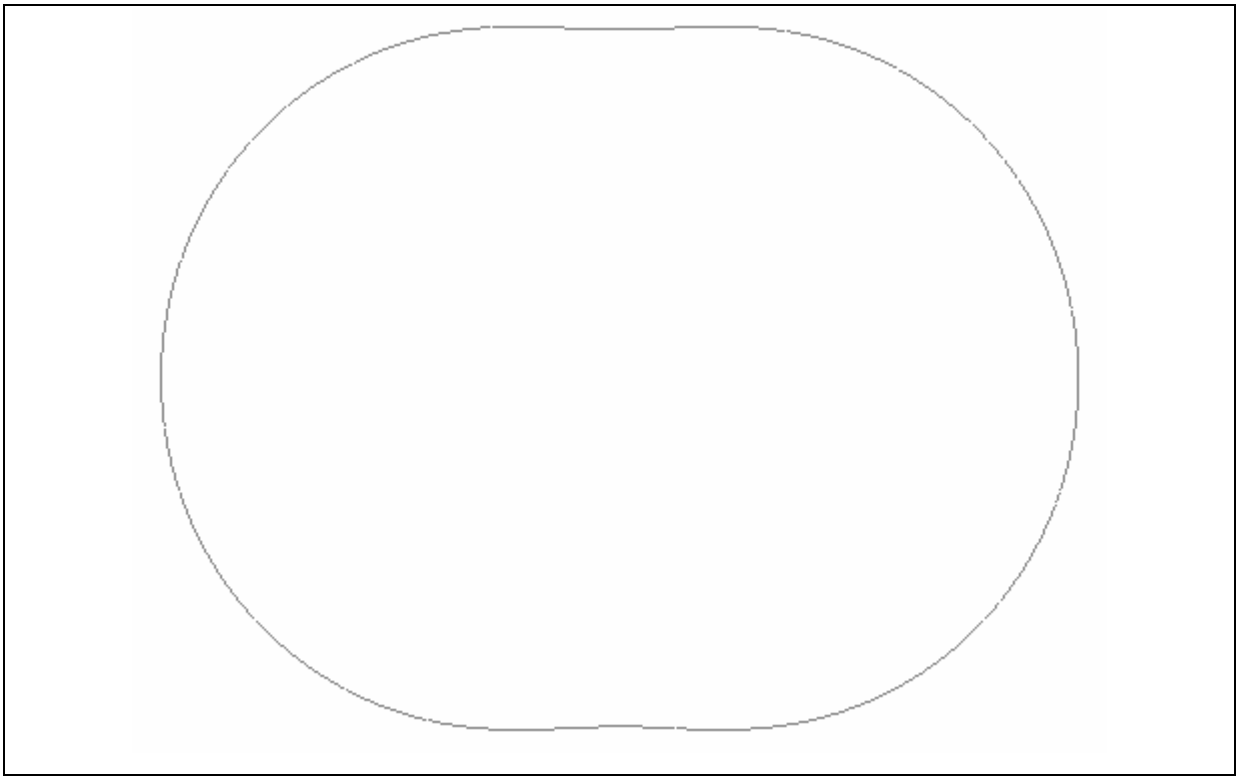

Fig.5. 6 engine trochoid

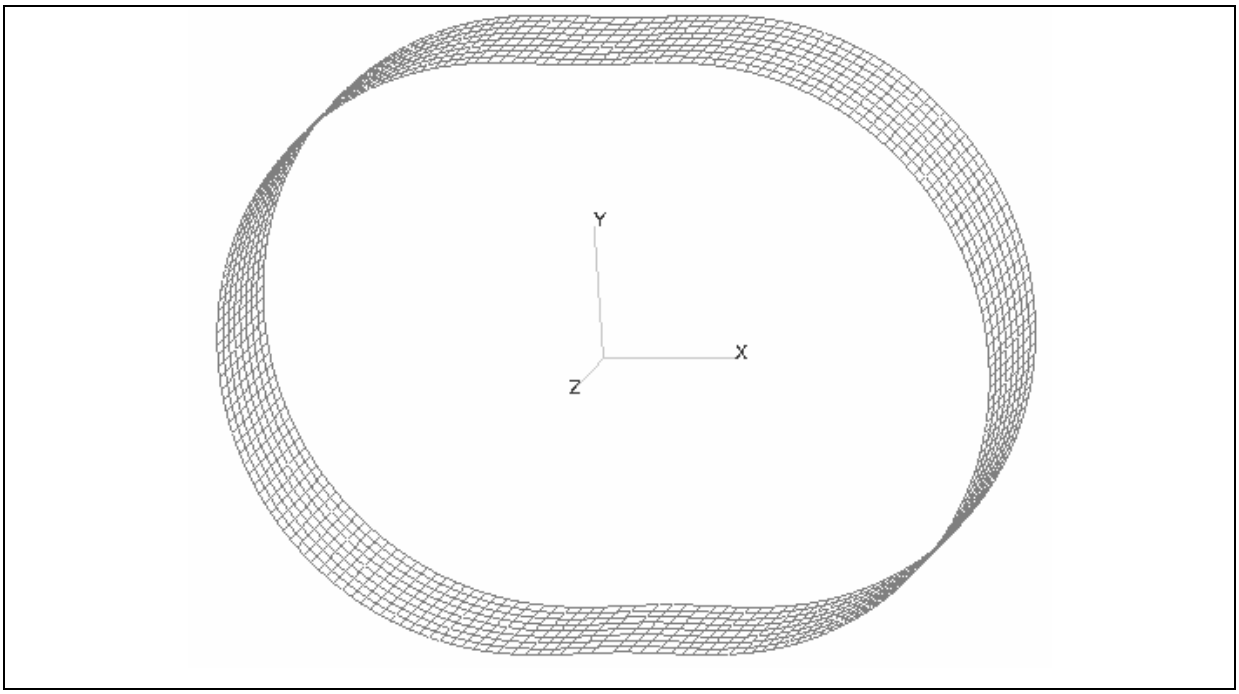

Fig.5. 7 Engine housing surface

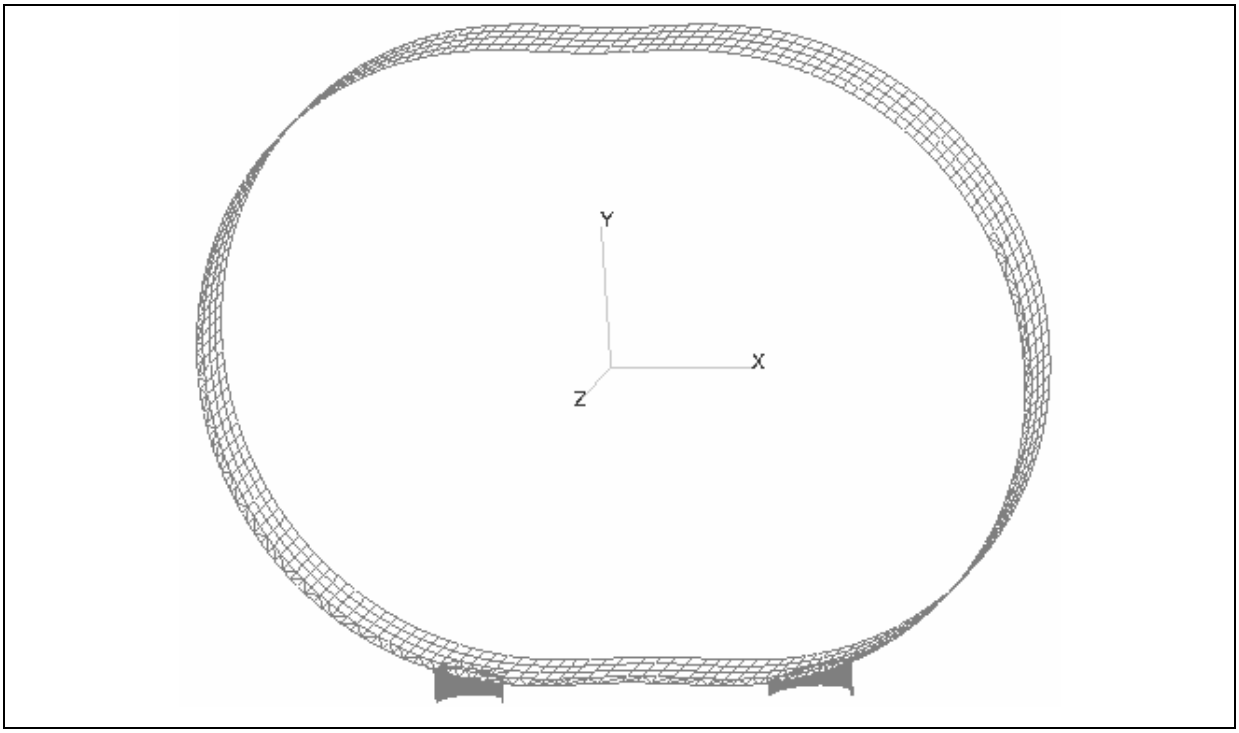

Fig.5. 8 Engine housing with inlet/outlet ports connected

5.4.2.2 Rotor

The rotor contour equation (2.2) stated in chapter 2 was solved, between π/6- π/2, to find several coordinate of points (x,y) on the first rotor face.

Only one combustion chamber will be simulated, therefore one rotor face was created as shown in fig. 5.9a. Recess geometry was recreated from the engineering drawing available, and several points were presented to create the right recess shape and size. Fig. 5.9 b shows the rotor recess connected to the rotor.

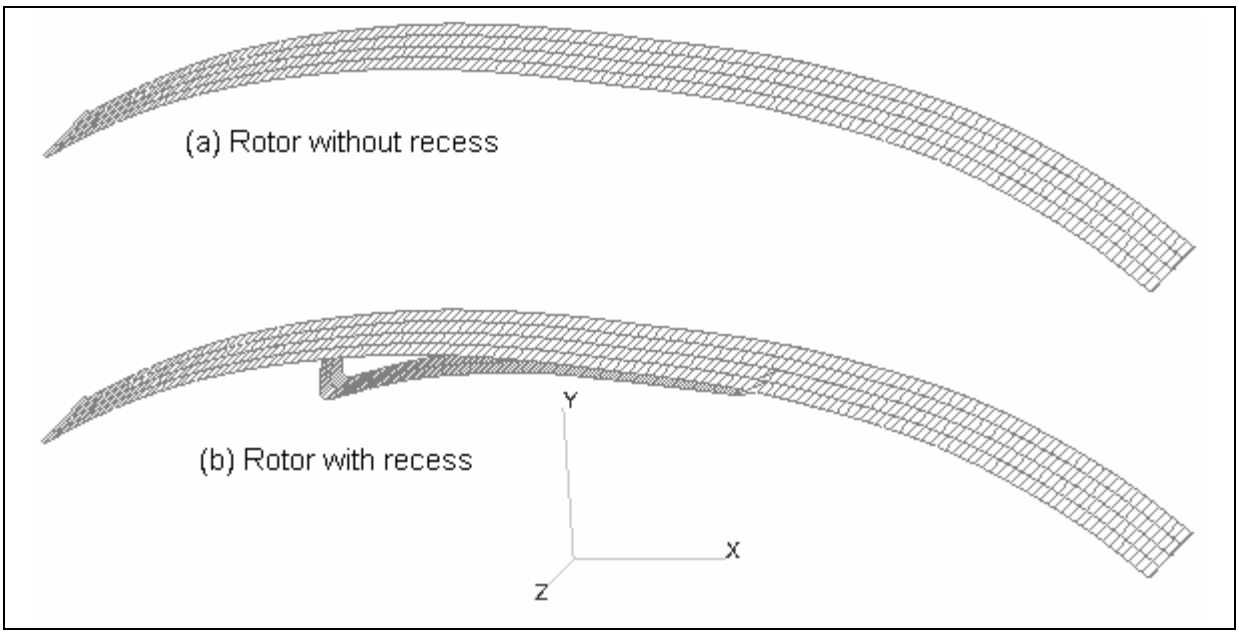

Fig.5. 9 Rotor surface and rotor recess connected.

One face rotor was connected to the engine housing (face 1 on fig. 5.10), at 50° degree of the output shaft angle, where the exhaust port just closed. The other surface positions (2,3,4…) were selected to be 18° degrees between each other (6° degrees of rotor angle), until it reaches the end of compression stroke or ignition at TDC, 540° output shaft angle (180° rotor angle). The rotation angle between each surface (6° degrees) was chosen to be small enough to produce smoother movement on the housing surface.

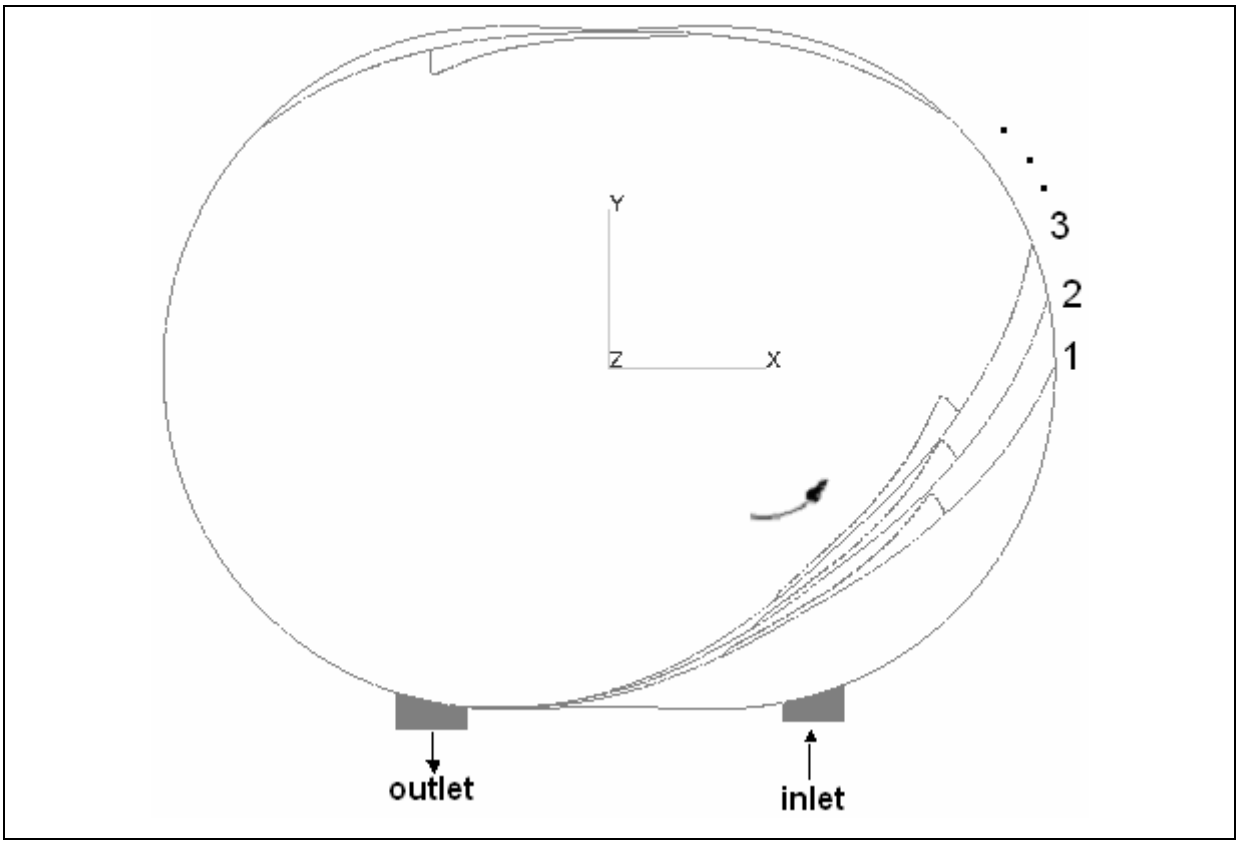

Fig.5. 10 Rotor surface connected to the housing.

The rotor contact points (0,1,2 on fig. 5.11), where the rotor and housing are in contact at the apex seals, can be calculated as follows:

$$\left.\begin{aligned} x &= e\cos 3\alpha + R\cos(\alpha + 2n\pi/3) \\ y &= e\sin 3\alpha + R\sin(\alpha + 2n\pi/3) \end{aligned}\right\} \qquad (5.3)$$

Where, n=0,1, or 2, the three values identifying the positions of the three rotor tips, each separated by 120°.

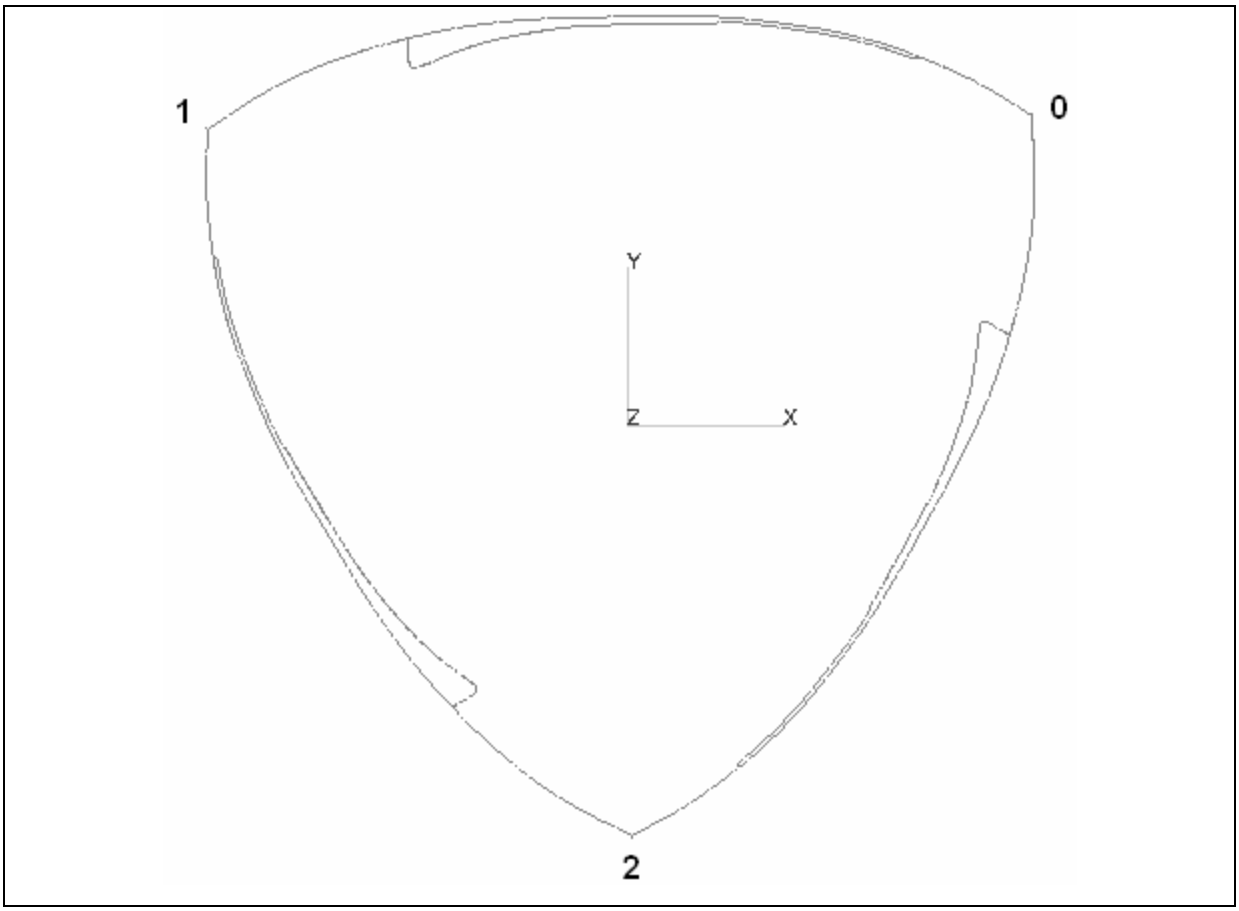

Fig.5. 11 The rotor three contact points

5.4.3 Volume grid preparation

As all surfaces prepared, a Hexahedron volume grid (Mesh) filled the space between the housing and the rotor, and the rotor recess. This volume grid presents the working fluid of one of the three rotor faces. Fig. 5.12, A, B and C, show the volume grid at 90°, 310° and 540°, (on the output shaft), correspond to the positions where the exhaust port just closed, the inlet port closed and the end of compression stroke at TDC respectively.

All volume grids then saved in one file after rearrange volume grid option applied to allow smooth interpolation ramping between data sets of start and end volume grids (.GEO data sets) over number of time steps.

Rezone volume grids were also used whenever the volume grids tend to be distorted.

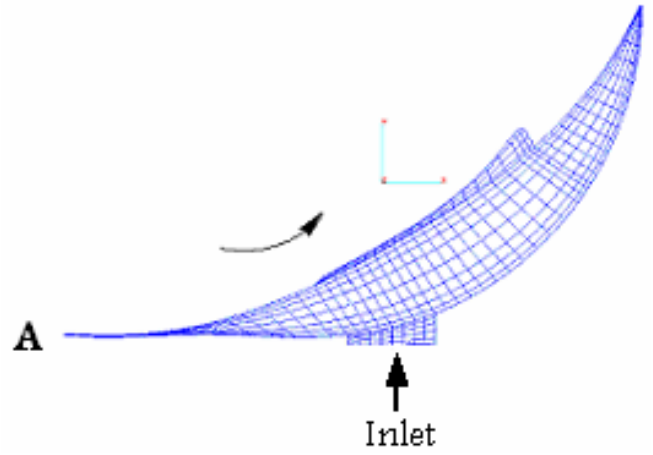

A, Start point at 90° output shaft position

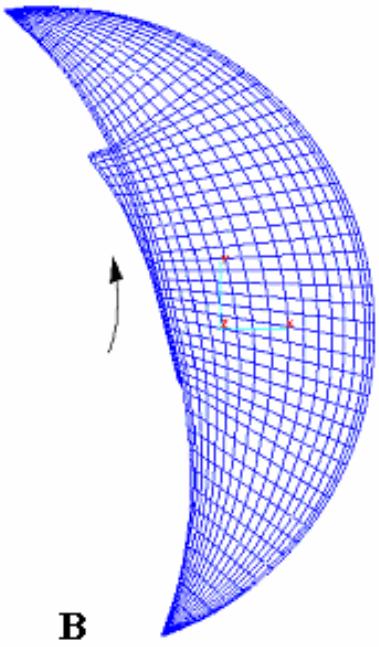

B, Mid point at 310° output shaft position

C, End point at 540° output shaft position.

Fig.5. 12 Volume grid at different angle positions

5.4.4 Simulating differences of various fuel systems

For a Simulation with different fuel systems the calculation grid and the rotation model would be the same. The main changes are in modeling the gas injector system and the liquid fuel spray file. Gas simulation in Fire has some differences when compared to liquid fuel simulation.

In liquid injection systems with a spray file nozzle size, nozzle position and spray angles can be change and also ignition parameters could be adjust. In the Hydrogen simulation the injector is prepared on the model, and only the injector holes a simulated on the model.

5.5 Effects of different variables on flow fields

The effect of the different variables such as rotor recess shape and inlet surface area on the flow fields were investigated and the results were presented and compared to the visualization results found in literature (Reference [37]) for the purpose of model validation. Also, simple fixed models were prepared and tested for validation purposes.

5.5.1 Effect of the rotor recess shape

5.5.1.1 Rotor geometry

For the purpose of comparison and engine performance improvement, five rotors geometries with different recess shapes were prepared. CFD models of the five rotor recess shapes were prepared analyzed and compared. The effect of recess shape on fluid flow fields and flow velocities were studied and compared in this chapter using CFD tools.

The five rotor recess shapes can be seen on Fig. 5.13, A, B, C, D and E.

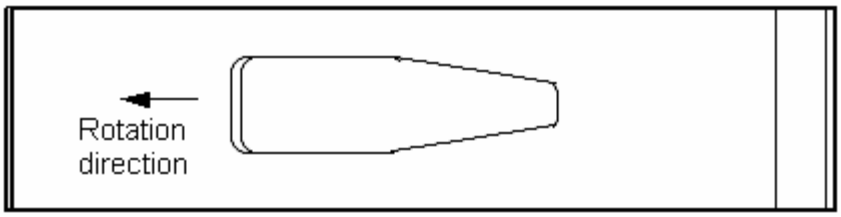

A Top view
Rotor no.1

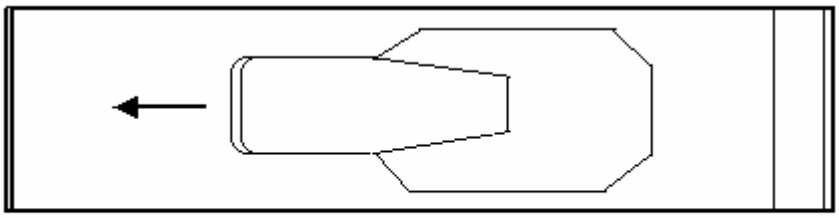

B Top view
Rotor no. 2

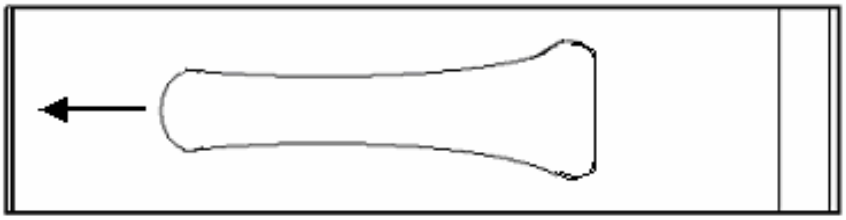

C Top view
Rotor no. 3

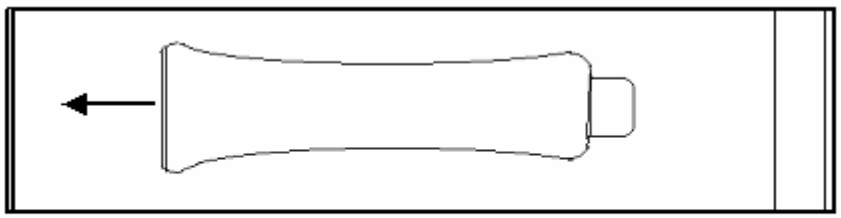

D Top view
Rotor no. 4

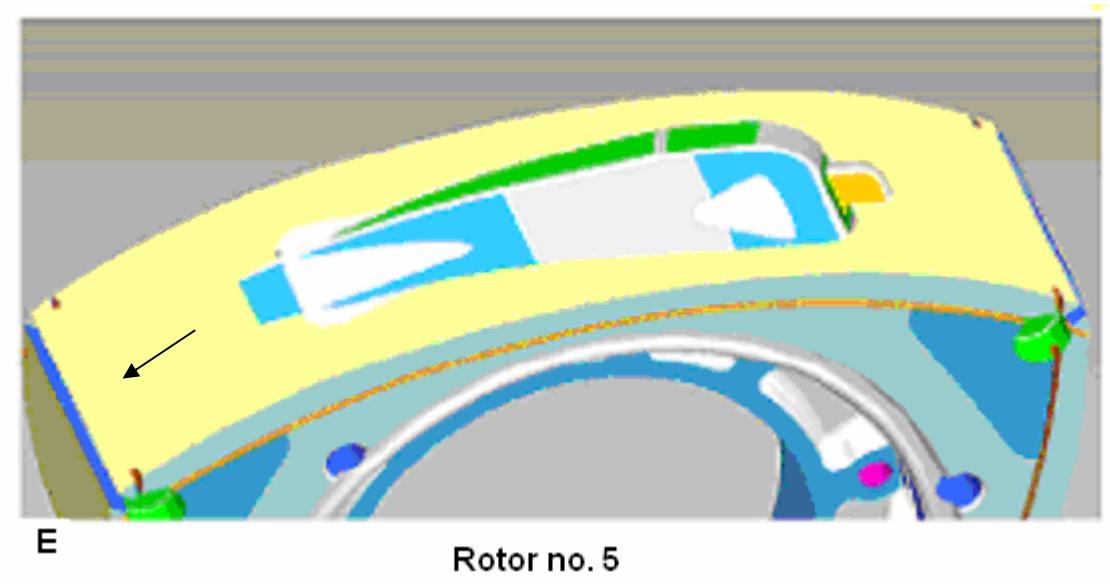

Fig.5. 13 Rotor different geometrical recess shapes

In addition to these five rotor recess shapes, another model for the KKM 407 prototype engine already available on market and running on diesel and kerosene for light aircraft application was compared to this engine. The base engine has 37 KW (50 PS) at 5700 rpm, and has 34 kg with its complete installation.

The main engine information as follows:

R=86.5 mm, generating radius.

a=3 mm, clearance distance, amount of parallel transfer.

e=13.5 mm, distance of eccentricity.

b=65 mm, rotor, housing width.

sp=0.5 mm, minimum clearance between rotor and housing.

The engine has a different peripheral inlet port shape. It has a rectangular inlet port with a surface area of 8.5 cm^2, (17mm x 50mm).

The rotor surface shape is presented on Fig. 5.14.

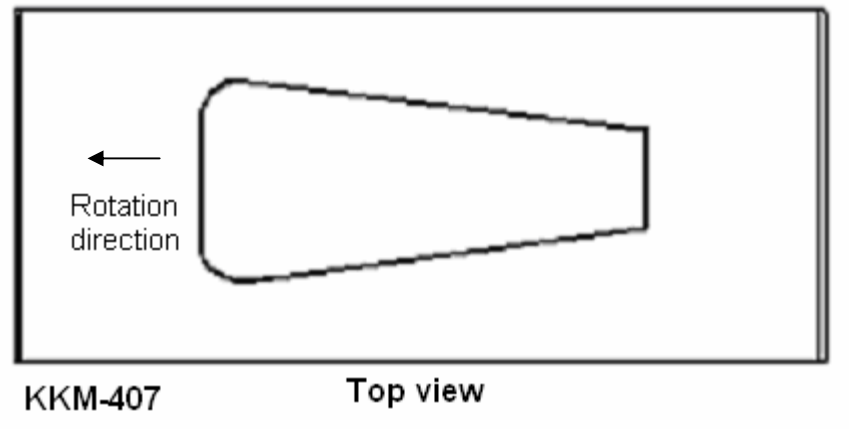

Fig.5. 14 KKM 407 Rotor recess shape

5.5.1.2 Volume grid (Mesh) preparation

All the surfaces were prepared using the AVL-FIRE surface tool, and the Hexahedral volume grid topology for mesh generation was used. The volume grid (mesh) example of all surfaces is presented in Fig. 5.15, at position where the inlet port is just closed. The numbers 1,2,3, 4 and 5, denote to the rotor numbers, presented in Fig.5.13, A, B, C, D and E, respectively, in addition to the KKM-407 rotor.

The number of cells of all meshes is not constant because of the different volume grid size at different positions. The number of cells ranges from, 5941 to 35846 cells.

5.5.1.3 Boundary condition

Three boundary conditions are necessary to be set:

1- Fixed wall, all fixed walls temperature was set at 300 k for comparison.
2- Symmetrical boundary at the symmetrical surface.
3- Inlet boundary was set as inlet total pressure at 10^5 pa.

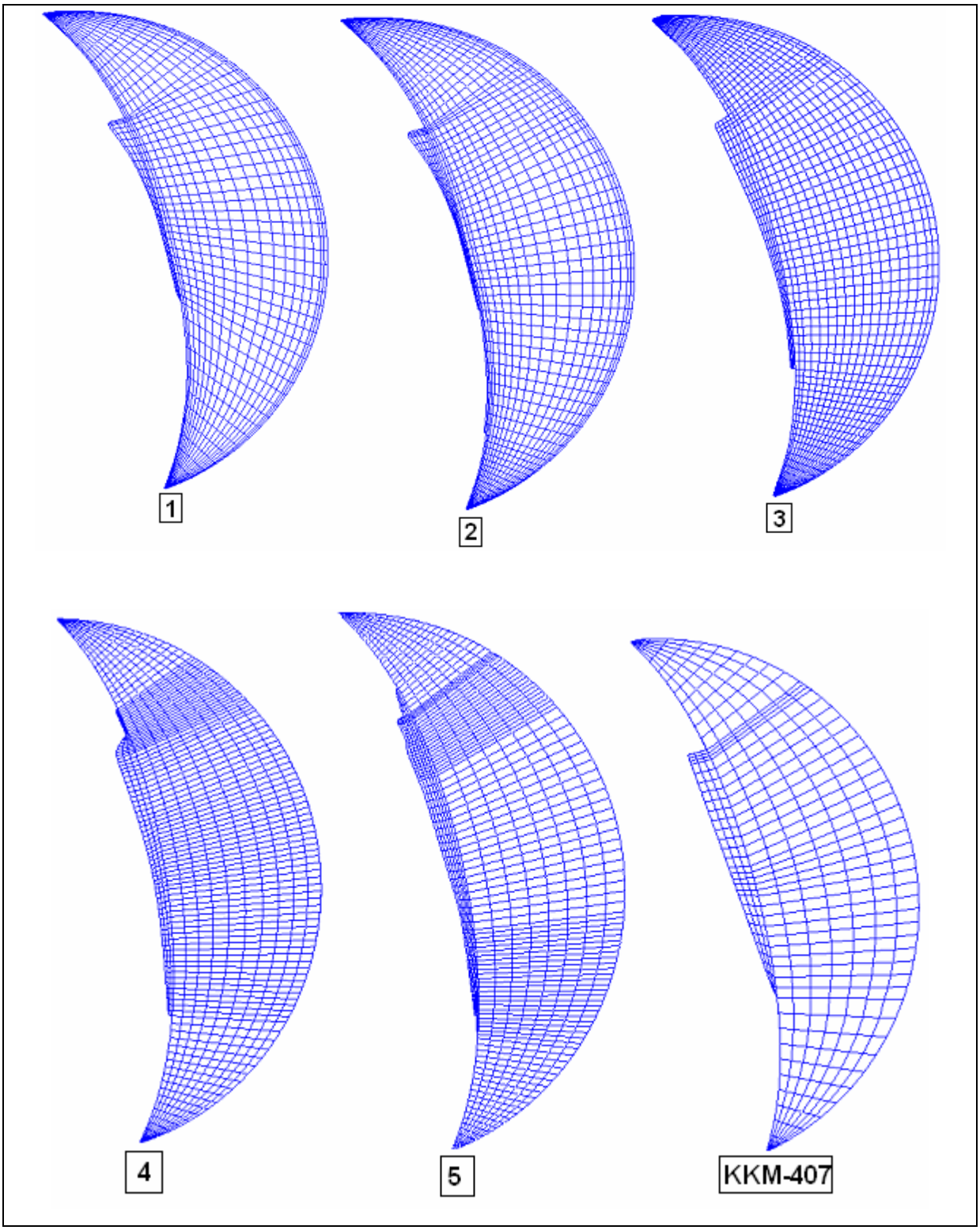

Fig.5. 15 Volume grid (mesh) at the inlet port is just closed.

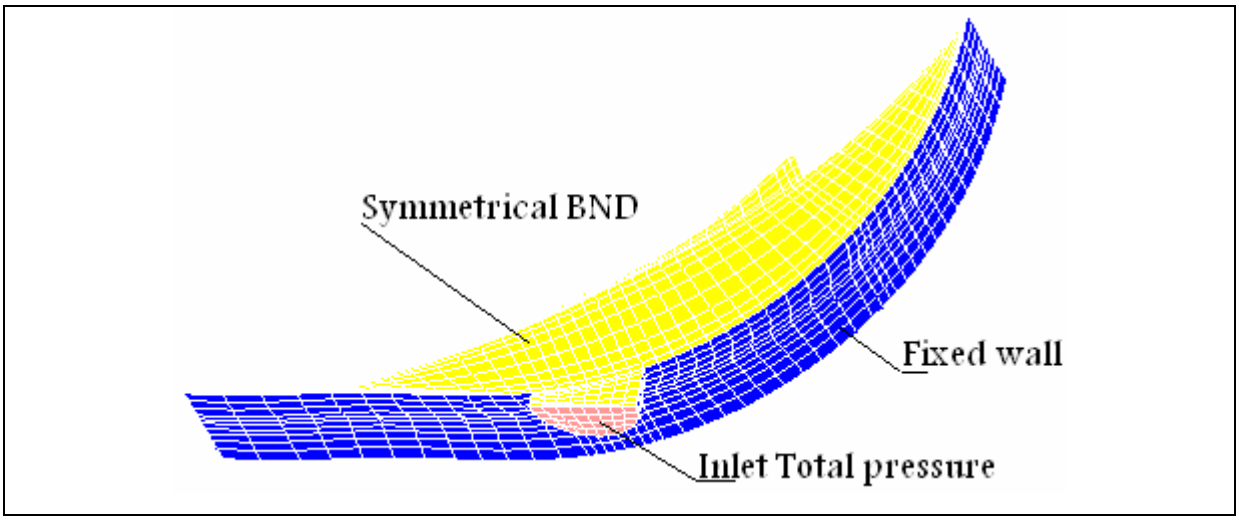

Fig.5. 16 Boundary condition

5.5.1.4 Initial condition

The total running time is dependent on the engine speed and the total movement of the rotor. In this model the rotor moves just after the exhaust port closes (90°) to the end of compression cycle (540°). In other words, the total movement is 450°.

Table 5.7 shows the initial condition set up.

Species	Air
Pressure, Pa	1e+05
Temperature, k	293
Density, kg/m^3	1.189
TKE, m^2/s^2	2
Length Scale, m	0.0012
(x, y, z), Velocity, m/s	(-10, 10, 0)
Turbulence Model	K-ε
Convergence criterion	2e-05

Table 5. 7 fluid initial conditions

5.5.2 Effect of inlet port surface area

As the KKM-407 has a different inlet port shape and size, (rectangular 17x50 mm, 8.5 cm^2 surface area), which develops much lower flow velocity during inlet and at the end of compression, which is (about 1/3 flow velocity) of the KKM-500 engine fitted with cylindrical 25 mm inlet port diameter and rotor number one. A new model with an inlet rectangular port of (17x44 mm) was built and its effect on the flow field and flow velocity was tested. The surface area of the new inlet port is 7.48 cm^2, which is higher than the cylindrical one, 4.9 cm^2, to reduce the inlet velocity at the inlet port.

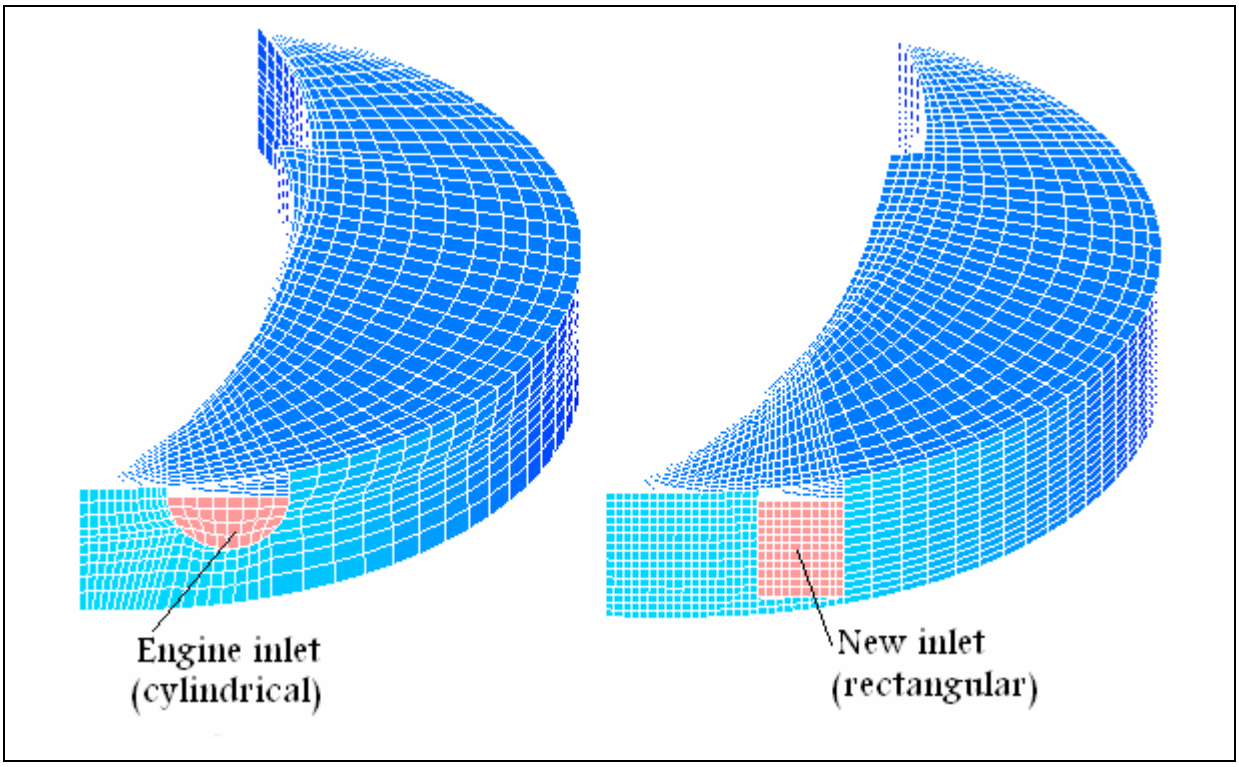

Fig.5. 17 Rectangular and cylindrical inlet ports

5.6 Results

The results will be divided here in three parts. The first part shows the flow velocity vector and turbulence kinetic energy, the second and third parts show the pressure and temperature changes, respectively.

5.6.1 Flow velocity analysis

After all models were prepared in pre-processor of Fire program, the analysis consists of preparing the time management files and running the analysis program was performed.

The post-processing focuses in this section on display of the velocity vector, this makes sure that the flow field is realistic, and reveals the regions of high flow velocity and its direction.

All the models prepared and run under the same boundary and initial conditions for the reason of comparison.

The dimensionless rotation number R_0 was calculated and found to be 1065.2 and 935.5 for KKM-407 and KKM-500 respectively.

The rotation number R_0 is calculated as follows:

$$R_0 = \frac{\omega l}{\bar{u}} = \frac{2\pi n l}{\bar{u}}$$

$$\bar{u} = \frac{\dot{V}}{A}$$

ω is the angular velocity, n is the engine speed (in rpm), $\bar{u}$ is the calculated mean inlet flow velocity, $\dot{V}$ and A is the volume flow rate and inlet area respectively. The length scale l is the minimum distance from trochoid to the shaftcenter and calculated as:

$$l = R + a - e$$

Where, R is the generating radius, a is the clearance distance and e is the eccentricity.

Reynolds number is calculated as:

$$\mathrm{Re} = \frac{\bar{u} l}{v}$$

Table 5.9 shows the resulting rotation number R_0, Reynolds number Re and engine speed for KKM-407 and KKM-500.

Also, the flow velocity is expressed in terms of dimensionless flow velocity number (R_f.)

The flow velocity number, $R_f = \dfrac{Actual\ flow\ velocity\ (v_{act})}{\max imum\ flow\ velocity\ (v_{\max})}$

Or:

$$R_f = \frac{V_{act}}{V_{\max}} \quad \text{[Dimensionless]}$$

The maximum flow velocity was 250m/s ($R_f = 1$) as it is the maximum velocity recorded for these models.

The results example heir is presented in three rotor positions for all models to make the comparison much easier.

Engine	KKM-407				KKM-500			
Reynolds No.Re [-]	5615.3	3743.1	74870.2	112305	8060.0	53733.6	107467	161200.8
Velocity No. R_0 [-]	1065.2	1065.2	1065.2	1065.2	935.5	935.5	935.5	935.5
Engine speed [rpm]	300	2000	4000	6000	300	2000	4000	6000

Table 5. 8 Reynolds No., velocity No. and engine speed result comparison

5.6.1.1 Engine speed (2000 rpm), $Re = 53733.6$, $R_0 = 935.5$

Fig. 5.18 shows the velocity vector during the inlet cycle. On this figure it can be seen clearly two regions the first one (region 1) behind the inlet port. At this region, a part of the inlet flow makes an anti-clockwise circulation between the rotor surface and the engine housing. This circulation starts at the early stages of the inlet flow and shrinks as the rotor tip become closer to the inlet port. The second region, (region 2) is the leading flow part in direction of rotation. At this region, a clockwise circulation can be seen at the rotor recess end, which directs the flow to circulate backward or clockwise circulation. These regions can be seen more clearly on the enlarged plane on fig.5.19. This circulation effect has seen on all rotor geometrical surface models.

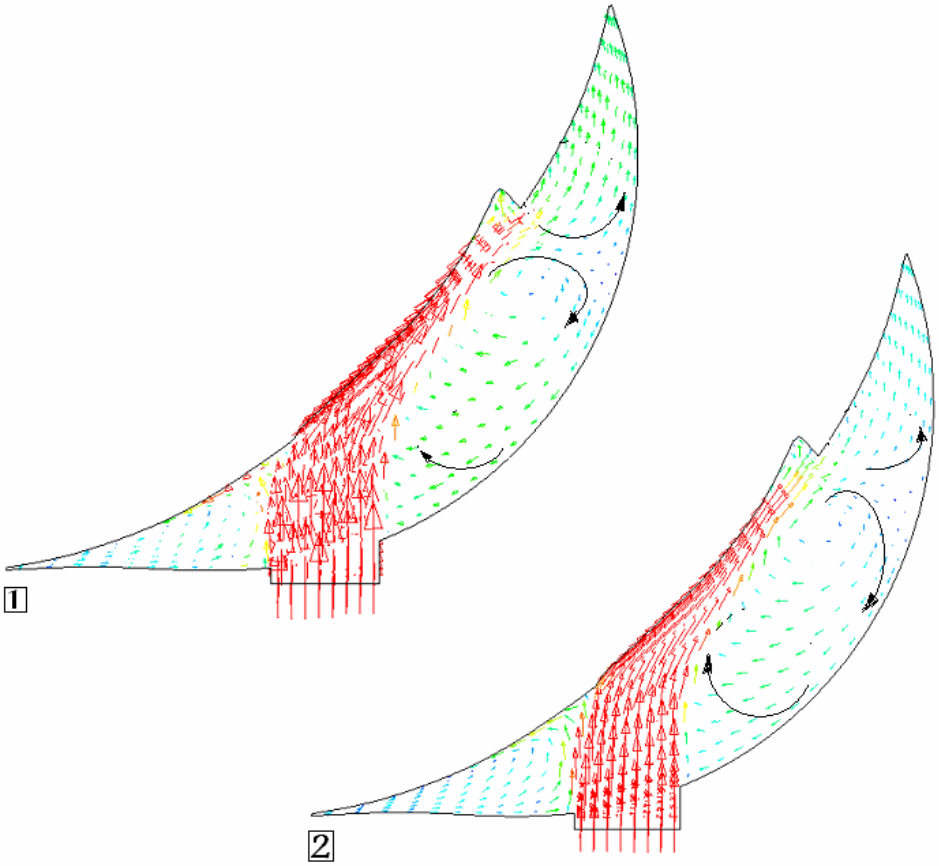

(1,2,3… refers to rotor Number)

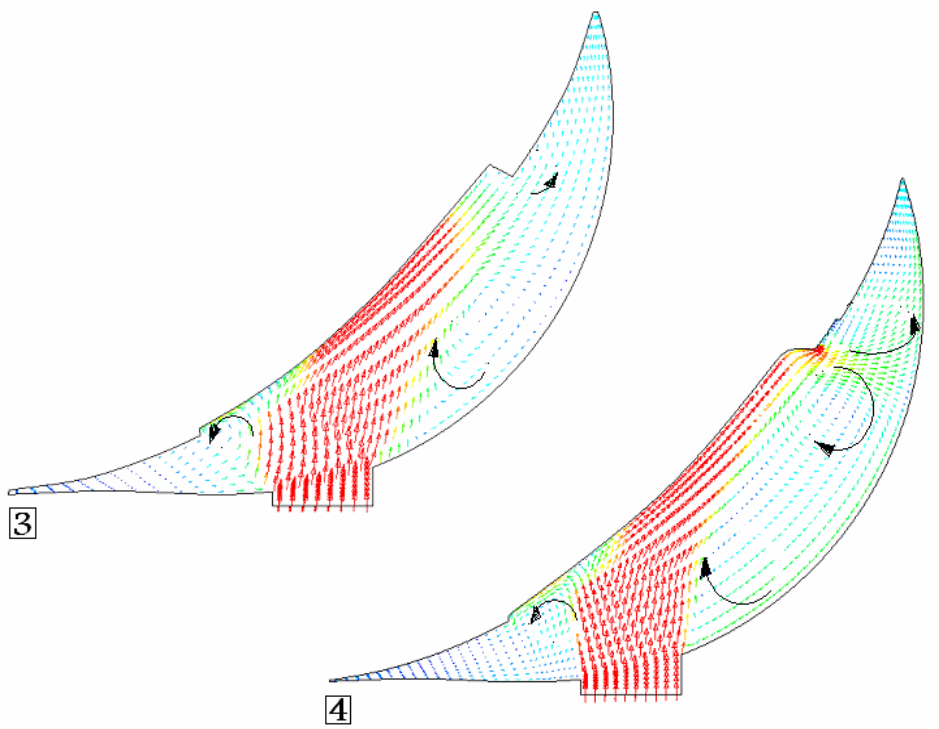

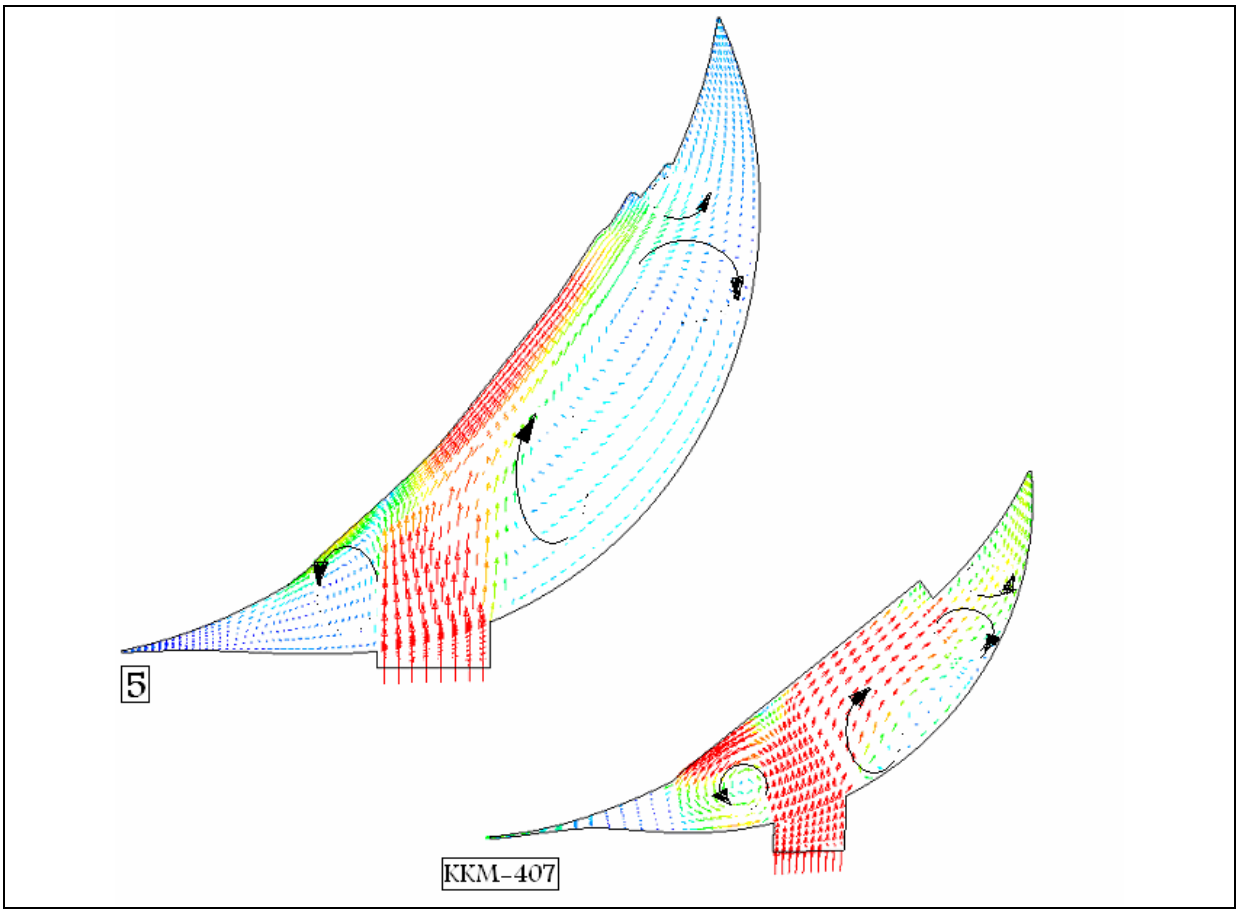

Fig.5. 18 Velocity vector during inlet cycle (2000 rpm), Re = 53733.6, R_0 = 935.5

Soon after inlet cycle starts another flow circulation has seen to be developed across the flow space when several cross-sectional plans were presented on fig.5.20. The circulation flow starts near the inlet port, rotates anti-clockwise on this figure, upwards near the fixed sidewall and rotates to the center of flow.

The rotor shape seems to has no effect on the cross circulation as it can be seen on all surface shape models of KKM-500 engine, and have similar intensity at the same engine speed. The cross circulation intensity of the KKM-407 engine model is much less than that of the KKM-500 engine models, at the same engine speed. This is clearly because of the inlet velocity at the inlet port and also port shape is different. The inlet port of the KKM-407 engine is rectangular and has a bigger surface area, which reduces the inlet velocity at the inlet port.

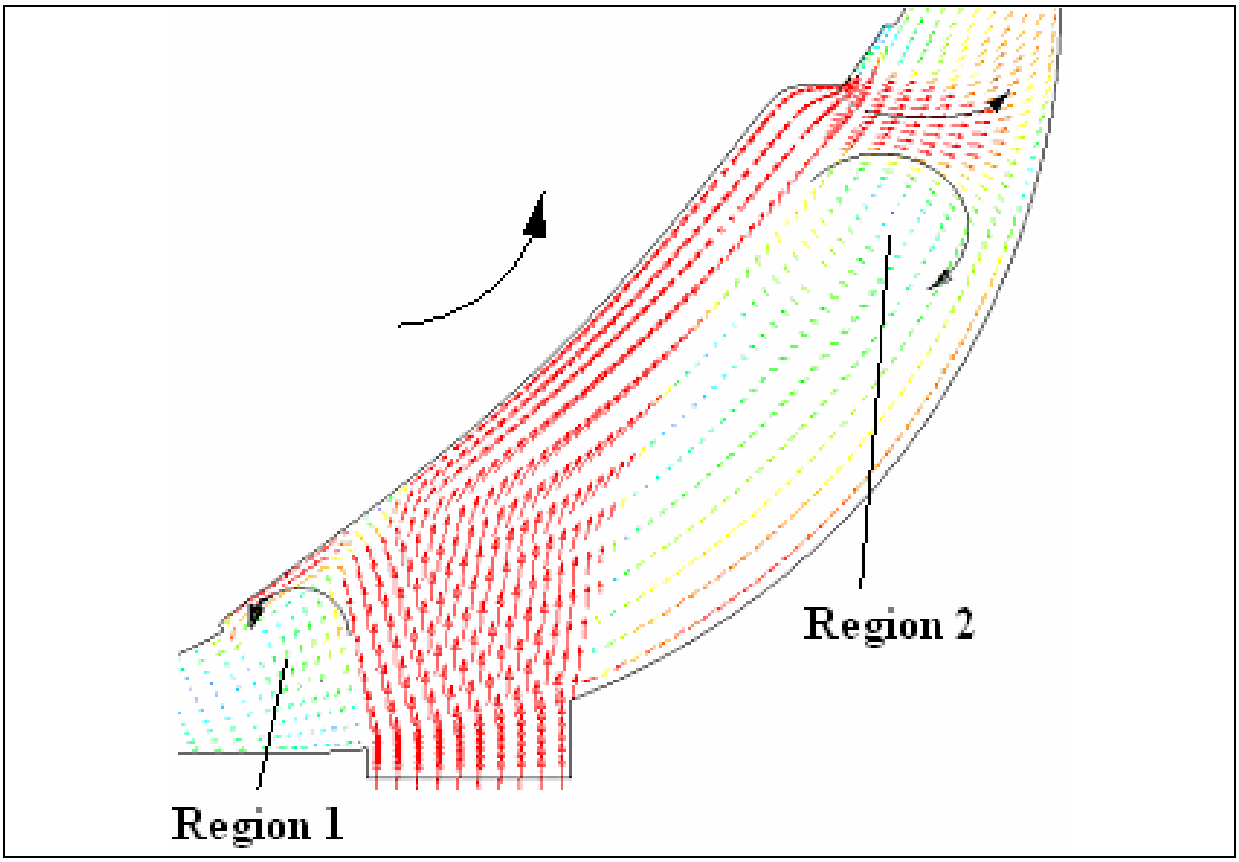

Fig.5. 19 Flow regions

The inlet velocity at the circular inlet port of the KKM-500 engine is up to maximum of (R_f=0.26) at engine speed (2000 rpm), Re = 53733.6, R_0 = 935.5, and for the rectangular inlet port of the KKM-407 engine is maximum of (R_f=0.12). Fig. 5.21 shows a comparison between both engines.

Fig.5.22 shows the flow velocity vector after the rotor tip passed the inlet port, which means that the inlet port is closed and the compression cycle is started.

On this figure it is not so clear how the fluid flow is behaves. All what can be seen on this plan cut, is that the flow vectors are pointed to the rotor surface, which means that there is flow comes from the housing surface and moves to the rotor surface.

Near the rotor surface, the flow is still moves directly in the same engine rotation direction, taking the flow coming from the housing with it.

This flow behavior become very clear when has looking to Fig.5.23, where the flow coming from the housing to the rotor surface is a part of the flow circulation through the flow field.

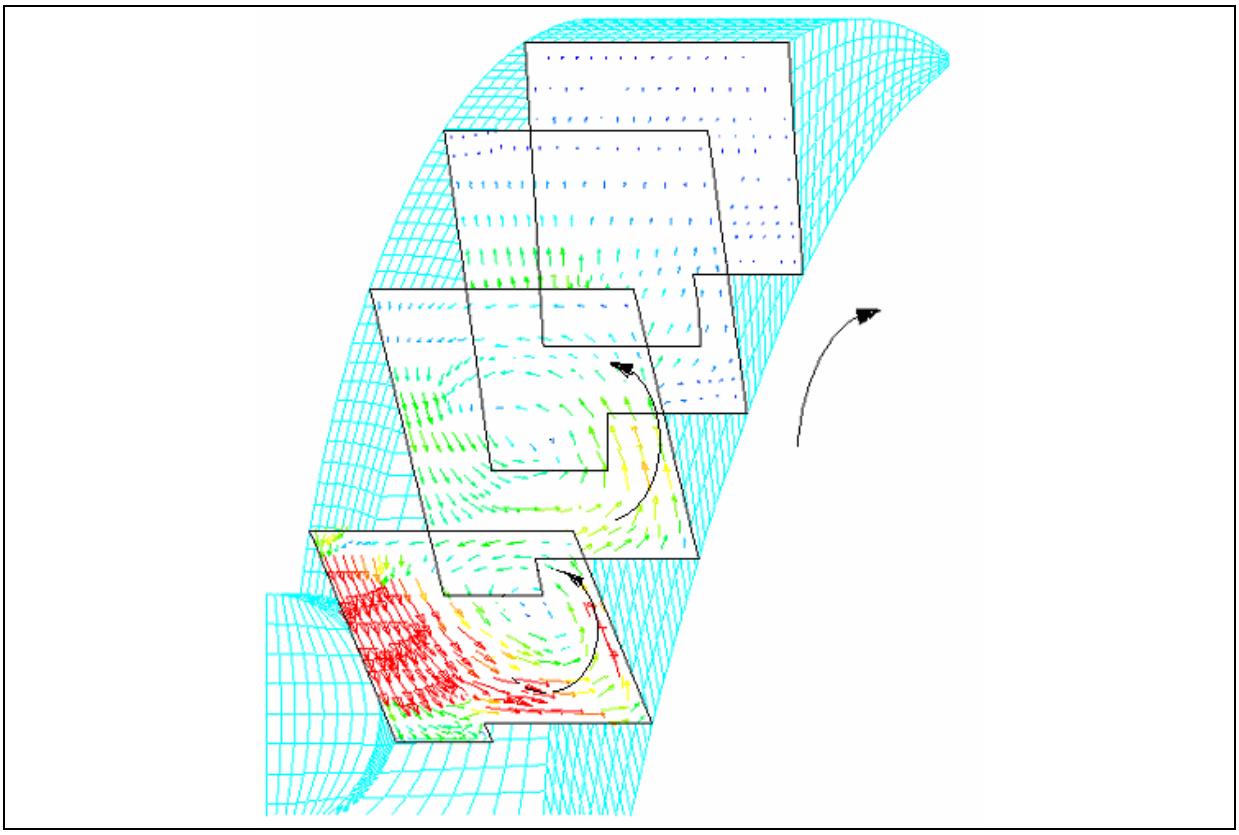

Fig.5. 20 Cross-sectional cut planes

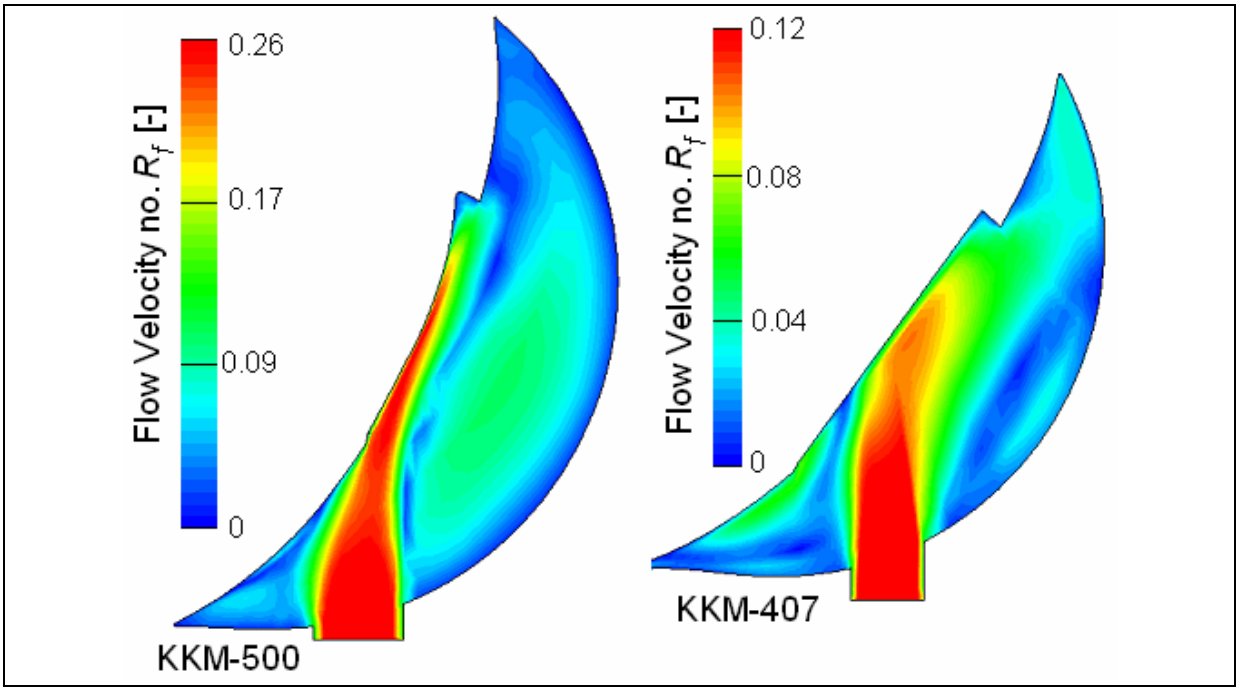

Fig.5. 21 Inlet flow velocity during inlet port open (2000 rpm), Re = 53733.6, R_0 = 935.5

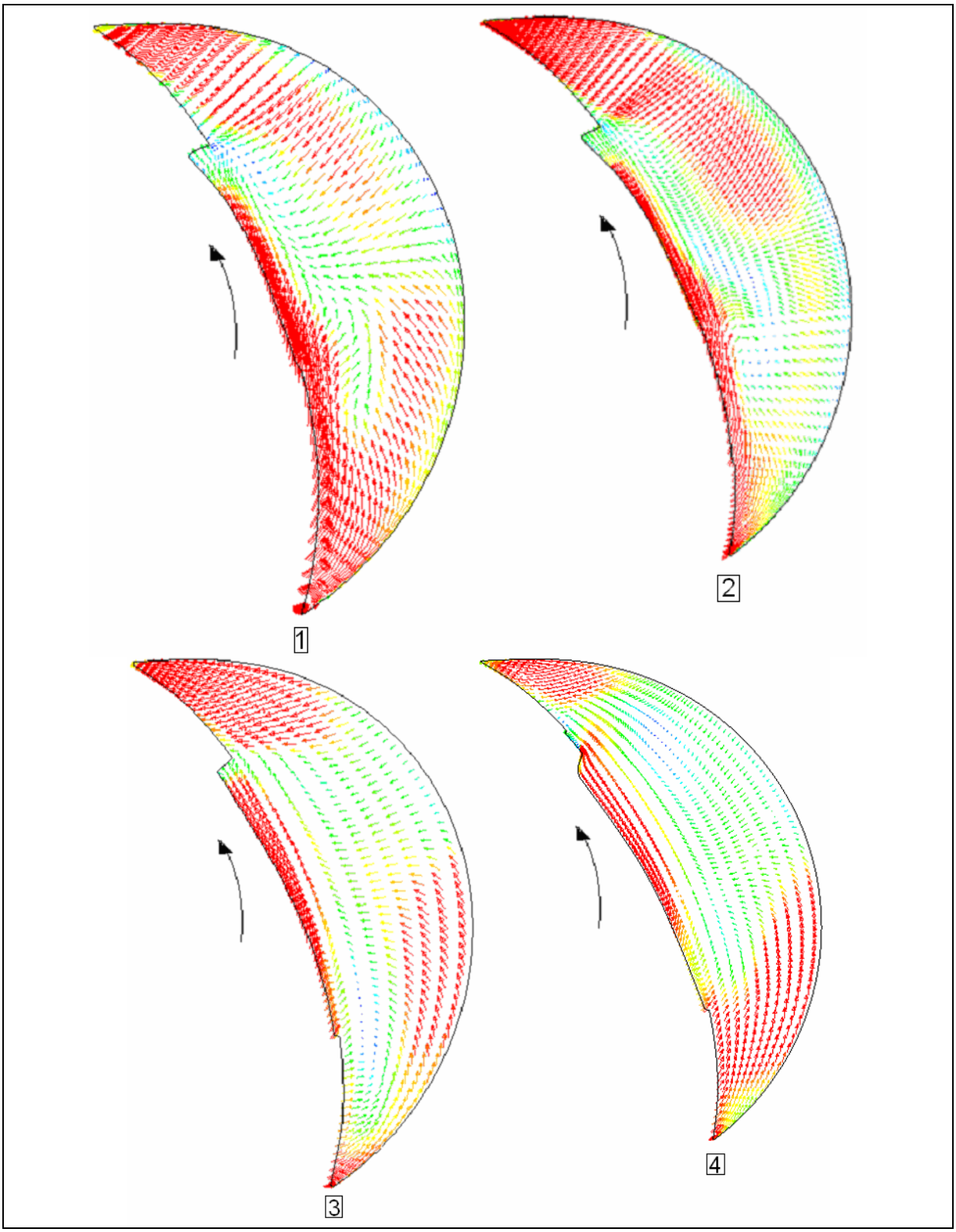
1
2
3
4

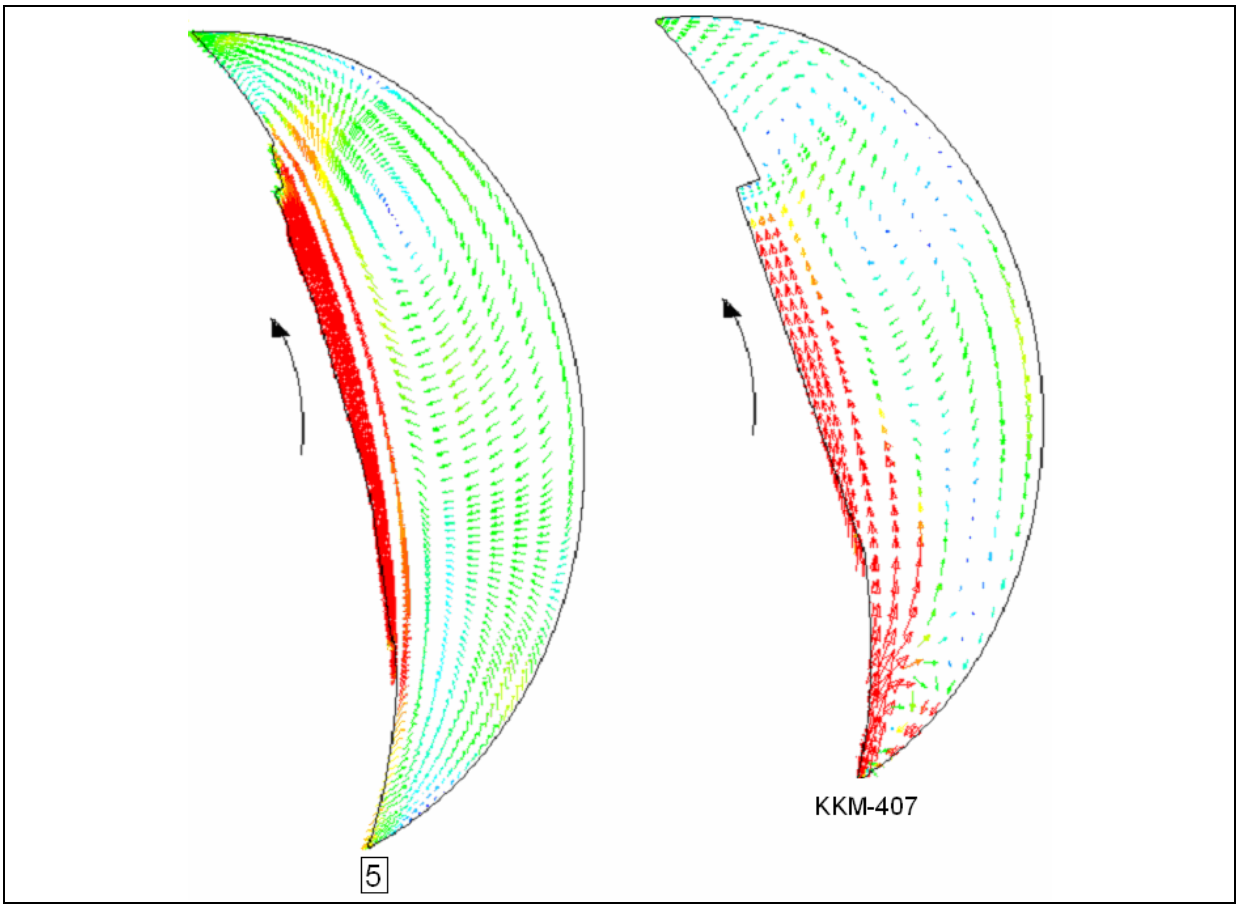

Fig.5. 22 Comparison of flow velocity vector at [310°], after inlet port closed

The cross flow circulation (can be called as swirl) growth starts at early stages of inlet cycle through the whole flow domain as the distance between the rotor and engine housing becomes bigger and bigger. This swirl flow continued during the compression cycle until the distance between the rotor and the engine housing become very small, before the engine TDC, and then the flow will take the same engine rotation direction.

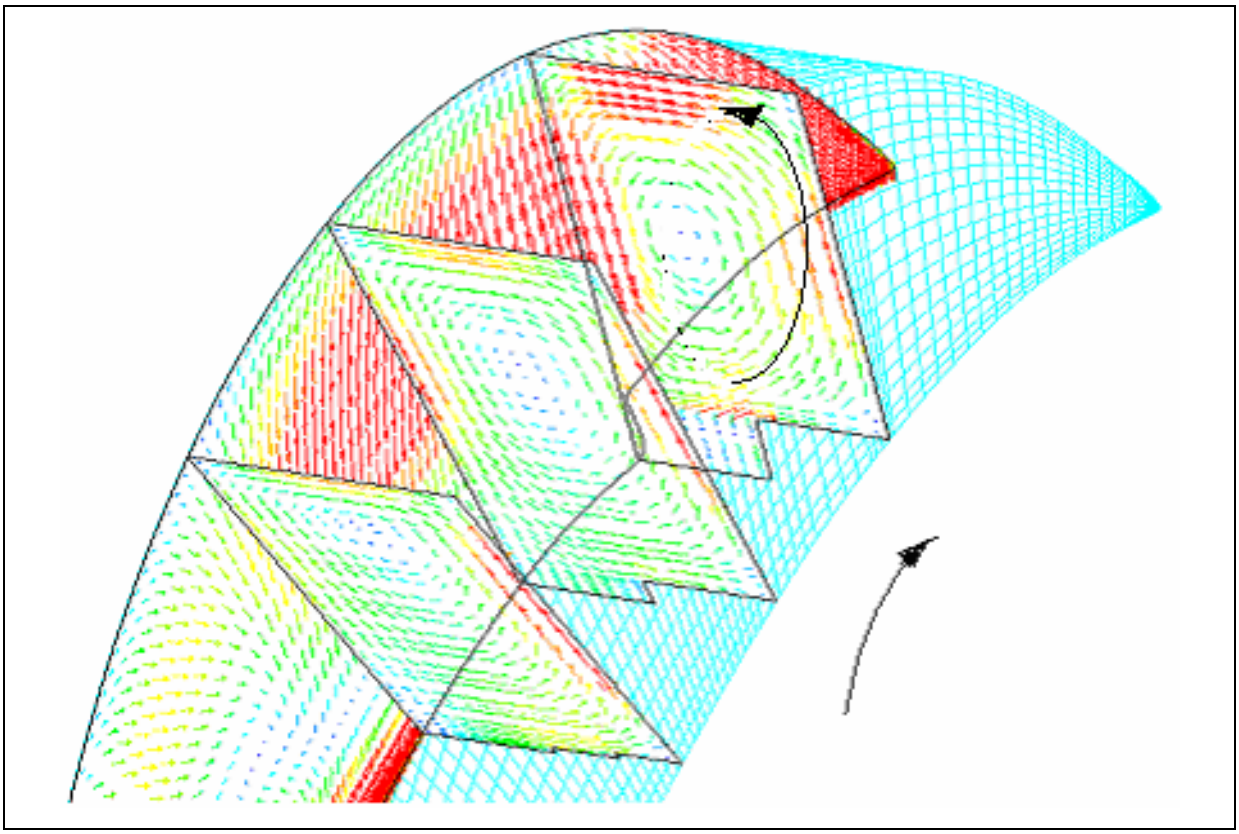

Fig.5. 23 Flow velocity vector during compression cycle

During compression phase the KKM-407 model with its rectangular inlet port has no such cross swirl can be clearly seen. It develops a bigger clockwise vortex along the flow stream, with its center near to the recess end on the rotor, as it can be seen on Fig.5.24.

At the end of compression phase (TDC), it can be clearly seen on fig.5.25, that all models have similar flow in the direction of engine rotation.

The maximum velocity during the inlet phase is at the inlet port and reaches 65m/s for the KKM-500 engine model with its inlet port of 25mm diameter, and 30m/s for the KKM-407 engine model with its rectangular (17mmx50mm) inlet port.

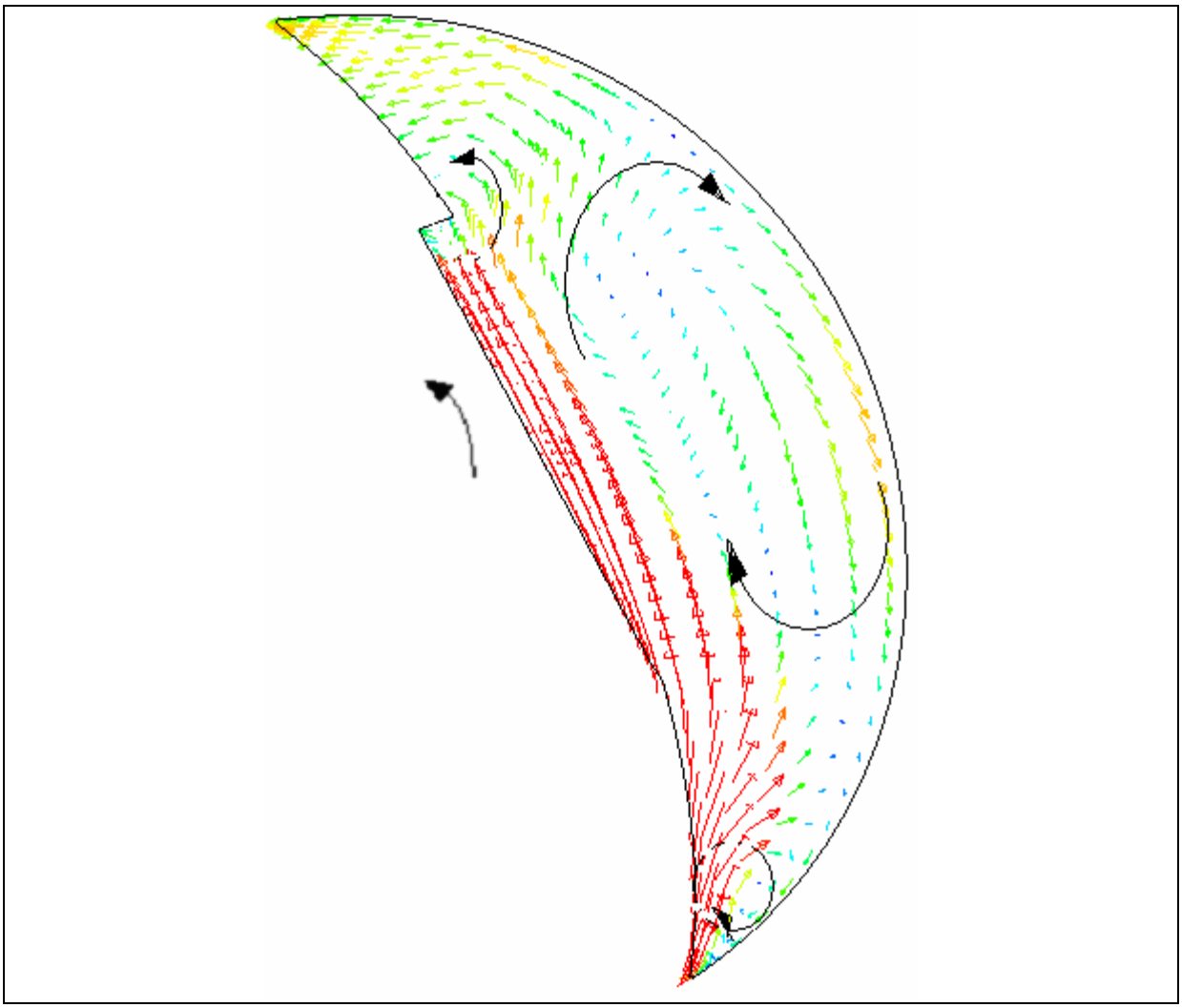

Fig.5. 24 KKM-407 Model during compression

During the compression phase the fluid flow velocity is relatively low (in average of 5 to 10m/s) through the whole domain, as only the rotor movement drives it and there is no inlet flow accelerated the flow velocity.

When the rotor becomes closer to the end of compression phase, the rotor divides the flow domain into two chambers. The leading chamber zone is at the leading part of the rotor (the chamber after the housing tip, short axis) and tailing chamber zone at the tailing part of the rotor (before housing short axis). The tailing chamber has a relatively higher pressure and hence the flow velocity between these two chambers becomes high depending on the rotor recess depth and engine speed.

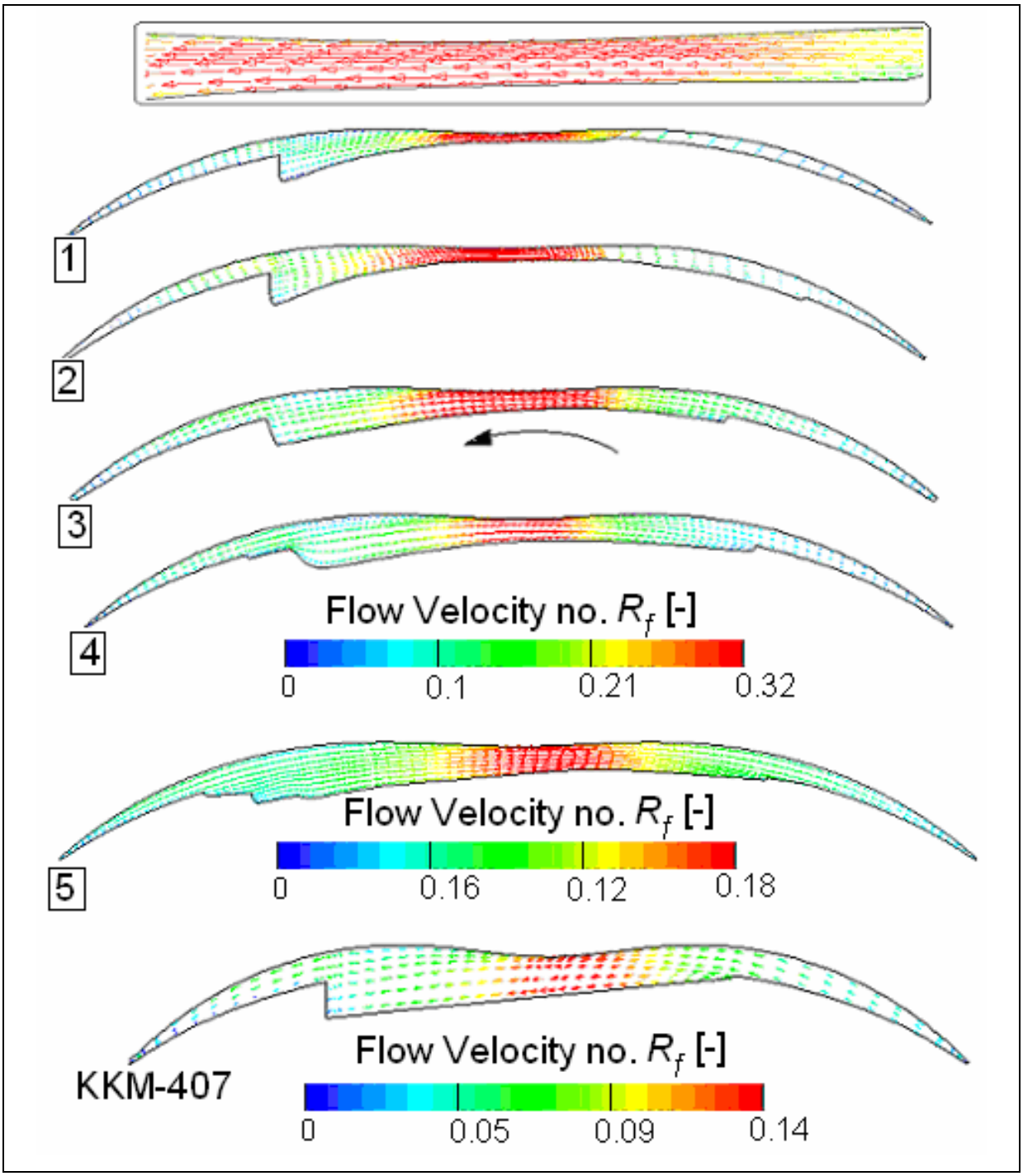

Fig.5. 25 Flow velocity vector, TDC-540°, at (2000 rpm) Re = 53733.6, R_0 = 935.5

The maximum flow velocity value for the different rotor models with its different recess shapes and depths at the end of compression phase can be seen on figure 5.28.

5.6.1.2 Engine speed (4000 rpm), Re = 107467.2, R_0 = 935.5

Similar velocity vector has been produced when the engine is running at (4000 rpm), Re = 107467.2, R_0 = 935.5. The main difference is the velocity values, the higher engine speed is, the higher inlet flow velocity and also the velocity at the end of compression become higher. The KKM-500 engine has maximum inlet flow velocity number of (R_f = 0.54), and (R_f = 0.22) for the KKM-407 engine at (4000 rpm), Re = 7487, R_0 = 1065, as it can be seen on Fig.5.26.

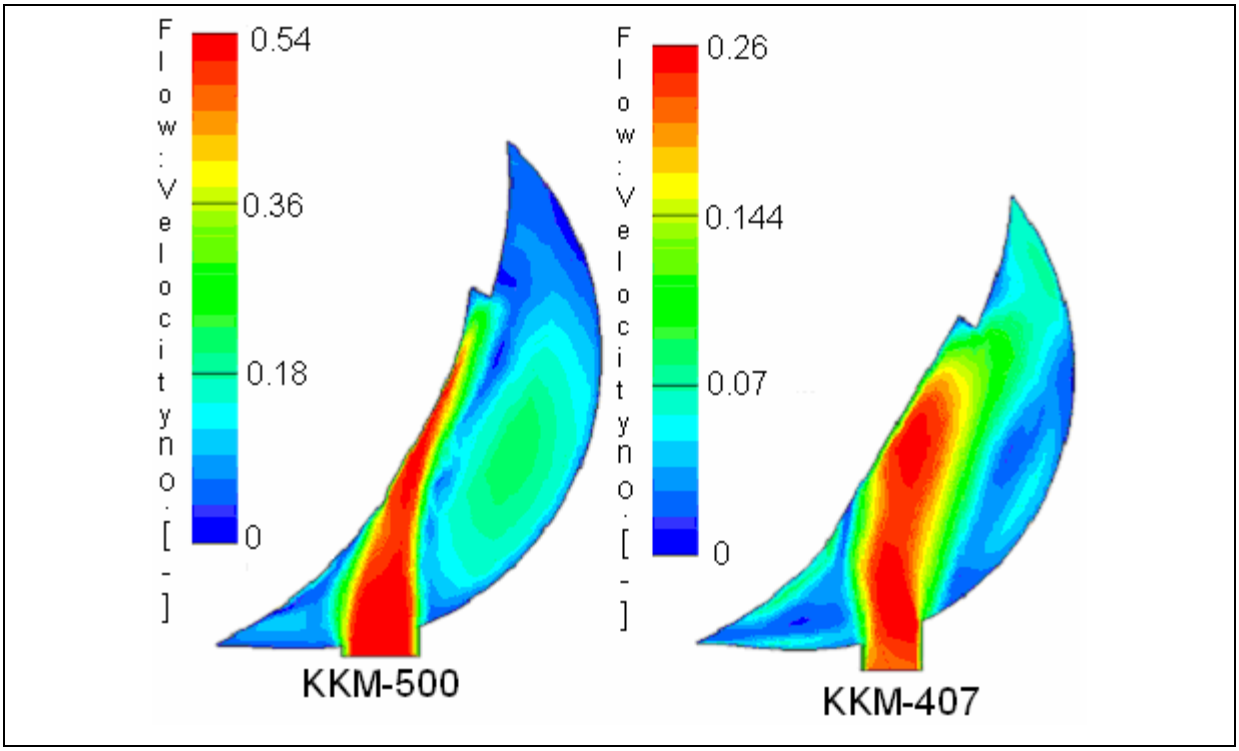

Fig.5. 26 Inlet flow velocity at (6000 rpm), Re = 161200.8, R_0 = 935.5

The swirl flow intensity increased as the engine speed increased that can be clearly seen on Fig. 5.27. When the rotor reaches the TDC (540°), the flow velocity become higher depends on the distance between the rotor surface including recess and the engine-housing tip. The wider and deeper recess produces lower flow velocity, clearly because of the bigger flow area. When a high-pressure injection is employed, it is important to keep the flow velocity low during injection to avoid fuel to be accelerated to the narrow end at the rotor apex.

Fig.5.29 shows the flow velocity at the end of compression at (4000 rpm), Re = 107467.2, R_0 = 935.5.

The maximum flow velocity indicates the different recess solutions. A small recess leads to high flow velocities in TDC-position, which reduced the contact time for the mixture formation between gas and fuel phase. The simulation of KKM407 shows a smaller velocity range because of the reduced rotor dimensions and therefore reduced angle velocity corresponding with a bigger volumetric recess depth proportion in TDC-overflow position. Because of the fast flow in this small gap every swirl from the compression stroke was lost.

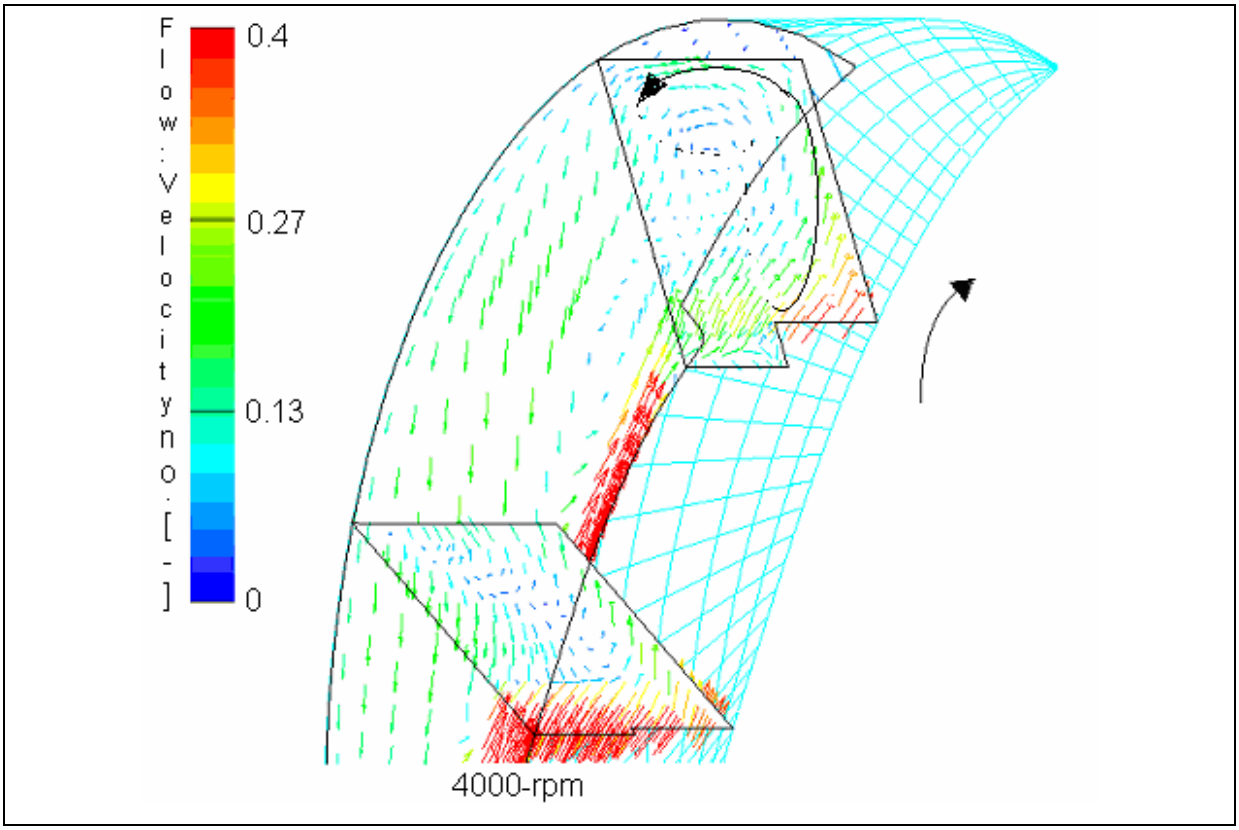

Fig.5. 27 Swirl flow, at (4000 rpm), Re = 107467.2, R_0 = 935.5

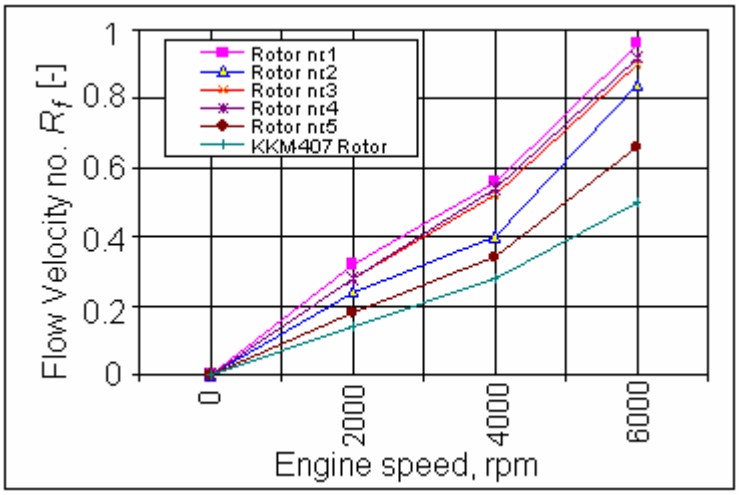

Fig.5. 28 Maximum Flow velocity vs. Engine speed at TDC, 540°

Fig.5.28 shows the plot of flow velocity at the end of compression (540°) for different rotors at different engine speed. The KKM-407 engine has the lowest flow velocity that is clearly because it has a wider and deeper rotor recess. The engine fitted with rotor no.1 has the highest flow velocity, clearly because it has the smallest and narrowest rotor recess.

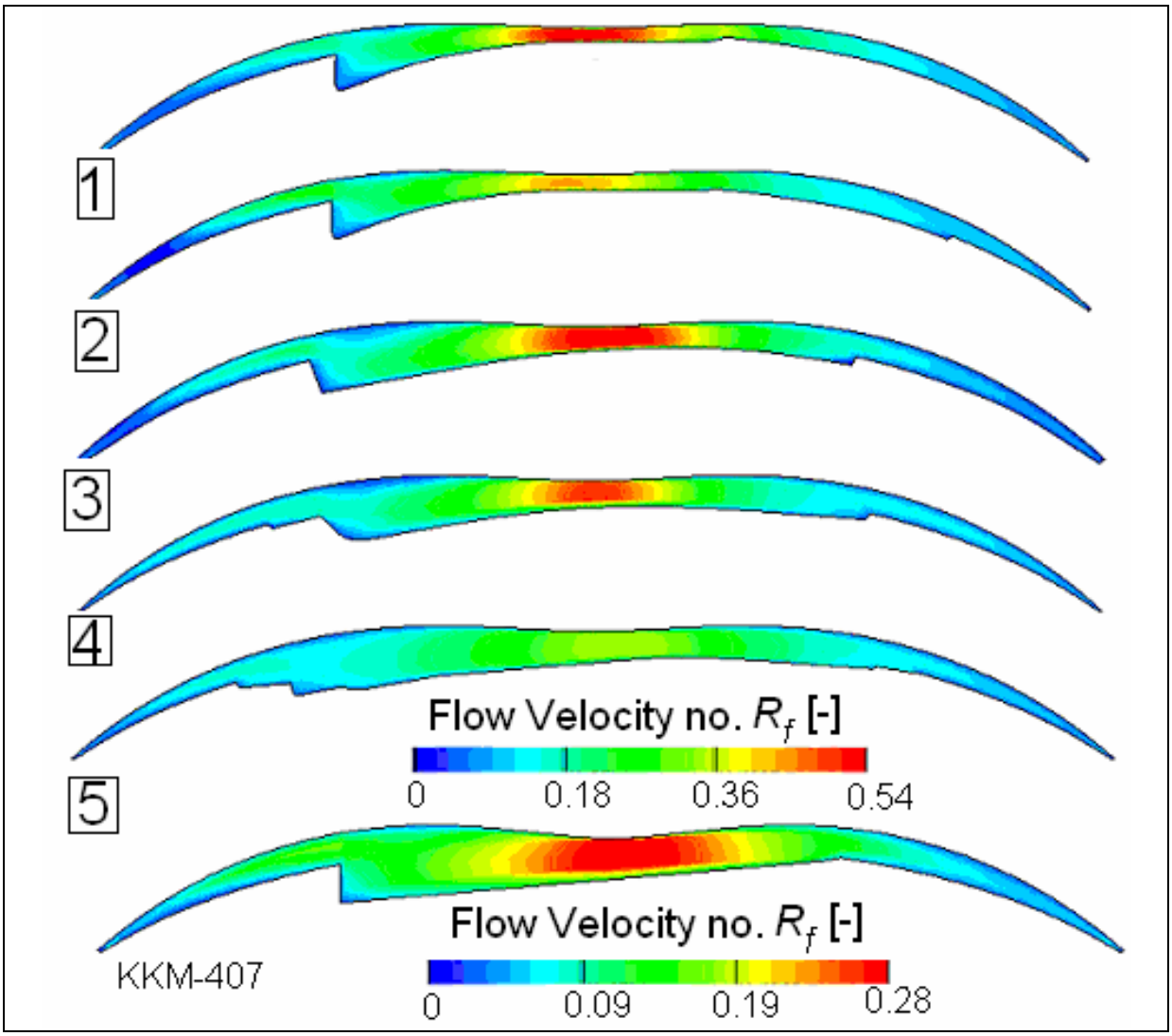

Fig.5. 29 Flow velocity at the end of compression (TDC-540°, (6000 rpm), *Re* = 161200.8, R_0 = 935.5

5.6.2 Effect of inlet port surface area

A new model for KKM-500 with an inlet rectangular port of (17mmx44 mm) was built to test the inlet port effects on flow fields. The results on figure 5.30 shows flow vector are similar to the KKM-407 engine clearly because they have similar inlet port. A big clockwise flow vortex formed along the leading part of the rotor and anti-clockwise vortex along the tailing part of rotor.

The inlet flow velocity during inlet cycle is much less than model fitted with circular inlet port, which reaches its maximum of (R_f = 0.14) at engine speed of (2000 rpm), *Re* = 53733.6, R_0 = 935.5, clearly because of the inlet port size.

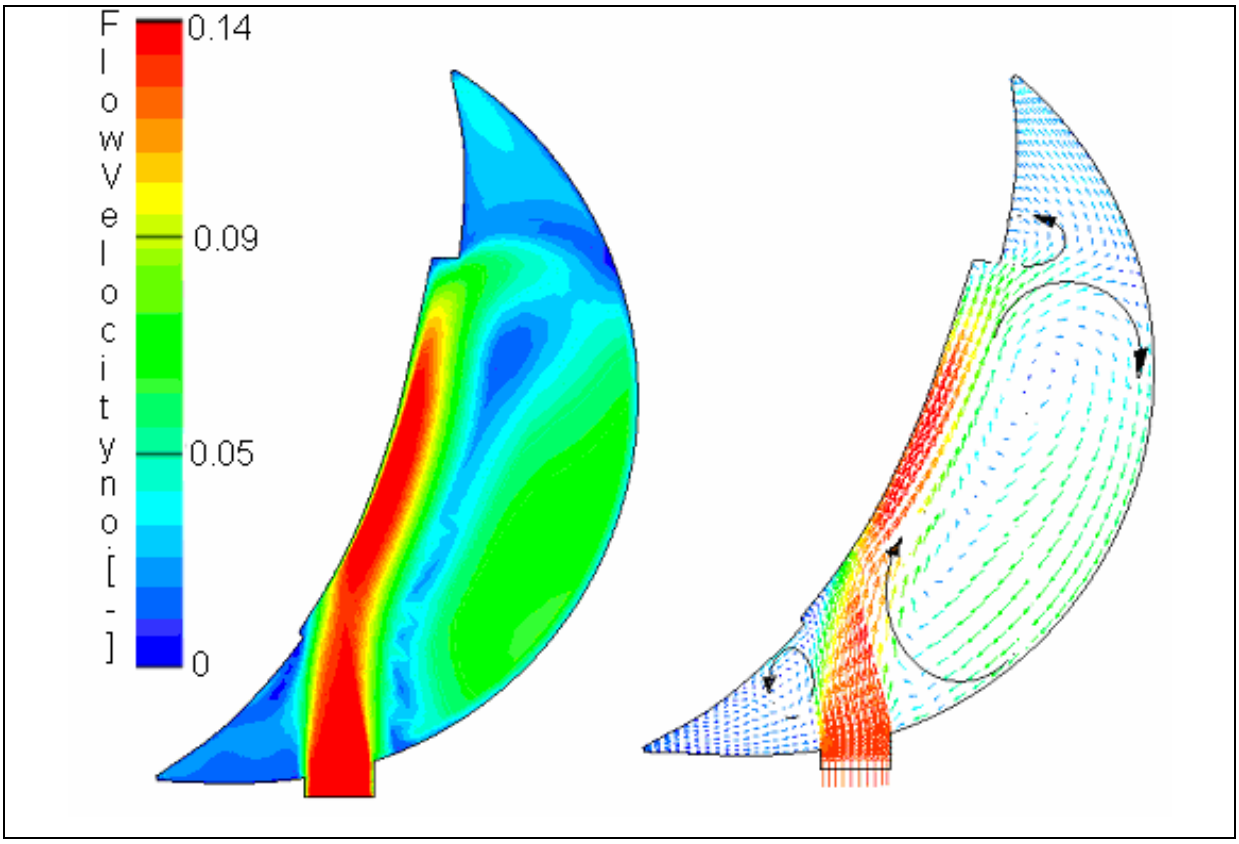

Fig.5. 30 Velocity vector during inlet cycle at (6000 rpm), *Re* = 161200.8, R_0 = 935.5 (rectangular port)

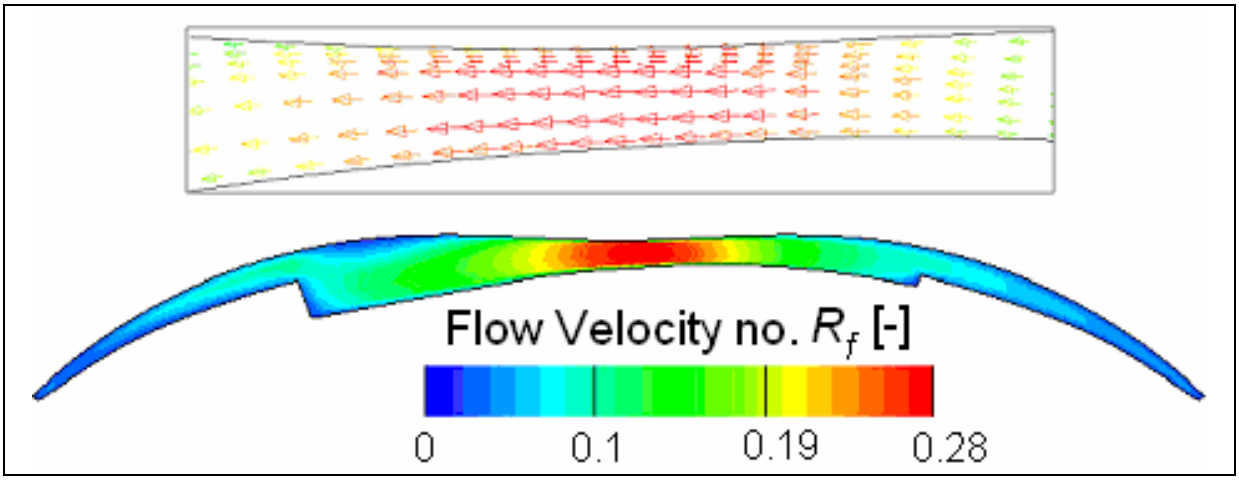

Fig.5. 31 Flow velocity at TDC, (2000 rpm), *Re* = 53733.6, R_0 = 935.5

At the end of compression, figure 5.31 shows no change in flow direction or velocity for the same model fitted with circular inlet port at the same engine speed, at TDC position.

5.7 Total pressure

The total pressure is displayed and presented in figures (5.34, 5.35) at different engine speeds, (2000 rpm), Re = 53733.6, R_0 = 935.5 and (6000 rpm), Re = 161200.8, R_0 = 935.5. However, a different scale is used to make the display more clear. The total pressure difference between the leading region and the tailing region is higher on the rotor with small and narrow recess than that with deeper and wider recess. The smallest and narrowest recess on rotor no.1 has developed the highest-pressure difference of about 5.5 bars at (6000 rpm), Re = 161200.8, R_0 = 935.5. The KKM-407 rotor and the rotor no.2 have almost less pressure difference between the two regions and the pressure is equally distributed along the combustion chamber. This is clearly because both rotors have a wider or deeper rotor recess than the other three rotors.

The rotor movement and the pressure difference at this position create the flow velocity and the lower pressure difference creates a lower velocity at the housing tip separating the two regions. In order to reduce the flow velocity at this position, it is important to increase the rotor recess width and/or depth on the penalty of compression ratio reduction. In this case, the increasing of the charging pressure can compensate the reduction of compression ratio.

The average total pressure at the end of compression is presented in table 5.8. It is clear that the rotor with a bigger recess develops lower end pressure, which can be compensated by turbocharger using.

Geometry No.		1	2	3	4	5	KKM-407
Compression ratio [-]		13.1	12.5	12.9	12.8	10.8	11.2
		Average total pressure, [pa]					
Engine velocity Re, [-] R_0, [-]	(4000 rpm) Re = 107467 R_0 = 935.5	3.4e+6	3.0e+6	2.4e+6	2.4e+6	2.0e+6	1.65e+6
	(2000 rpm) Re = 53733.6 R_0 = 935.5	3.7e+6	3.2e+6	2.6e+6	2.6e+6	2.1e+6	1.78e+6
	(6000 rpm) Re=161200 R_0 = 935.5	3.7e+6	3.2e+6	2.6e+6	2.6e+6	2.7e+6	1.8e+6

Table 5. 9 Average total pressure [Pa], all rotor geometries, different engine speeds

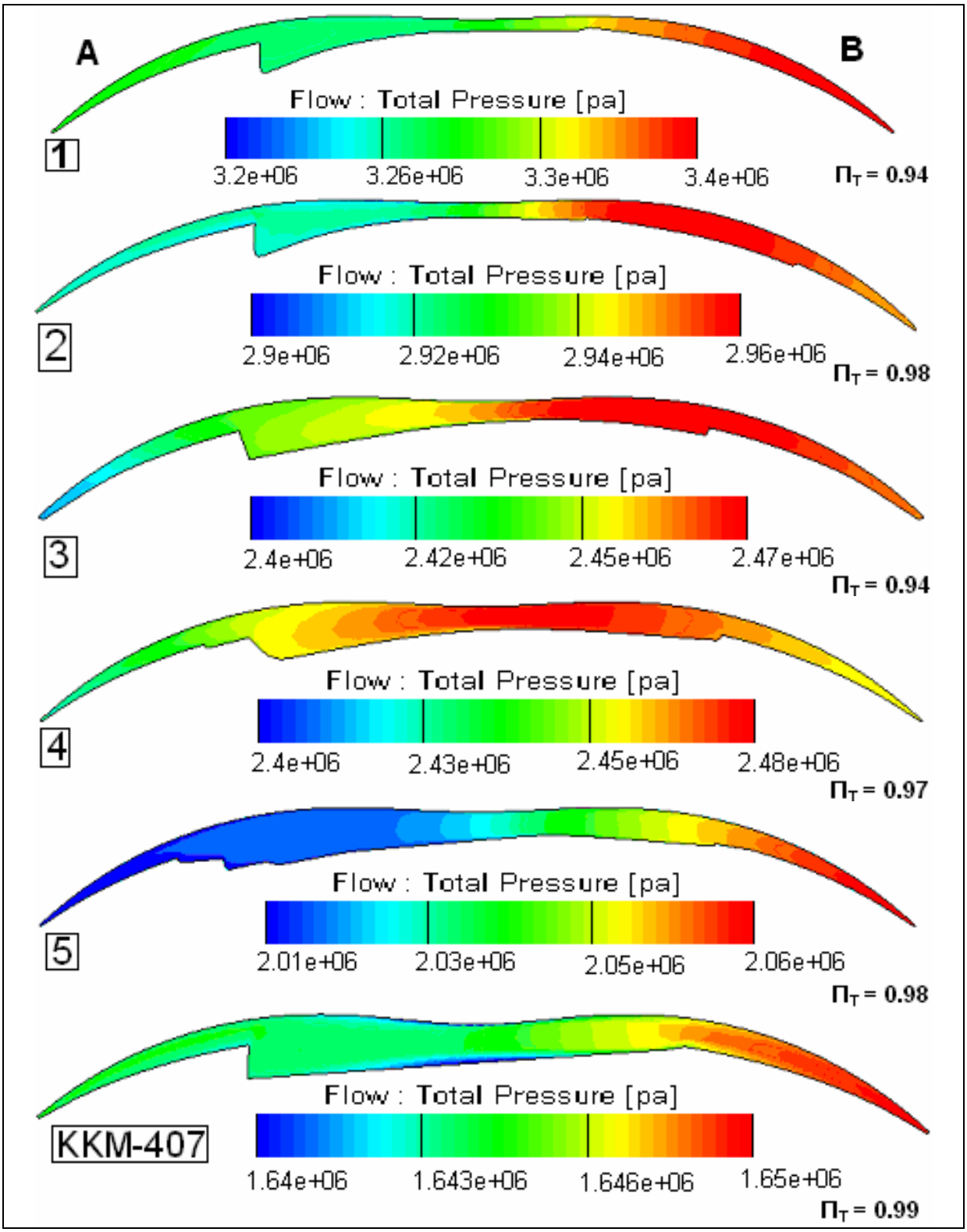

Fig.5. 32 Fluid mean total pressure [pa] at (2000 rpm), *Re* = 53733.6, *R0* = 935.5

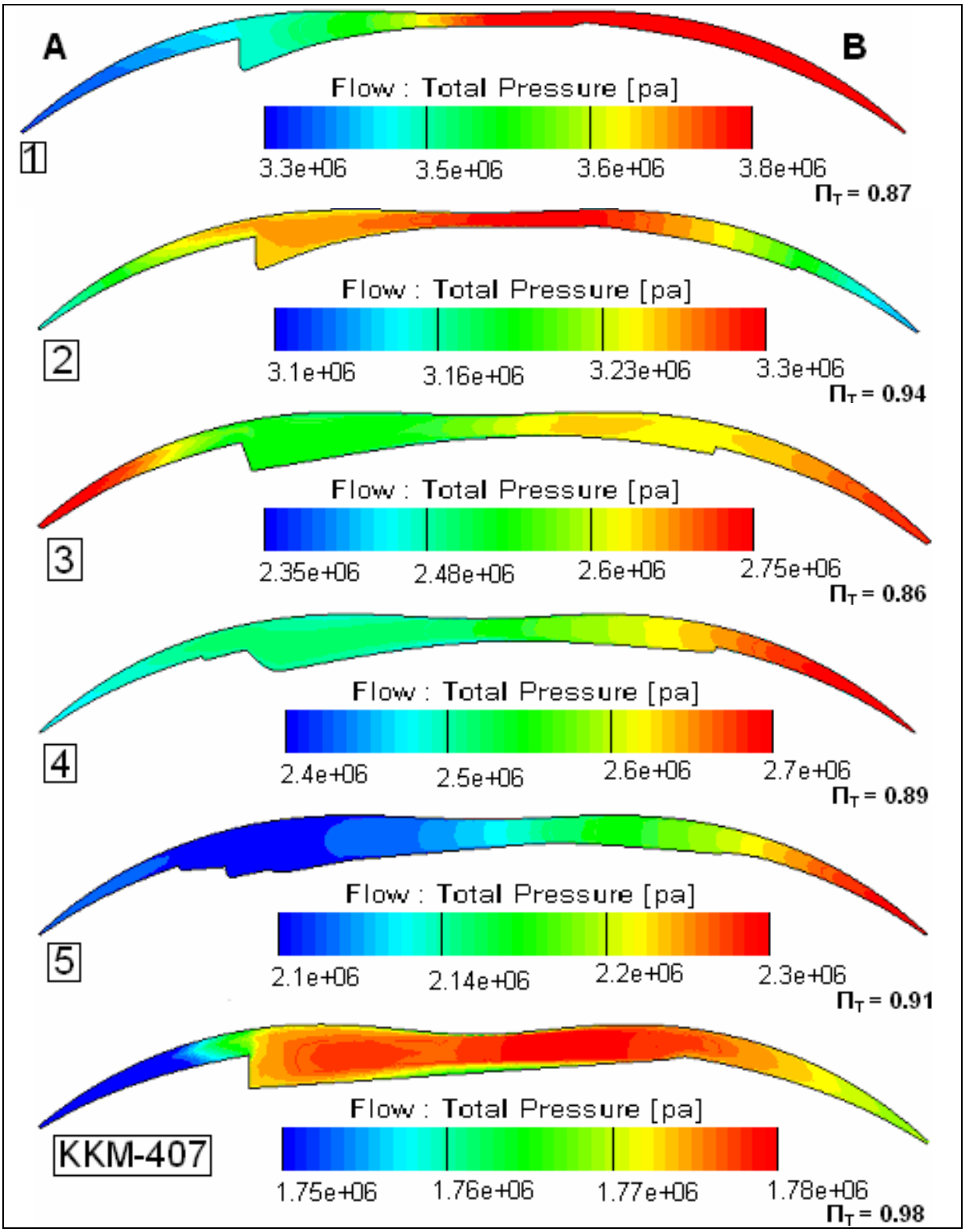

Fig.5. 33 Fluid mean total pressure [pa] at (4000 rpm), Re = 107467, R_0=935.5

On the following, figure (Fig.5.32), Π_T is the dimensionless ratio between low pressure side (side A) and high pressure (side B): $\prod_T = \frac{P_{TA}}{P_{TB}}$

The difference between the maximum pressure levels of the rotors depends on the different compression ratio depending on the recess volume.

5.8 Temperature

The mean temperature at the end of compression and without combustion is displayed and presented in figures (5.36, 5.37). On these figures of display and from table 5.9, it can be seen clearly that the end temperature of rotors with bigger recess and a smaller compression ratio is lower. The lowest end temperature is developed by the KKM-407 (591-519 k, between ((2000 rpm), Re = 53733.6, R_0 = 935.5) to ((6000 rpm), Re = 161200, R_0 = 935.5) with a homogeneous temperature distribution and smallest temperature difference from the flow centre to the wall.

The fluid initial temperature is 293 k has been taken as reference temperature (T_{TR}) to define the dimensionless total temperature number (T_0). (T_{TA}) is the actual calculated temperature. The temperature number is calculated as: $T_0 = \frac{T_{TA}}{T_{TR}}$

Geometry No.		Average temperature no. [-]					
		1	2	3	4	5	KKM-407
Engine velocity Re, [-] R_0, [-]	(2000 rpm), Re = 53733.6 R_0 = 935.5	2.3	2.32	2.2	2.2	2.13	2.02
	(4000 rpm) Re = 107467 R_0 = 935.5	2.45	2.42	2.30	2.28	2.20	2.08
	(6000 rpm) Re = 161200 R_0 = 935.5	2.49	2.47	2.35	2.36	2.26	2.11

Table 5. 10 Mean fluid temperature [k], all rotor geometries, different engine speeds

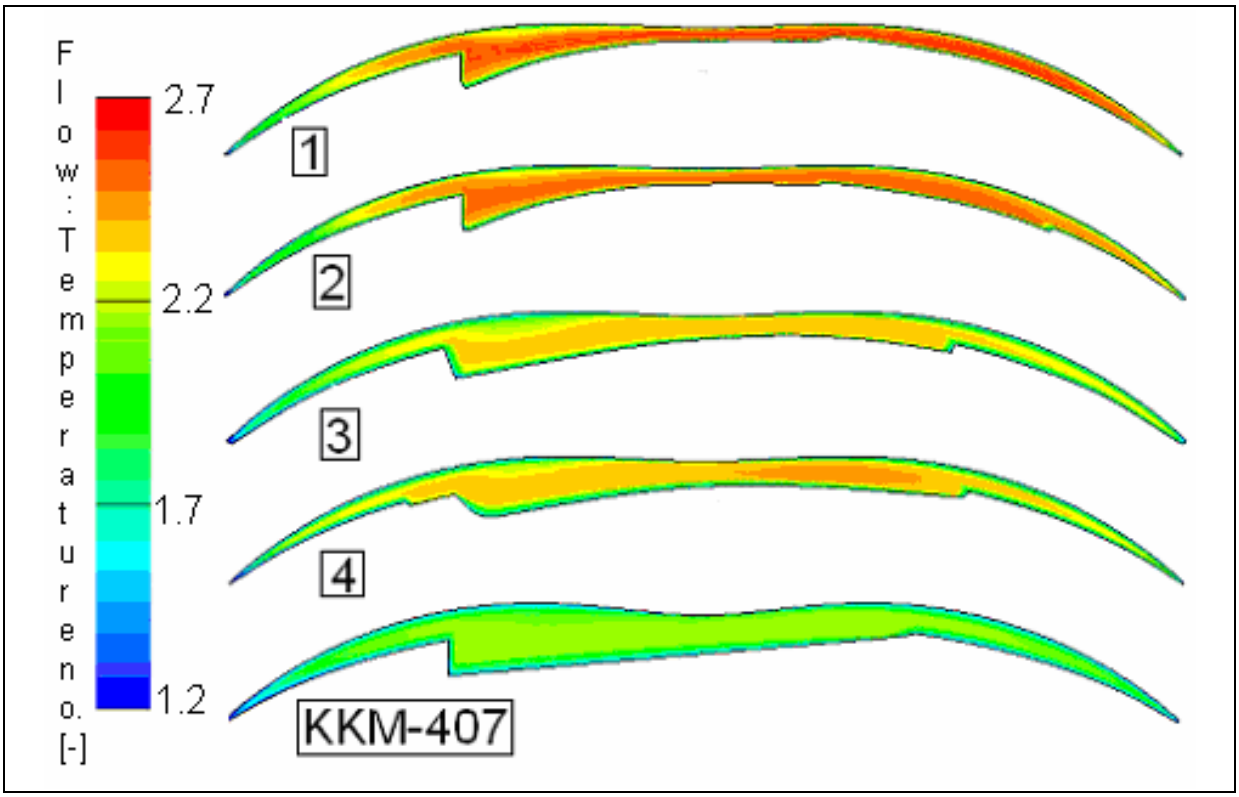

Fig.5. 34 Fluid mean temperature [K] at (2000 rpm) *Re*= 53733.6, R_0= 935.5

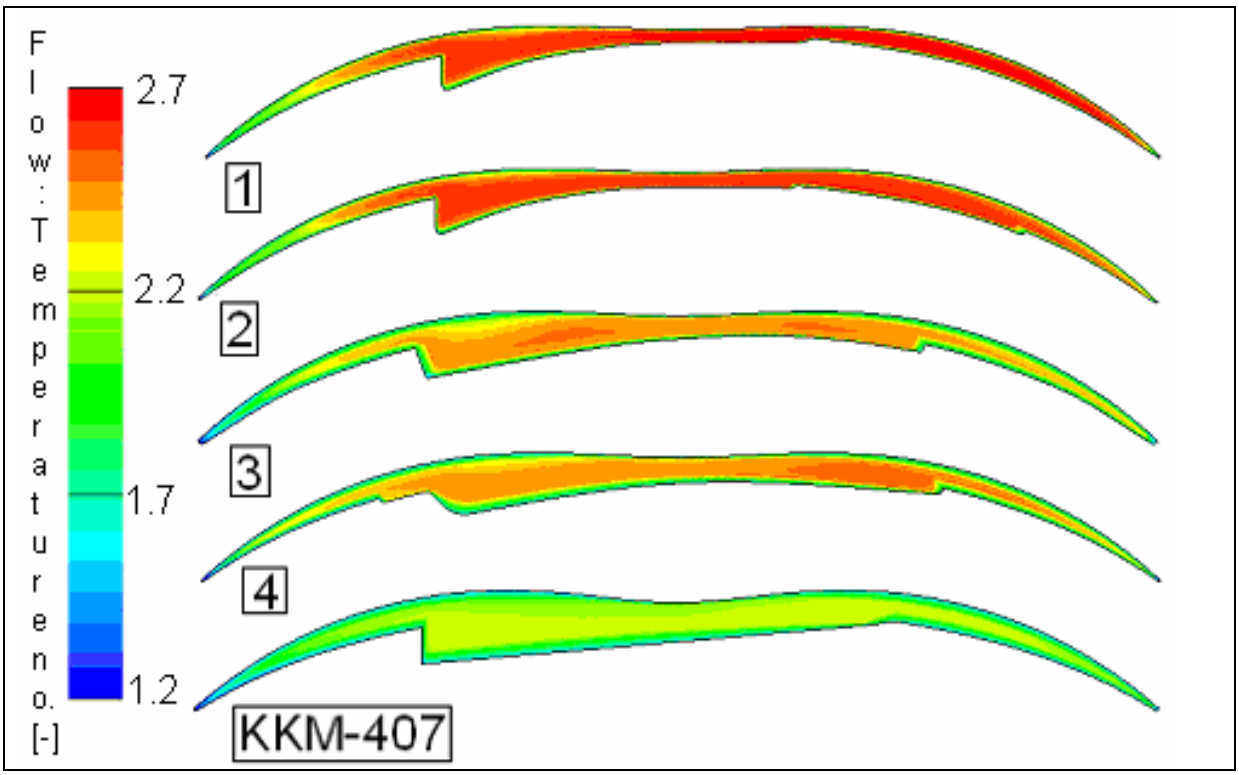

Fig.5. 35 Fluid mean Temperature [k] at (4000 rpm) *Re*= 107467, R_0= 935.5

5.9 Model validation

5.9.1 CFD models

For purpose of validation of the flow models introduced in this chapter and to study the flow behaviour when two flow different velocities affecting the flow domain. In Wankel rotary engine there are two flows affecting each other during intake port opening. The first flow is that in-flow through engine port, the second flow is that created by rotor apex movement.

To simulate and study such flow interface, a simple fixed model was built to present the in-flow through inlet port affected by another flow represent the rotor movement.

Figure 5.38 shows the flow domain and inlet boundaries. Inlet-1 presents port inlet flow and inlet-2 presents flow created by rotor movement, the rest domain presents the combustion chamber.

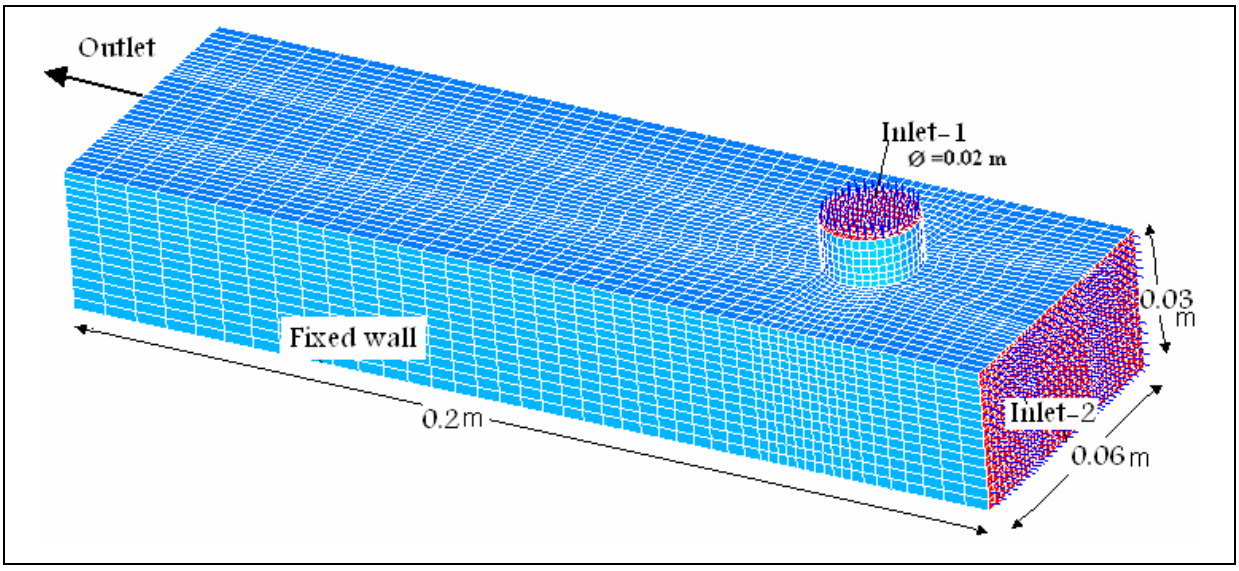

Fig.5. 36 Flow model and boundary condition

Table 5.9 presented initial and boundary condition for this model, it can be seen that inlet-1 velocity set to be 70 m/s and inlet-2 velocity is 10 m/s.

Total number of cells, [-]	31503
Initial pressure, [pa]	1e+05
Initial temperature, [k]	293
Inlet-1 velocity, [m/s]	70
Inlet-2 velocity, [m/s]	10
Outlet boundary, [-]	Address
Turbulent model, [-]	k-ε

Table 5. 11 Initial and boundary condition

The results were displayed in three planes as it can be seen in figure 5.39. The velocity vector display shows that two vertices formed on both sides of the inlet port (inlet-1), and then moved along the flow stream, accelerated by secondary flow (inlet-2), forming a circulated flow on both sides of flow domain.

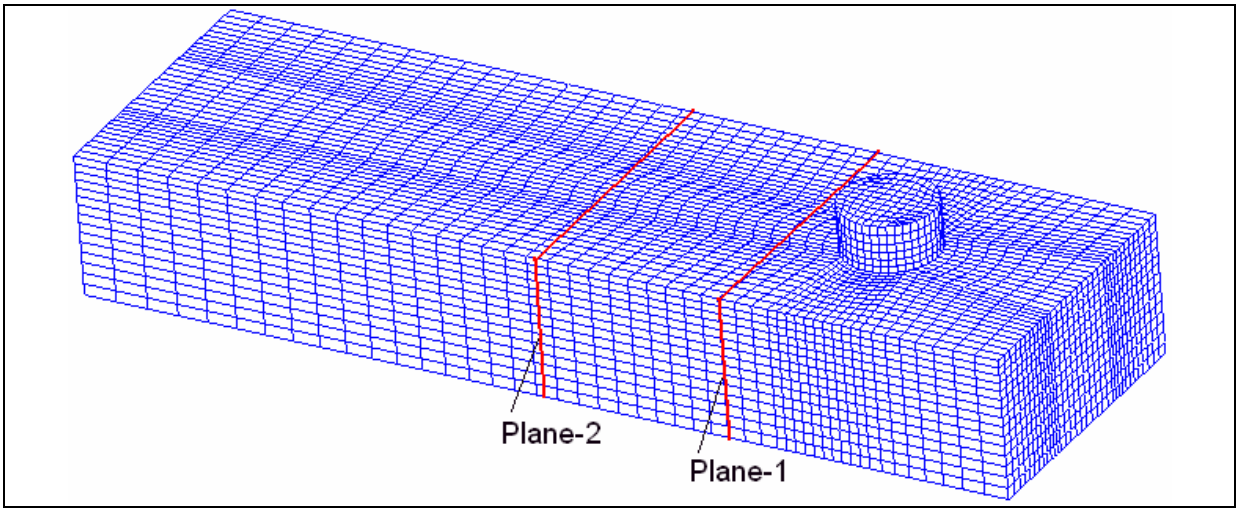

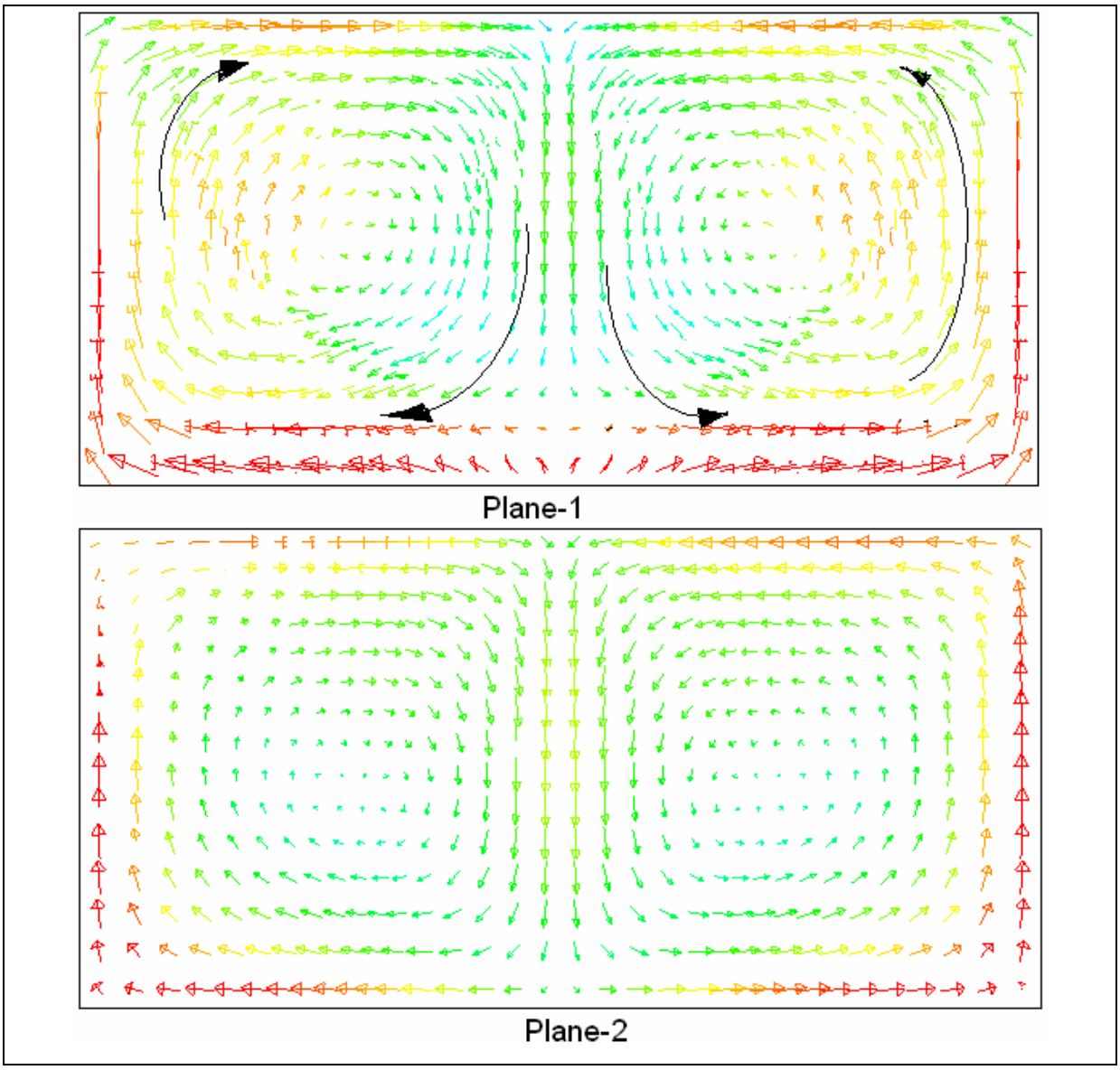

Fig.5. 37 Velocity vector display of three planes

Similarly, another fixed model of Wankel engine at a position that the inlet port is open, were also tested in similar way with both ends opened as a secondary inlet presents rotor movement flow and the other end is outlet flow. Figure 5.40 shows the boundary condition setup. Figure 5.41 show similar results as in the previous example and proves that the flow behavior is more depending on inlet flows rather than on geometrical shape in these two cases.

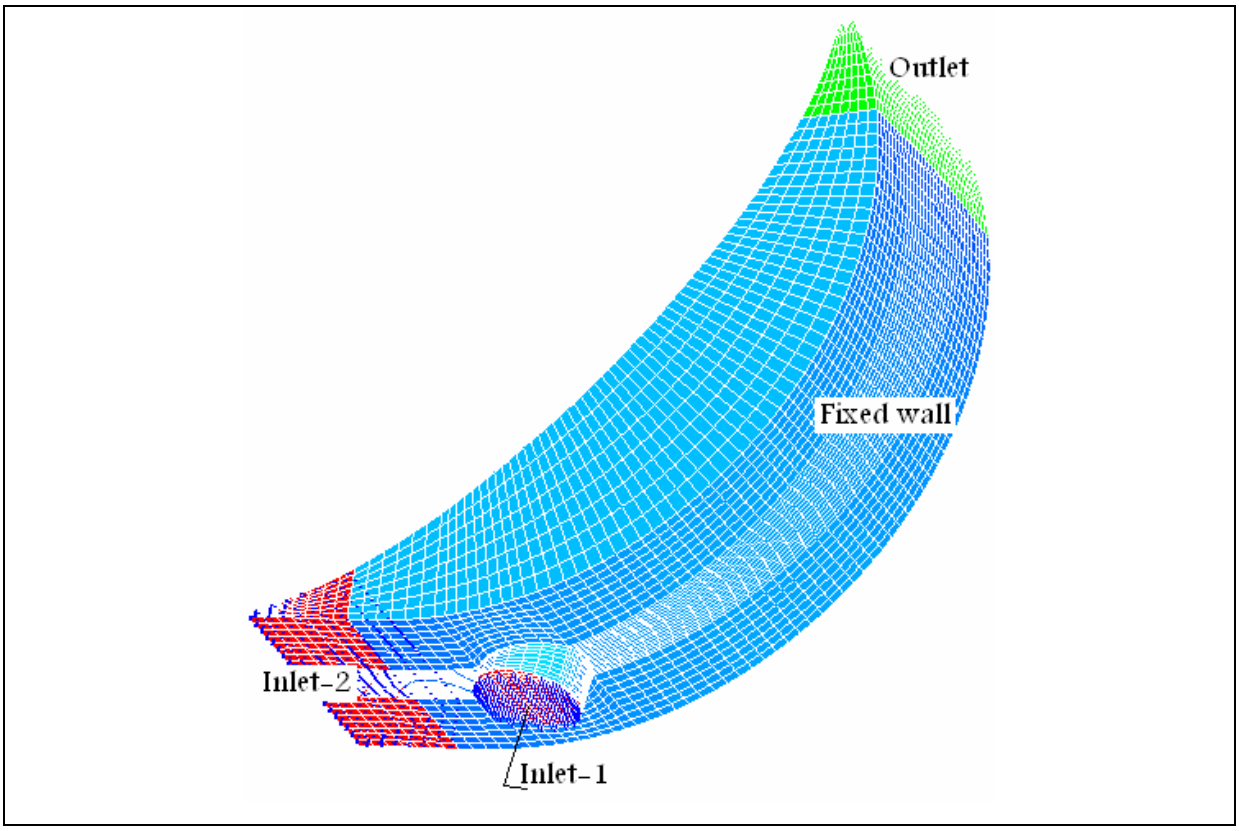

Fig.5.38 Boundary condition

Total number of cells, [-]	30839
Initial pressure, [pa]	1e+05
Initial temperature, [k]	293
Inlet-1 velocity, [m/s]	70
Inlet-2 velocity, [m/s]	10
Outlet boundary, [-]	Address
Turbulent model, [-]	k-ε

Table 5. 12 Initial and boundary condition

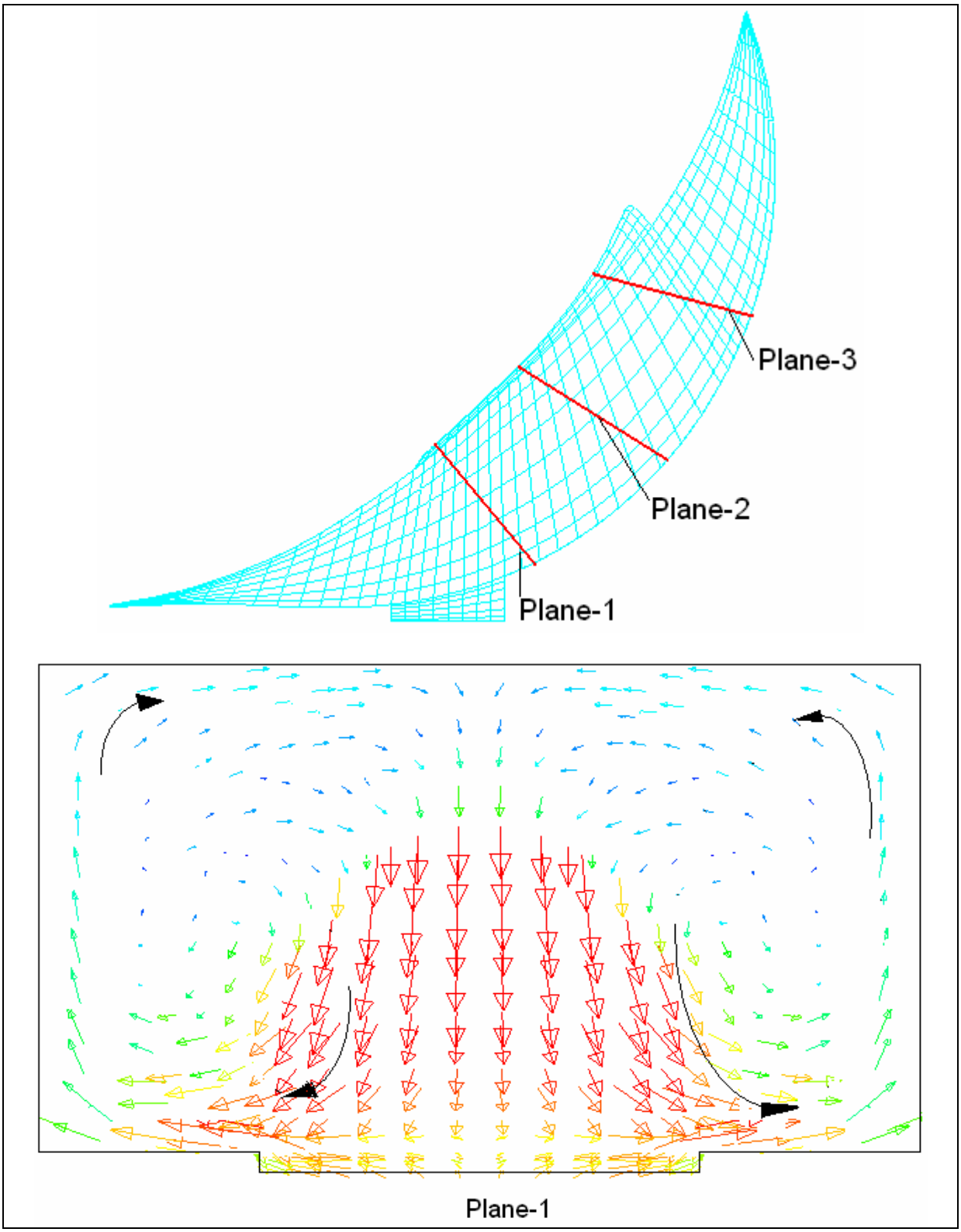
Plane-3
Plane-2
Plane-1
Plane-1

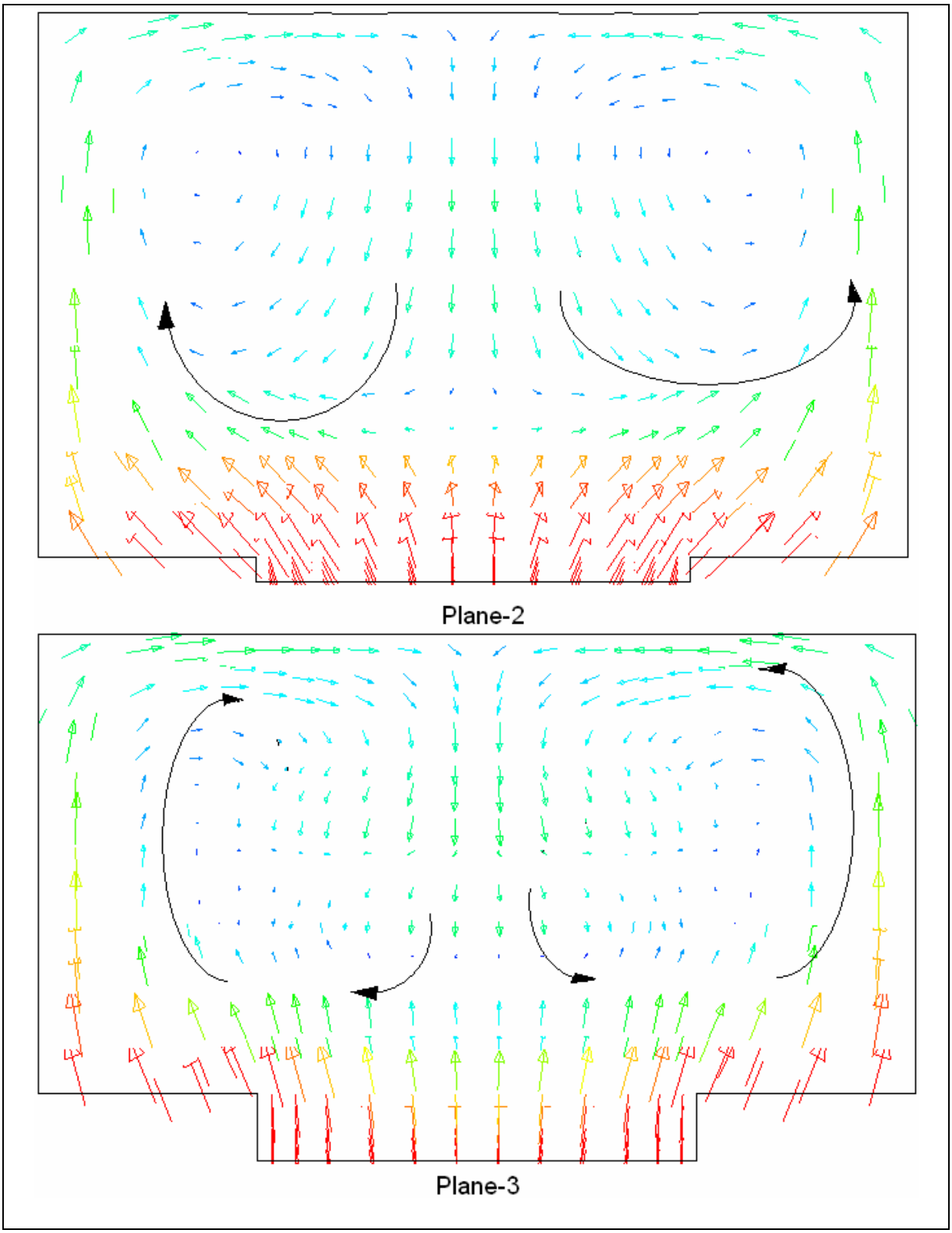

Fig.5. 39 Velocity vector display

5.9.2 Engine visualization

Yasuaki, et al [37], have conducted a visualized experimental investigation on flow inside Wankel engine at Mazda Motors Corporation, his results were compared here for purpose of validation of this models presented in this chapter. In his work, five different rotor recesses were investigated. The forms of recesses are given in figure 5.42, in two-dimensional forms as the recesses are continued across the full width of the rotor to see the fields inside the recesses. The illustration of the transparent rotary engine setup for flow visualization is given also on this figure, (5.42).

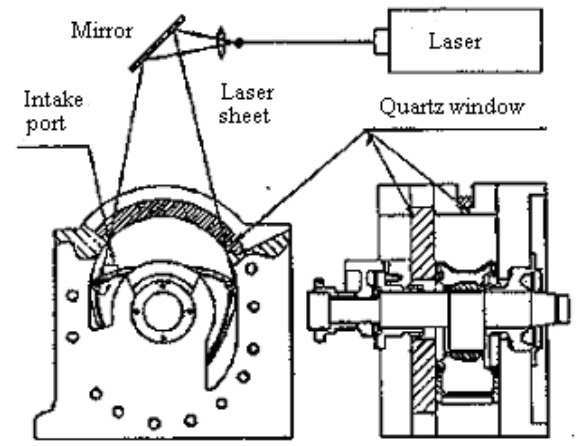

Rotor Type	Compression ratio	Recess Shape
MDR	9.4	
MDR-2D	7.1	
LDR1-2D	7.1	
LDR2-2D	7.1	
LDR2	9.0	

Rotor types

Fig.5. 40 Illustration of the transparent rotary engine for flow visualization, [37]

The results given in figure 5.43 show a little effect on the flow vortex by different rotor recess shapes only the vortex position are affected by the recess position, when the recess is in the leading side of the rotor or at middle or tailing side of the rotor.

Similar conclusion was predicted by CFD simulation in this chapter as the flow affected mainly by the inlet port shape and position (peripheral or side intake, circular or rectangular port). Most of the results displayed of this work, [37], are presented for the side intake port, which gives a slightly different vortex shape compared to the CFD simulation work presented in this chapter. Only one display presented for the peripheral intake port and it is comparable to the flow display of the engine KKM-500 with rectangular peripheral intake port in 2D-model, figure 5.44 shows this results.

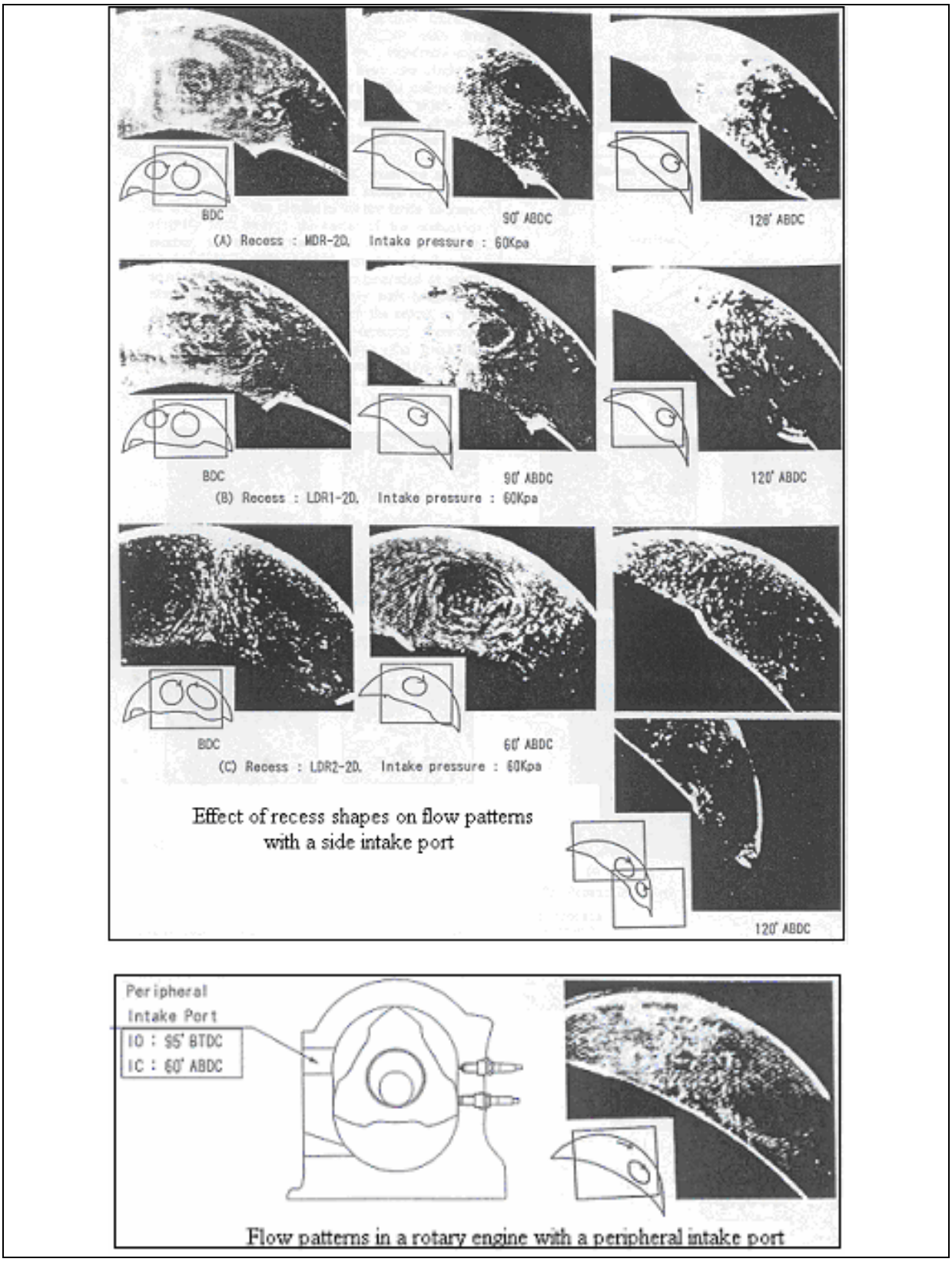

Fig.5. 41 Effect of recess shapes on flow fields, [37]

In 2D-Model specially prepared with the recess takes the whole width of the rotor to be compared to the results presented by experimental work conducted by Yasuaki, et al,[37].

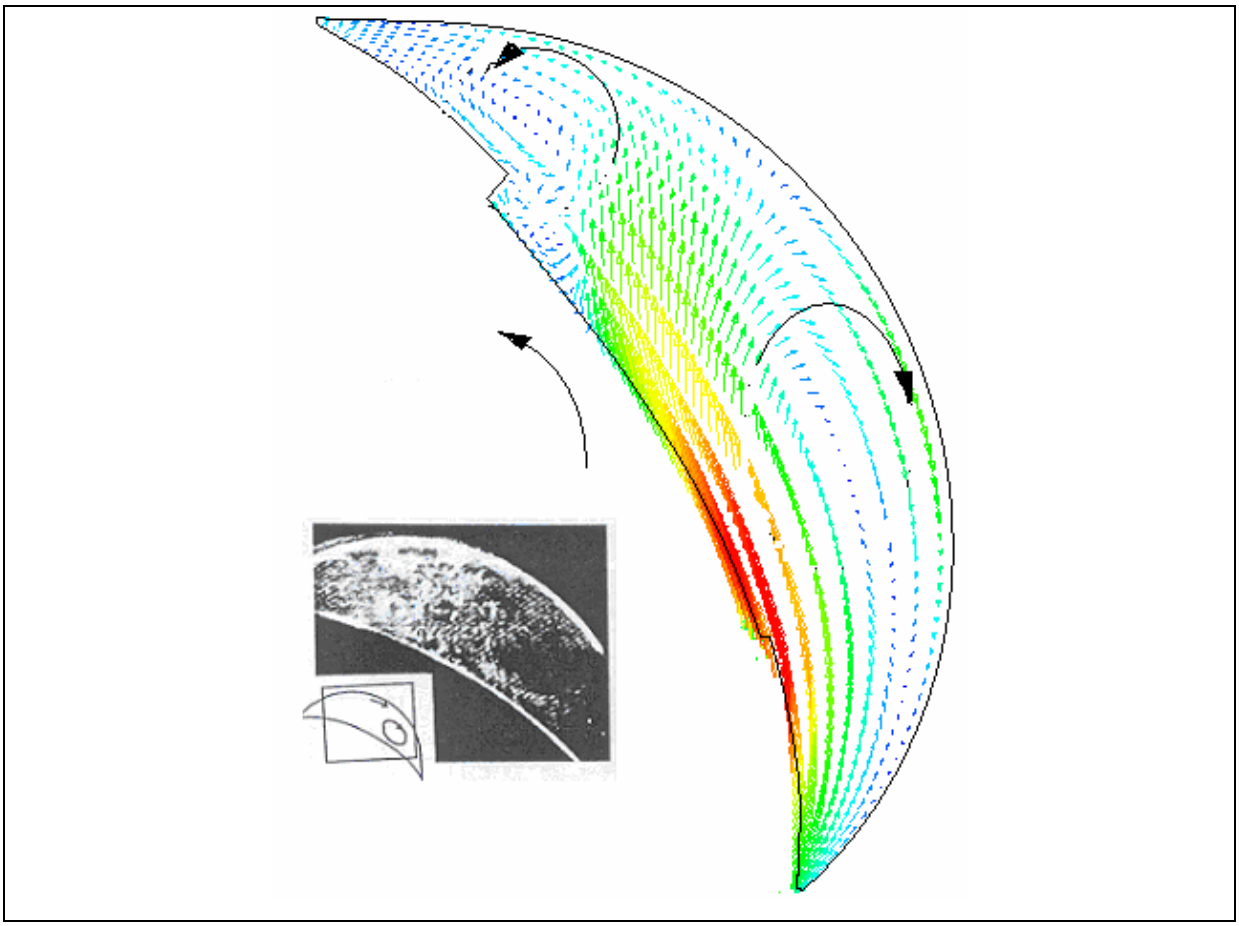

Fig.5. 42 Experimental results [37] and CFD 2D-Model, comparison

5.10 Discussion and conclusion

5.10.1 Discussion

It is important to understand the flow inside any engine combustion chamber in order to design an efficient fuel feeding system to improve the engine output power and to reduce the exhaust pollutant emissions. However, as air/fuel mixing process improved, the combustion process will be improved and therefore the engine thermal efficiency will be improved.

Introducing fuel into combustion chamber has different strategies discussed earlier in chapter (1), of this thesis indicated that each has its own advantage. Port or low-pressure fuel injection has more time for mixture preparation, and the creation of swirl or tumble inside combustion chamber will give a better chance for fuel to be mixed properly with air and gives better or complete fuel combustion, and hence less pollutant products.

However, the swirl flow has less effect on high-pressure fuel injection when the fuel is injected near the engine TDC as the ignition is normally started shortly after fuel injection, but the swirl which can affect and improve the turbulent combustion was not clearly noticed at TDC.

In general, it is possible to inject most of liquid or gas fuels at port or low pressure after the inlet valve closed directly into the combustion chamber, the mixture prepared should fill the whole combustion chamber and should be near stoichiometric fuel/air ratio. So, the use of throttling valve is necessary to control air fuel inlet in order to keep the correct fuel/air ratio at all engine speeds. Unfortunately, this air throttling system will reduce the engine thermal efficiency. When consider diesel engine there is no need to control airflow using such throttling system and the engine speed and load are controlled only by diesel mass flow, which means it is not necessary to keep the air/fuel ratio around stoichiometric ratio and any amount of diesel injected will be self ignited at a high engine pressure near TDC.

In the case of injecting diesel fuel at port or low pressure injection, the diesel fuel and air mixture should be around stoichiometric and the mixture ignited by the use of sparkplug similar to gasoline engine and that will reduce engine efficiency badly. From this assumption diesel should be only injected at a high pressure near the TDC, and can be ignited with the help of sparkplug for low compression ratio engines.

CFD simulation shows that the Wankel rotary engine develops a swirl or tumble vortex inside the combustion chamber along the flow domain during inlet and compression periods and that will very useful for port or low-pressure injection if the fuel is injected directly into the swirl vortex. A good mixture concentration distribution expected, if the fuel injected directly to the swirl vortex just above inlet and will be tested in the next chapter.

In Wankel engine, even if the air/fuel mixtures is well prepared, there is another factors drawback the combustion process, such as the long and narrow combustion chamber, needs

to fit two spark plugs to make the combustion process faster. Also, the fuel at both ends is normally not completely burned.

High pressure injection, the fuel is normally injected just before the engine reaches its TDC and the mixture ignited and burned with locally rich region and air is supplied during combustion from locally lean regions. The CFD simulation shows that, the swirl vortex become smaller and smaller until the flow takes rotation direction near TDC with higher flow velocity at the housing mid point where the distance between the rotor and housing is very close. Normally when fuel is injected at engine high pressure, the fuel injector is fitted at the housing mid point, (short axis), and inject fuel at this point where the flow velocity is very high, that will accelerate fuel to one side of combustion chamber or to the narrow end. To avoid such action, it is necessary to reduce flow velocity at this point by increasing the recess size.

5.10.2 Brief summary

Modeling in science and engineering, may be generally regarded as the process of describing a physical phenomena in a particular system with the help of mathematical equations (subject to a reasonable assumptions), and solving the same to understand more about the nature of such phenomena. Usually, engineering models help in designing better devices by understanding more about the fundamental physical process occurring therein. Engine modeling activities, at least in recent decades, have largely concentrated in the direction of designing better performing engines with lower fuel consumption and emissions. In this regard, modeling of flow inside the engine combustion chamber has a great importance in order to design better engine with higher performance.

Understanding this flow phenomena helps to design the right combustion chamber for specific application such as in direct injection engine, the injected fuel is directed to spark plug, and creation of swirl or tumble is important for better mixture formation.

In this flow simulation work, presented in this chapter, all models were prepared and tested using well-known CFD simulation software with its capability of moving or dynamic mesh. K-ε turbulent flow model is the most widely used turbulent model in engineering flow calculations were applied.

The main conclusion of Wankel engine flow modeling can be summarized as follows:

- Flow during intake and compression strokes is considered to be more important in case of concentrating on mixture formation investigation study**.** In case of including combustion investigations, the model should be extended to include the expansion stroke**.**
- The results show (Fig.5.20), that two flow vortexes formed on both sides of the rotor during the early stage of the intake stroke continued until the tailing rotor apex become closer to inlet port.
- During intake stroke, a swirl flow starts to develop along the combustion chamber and continued during compression.
- The rotor geometry and recess shape has a little effect on the flow patterns during intake and compression strokes, the flow affected mainly by the inlet geometry and position (peripheral or side intake)**.**
- At the end of compression, the fluid flows along the rotor surface in direction of rotation without any sign of flow vortex, clearly because of the long narrow distance between the rotor and housing.
- The flow velocity at the end of compression could reach high level at the housing tip (short axis), depending on the rotor recess size.
- The change in the inlet port configuration and size will change the inlet flow velocity and the vortex shape during inlet period but does not affect the end of compression velocity, this velocity affected only by the rotor recess size and engine velocity.
- The two simple fixed models presented in section 5.9.1, can validate the flow inside ducts, with its size and configuration similar to the engine combustion chamber, and hence produce similar swirl flow produced by fixed and moving engine models.
- The experimental visualization presented in section 5.9.2, by Yasuaki, et al [37], can validate the 2D model prepared specially to be comparable to the 2D experimental results, Fig.5.42.

The next chapter will deal with mixture formation including liquid diesel fuel injection strategies and diesel injector configuration.

6

Diesel Spray and Mixture Formation for Wankel Rotary Engine

6.1 Introduction

In recent years CFD has been successfully established for three-dimensional simulation of fluid flow, mixture formation, combustion, and pollutant formation in direct injection diesel and gasoline engines. The accuracy of simulation results and hence their contribution to design analysis and optimization, however, strongly depends on the predictive capabilities of the models adapted for simulation injector flow, spray propagation, combustion and pollutant formation. In the last decade, intensive worldwide research has led to the development of a large number of models for simulation of such processes. In the IC engine simulation, AVL-Fire has already been recognized of being the leading CFD solution in terms of its capabilities of simulating flow, fuel injection, mixture formation, combustion, and pollutant formation, by its own broad range of validated models.

In this chapter with the help of AVL-Fire Code, and its well known validated spray models [38,37], such as Breakup Models, Wave Breakup Model, Eddy Life Time Model, Diesel Nozzle Model etc. And because the engine is still running on diesel fuel on the test bed, investigations on the diesel spray mixture formation have been carried out and the fuel injection parameters have been studied, such as injector position and spray angles inside the engine combustion chamber and spark plug position.

Two selected rotor geometries (rotor geometry 3, and 5); these rotors have been already introduced in the previous flow simulation chapter. The engineers of WST GmbH have suggested these two rotor geometries to be studied and considered to give better test results.

A three and four bore (holes) injector has been used and the adjustment of angles between holes and its declination angle have been studied to predict best injection angles.

As the engine is considered to be capable of burning different kind of fuels, and is better engine that suits hydrogen combustion, the second part of this chapter will study different hydrogen injection strategies and hydrogen mixture formation and will concentrate on low and high-pressure direct injection.

6.2 Model preparation

6.2.1 Geometrical model

Normally in diesel engine, fuel is injected at high pressure just before the piston reaches its TDC and self ignited without the help of a spark plug. In engines with low compression ratio, the pressure and temperature developed inside the combustion chamber is not enough to ignite the mixture, therefore it is important to use a spark plug to start the combustion process.

The Wankel engine tested is now running on diesel injected at engine high pressure (15º-40º BTDC), used a high-pressure common rail system.

However, to save model preparation and running time, only 54º before engine TDC to the end of compression (TDC) was simulated as dynamic mesh (moving mesh). The initial conditions, pressure, temperature, and velocity, were set at this position according to the flow model results introduced in the last chapter.

Figure 6.1 shows a 3-D geometrical surface for the engine fitted with selected rotor no.5 introduced in last chapter. The injector is fitted at the center position of the housing short axis. Two spark plug positions were tested for better ignitable mixture concentration, (18mm and 31mm, from short axis).

6.2.2 Nozzle configuration

Three holes injector is fitted at the center position of the housing short axis with an angle of 45º to the normal long axis to inject the fuel to the leading rotor side direction. Figure 5.2 shows injector and spark plug configuration.

The objective of this work is to determine the best angle between the nozzle holes and the declination angle of the spray cone to the injector axis, which gives better penetration and hence better mixture formation. Fig. 6.3 and fig. 6.4 show different declination angles and the angle between holes possibilities. Several injection angles have been investigated and the results were presented in this chapter.

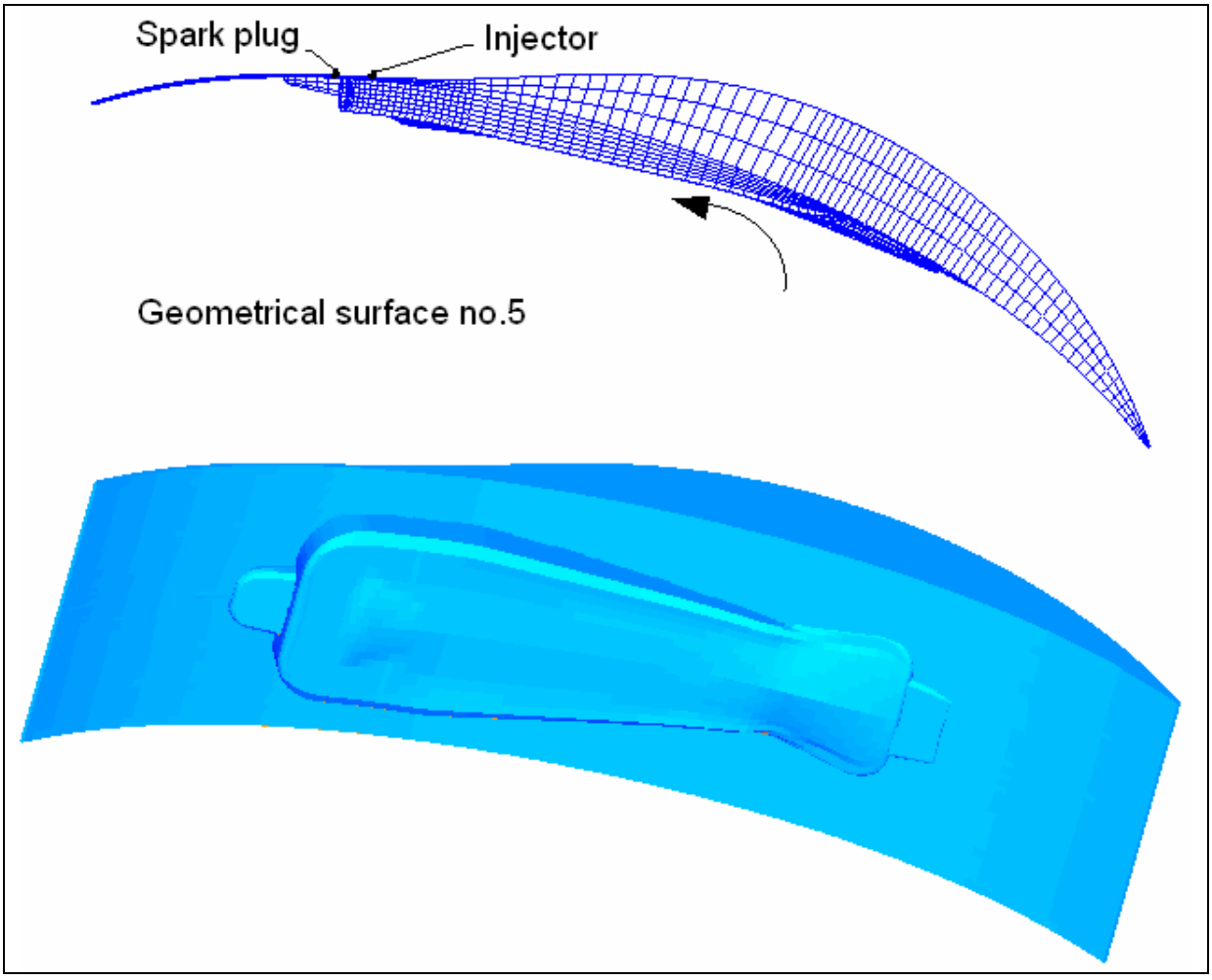

Fig.6. 1 3-D geometrical surface of rotor No. 5 at 54° BTDC

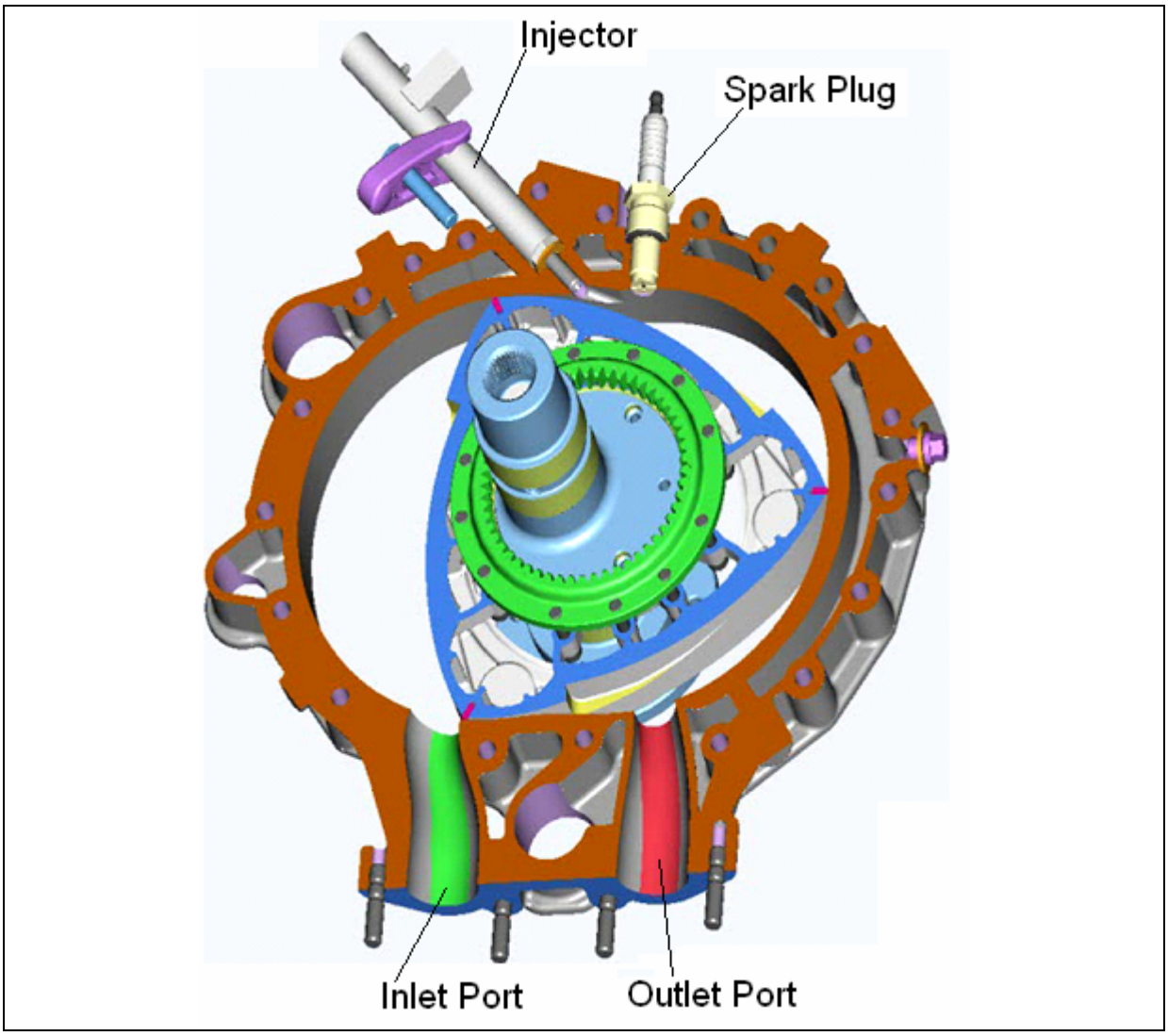

Fig.6. 2 Injector and spark plug configuration

6.2.3 Boundary condition

Two boundaries are necessary to be set; the first one is for the fixed wall and the second one for moving wall. Fixed and moving wall temperatures were fixed to be 300 ºC.

6.2.4 Initial condition

The initial fluid condition for each model (pressure, temperature, flow velocity, etc), were set according to the flow models results introduced earlier in the previous chapter. Accordingly, the two spray models investigated in this chapter for geometrical surface of rotor no.3 and

rotor no.5 have different initial conditions (temperature, pressure) due to pressure ratio different. Table 6.1 shows the initial conditions set for both models.

	Temperature [k]	Pressure [Pa]	Initial velocity, (x,y,z) [m/s]	Turbulent Model	Tke [m^2/s^2]	Length scale [m]	Species [-]
Geo.3	530	8.95e+5	(-10,5,0)	k-e	2	0,002	Air
Geo.5	520	8.60e+5	(-10,5,0)	k-e	2	0,002	Air

Table 6. 1 Models initial condition

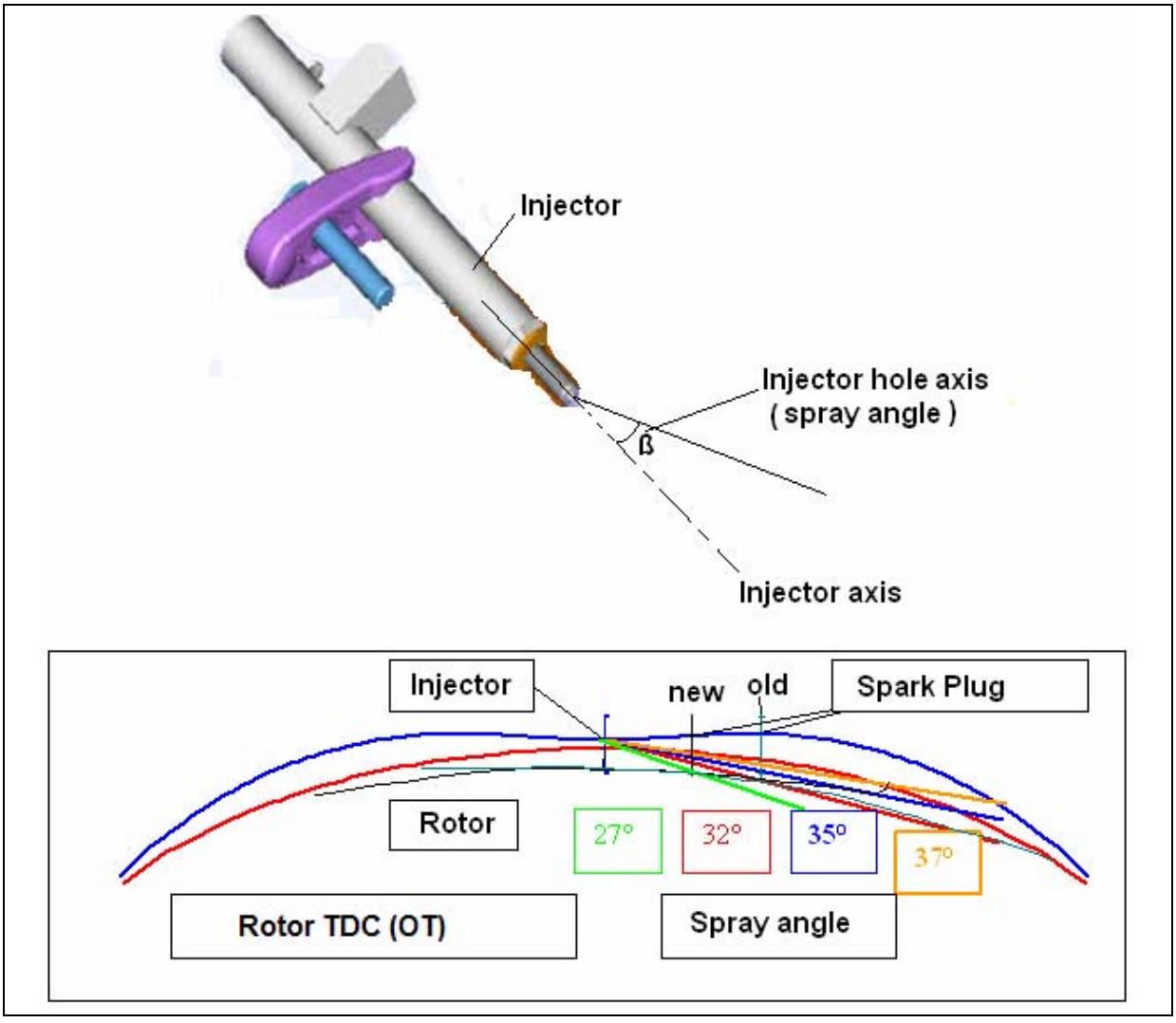

Fig.6. 3 Different spray angles at engine TDC

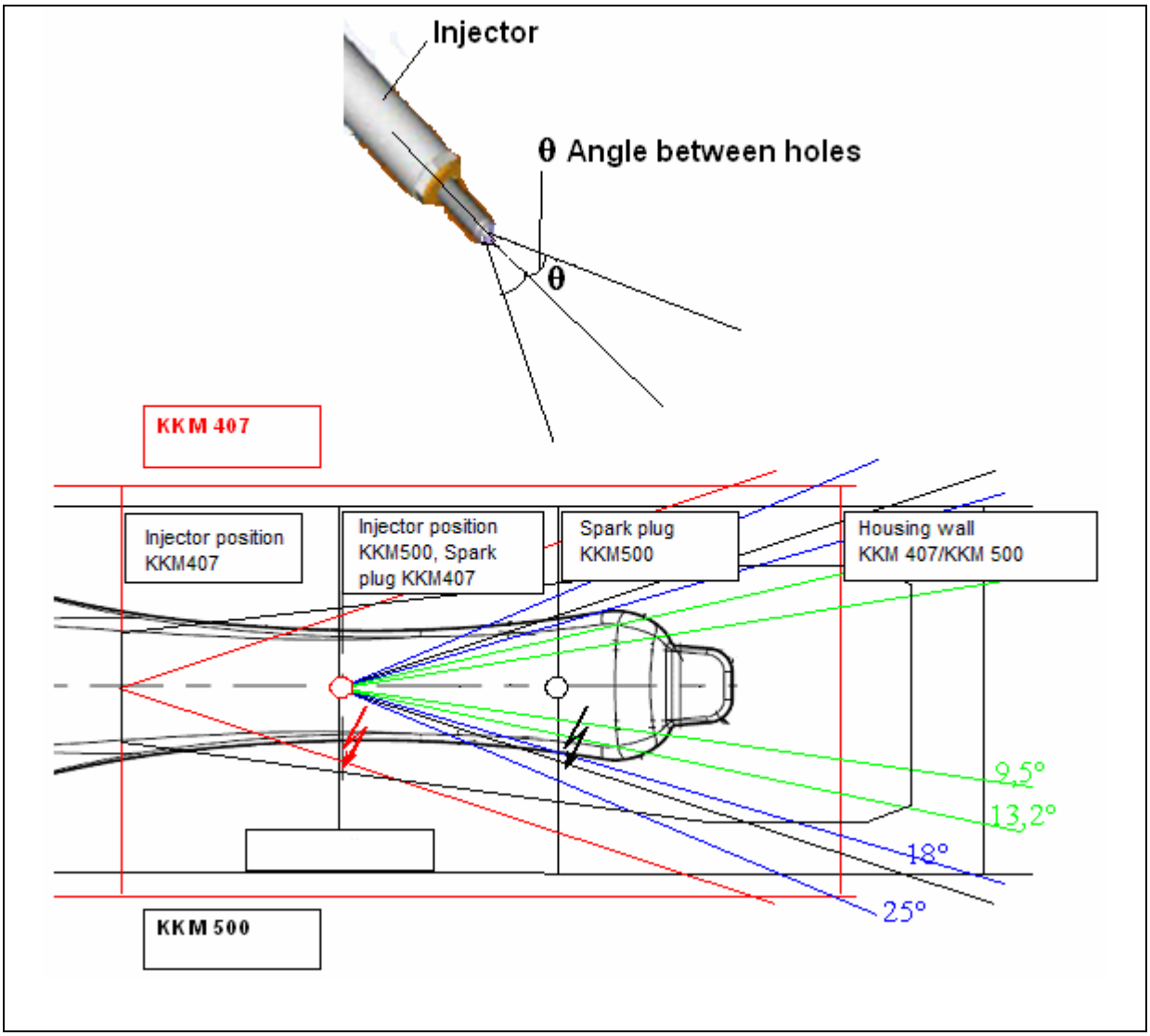

Fig.6. 4 Angles between holes possibilities

6.2.5 Spray file

The spray file was prepared with three holes injector located in the center position of the housing short axis; each hole has 0.15mm in diameter. Angle between the spray cones axis is adjusted at first to be, 13.2º, 18º, and 25º for mixture formation comparison. Spray angle is also adjusted and tested at 27º, 29º and 32º.

Wave breakup model was applied to calculate the droplet breakup; this model is recommended by AVL to calculate diesel engine nozzle flow. Figure 6.6 shows a three-bore nozzle with 18º between each spray cone axis and 32º spray angle.

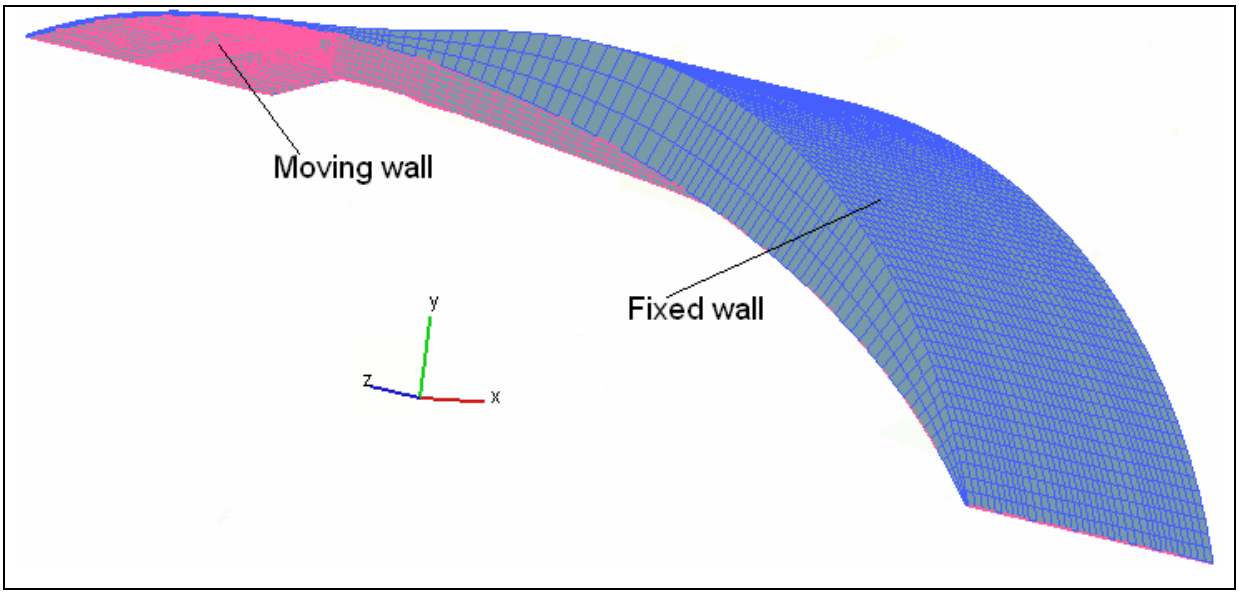

Fig.6. 5 Model boundary condition

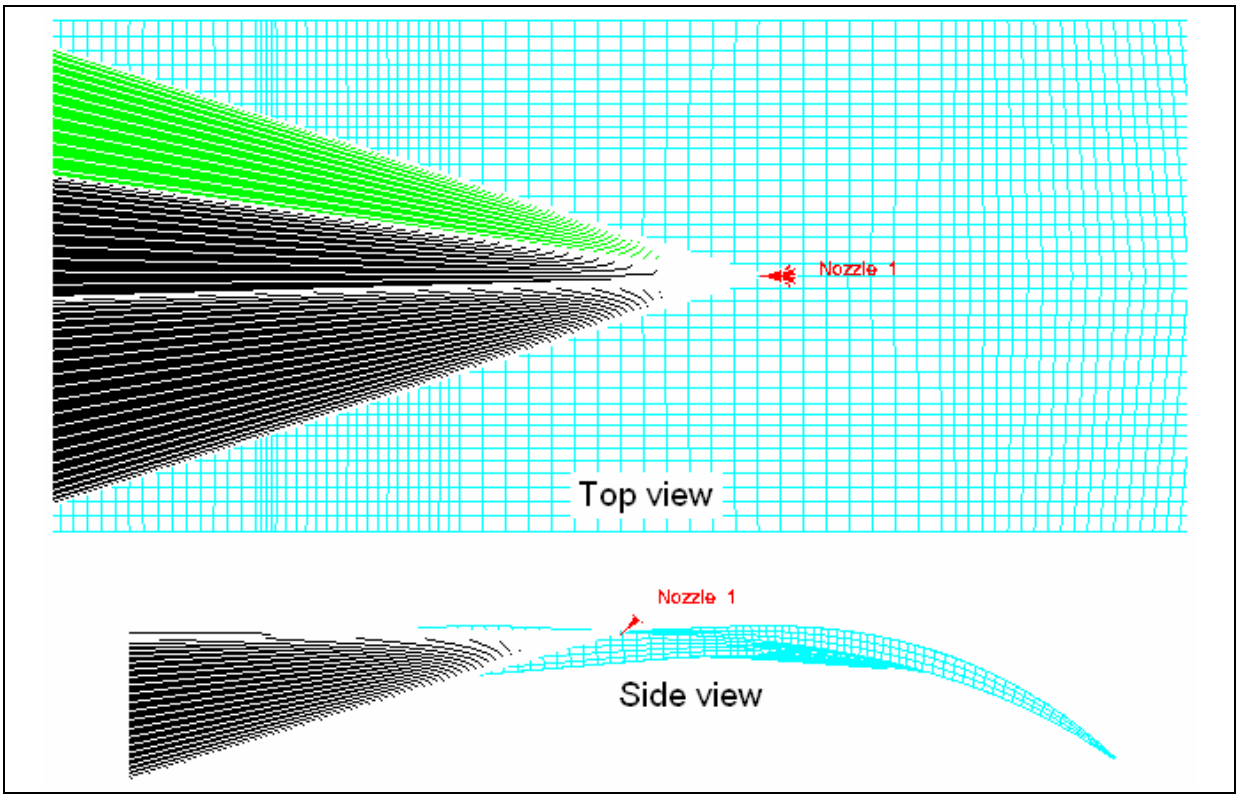

Fig.6. 6 Spray cone at 18º angle between holes and 32º spray angle

The amount of fuel injected was varied between 8µl pre-injection to 50µl main injection. Calculations were carried out at engine speed of 300-rpm, starting engine speed, and 2000-

rpm, with pre-injection and main injection only and with pre-injection and main injection together for layering injection.

6.2.6 Nozzle validation

Before the spray model calculation starts, validation of the diesel nozzle model (available in AVL-Fire) was investigated for the reason of validation and comparison. A spray model was prepared with a single-hole nozzle and runs with different flow rates to atmospheric pressure Pg. The results were presented and compared to [68], visualization results in figure 6.7. The nozzle flow profile agreed well with visualization available results by [68]. AVL GmbH subjected the diesel nozzle model available in AVL-fire to a comprehensive validation tests and compared to experimental test results.

R. Tatschi, [27], has validated this diesel nozzle model and compared his results to the available experimental measured results. His results show very good agreement to between experiment and simulation in both vapor and liquid penetration characteristics.

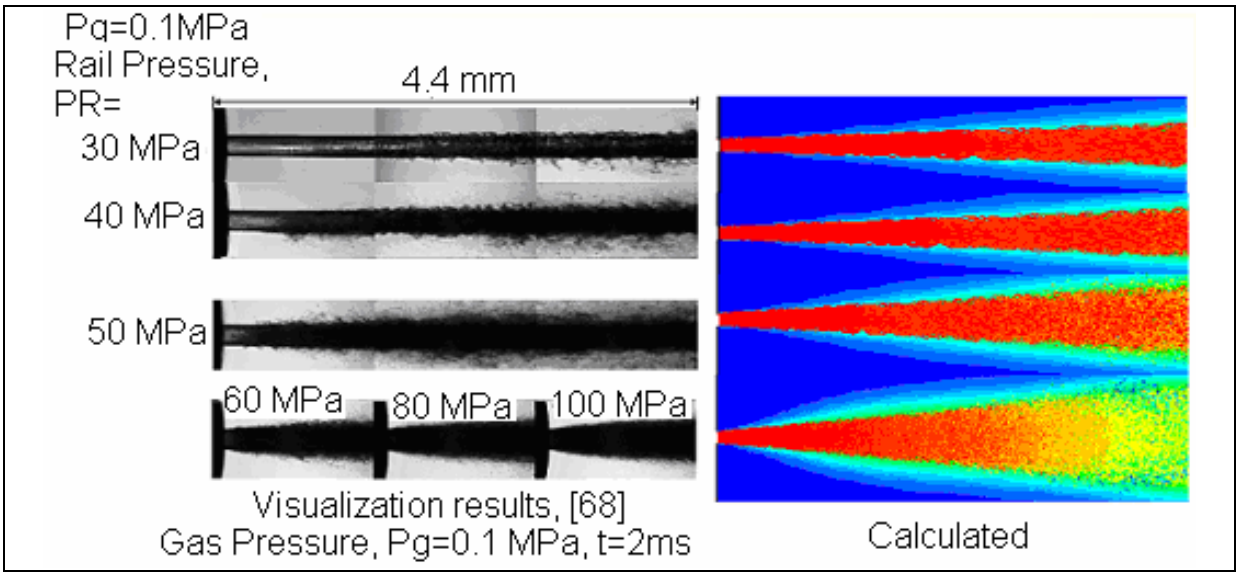

Fig.6. 7 Nozzle flow profile comparison

Figure 6.8 shows the comparison of simulation and experiment results. The spray model was set at temperature of 800 K and chamber density of 25 kg/m^3. All other model parameters of

the spray and injector flow models have been kept constant and the injection pressure varied from 800 bar to 1500 bar.

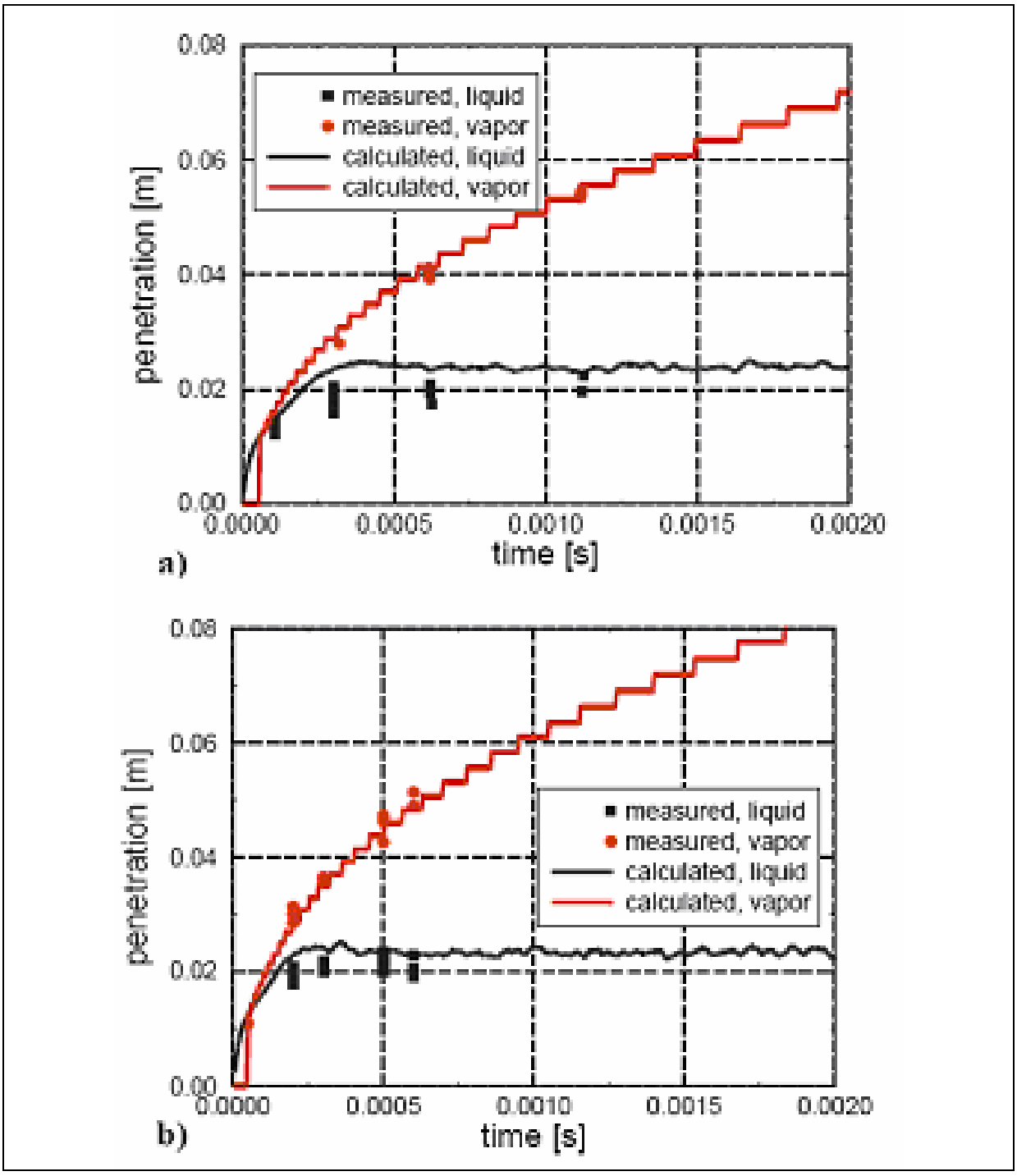

Fig.6. 8 Liquid and fuel vapor penetration evaluation; (a) 800 bar injection pressure, (b), 1500 bar injection pressure. [27].

6.3 Results

6.3.1 Spray angles

The following figures (Fig.6.10, Fig.6.11, Fig.6.12) show the results of different spray angles of 27º, 29º, 32º, for nozzles with angle between holes -13.2º/0º/13.2º, -18º/0º/18º, -25º/0º/25º. The engine speed is adjusted at (2000 rpm), Re = 53733.6, R0 = 935.5, and only a pre-injection of 8µl is applied and injected at 29º BTDC in this example results.

Angle between holes below 13º is very small and spray cones will be interfaced together and may act like one bore injector and angle bigger than 25º will inject the fuel directly to the engine walls. Spray angle of less than 27º will spray the fuel directly to the rotor surface and reflected on this surface to the housing and the rotor recess walls and may cause a liquid film on these surfaces difficult to be evaporated when the engine is cold. Higher spray angles more than 35º may be is a good choice but the injector is normally fitted some millimeters behind the housing surface and injection at higher angles may cause a liquid film on the housing surface and reaches the spark plug causing ignition difficulties.

The injection start time for pre and main injection is also investigated and example results are presented in figure 6.13. Figure 6.9, shows the planes cut distance from the nozzle center, and this distance are applied for all next results figures unless otherwise stated.

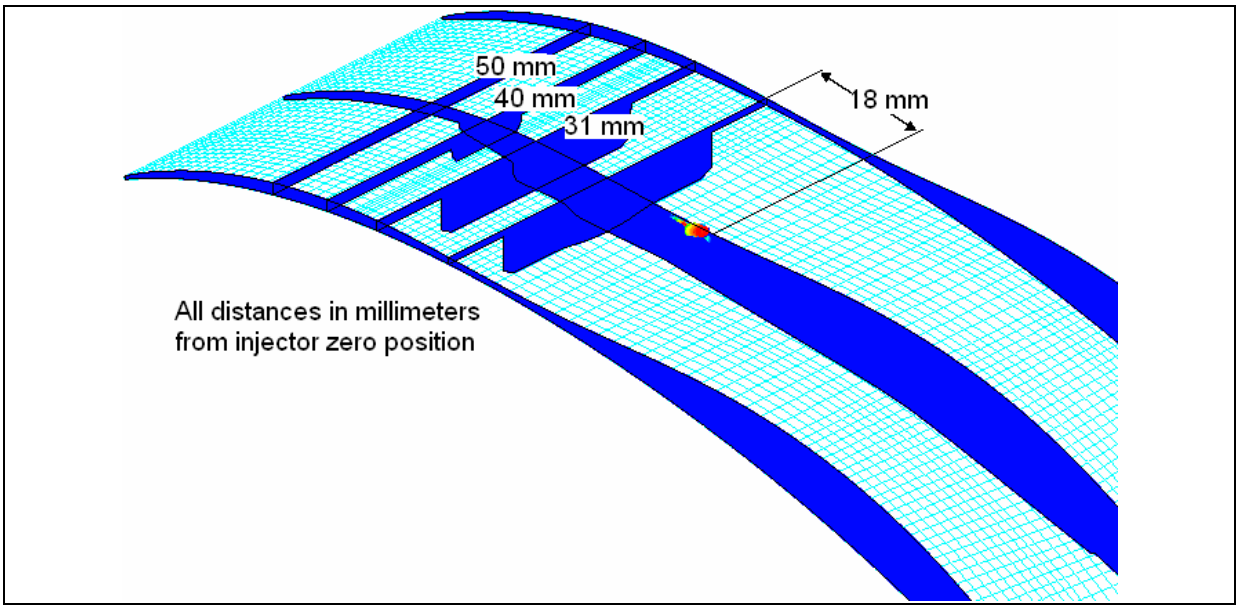

Fig.6. 9 The plane cut distances from nozzle center

Figure 6.10, shows the results of the effect of angle between holes (-13.2º/0º/13.2º, -18º/0º/18º, -25º/0º/25º, on mixture formation at a spray angle of 27º, and constant spray start angle of 29º BTDC.

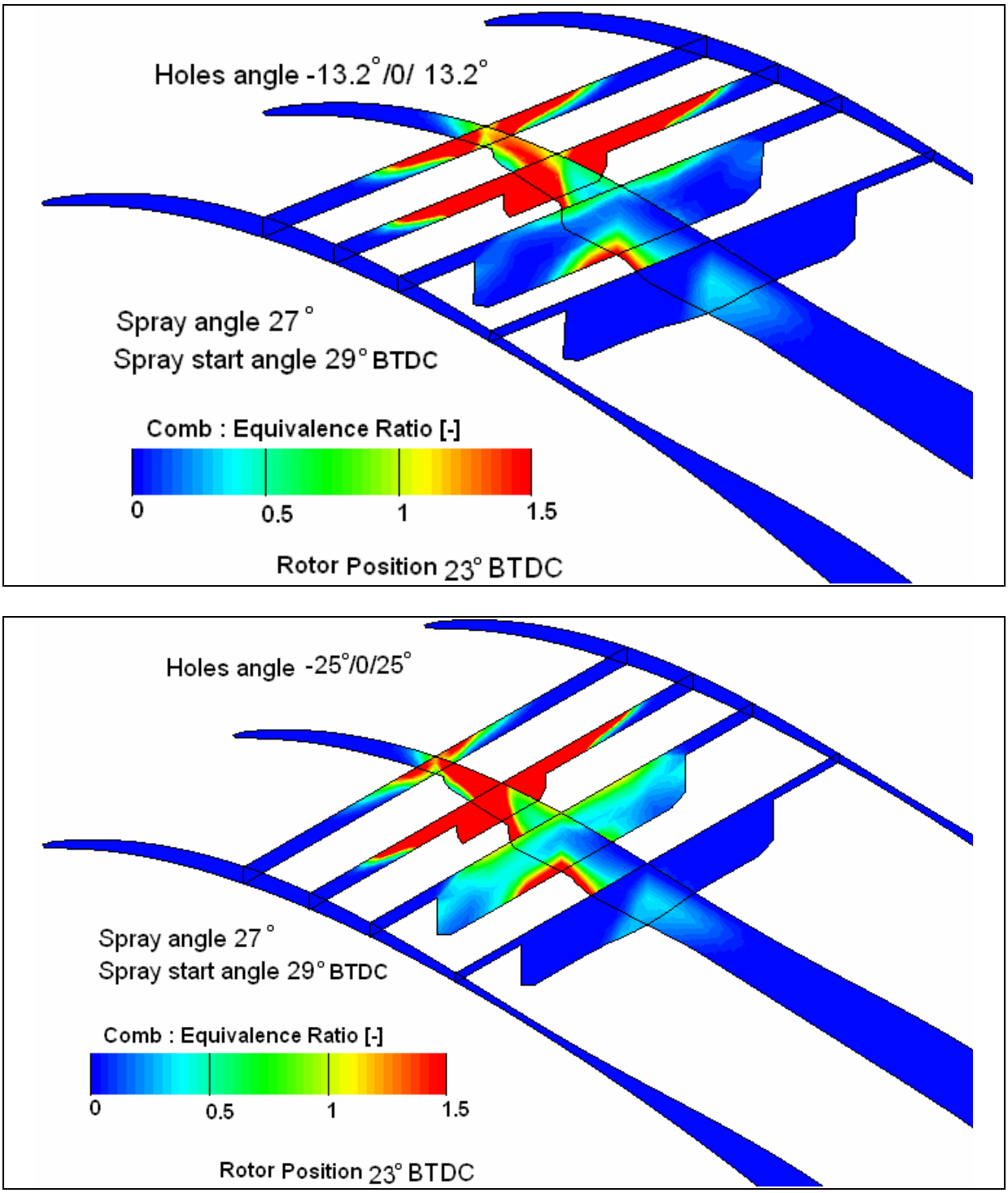

Fig.6. 10 Mixture equivalent ratio [-], spray angle 27º

Figure 6.11, shows the results of the effect of angle between holes (-13.2º/0º/13.2º, -18º/0º/18º, -25º/0º/25º), on mixture formation at a spray angle of 29º, and constant spray start angle of 29º BTDC.

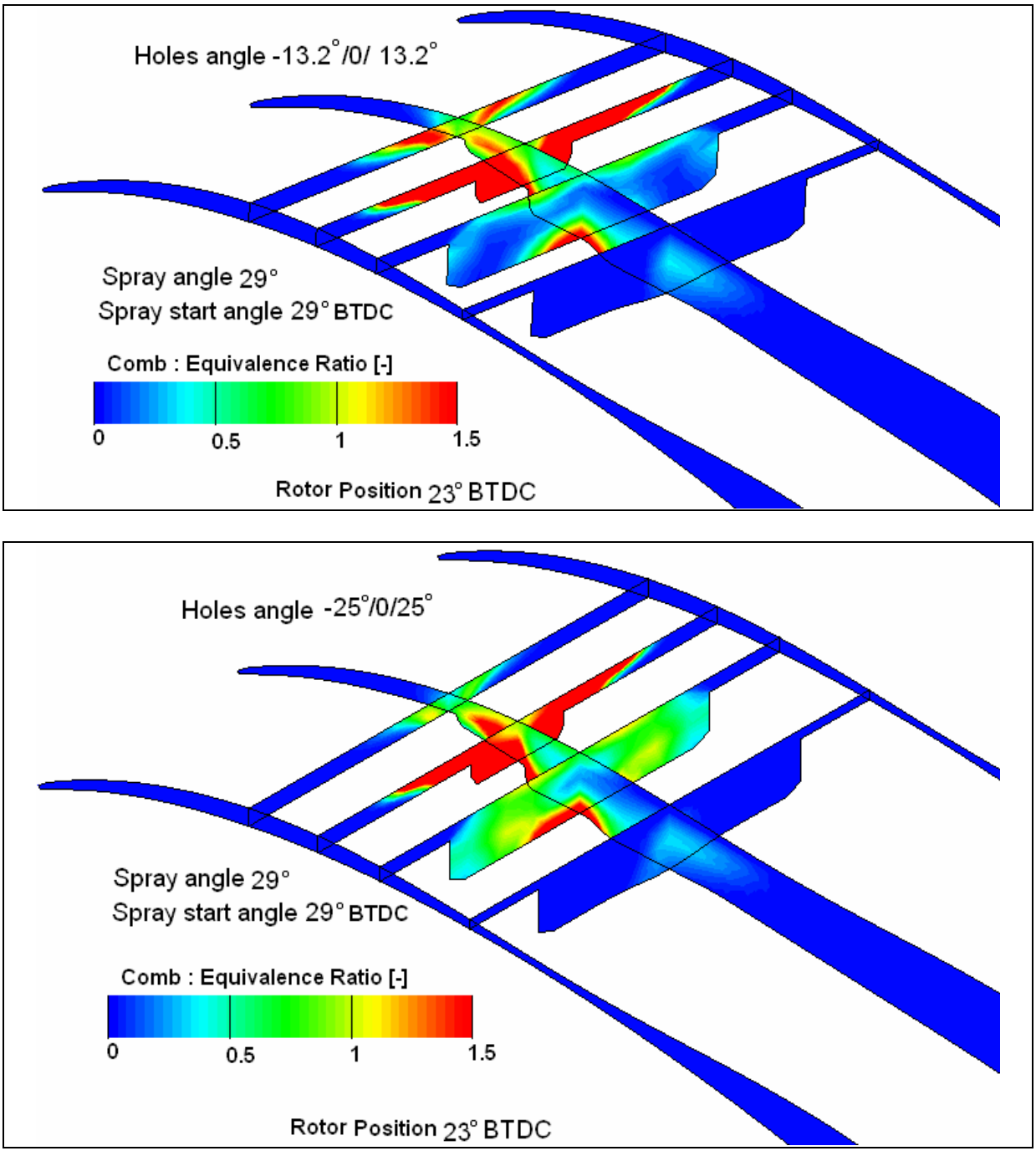

Fig.6. 11 Mixture equivalent ratio [-], spray angle 29º

Figure 6.12, shows the results of the effect of angle between holes (-13.2º/0º/13.2º, -18º/0º/18º, -25º/0º/25º), on mixture formation at a spray angle of 32º, and constant spray start angle of 29º BTDC.

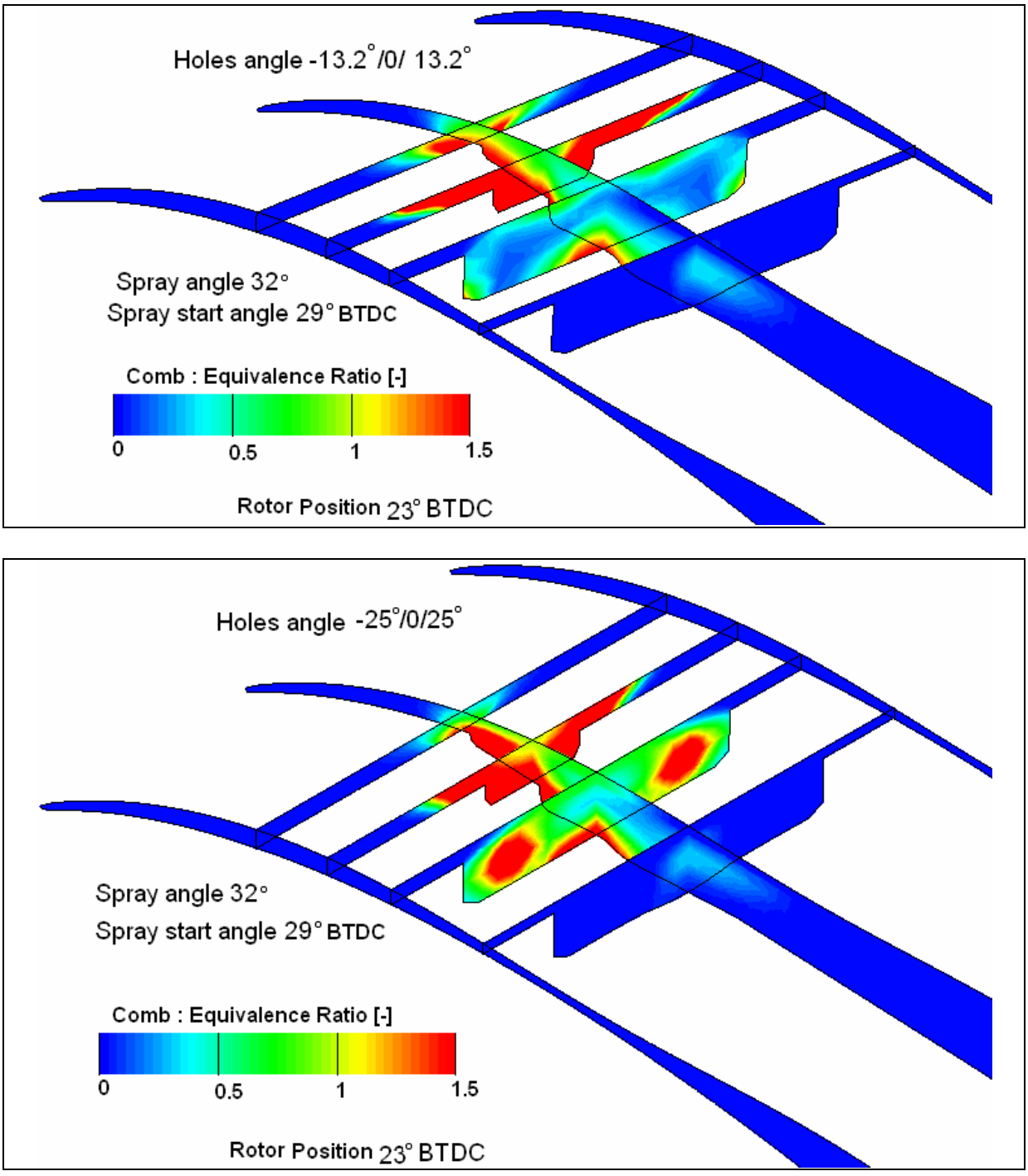

Fig.6. 12 Mixture equivalent ratio [-], spray angle 32º

Figure 6.13, shows the results of the effect of spray angle, (27º, 32º) on mixture formation using a nozzle of, -16º/0º/16º, angle between holes and fixed spray start angle of 29º BTDC.

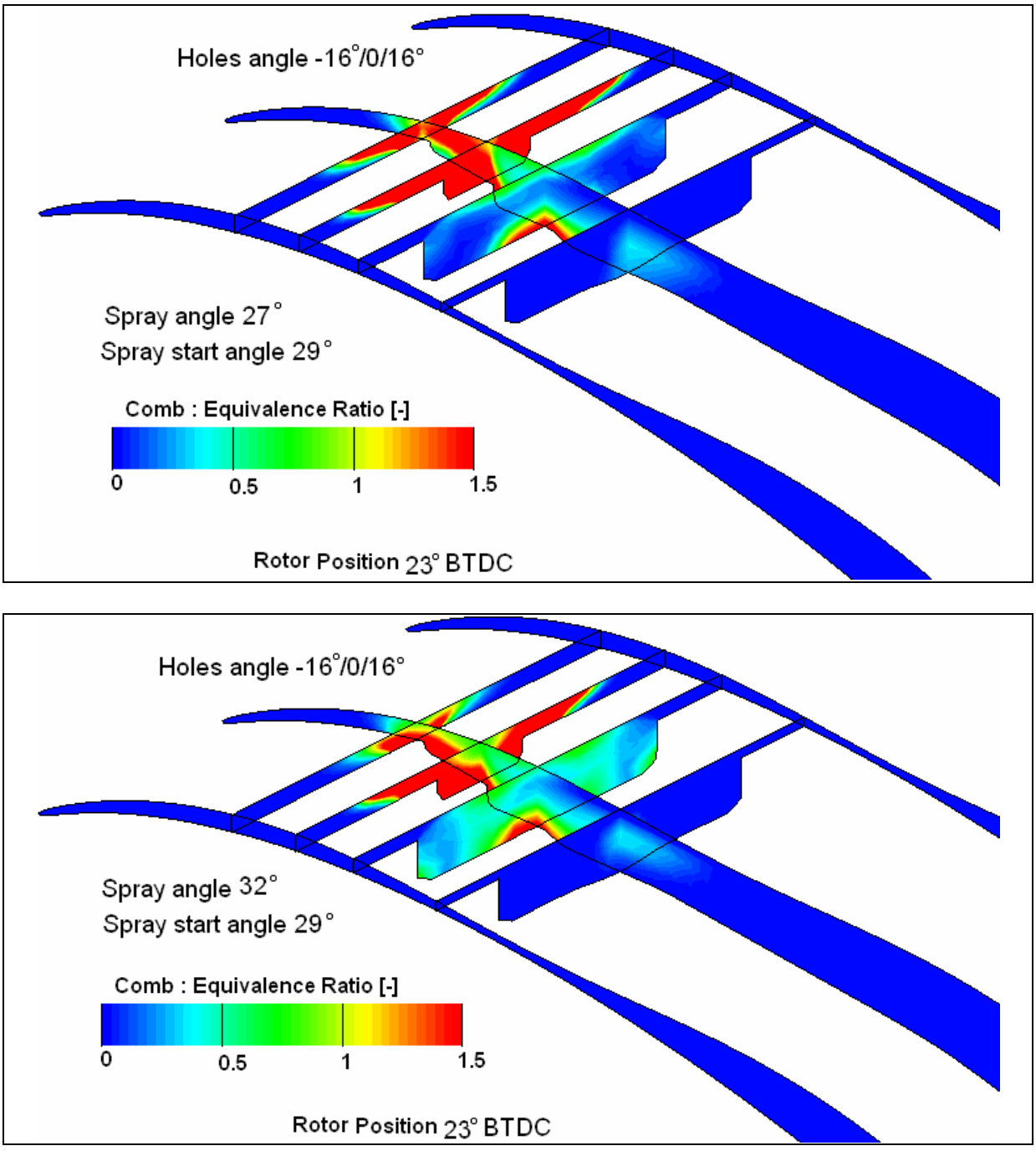

Fig.6. 13 Mixture equivalent ratio [-], for different spray angles 27º, 32º, Angle between holes, -16º/0º/16º

6.3.2 Spray starting angle

Spray starting time is important for mixture formation prior to ignition and hence determines the ignition timing. Early pre injection as early as 39º BTDC, of 8mm^3 is presented in (Fig.6.16), and as late as 20º BTDC is presented in (Fig.6.14). The results show that it is difficult for the early pre-injected charge to be ignited when reaches the ignition time (normally 10º-20º BTDC), because the charge is very lean at the spark plug.

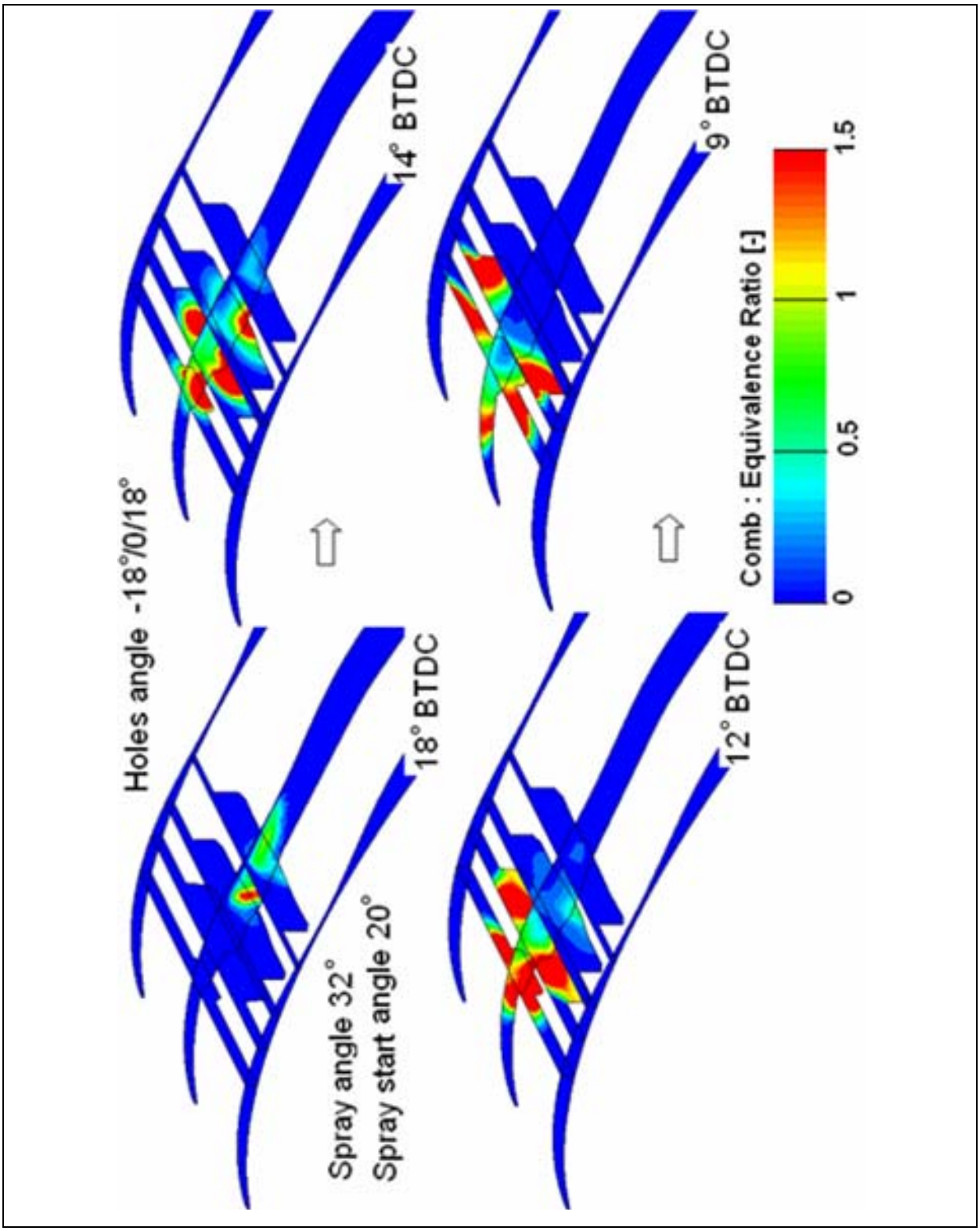

Fig.6. 14 Equivalence ratio, spray starts 20º BTDC

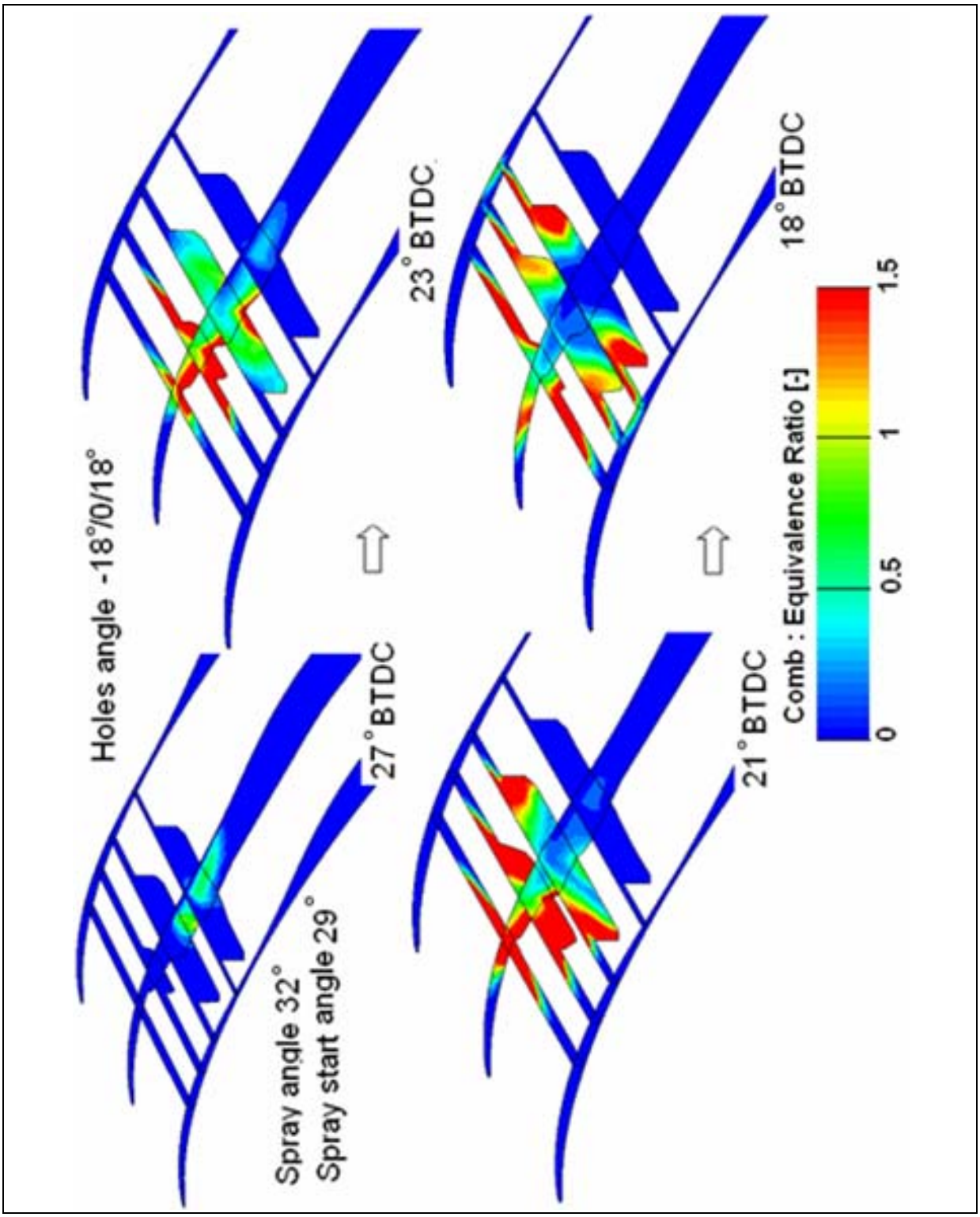

Fig.6. 15 Equivalence ratio, spray starts 29° BTDC

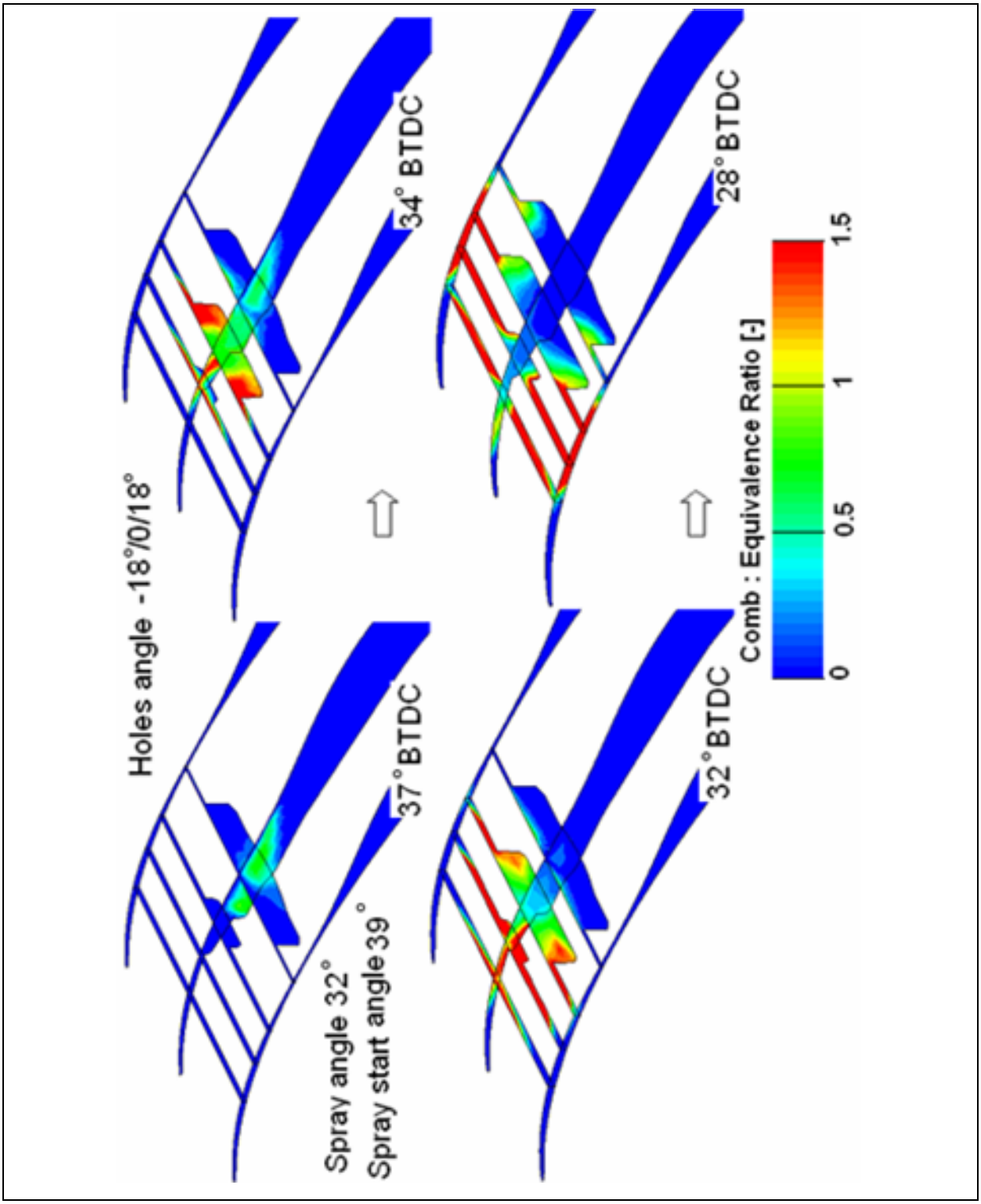

Fig.6. 16 Equivalence ratio, spray starts 39º BTDC

6.3.3 Engine speed

All the above results examples are carried out at constant speed of 2000-rpm. In this results example, the engine speed was fixed to be (300 rpm), Re = 8060, R_0 = 935.5, (2000 rpm), Re = 53733.6, R_0 = 935.5 and (4000 rpm), Re = 107467, R_0 = 935.5. The (300 rpm), Re = 8060, R_0 = 935.5 is the engine speed during startup, and (2000 rpm), Re = 53733.6, R_0 = 935.5 and (4000 rpm), Re = 107467, R_0 = 935.5 is the engine running speed. The effect of engine speed on mixture concentration through the engine combustion chamber was compared and its effect on mixture ignitability at the spark plug. Three holes injector with angle between holes of, -18, 0, 18, are selected for this results comparison, and injector spray angle was 32º. The amount of fuel injected is 8 mm^3, as pre-injection and spray started at 29º BTDC. Figures (Fig.6.18, 6.19, 6.20) show the mixture equivalence ratio at different engine speed.

Figure 6.17, shows the original spark plug position (position P2, at 31 mm from injector center), and the suggested position, P1 at 18 mm from the injector center. The injector is positioned at the center of housing short axis.

The results show ignition difficulty at the new suggested spark plug position (P1), especially at high engine speed. The spark plug is to close to the injector and evaporation in this region is normally low, and hence lowers the ignitable mixture concentration at the spark plug.

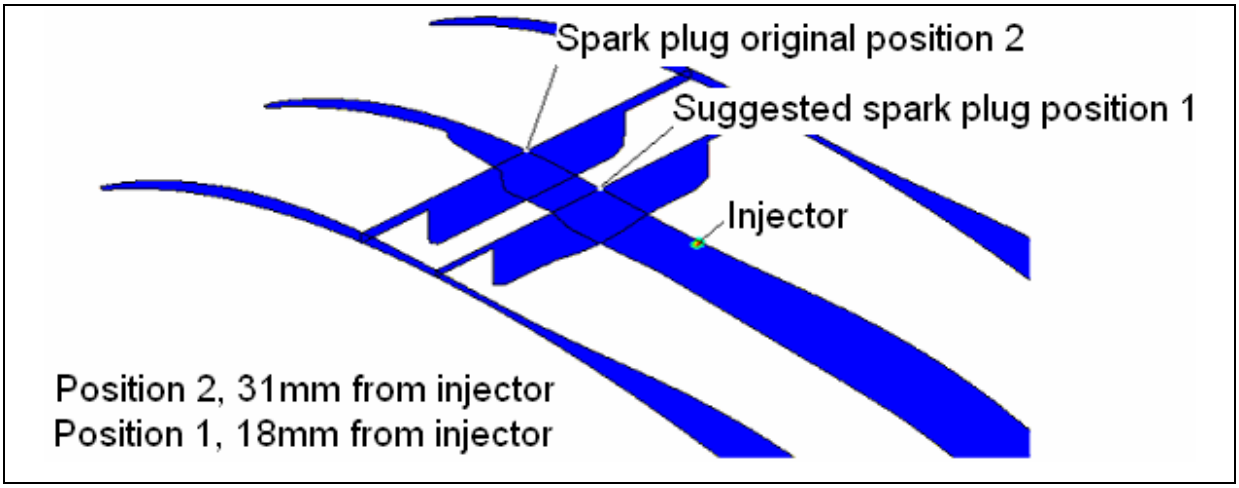

Fig.6. 17 Injector and spark plug positions

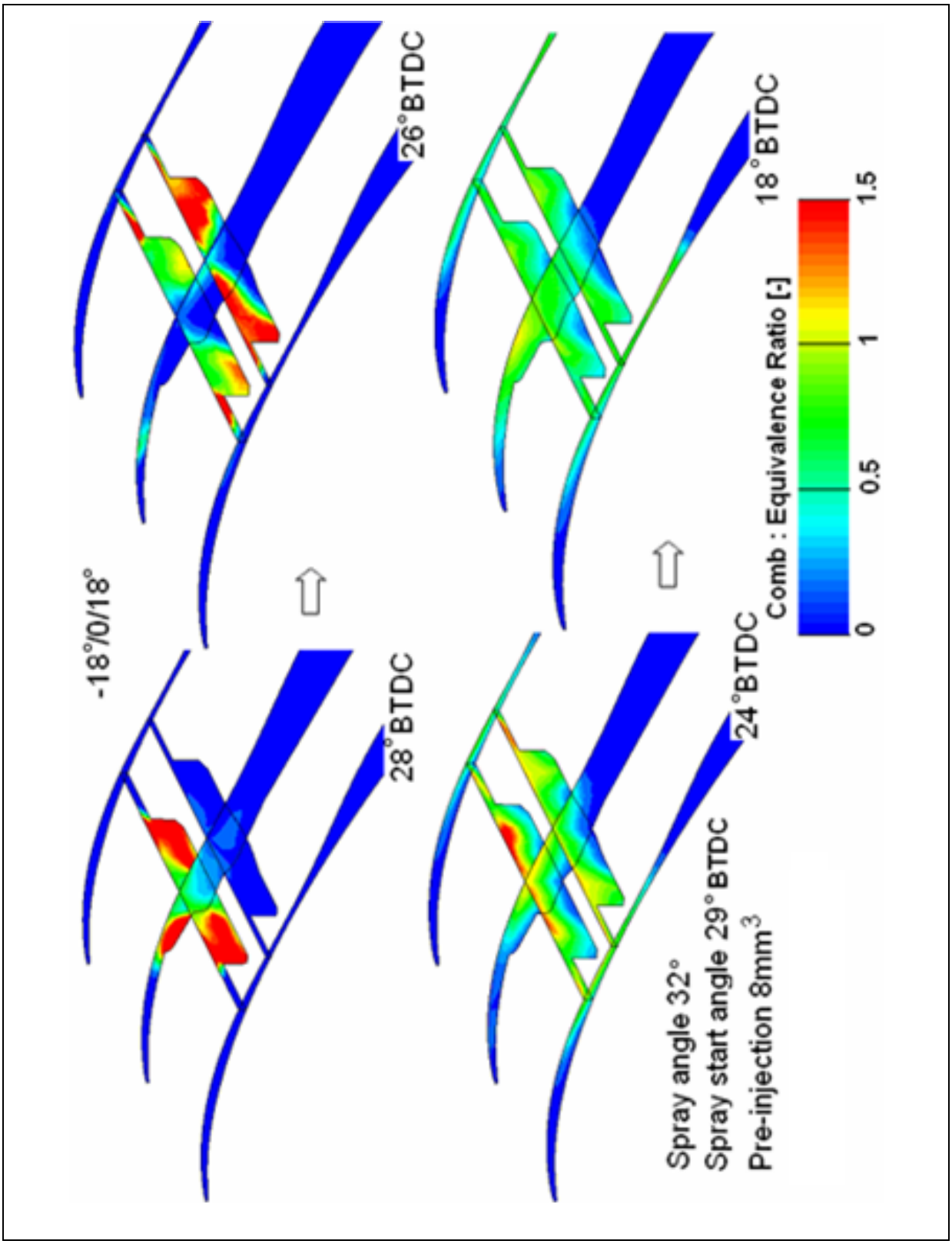

Fig.6. 18 Mixture equivalence ratio at engine speed (300 rpm), Re = 8060, R_0 = 935.5

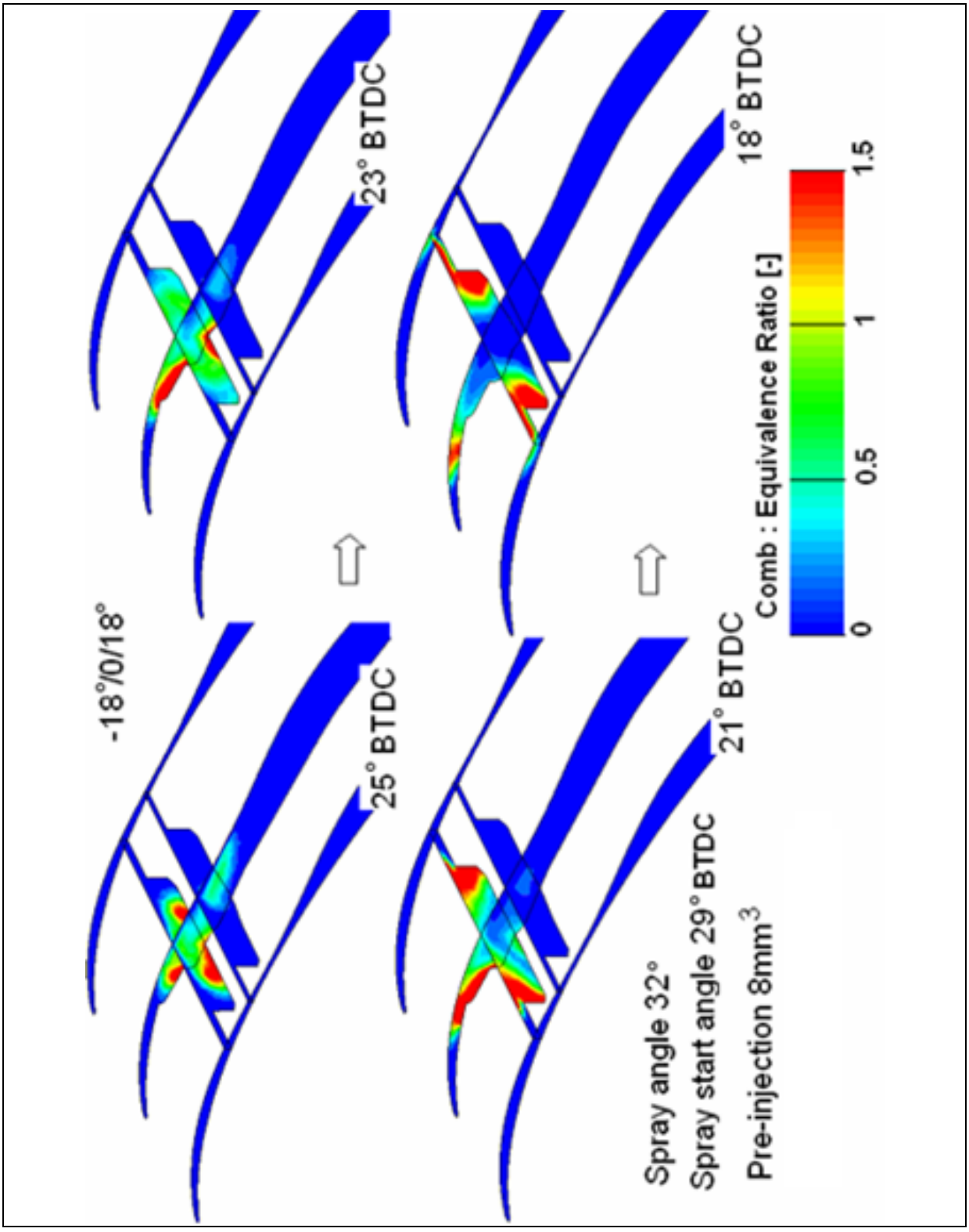

Fig.6. 19 Mixture equivalence ratio at engine speed (2000 rpm), Re = 53733.6, R_0 = 935.5

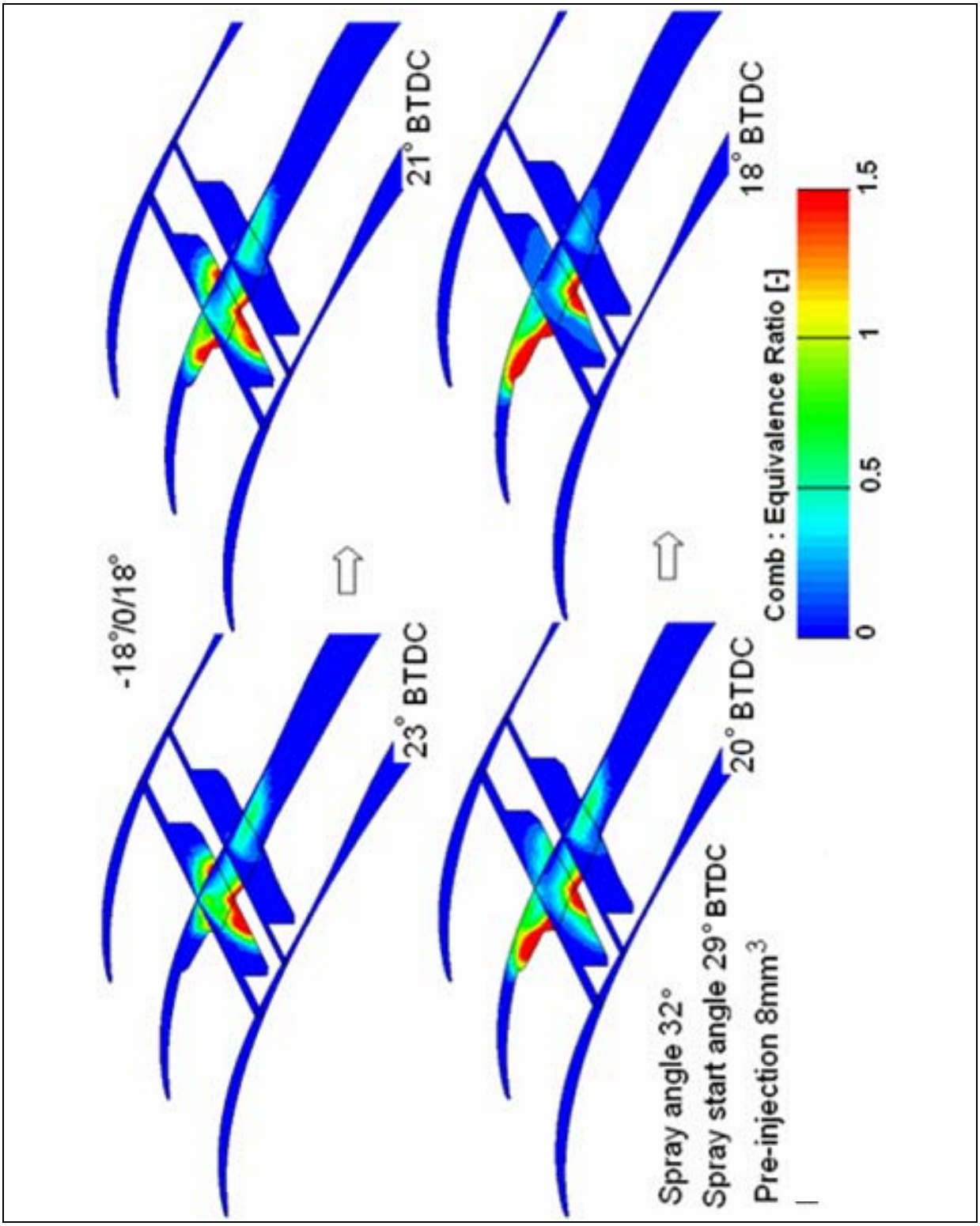

Fig.6. 20 Mixture equivalence ratio at engine speed (4000 rpm), *Re* = 107467, R_0=935.5

This figure shows the effect of engine speed on mixture concentration at the spark plug position plans. It can be seen that the mixture concentration on spark plug planes is shortly become very low at higher engine speed.

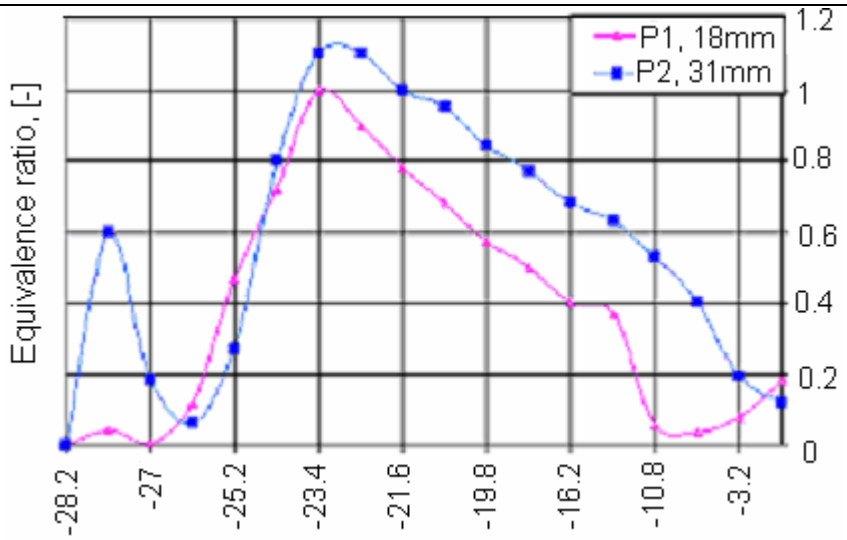

Rotation angle, deg. BTDC, (300 rpm), *Re* = 8060, R_0 = 935.5

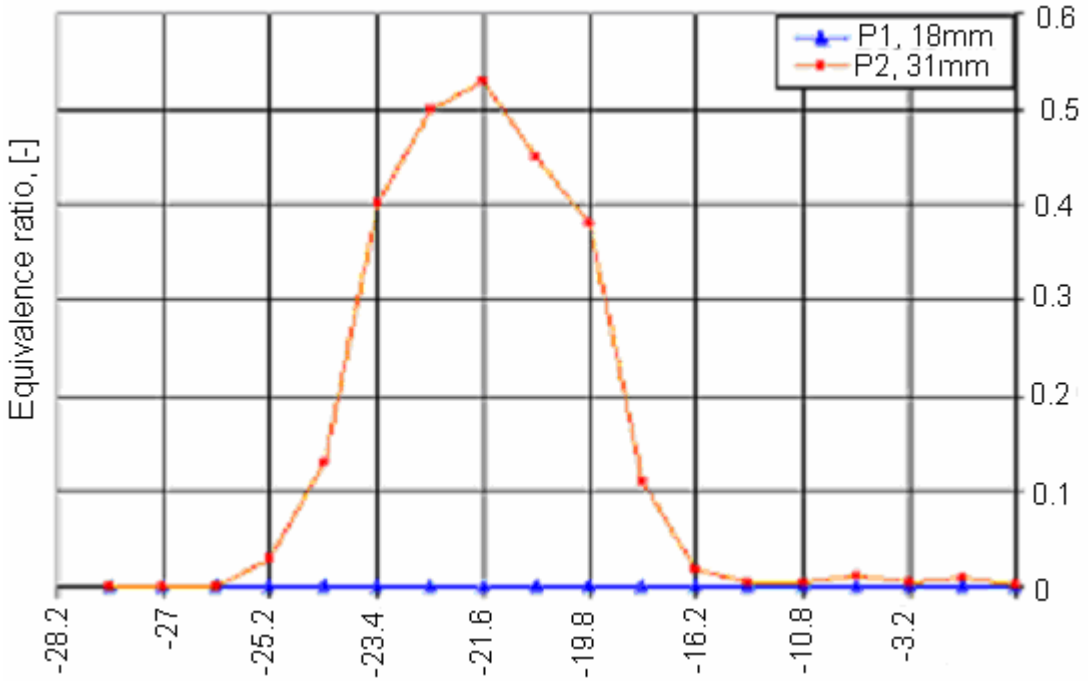

Rotation angle, deg. BTDC, (2000 rpm), *Re* = 53733.6, R_0 = 935.5

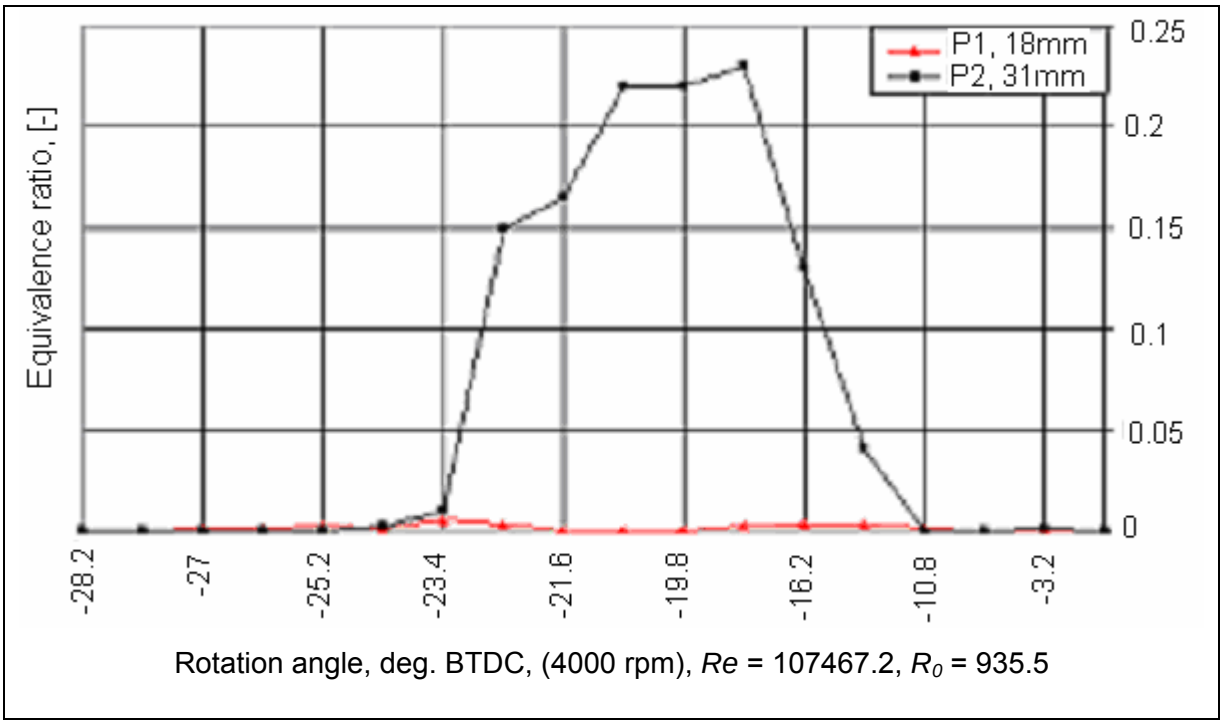

Fig.6. 21 Mixture equivalent ratio, [-], at (P1, and P2), for different engine speed

Figures (6.22 and 6.23); show the equivalence ratio at the spark plug positions (P1 and P2), for main spray of 50 mm^3 with injector of –18/0/18 angle between holes and 32º spray angle, with injection starts at 32º BTDC.

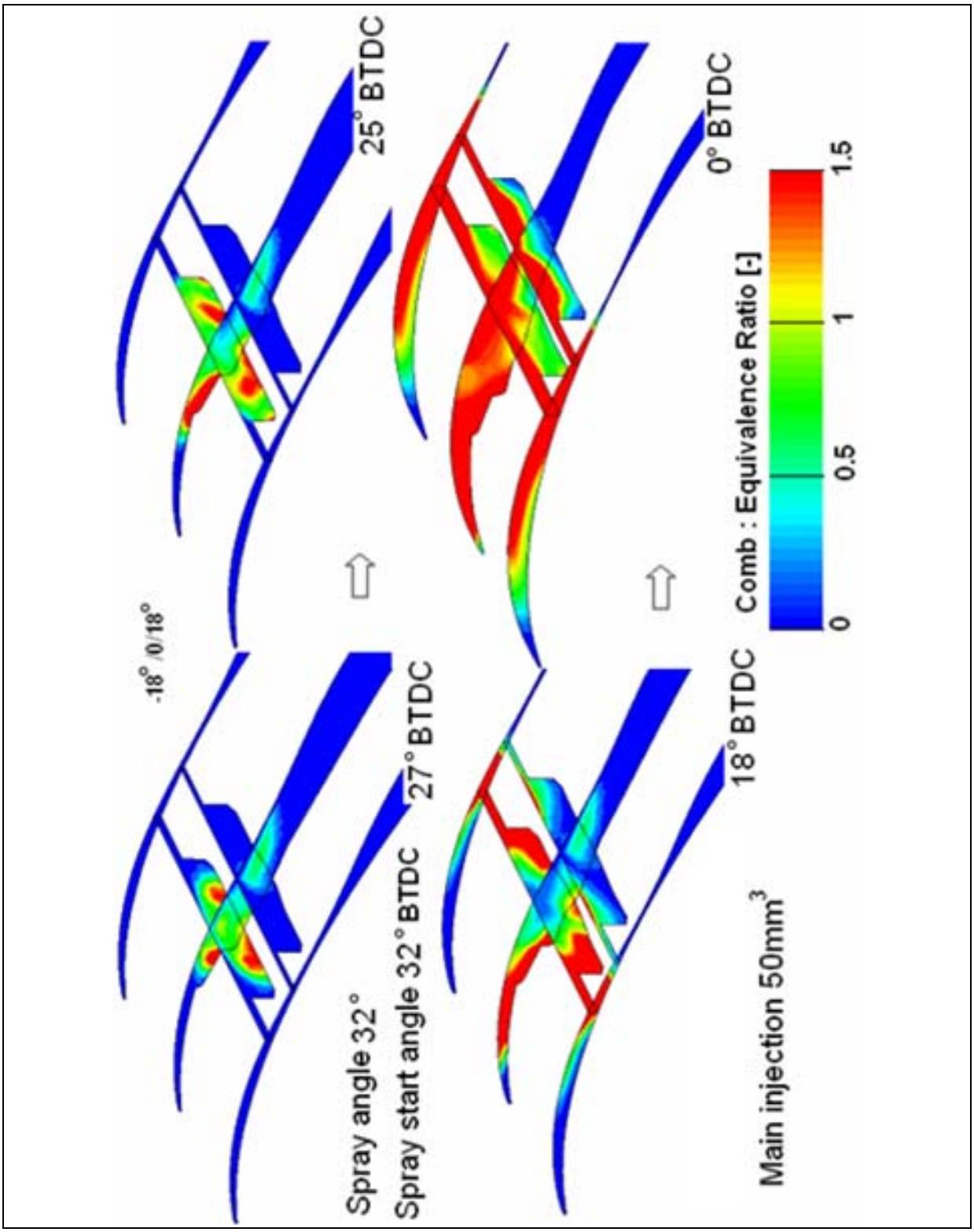

Fig.6. 22 Main spray 50 mm^3, for (2000 rpm), Re = 53733.6, R_0 = 935.5

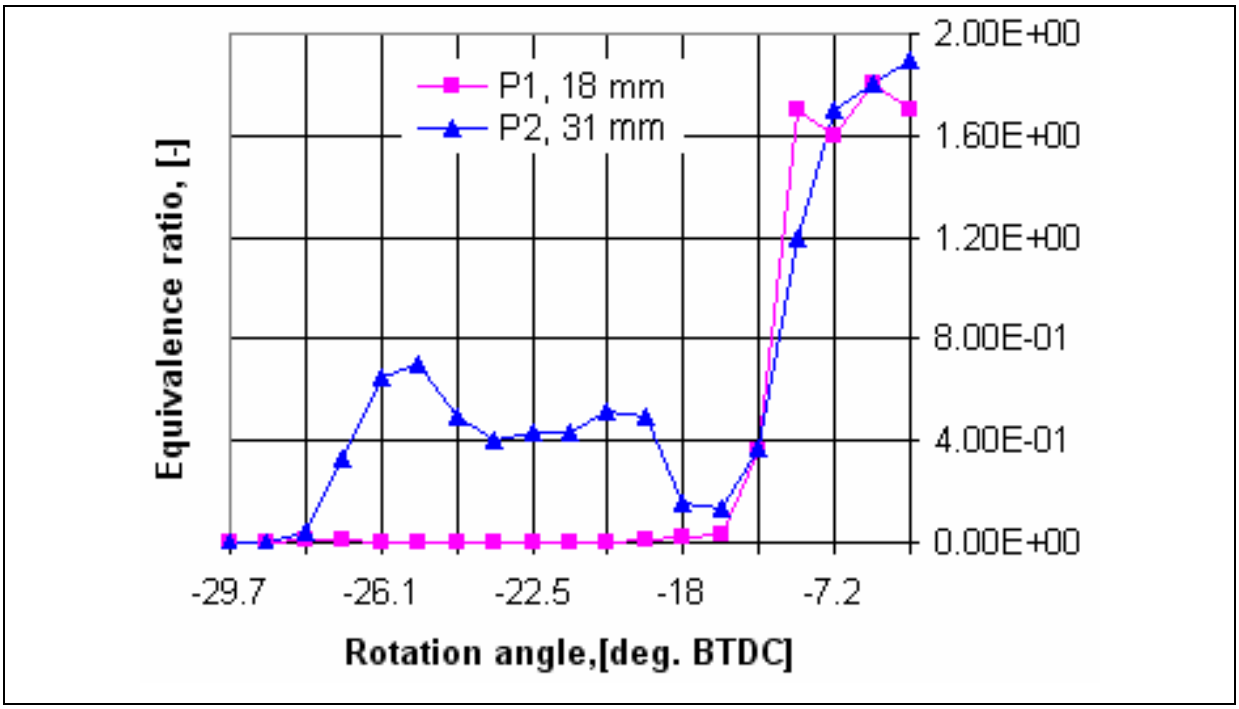

Fig.6. 23 Equivalence ratio [-], main spray 50 mm^3, (2000 rpm), Re = 53733.6, R_0 = 935.5

6.3.3 Injector position

The entire previous engine experimental and modeling tests were carried out with the injector installed at zero distance of short axis and with a spark plug fitted at 18mm or 31mm in front of the injector.

The new position suggested here is similar to that in the KKM-407 engine for comparison. In KKM-407 engine, the injector is fitted 31mm before short axis and the spark plug fitted in zero distance from short axis, as it can be seen on Fig.6.25. Three holes injector with 20º angle between holes, and 30º spray angle is fitted in this engine. The amount of fuel injected is 35mm^3 with spray start angle of 32º BTDC.

In KKM-500 the new injector suggested position is 31mm before the short axis and spark plug tested positions are (0mm, 18mm, 31mm from short axis), that can be seen on Fig.6.27. Three holes injector is used with 18º angle between holes and 32º spray angle. The fuel-injected volume is 50mm^3 with spray start angle of 32º BTDC. All other parameters are kept constant and the engine running rotationof (2000 rpm), Re = 53733.6, R_0 = 935.5.

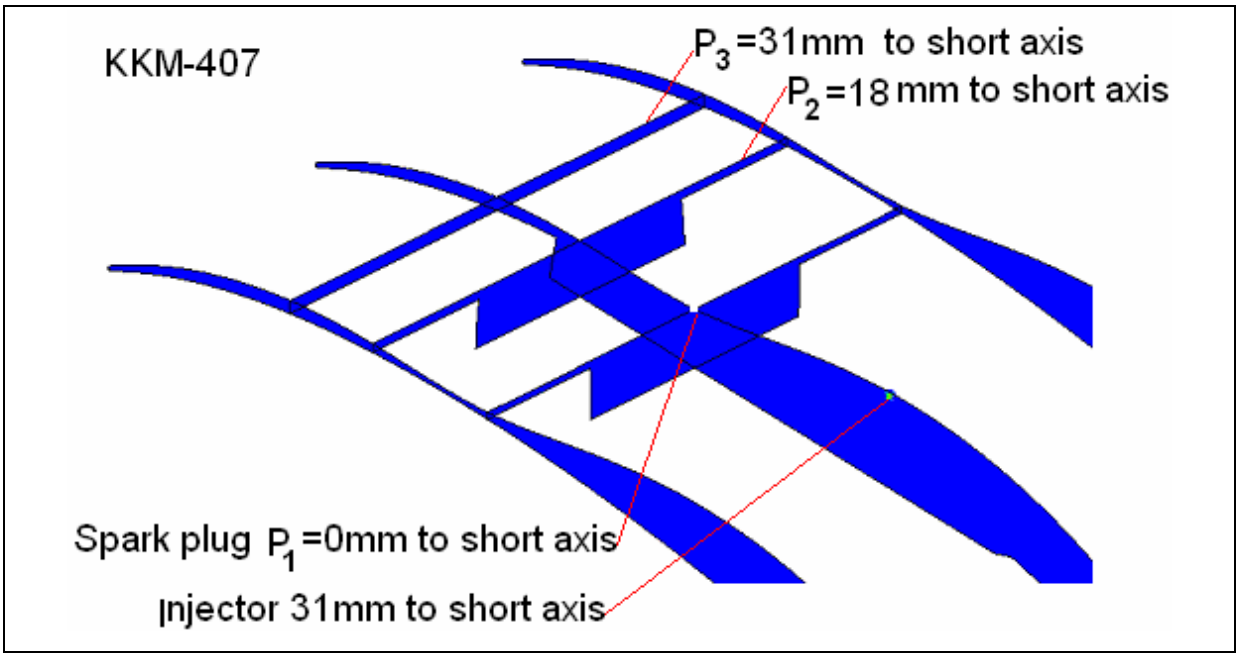

Fig.6. 24 Injector, spark plug position and result planes (KKM-407)

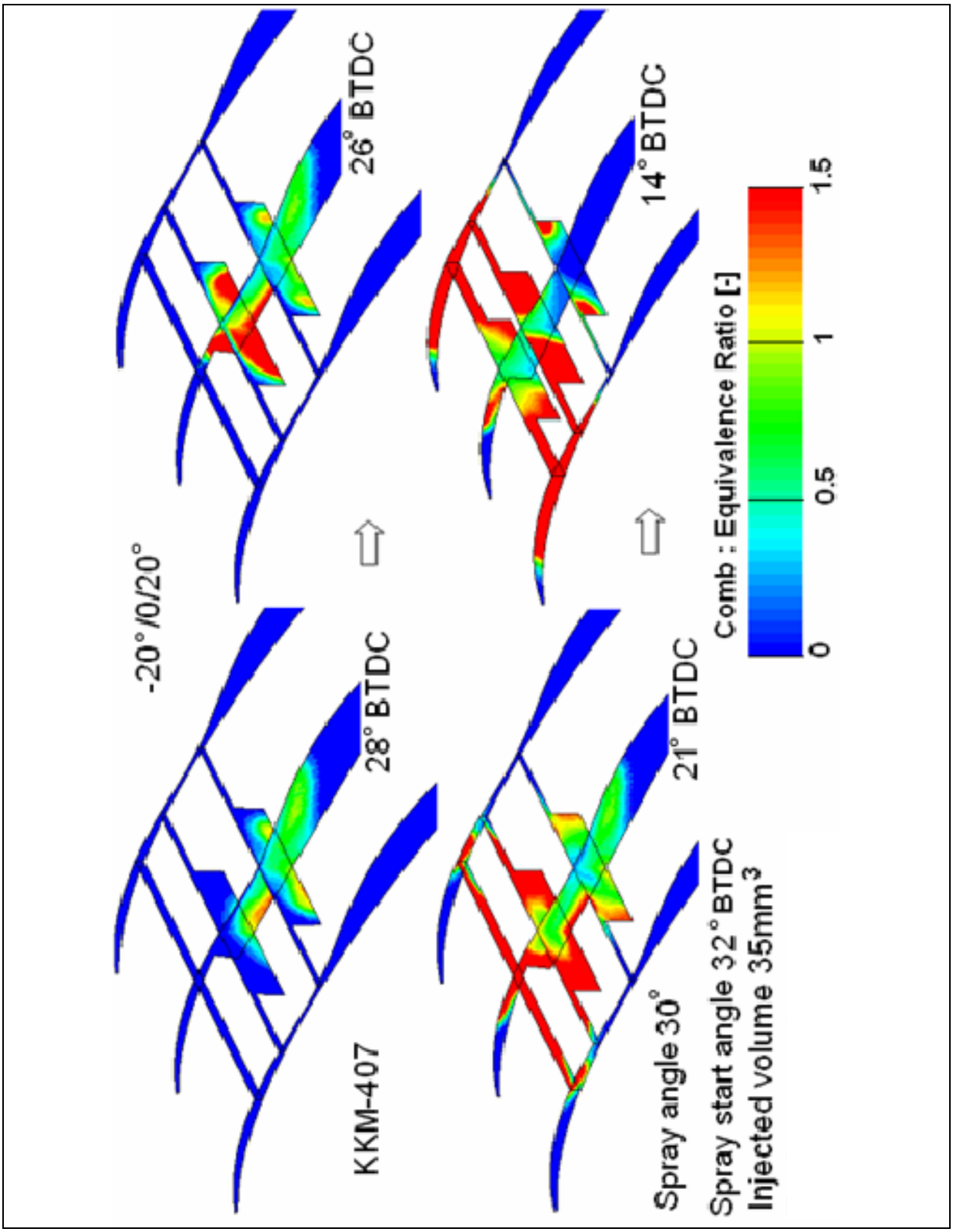

Fig.6. 25 KKM-407 with injector fitted at 31 mm before short axis, spray angle 32°, (2000 rpm), *Re* = 53733.6, R_0 = 935.5

The results of KKM-407 spray settings show that the fuel concentration covers widely most of the combustion chamber in front of the injector and is ignitable after 6º of the spray starting time. The injector installation before short axis gives more fuel penetration distance and hence more air to be mixed with fuel.

Similar effect can be seen on Fig.6.27 of the KKM-500 results and more fuel penetration can be seen on Fig.6.28 when the spray angle changed to 40º.

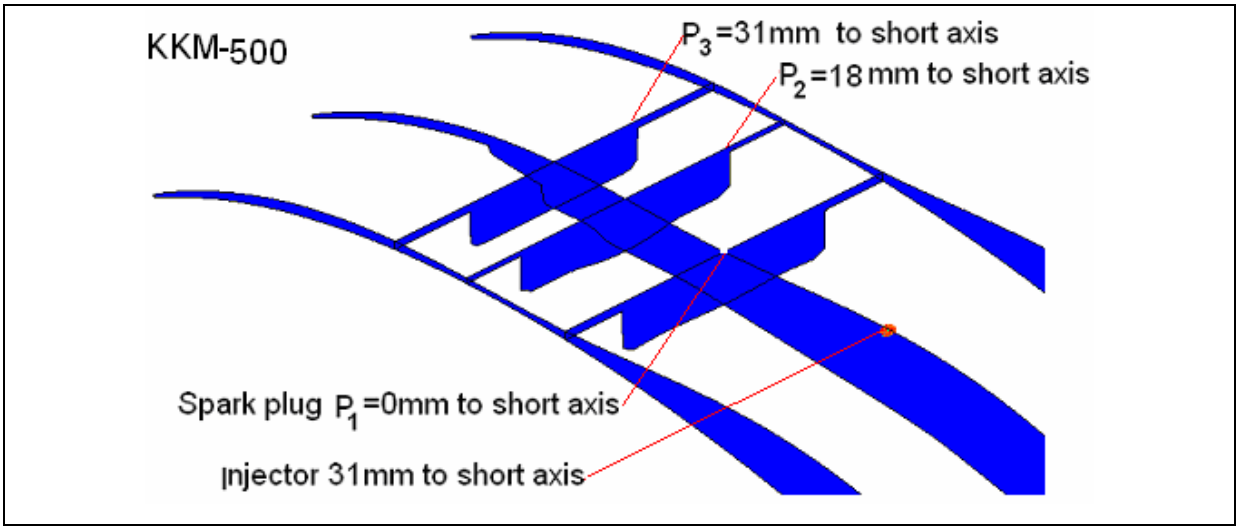

Fig.6. 26 Injector, spark plug position and result planes (KKM-500)

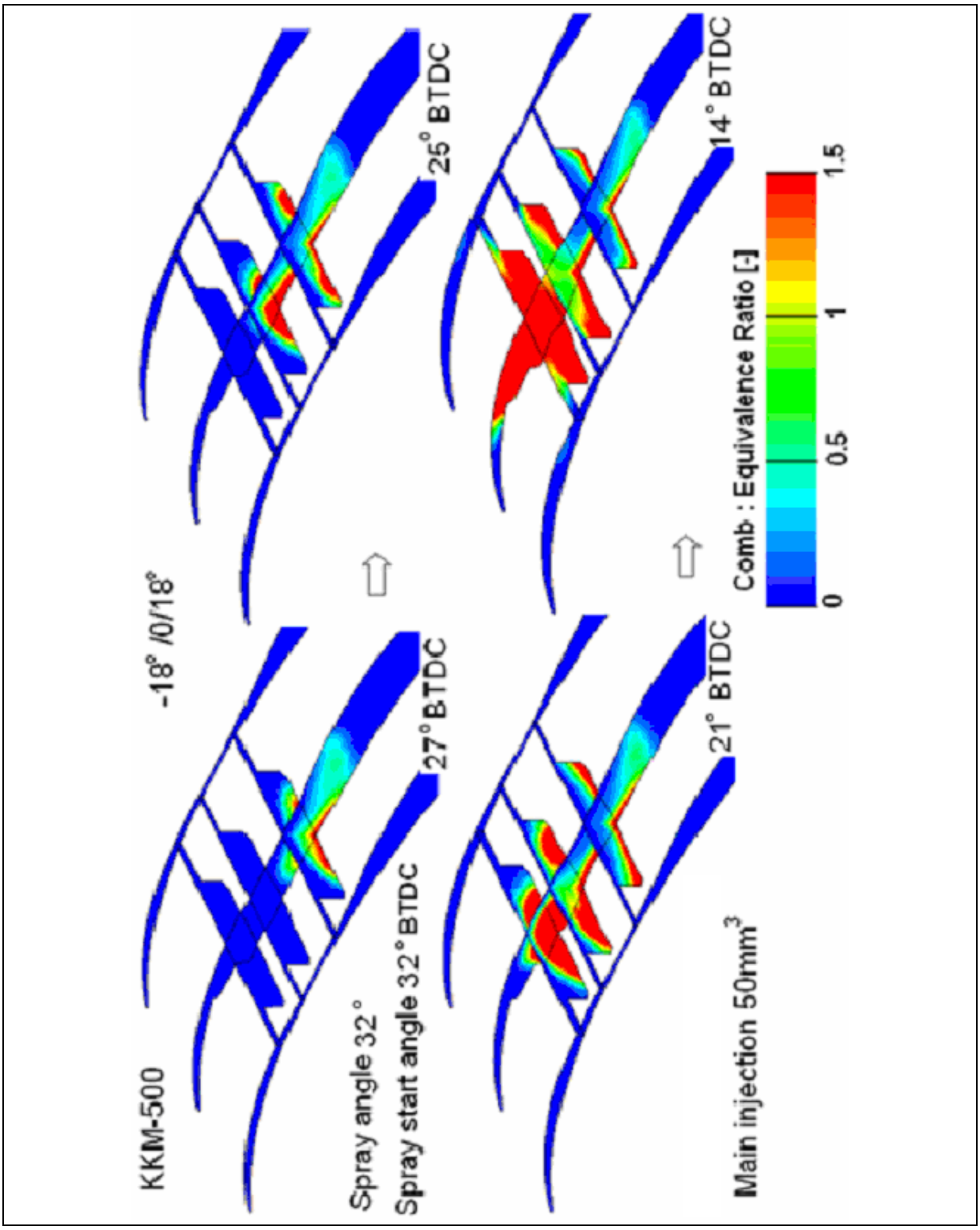

Fig.6. 27 KKM-500, spray angle 32°, 31 mm to short axis, (2000 rpm), Re = 53733.6, R_0 = 935.5

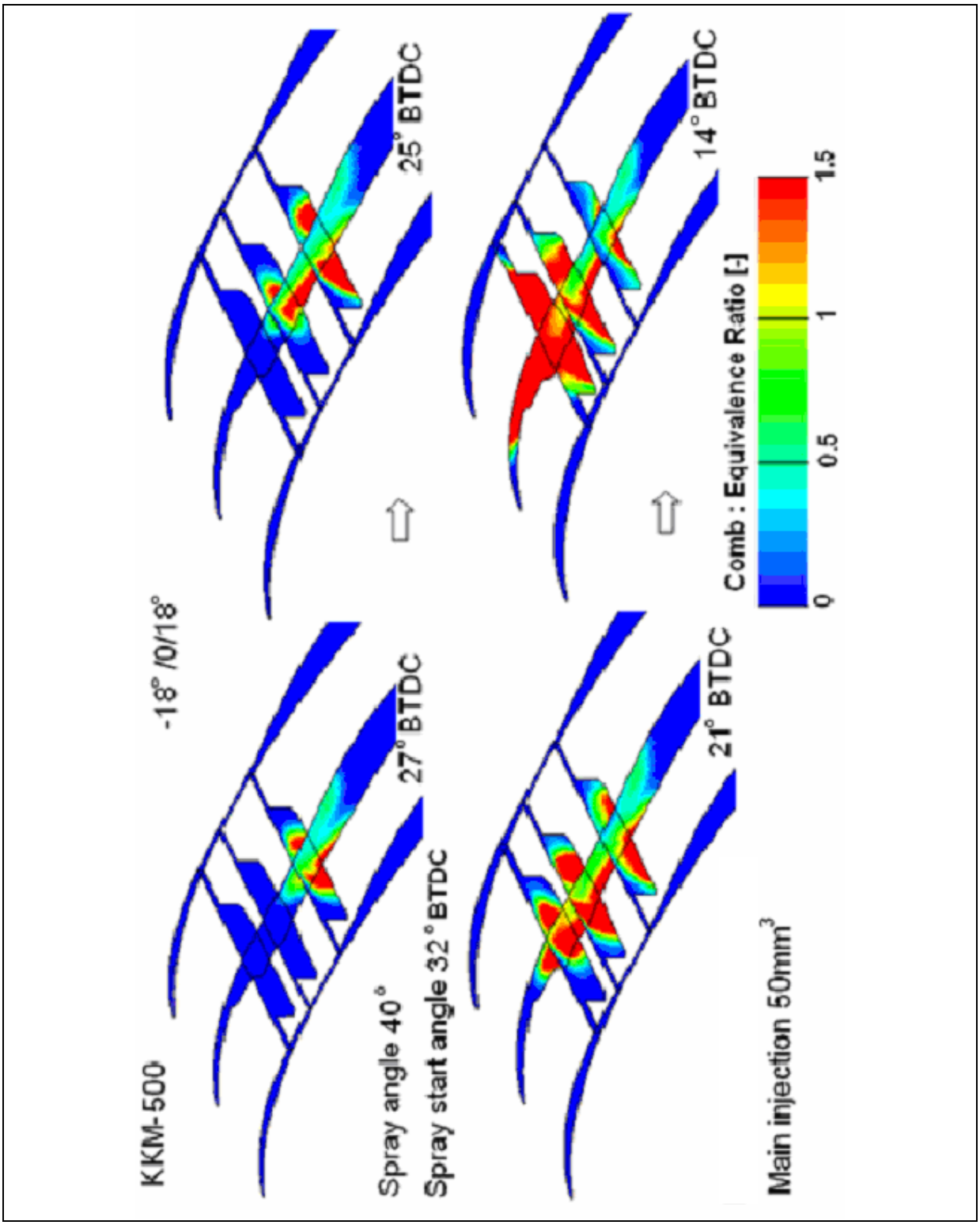

Fig.6. 28 KKM-500 spray angle 40°,31 mm to short axis, (2000 rpm), Re = 53733.6, R_0 = 935.5

6.4 Discussion and summary

In normal diesel engine, only air is compressed to high-pressure levels and at the same time higher temperature. The high temperature inside combustion chamber of diesel engine is enough to self ignite any amount of diesel fuel injected without the need of any spark plug to initiate ignition. The constant pressure process followed by diesel engine, which means that the heat is introduced at constant pressure, has much lower thermal efficiency compared to constant volume process applied for gasoline engine at the same compression ratio. To increase the constant pressure process efficiency, diesel engine is running on much higher compression ratios. Also, varying the injected fuel quantity with out any air throttling controls engine load, and hence the engine can run very lean on idling and partial loads, which increases its thermal efficiency.

However in Wankel engine, compression ratio cannot go higher as much as in normal piston diesel engine (piston diesel engine is typically between 15:1-20:1), producing lower pressure and temperature not enough to self ignite the injected fuel, and hence the use of spark plug is necessary to ignite the charge. So, the diesel fuel concentration at the spark plug should be near stoichiometric to be ignited, (0.6% - 7.5% by volume, vapor).

Pre-mixed mixtures or low-pressure fuel injection in diesel engine is worthless, that means the mixture should be controlled near stoichiometric at all loads and the use of air throttling is necessary, and that will affect the thermal efficiency badly. However, high-pressure diesel spray, few degrees before the end of compression, is the best choice fore diesel Wankel engine. Combustion process then occurred in partially rich zone of combustion chamber and the rest of air supplied during turbulent combustion.

According to this, only high-pressure diesel fuel injection strategy has been investigated and presented in this chapter, to verify and improve the mixture for best nozzle position and spray angles.

The conclusion of this work in this chapter can summarized as follows:

- The distance between the engine rotor and its housing is very narrow, and hence fuel spray to the rotor surface is unavoidable. When the fuel droplets reflect on rotor surface, the rotor rotates and accelerates the droplets forward away from the injector

position. That means, the spark plug should be far enough from the injector to be able to ignite the mixture.

- Injector angle between holes below 13º is too small and the spray cones interfaced and act like one bore nozzle. 18º angle between injector holes show better penetration and cover most of the combustion chamber at spray angle of 32º.
- Early fuel spray (39º BTDC) gives more time for mixture formation, but the fuel concentration at the spark is lowered due to charge forward movement, when ignition time is on, (10º-15º BTDC). 29º BTDC spray start angle gives better results for engine speed less than (4000 RPM), RE = 107467.
- The new suggested spark plug position (18mm from short axis) shows ignition difficulties due to low fuel concentration on this position, as the fuel evaporation rate is low near the nozzle.
- The new suggested injector position (31mm before short axis), shows better results and covers more area of combustion chamber, and shows more fuel penetration at spray angle 40º.

7

Hydrogen Injection for Rotary Engine and Combustion

7.1 Introduction

Hydrogen makes an excellent fuel for combustion engines. The major drawbacks to hydrogen as an engine fuel are the tendency for backfire and pre-ignition.

However, the external mixture preparation by injecting hydrogen into the inlet manifold can produce more homogeneous mixtures, mainly because it has more mixing time during intake and compression periods. Homogeneous mixtures can be burned more efficiently and complete fuel combustion can be reached. Unfortunately, that on the penalty of about 20% less power output of hydrogen engine in comparison with similar size or when the same engine is running on gasoline. That is clearly because of about 30% of the engine cylinder space will be displaced by hydrogen and only 70% left for air, which means that the engine volumetric efficiency are dramatically reduced.

Direct injection of the hydrogen into the engine cylinder overcomes most of these problems, and to avoid this reduction in the engine volumetric efficiency and hence the overall engine power output, the hydrogen direct injection were introduced. The hydrogen is injected directly into the engine cylinder after all valves or ports are closed and the cylinder is only displaced by air, this technique can add about 35% higher power output than the external mixture formation.

The low pressure direct injection, where the hydrogen fuel is injected at low cylinder pressure during early stage of compression stroke and after the valves closed, gives some time for homogeneous mixture and hence better combustion. The hydrogen injection pressure is normally not high and is about (3-6 Bar). Direct injection during intake stroke may gives more time for mixture formation, but it will reduce the engine volumetric efficiency similar

to the external mixture preparation. P.A. Salanki, et. al, [66], have reported more than 20% less power output when they injected directly hydrogen during intake of a Wankel engine in comparison of the same engine running on gasoline. In their experimental work they proved that the Wankel engine is running smoothly up to full load (Φ=1), and no sign of any backfire or pre-ignition, even they are injecting hydrogen during intake port is still open.

In High-pressure direct injection, the hydrogen fuel is injected at high cylinder pressure, near TDC, or few degrees before TDC and then ignited directly after injection to be burned in locally rich zones, because there is no time form a homogeneous mixture.

In this method, the hydrogen should be injected in a very high pressure, up 40-50 bar, and even more pressure is needed to inject the great volume of hydrogen in very short time, (0.001-0.002 s). The high-pressure injector, is still under development by several companies to handle such high pressure and still not widely available in domestic market.

In this chapter it will be concentrated on the direct hydrogen injection mixture formation rather than external mixtures.

7.2 General hydrogen injection research

In cylinder mixing phenomena are complicated and require a good knowledge of injection characteristics and injection behavior. However, injecting a huge volume of hydrogen (about 29% by volume at stoichiometric), into the engine cylinder in very limited time, makes the injection pressure and velocity to be very high (up to mach II).

The supersonic flow of hydrogen and the intensive gradient changes of characteristic parameters, (pressure, temperature, density, velocity, etc.), makes the simulation of hydrogen injection somehow difficult and most of CFD-codes not capable or stable of handling such supersonic flow calculations.

The AVL-Fire code with its both versions (v8.31 and v7.3) have been proved its capability and stability for supersonic hydrogen injection, by Fushui Liu [1]. However, some conditions have been studied and recommended by Liu, when a volume grid (mesh) is prepared for hydrogen injection and should be followed in order to get reliable results.

The author of this thesis was a part of that work conducted by Liu, and a lot of experience in hydrogen injection grid preparation has gained.

7.2.1 Volume grid validation

For the purpose of mesh optimization and model validation, a simple models were built to prove the CFD-Code capability of capturing the supersonic high velocity and pressure shock, and compared to the experiment shock image capture using schlieren technique.

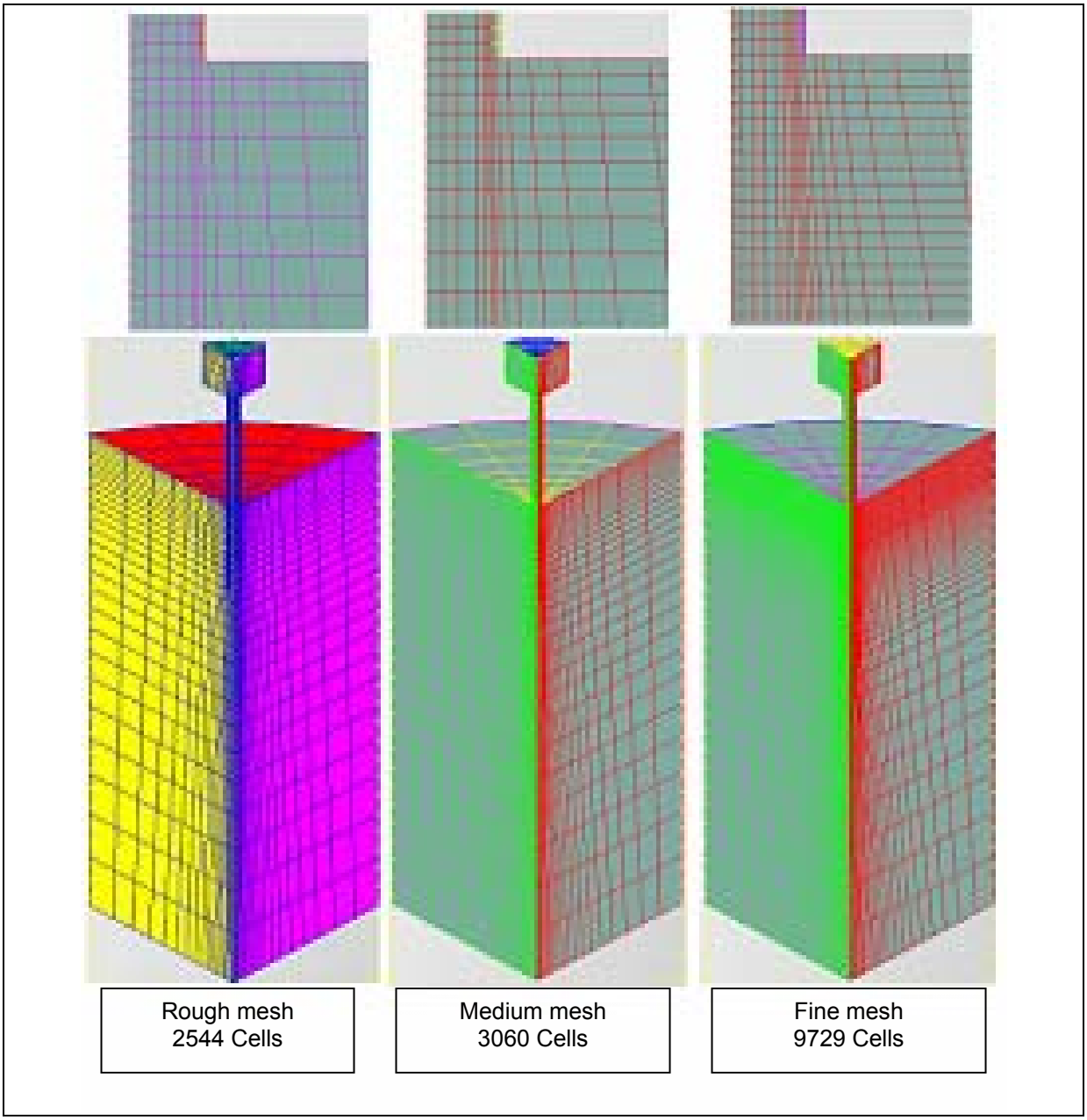

Fig.7. 1 Three validation meshes with different smoothness

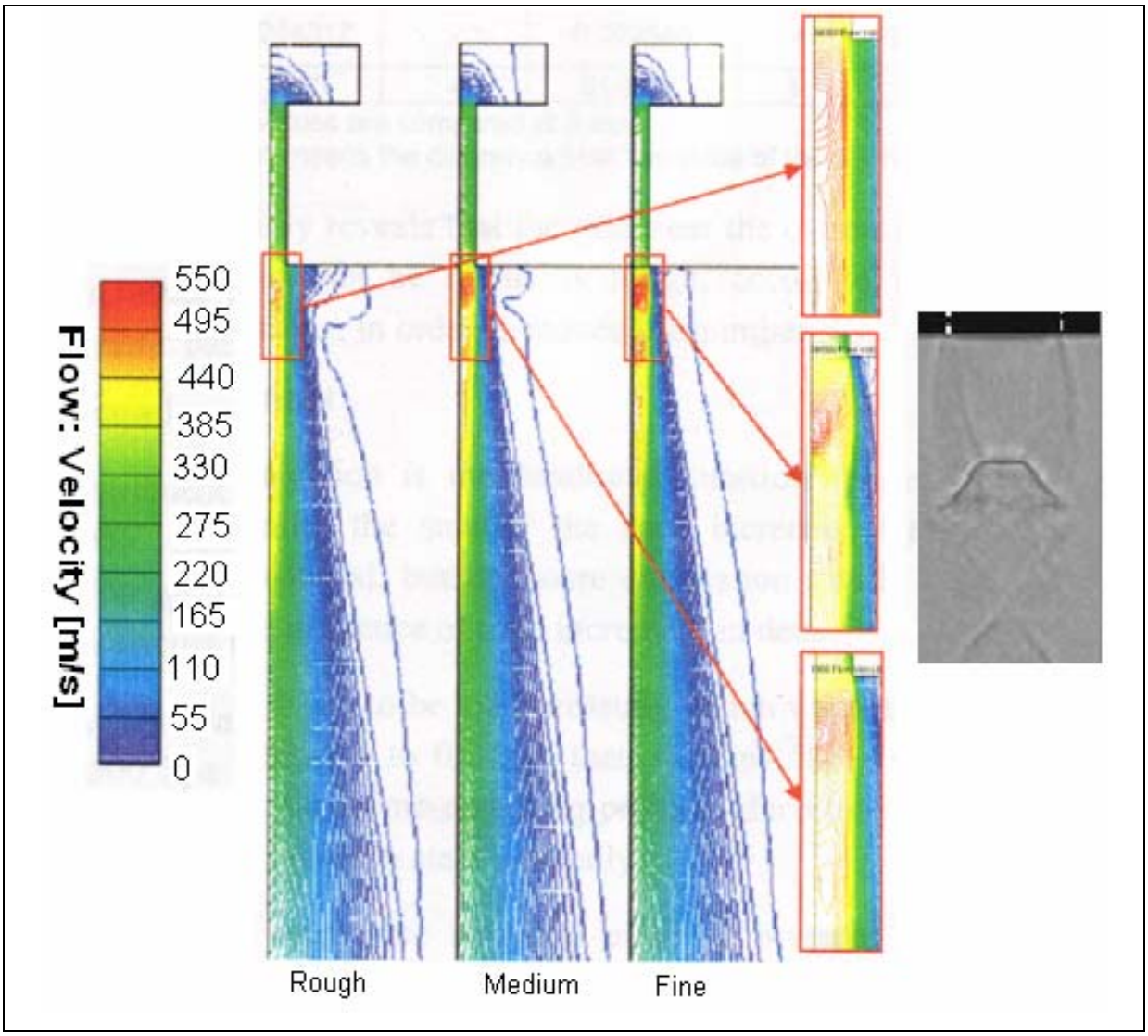

Fig.7. 2 The calculated velocity fields of three meshes comparison, [1]

Figure 7.1, shows three simple models were built with a single hole injector and with different cell number or roughness (rough, medium, and fine). The results on figure 7.2, show that the mesh surface should be fine enough to be able of shock capture near the injector hole outlet, and then can be gradually rough as it becomes far from injector outlet, saving running time.

The time increment is also critical for hydrogen injection and should be carefully adjusted for smooth convergence and to save the CPU time. The time increment can be adjusted as small as 1e-7s at the early stage of injection and after a few time steps it can be gradually increased up to 2e-5s.

7.2.2 Hydrogen injection validation

A single hole hydrogen injector model were also compared to the experimental schlieren density image on figure 7.3 and figure 7.4, with respective to the penetration distance and stream angle. The results show a very good agreement with very small error percentage up to maximum of 8% difference in its penetration distance and up to maximum of 4% in the spray cone angle. Figure 7.5; shows a comparison of simulated and measured penetration distance of a single hole injector.

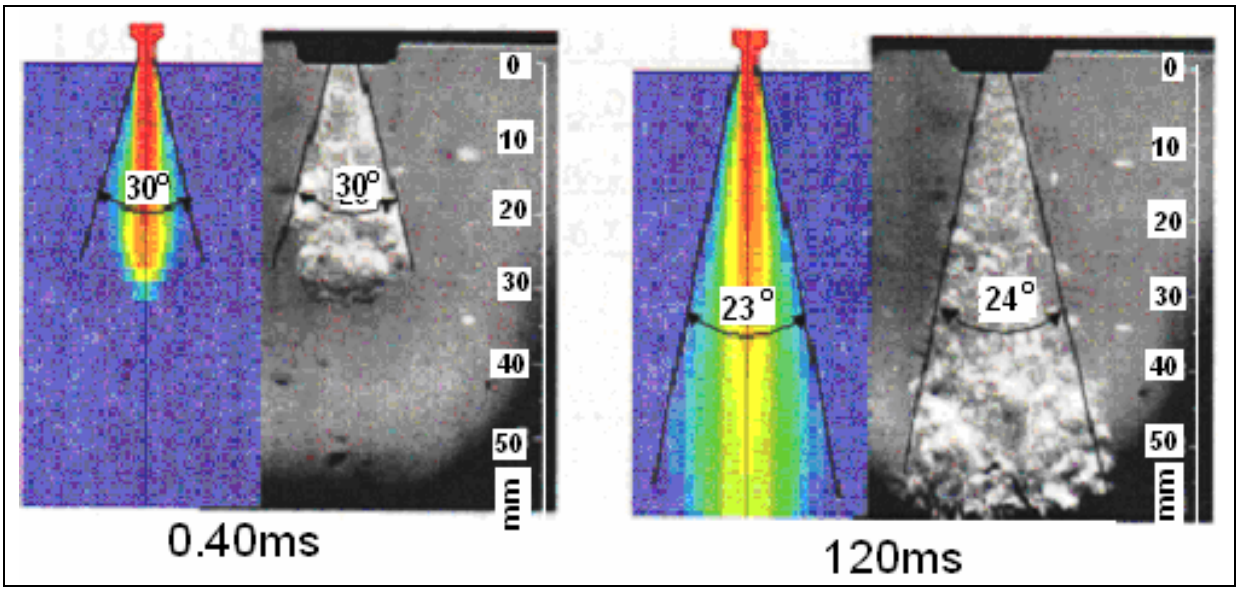

Fig.7. 3 Injection stream penetration and angle comparison to the schlieren capture

7.3 Wankel engine hydrogen injection strategies

It has been indicated in the introduction of this chapter that the direct hydrogen injection into the engine chamber is more advantageous than external port injection. In this research work, it will be concentrated on mixture formation by injecting hydrogen directly, after inlet port is completely closed, avoiding the possibility of backfire and to allow the chamber to be displaced only by air, increasing the engine volumetric efficiency. The hydrogen is then added by pressure injection at the beginning of compression (low chamber pressure), or at high chamber pressure, few degrees BTDC.

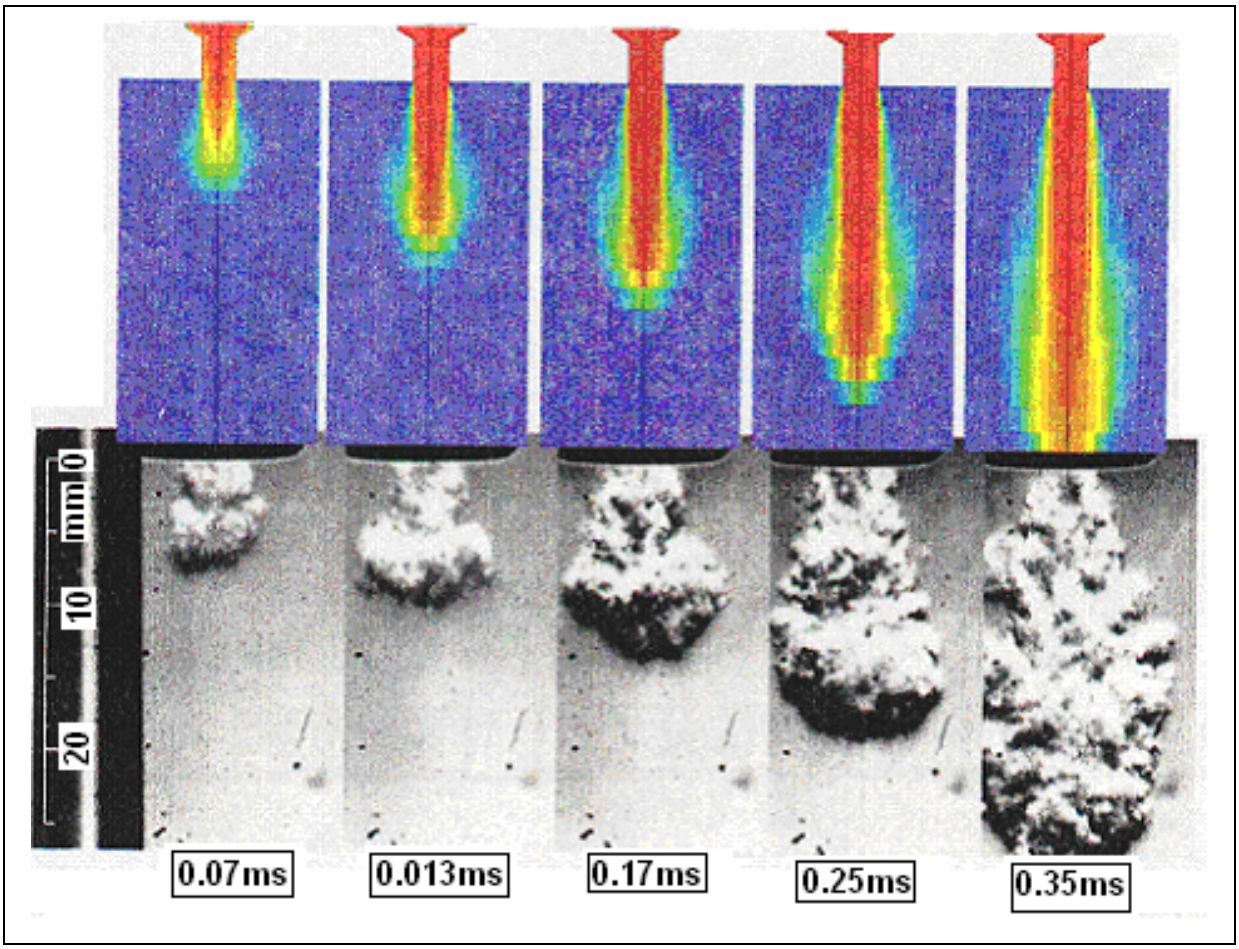

Fig.7. 4 Simulated and experimental density gradients of one hole injector, [1]

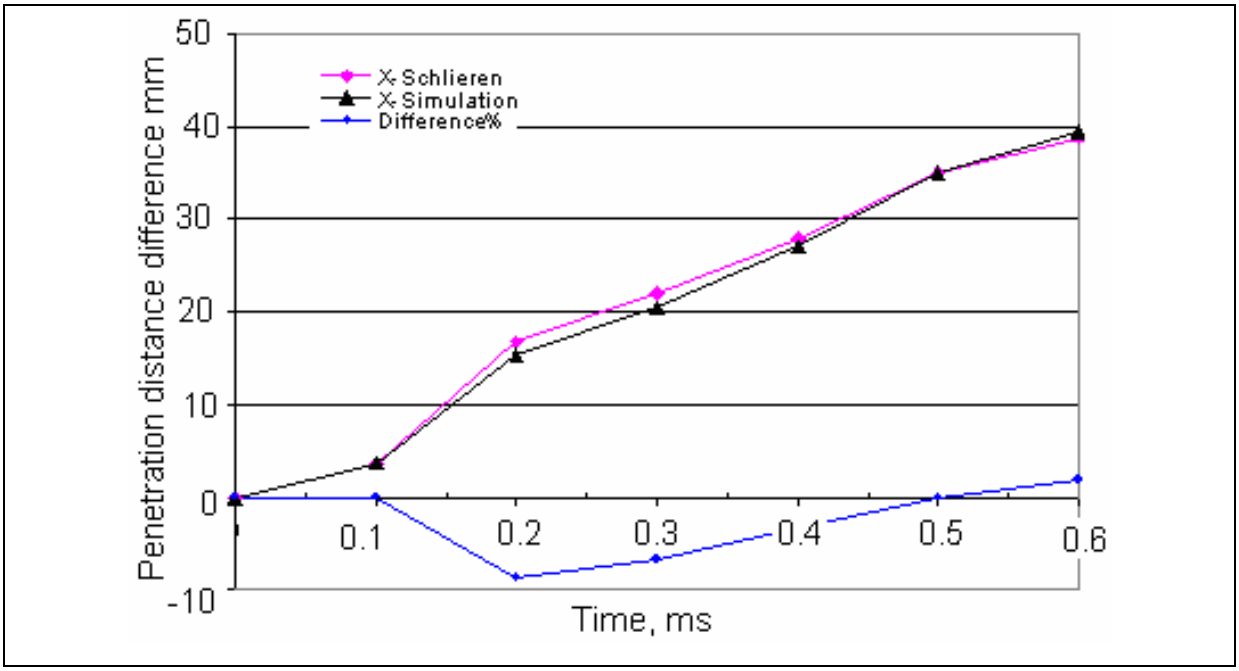

Fig.7. 5 Single hole injector, stream penetration comparison

In case of running Wankel engine on liquid and gas fuels (in this case diesel and hydrogen), it is necessary to have liquid and gas injectors connected to the engine chamber. The diesel fuel is normally injected at high pressure and it has been already discussed in previous chapter. Therefore, diesel injector is installed around the center area of housing short axis, makes it difficult to install another gas injector around this area in order to use high-pressure gas injection. However, with reference to the engine and housing engineering drawing, there are two possibilities to install the gas injector for low-pressure injection to the engine housing. Both positions were tested and compared in this chapter.

Figure 7.6 show the suggested positions of low-pressure injector installation, with reference to the housing long axis.

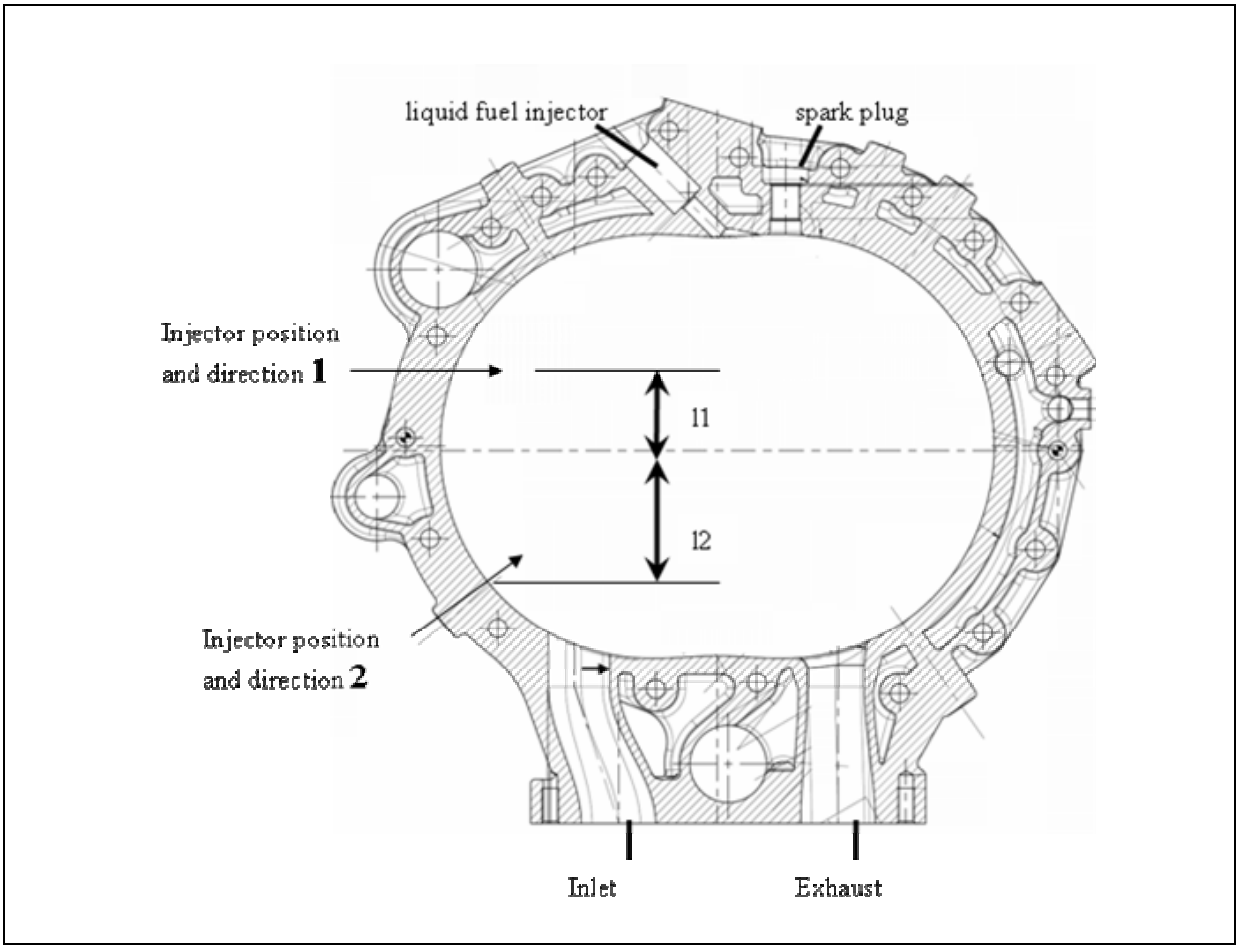

Fig.7. 6 Injectors position and direction

The hydrogen gas injector is installed a few millimeters behind the inner surface, and then only small holes drilled through the engine housing to connect the injector main hole to the engine chamber. This installation avoids the big hole effect of injector, which mixes high

pressure and low pressure zones when the rotor apex passed on. The injection holes diameter should be equal or less than the rotor apex seal thickness.

Figure 7.7, shows low-pressure injector installation. The effect of big hole for the injector installation in this region can be clearly seen on figure 7.8.

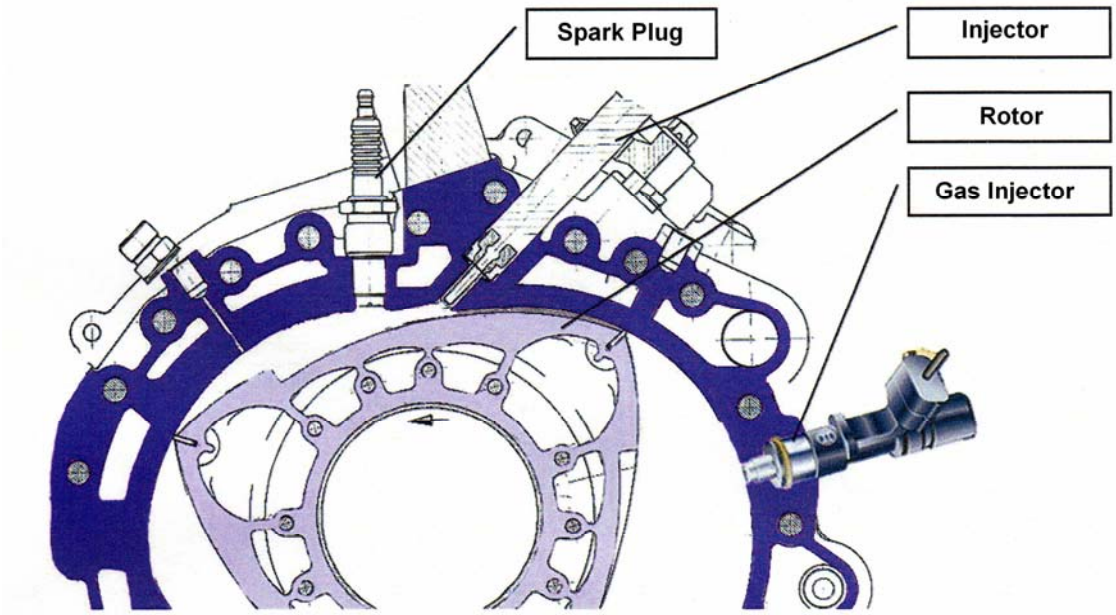

Fig.7. 7 Low-pressure gas injector installation

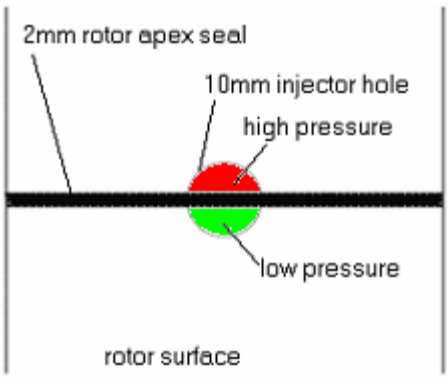

Fig.7. 8 Effect of injector installation hole

7.3.1 Injection hole size

Because hydrogen has an extremely low density, a great injection volume is required to be injected to the chamber in very limited short time.

In low-pressure injection it is important to keep the injection common rail pressure low to make use of the hydrogen tank bigger pressure difference, especially when the hydrogen tank nearly ended. When the hydrogen is injected after inlet port closed, only about 4.5ms time, in this installation position 1, is available to inject the stoichiometric mass of hydrogen into the chamber, when the engine is running full load at 6000-rpm.

In low-pressure injection, the hydrogen is injected when inlet port closed and ends in very short time where the chamber pressure is still very low. The gas pressure behind the hydrogen injector should be higher than the chamber pressure to deliver the required mass in certain time. The hydrogen density is extremely low at this low pressure, and hence the volume to be injected is very high and needs bigger injector hole size to deliver the right mass needed. At high pressure injection, the hydrogen density is higher and hence less volume to be injected, resulting that the injector hole size could be smaller for the same mass need to be injected.

Based on the above argument, three simple models were build with different nozzle sizes; 1mm, 1.5mm and 2mm diameter, to investigate the effect of nozzle size on flow velocity, and injection pressure required to inject a certain mass of H_2 into a chamber with different initial chamber pressures. The chamber initial pressure was set to be, 1e+5 pa, 5e+5 pa, 1.0e+6 pa, 1.5e+6 pa and 2.0e+6 pa.

Figure 7.9 shows the three models with different inlet hole diameter size. The three models have the same number of cells and the same boundary condition.

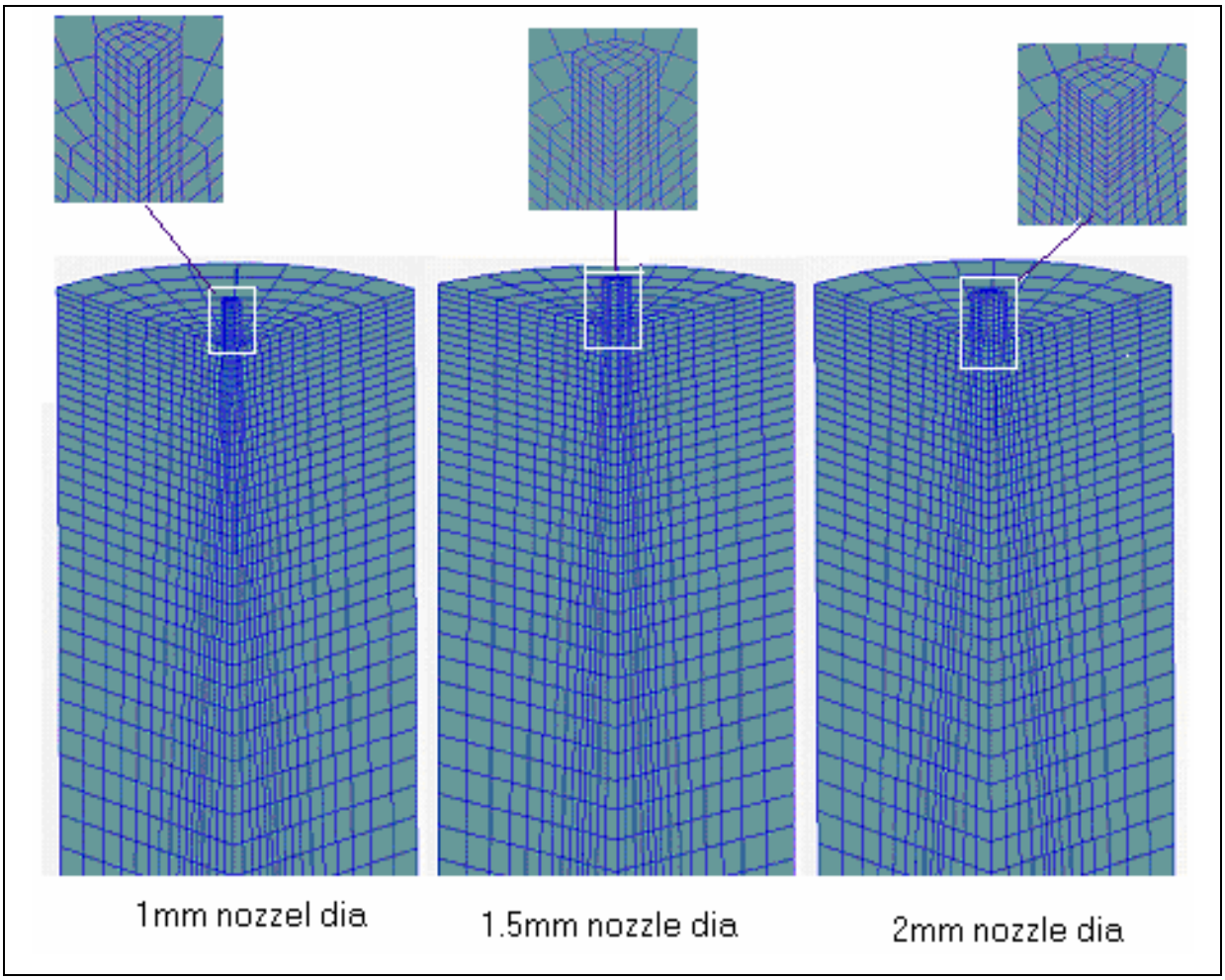

Fig.7. 9 Three models with different nozzle-hole size

The inlet mass flow rate is set to be 0.0006.kg/s, 0.001.kg/s and 0.0015.kg/s for 1mm, 1.5mm and 2mm diameter respectively, at cylinder pressure 1e+5 pa and 5e+5 pa; and 0.001.kg/s, 0.0015.kg/s and 0.0025.kg/s respectively for 1.0e+6 pa, 1.5 e+6 pa, 2.0 e+6 pa cylinder pressure. Table 7.1 presents mass flow rate and pressure initial conditions for all models.

7.3.2 Results

The result is plotted and presented on three graphical groups; each group consists of four figures for each model separately. The first two figures in each group (Fig.7.13, Fig.714, in first group for 1-mm nozzle diameter), presents the total hydrogen injected mass and hydrogen mass flow rate at different cylinder pressure. The third and fourth figures (Fig.7.15

and Fig.7.16), show the maximum total pressure and the maximum flow Mach number respectively. Similar graphical figures were presented for 1.5-mm and 2-mm nozzle diameter.

Model	**1-mm Diameter**				
Cylinder initial pressure, pa	1e+5	5 e+5	1.0 e+6	1.5 e+6	2.0 e+6
Inlet mass flow, kg/s	0.0006	0.0006	0.001	0.001	0.001
Model	**1.5-mm Diameter**				
Cylinder initial pressure, pa	1e+5	5 e+5	1.0 e+6	1.5 e+6	2.0 e+6
Inlet mass flow, kg/s	0.001	0.001	0.0015	0.0015	0.0015
Model	**2-mm Diameter**				
Cylinder initial pressure, pa	1e+5	5 e+5	1.0 e+6	1.5 e+6	2.0 e+6
Inlet mass flow, kg/s	0.0015	0.0015	0.0025	0.0025	0.0025

Table-7. 1 Models initial condition

7.3.2.1 1-mm Diameter

Fig.7.10 shows the flow Mach number, it can be clearly seen that the maximum flow velocity is concentrated at the nozzle outlet during gas expansion and velocity shock can be seen on the iso-lines display, due to super sonic flow. Fig.7.11 shows that the maximum total pressure is concentrated at the nozzle hole inlet denoting the rail total pressure.

Fig.7.13 shows the hydrogen total mass injected against time for different cylinder pressure, and hence the mass or injection time can be found for specific case. Fig.7.14 shows the mass flow rate settings for different initial pressure. It can be seen that for low initial cylinder pressure (1e+5 pa, 5e+5 pa), the mass flow rate has set to be less than that for higher pressures (1e+6 pa, 1.5e+6 pa, 2e+6 pa), to reduce inlet velocity and hence calculation diverge. It can be clearly seen on Fig.7.16 that the flow Mach number is very high at lower cylinder pressure.

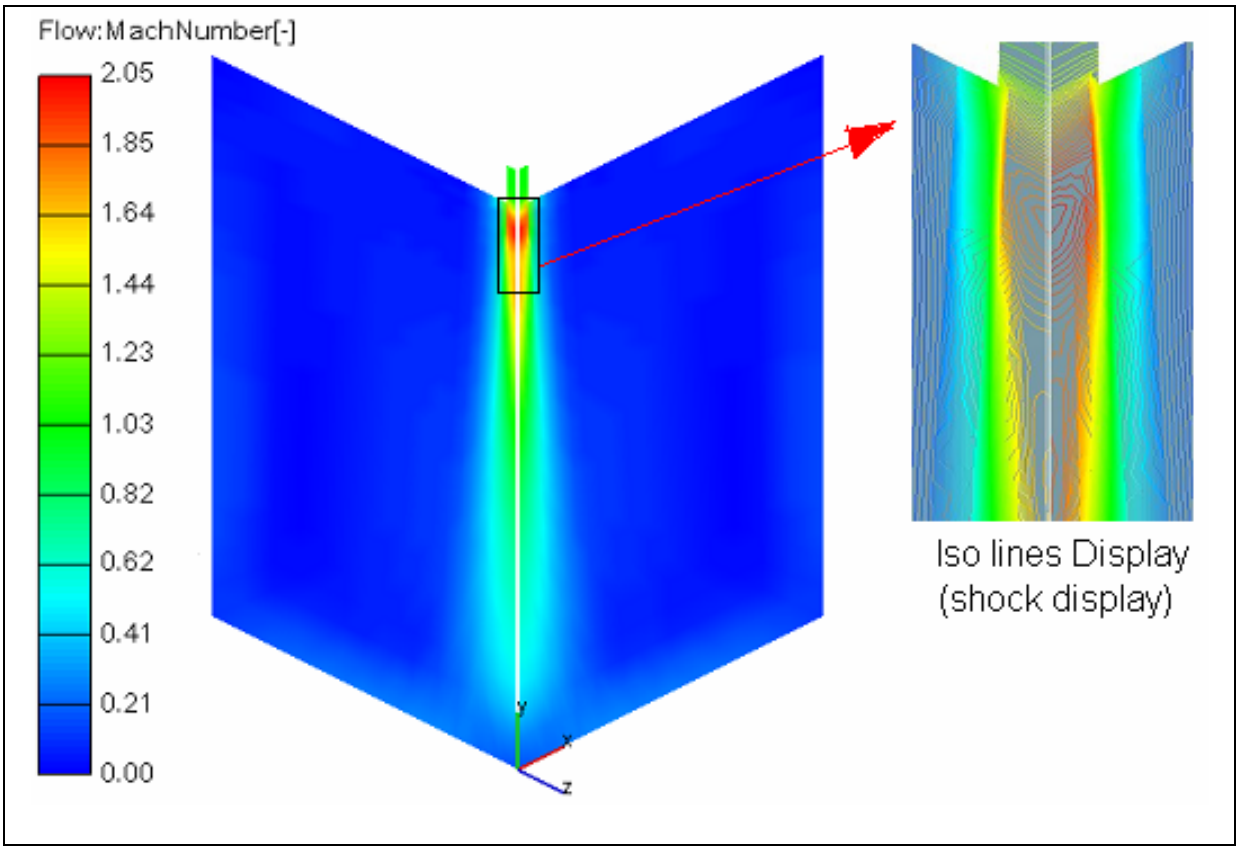

Fig.7. 10 Flow Mach number

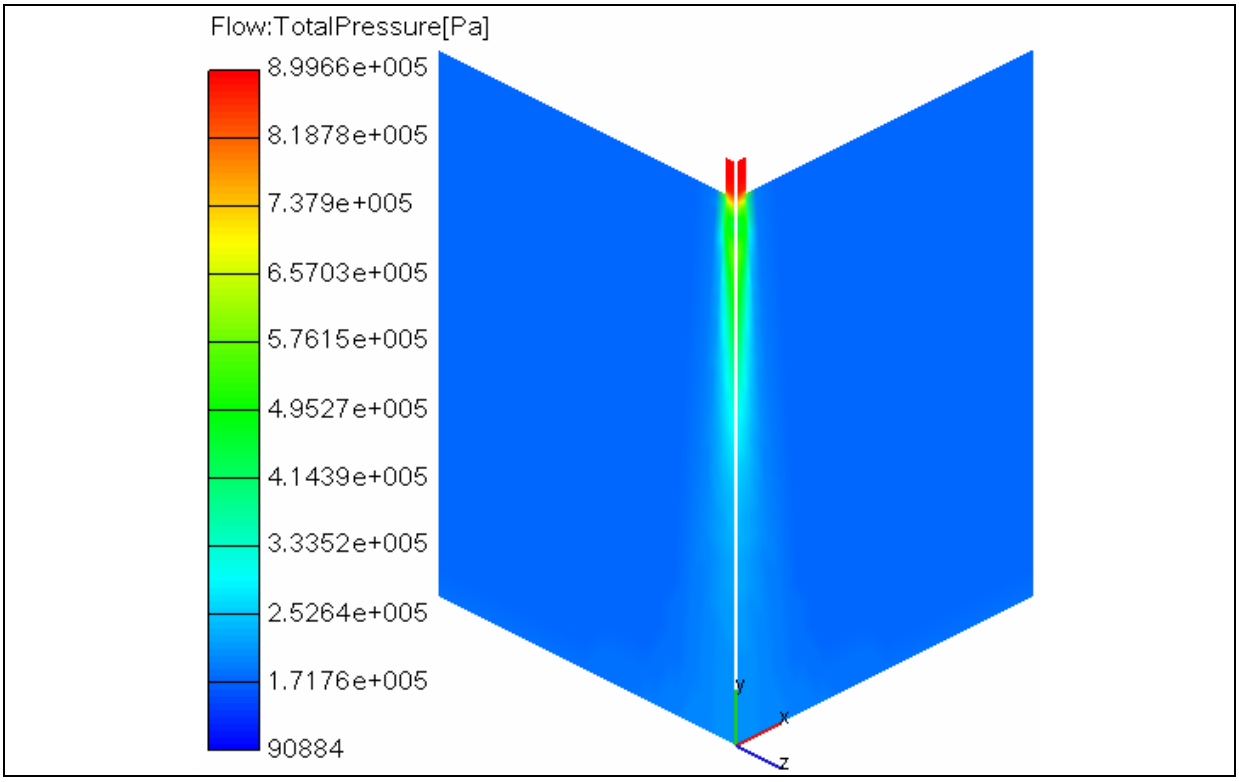

Fig.7. 11 Flow total pressure

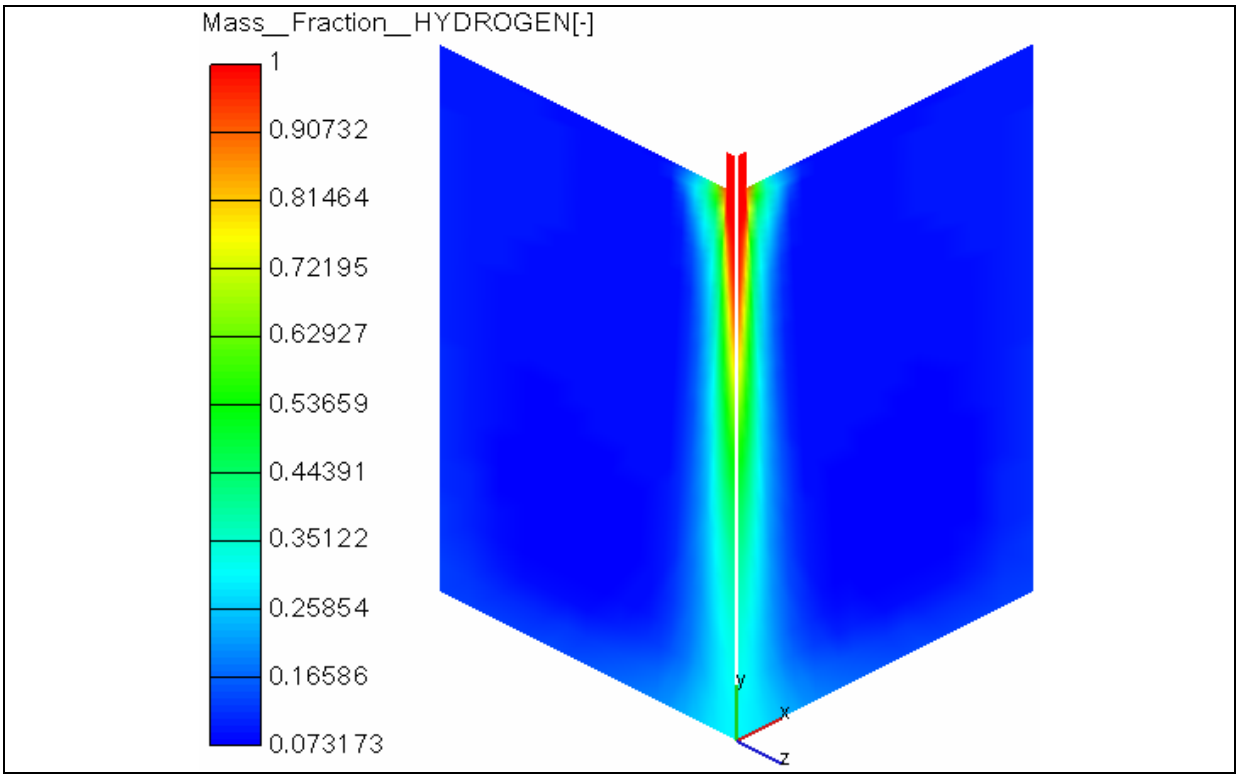

Fig.7. 12 H2 mass fraction

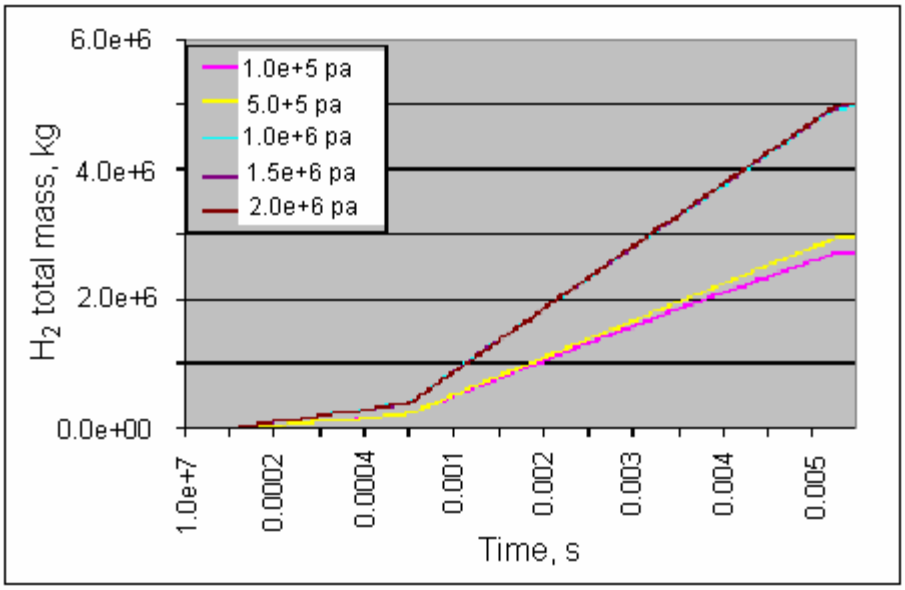

Fig.7. 13 H2 total mass for different cylinder pressure

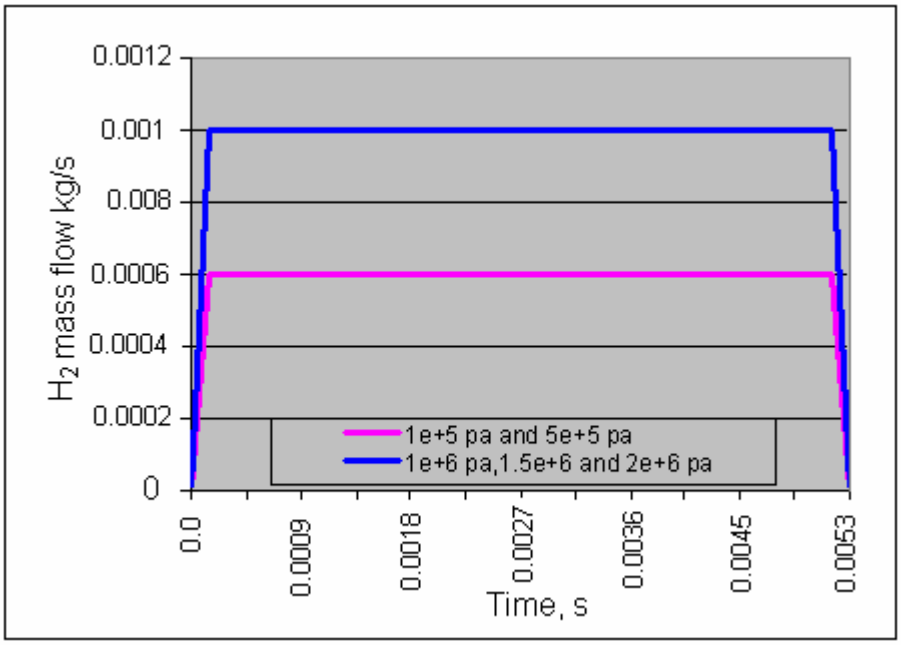

Fig.7. 14 H2 mass flow rate for different cylinder pressure

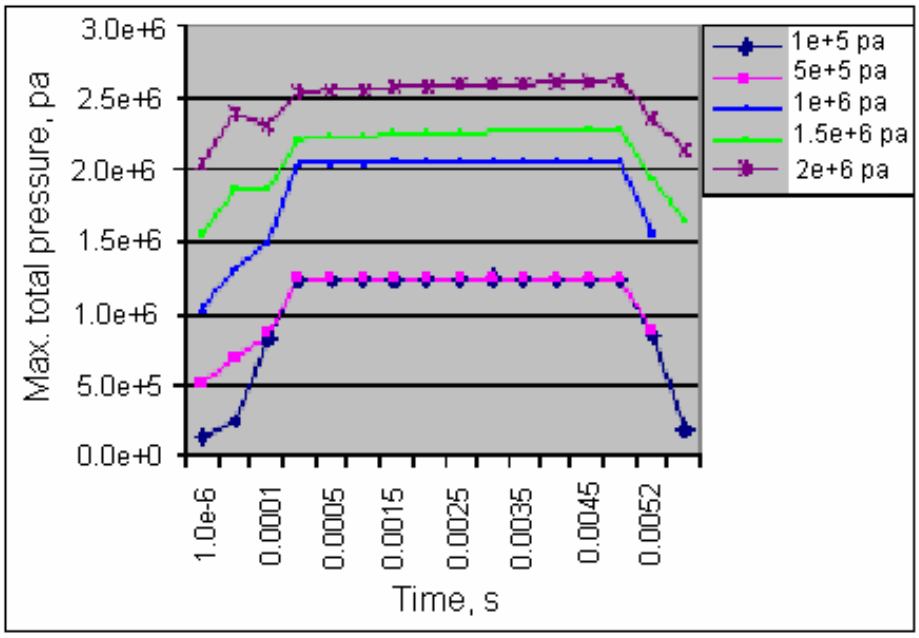

Fig.7. 15 Maximum total pressure for different cylinder pressure

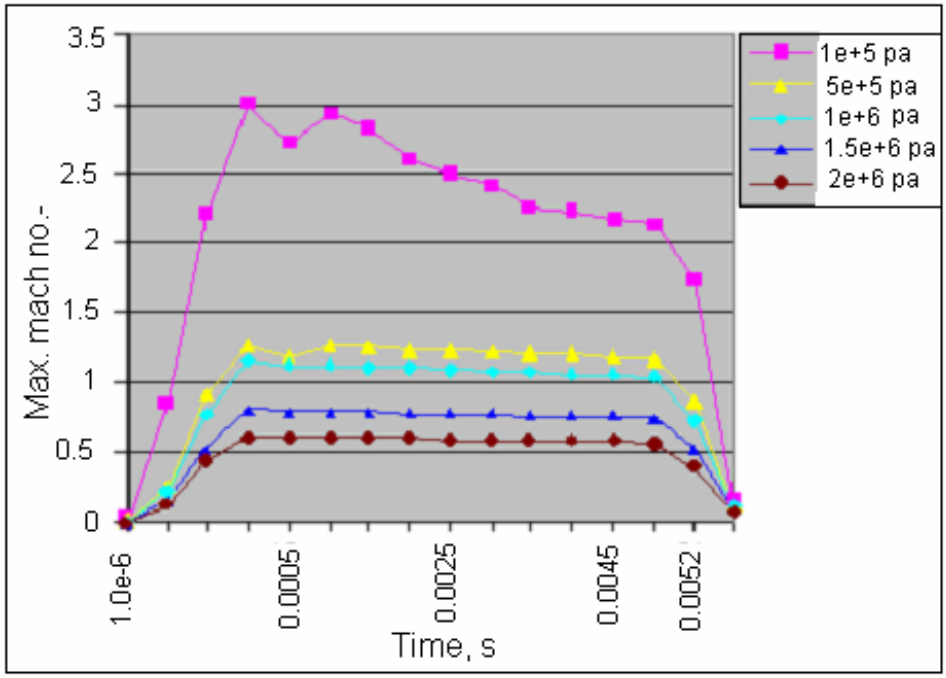

Fig.7. 16 Maximum flow Mach no. for different cylinder pressure

7.3.2.2 1.5-mm Diameter

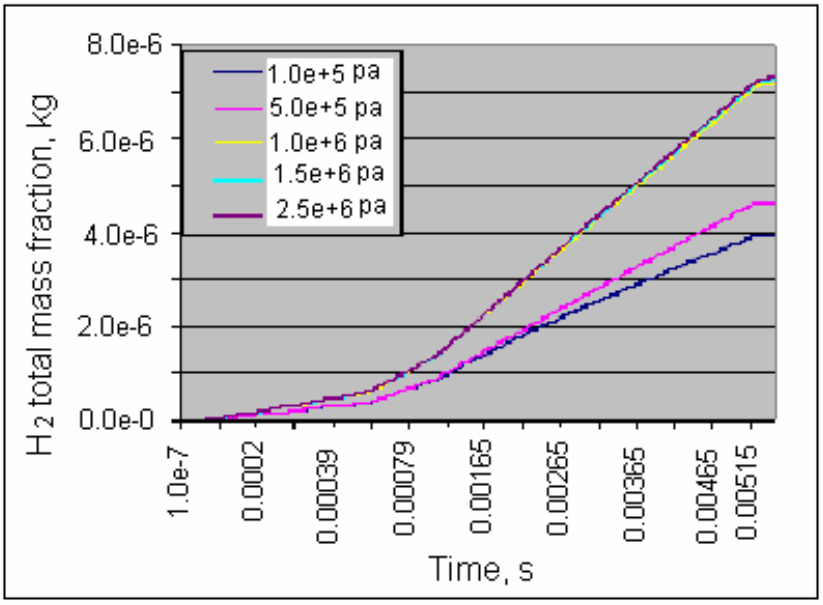

Fig.7. 17 H2 total mass for different cylinder pressure

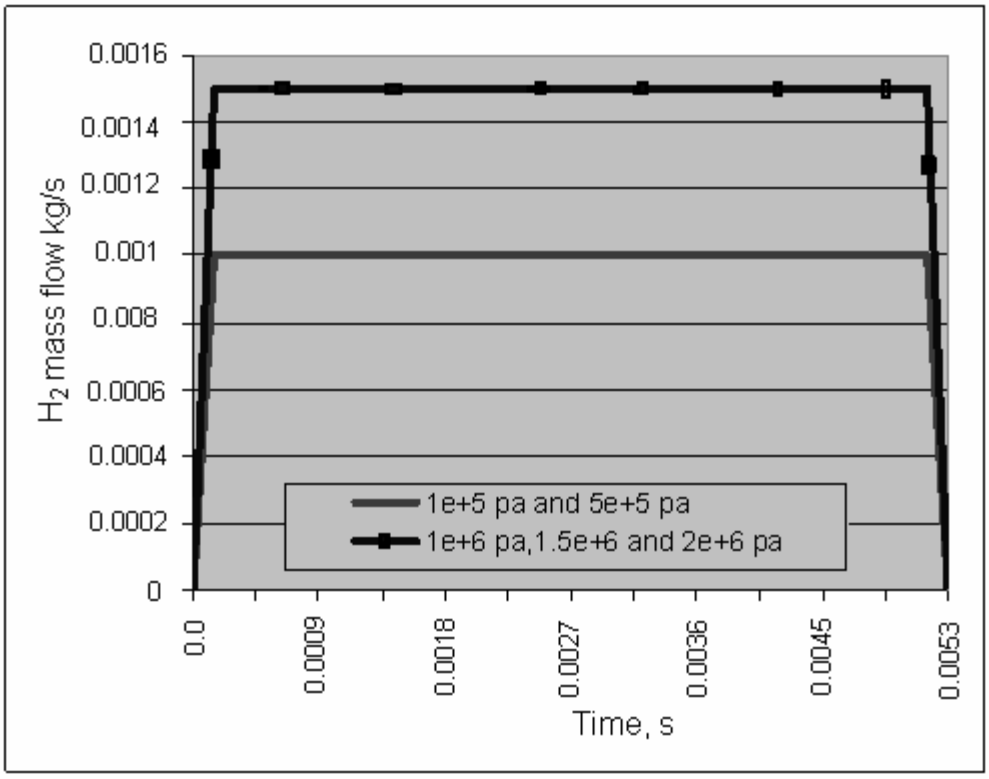

Fig.7. 18 H2 mass flow rate for different cylinder pressure

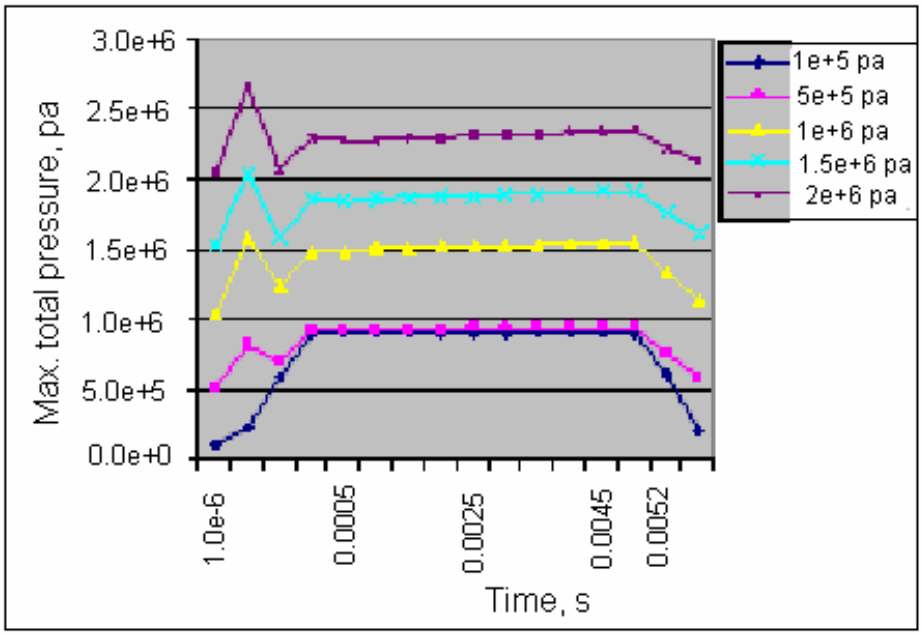

Fig.7. 19 Maximum total pressure for different cylinder pressure

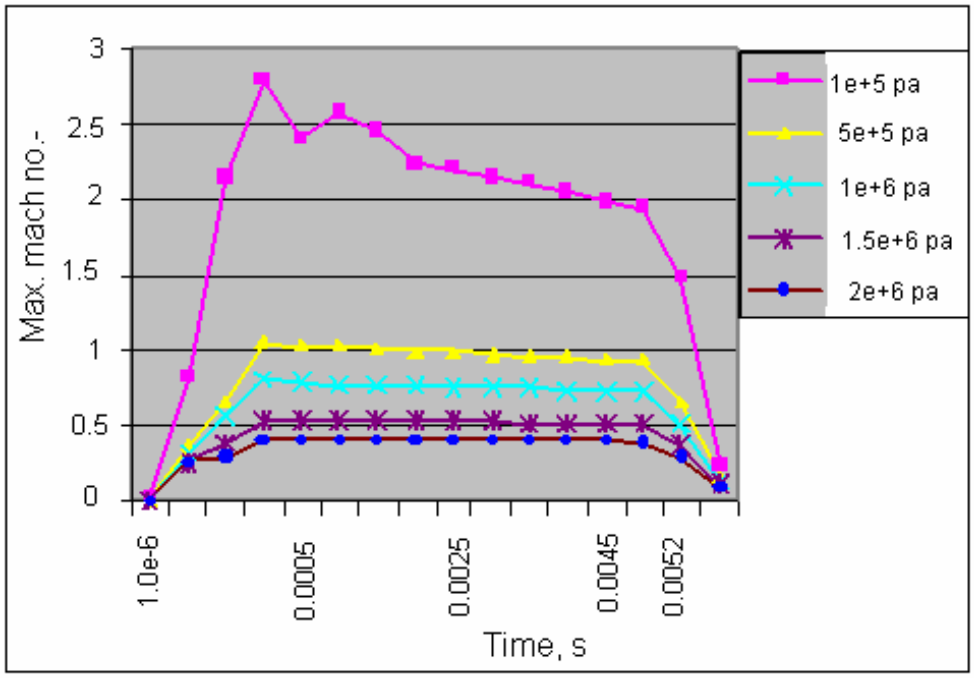

Fig.7. 20 Maximum flow Mach no. for different cylinder pressure

7.3.2.3 2-mm Diameter

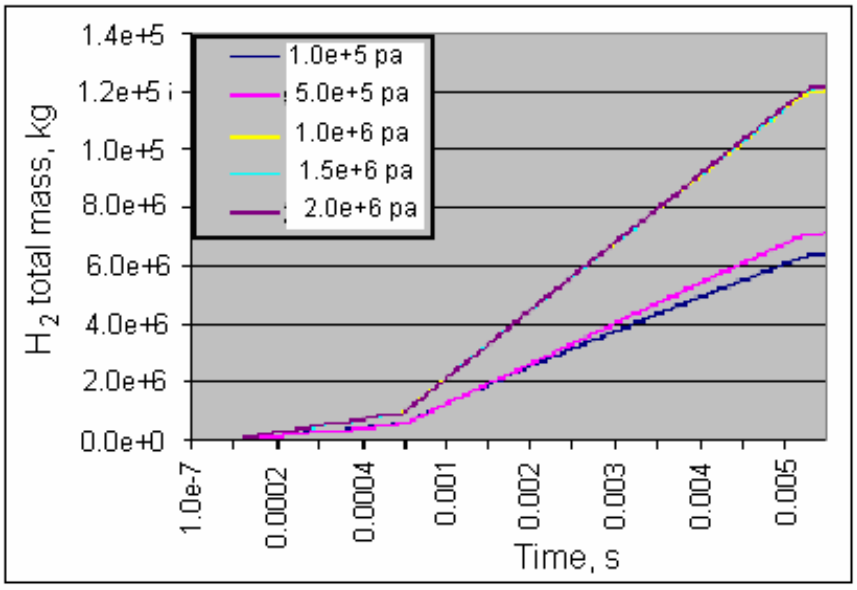

Fig.7. 21 H2 total mass for different cylinder pressure

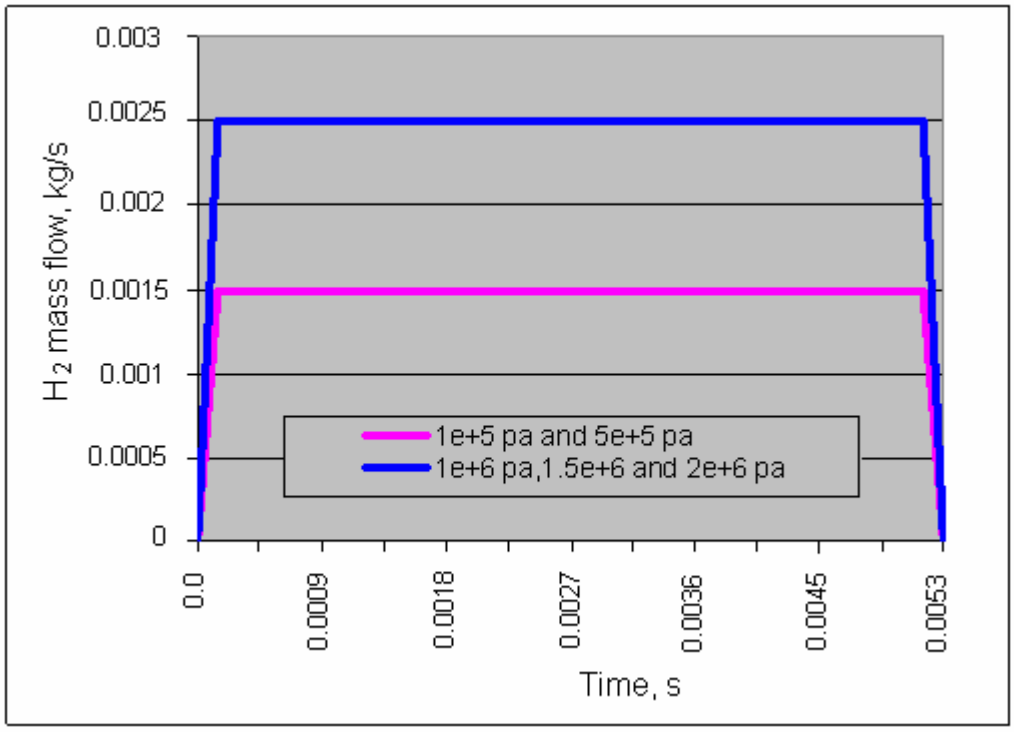

Fig.7. 22 H2 mass flow rate for different cylinder pressure

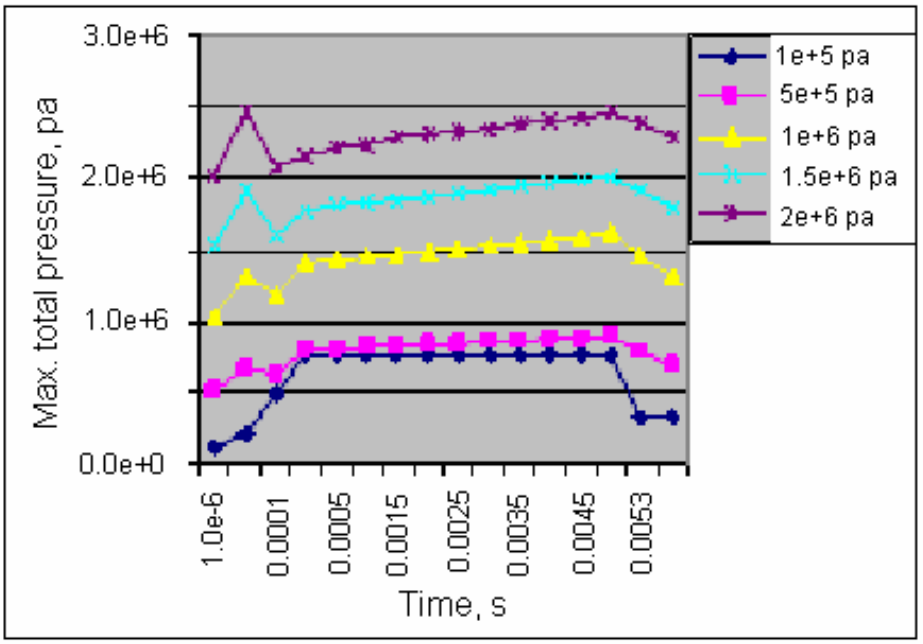

Fig.7. 23 Maximum total pressure for different cylinder pressure

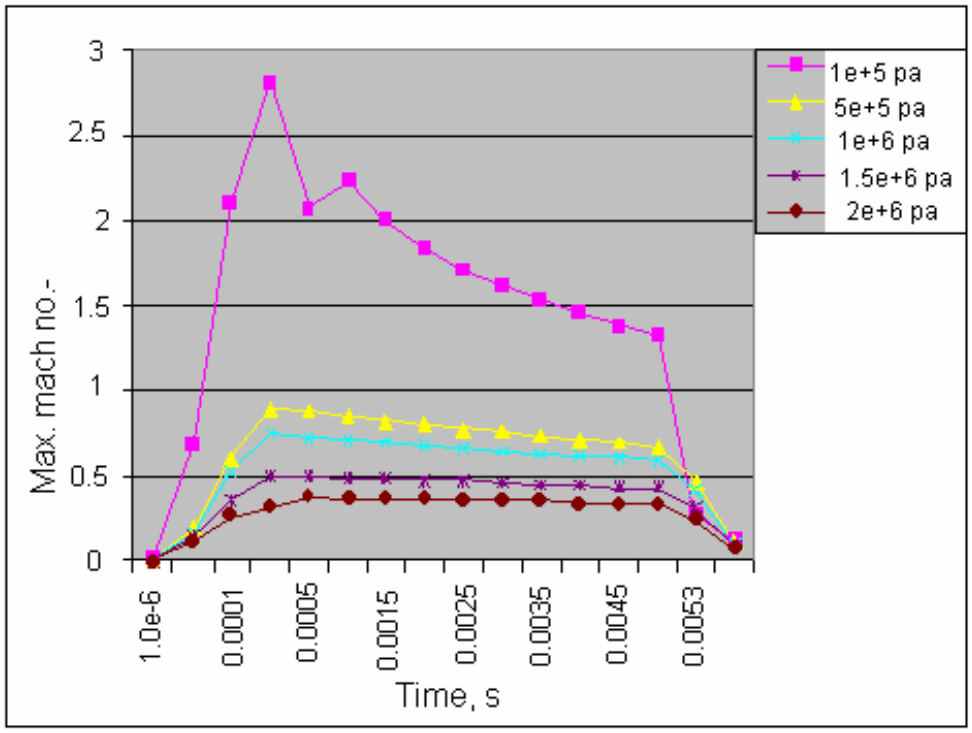

Fig.7. 24 Maximum flow Mach no. for different cylinder pressure

Similar results can be seen for the second and third models (1.5-mm diameter and 2-mm diameter). It can be notice that the inlet mass flow rate is increased as the nozzle hole diameter increased and hence the total mass injected.

7.3.2.4 Total injected mass comparison

The average total mass injected for 1e+5 pa and 5e+5 pa cylinder pressures was taken and plotted on figure 7.25 for the three nozzle sizes. Similar plot is presented on figure 7.26 for higher cylinder pressures (1e+6 pa, 1.5e+6 pa and 2e+6 pa).

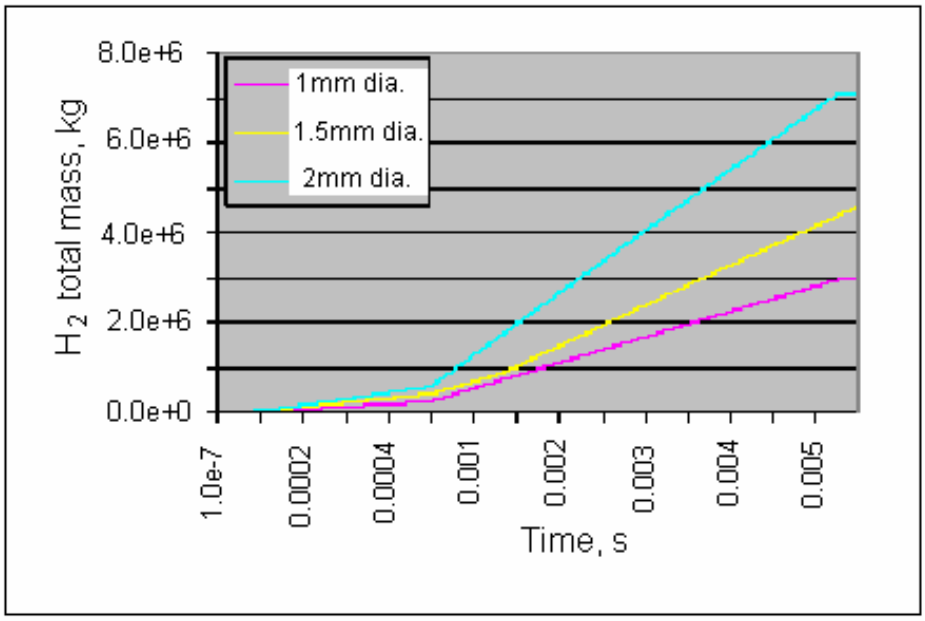

Fig.7. 25 H2 total mass, (1e+5 pa and 5e+5Pa)

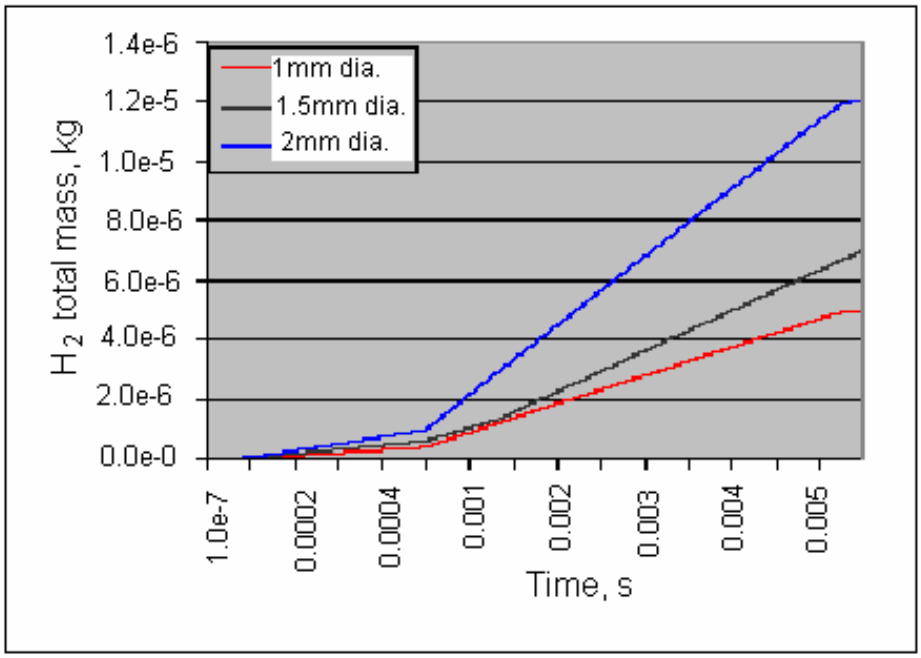

Fig.7. 26 H2 total mass, (1e+6pa, 1.5e+6pa and 2e+6pa)

7.5 H2 low-pressure injection, real engine models

7.5.1 Geometrical surface preparation

Real engine geometrical models were used to study the hydrogen injection and mixture formation with the help of moving mesh tool available in the CFD-Code. The injector position for hydrogen low-pressure injection was investigated on two positions as clarified earlier in this chapter, on figure 7.6. On figure 7.27, real geometrical surface model are presented with three holes injector in position-1 and position-2.

On position-1, there is 4.5ms time available for hydrogen injection before the rotor apex reaches the injector position at 6000-rpm, and only 2.5ms time is available for position-2 at the same engine speed.

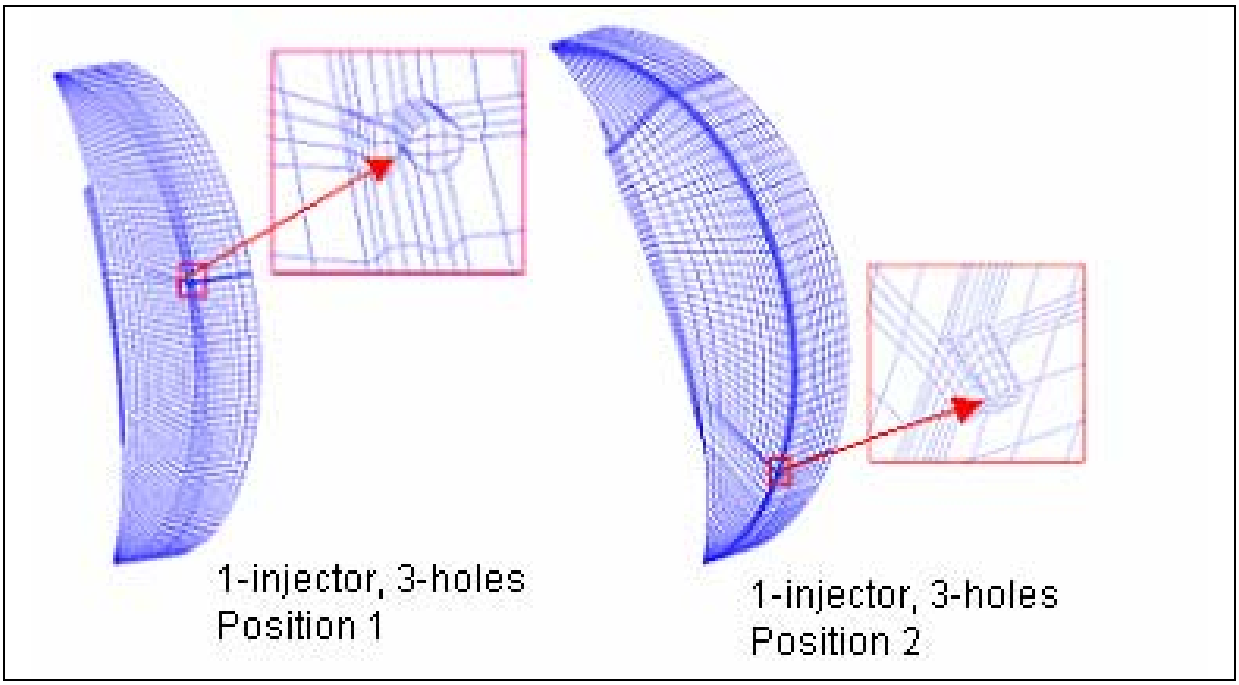

Fig.7. 27 Low pressure injector positions

Positon-1 was tested using a single injector with 1.5mm, three holes connected to the chamber at the housing mid line and the angle between holes was set to be 15º, as it can be seen on figure 7.28-a. A symmetrical boundary was used and only half of the geometry was simulated, as it can be seen on figure 7.28-b.

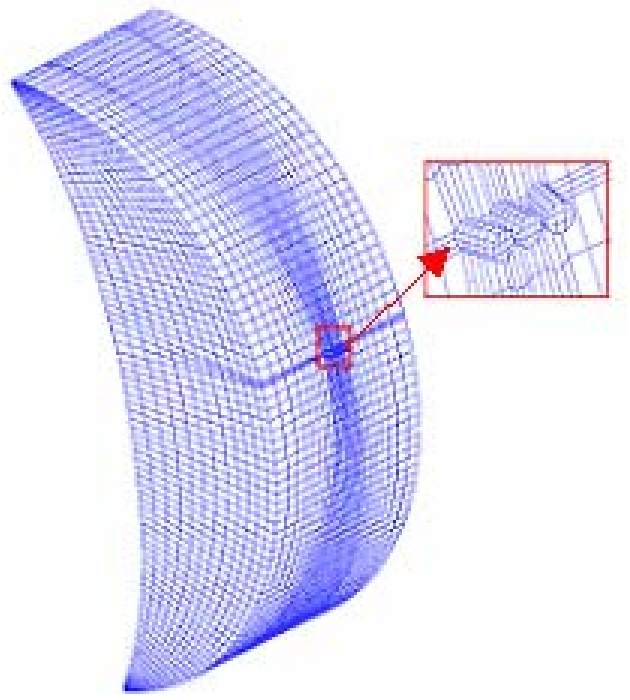

a)- 1 injector 3-hole, complete geometrical surface

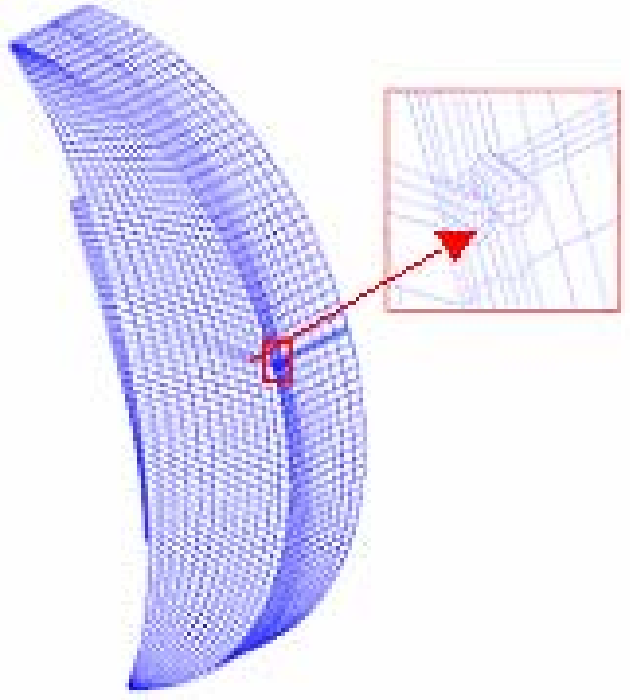

b)- Half of geometrical surface simulated

Fig.7. 28 A single 3-holes injector, position-1

Also, two injector installations in this position on the same level were tested, see figure 7.29, to reduce the injection time and injection pressure.

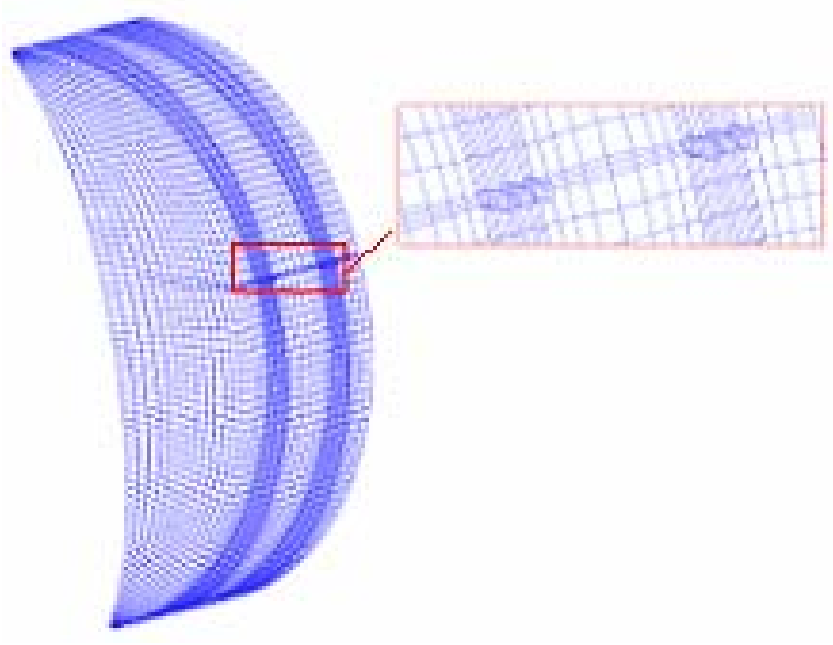

a)- 2-injector 3-hole each, complete geometrical surface

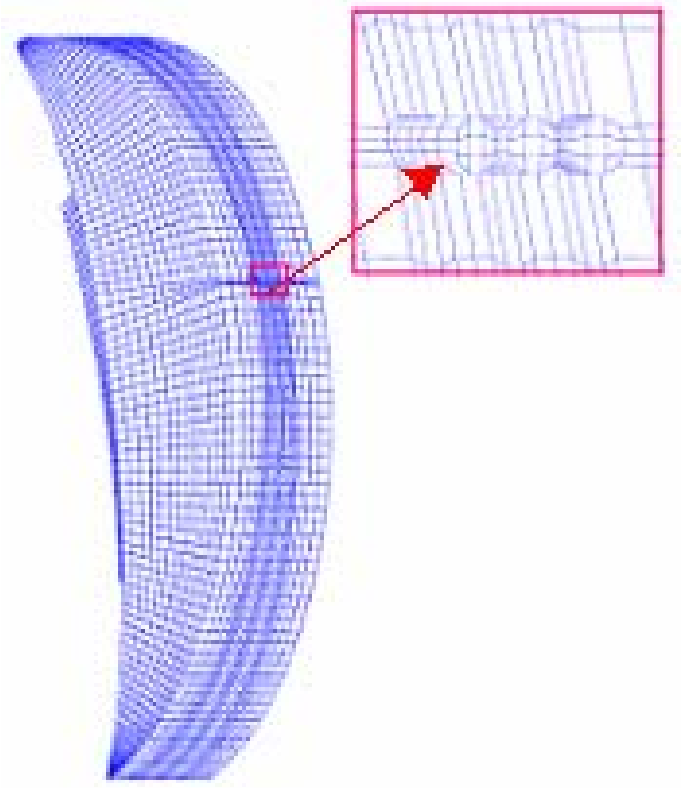

b)- Half of geometrical surface simulated

Fig.7. 29 Double, 3-holes injector installation, position-1

A single injector 3-hole installation in position-2 can be seen on figure 7.30.

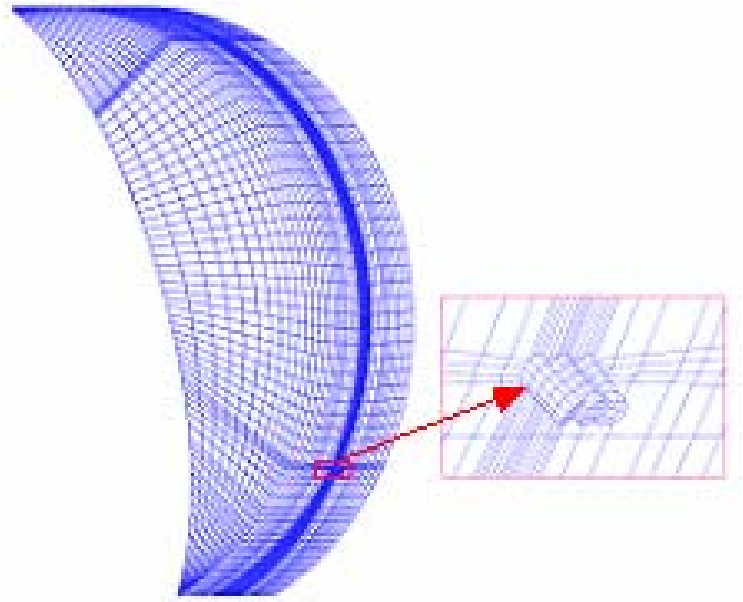

a)- 1 injector 3-hole, complete geometrical surface

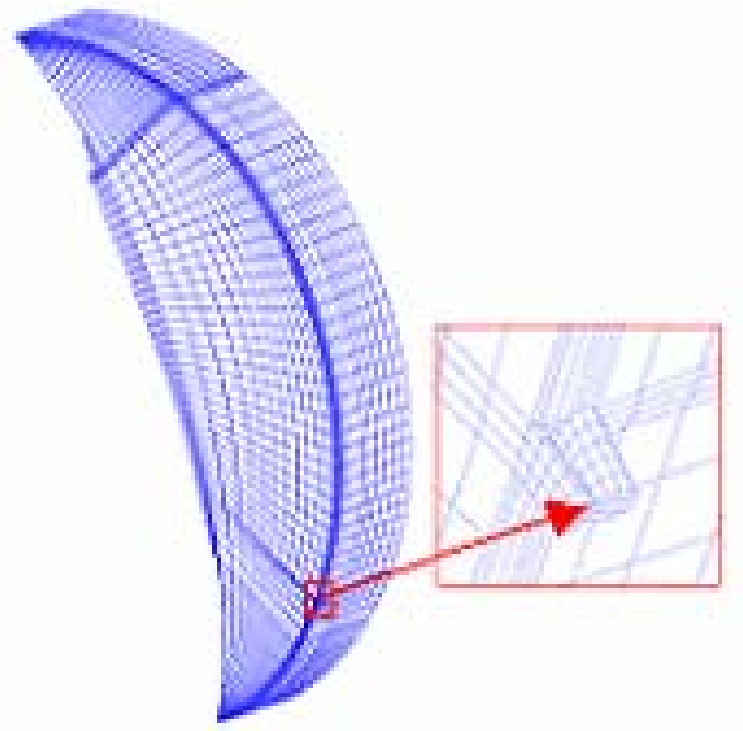

b)- Half of geometrical surface simulated

Fig.7. 30 A single 3-holes injector, position-2

7.5.2 Results

The results were presented and plotted on figures from, Fig.7.31 to Fig.7.36. The hydrogen mass fraction of single 3-hole injector display is presented on Fig.7.31, (a, b).

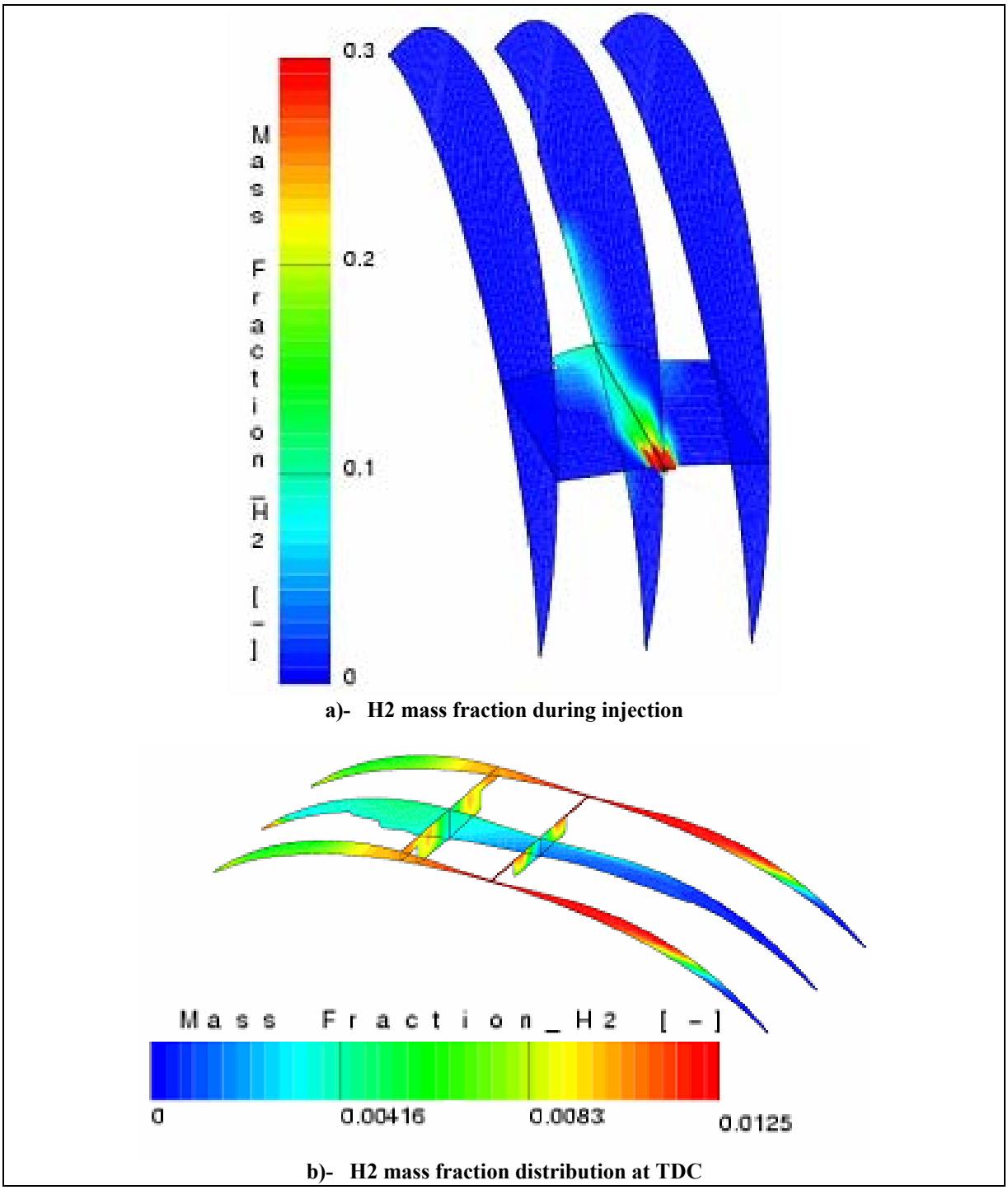

a)- H2 mass fraction during injection

b)- H2 mass fraction distribution at TDC

Fig.7. 31 Injected hydrogen mass fraction

Figure 7.32 shows the pressure and temperature display at TDC, the maximum total pressure during injection period is 6.9 Pascal. Figure 7.33 shows the equivalence ratio at the spark plug position against the engine rotation angle.

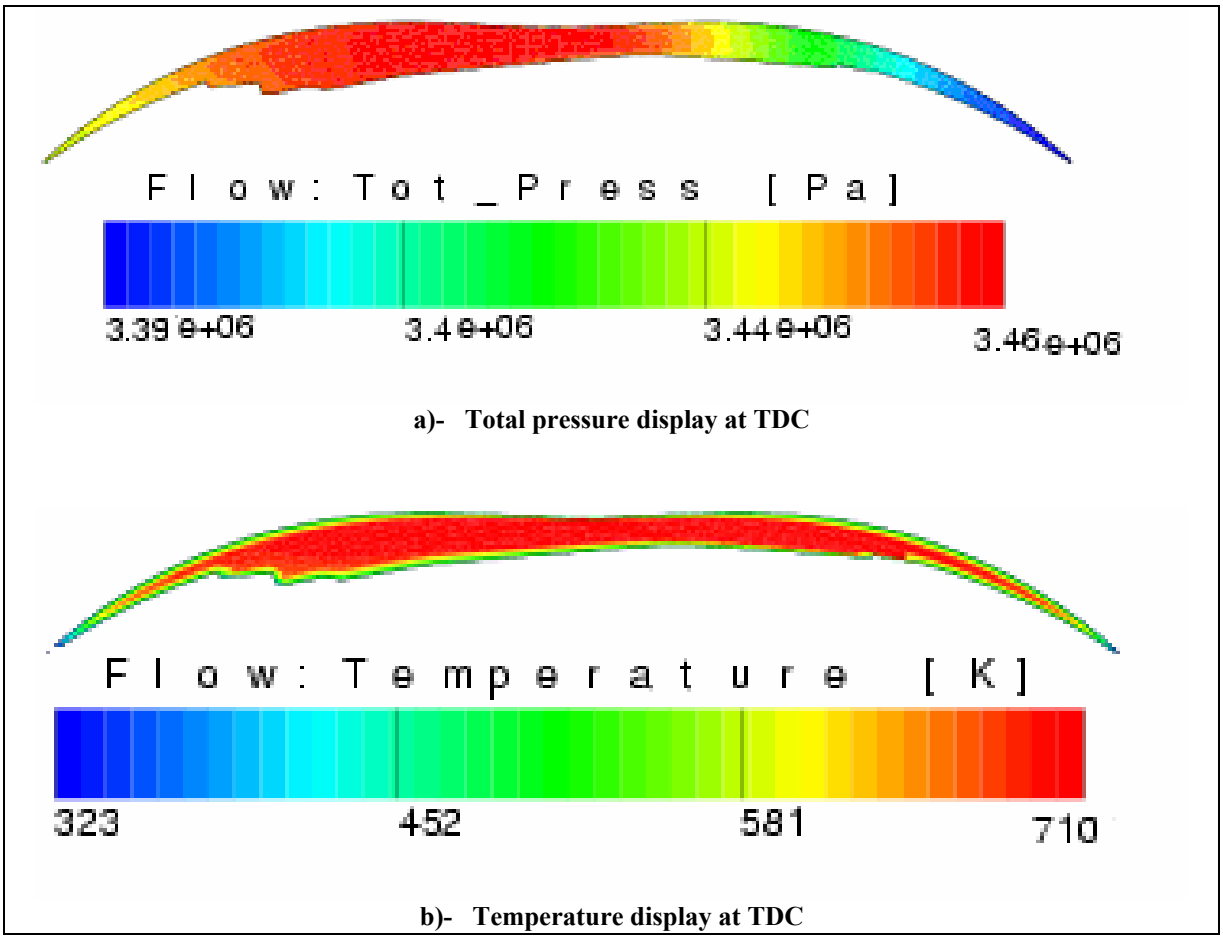

a)- Total pressure display at TDC

b)- Temperature display at TDC

Fig.7. 32 Pressure and temperature display at TDC

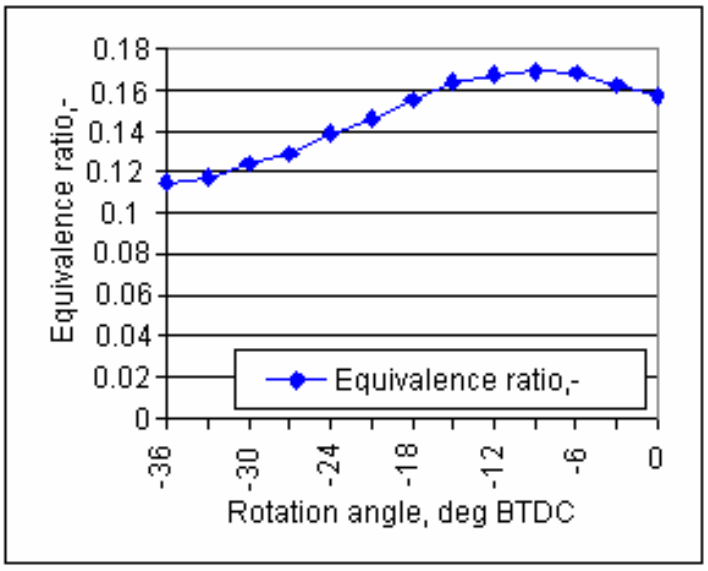

Fig.7. 33 Mixture equivalence ratio at spark plug position

Similar results of two injectors, 3-hole each, were presented and plotted on the following figures. During injection, figure 7.34 (a) shows the hydrogen mass fraction, and figure 7.34 (b) shows the hydrogen mass fraction at TDC.

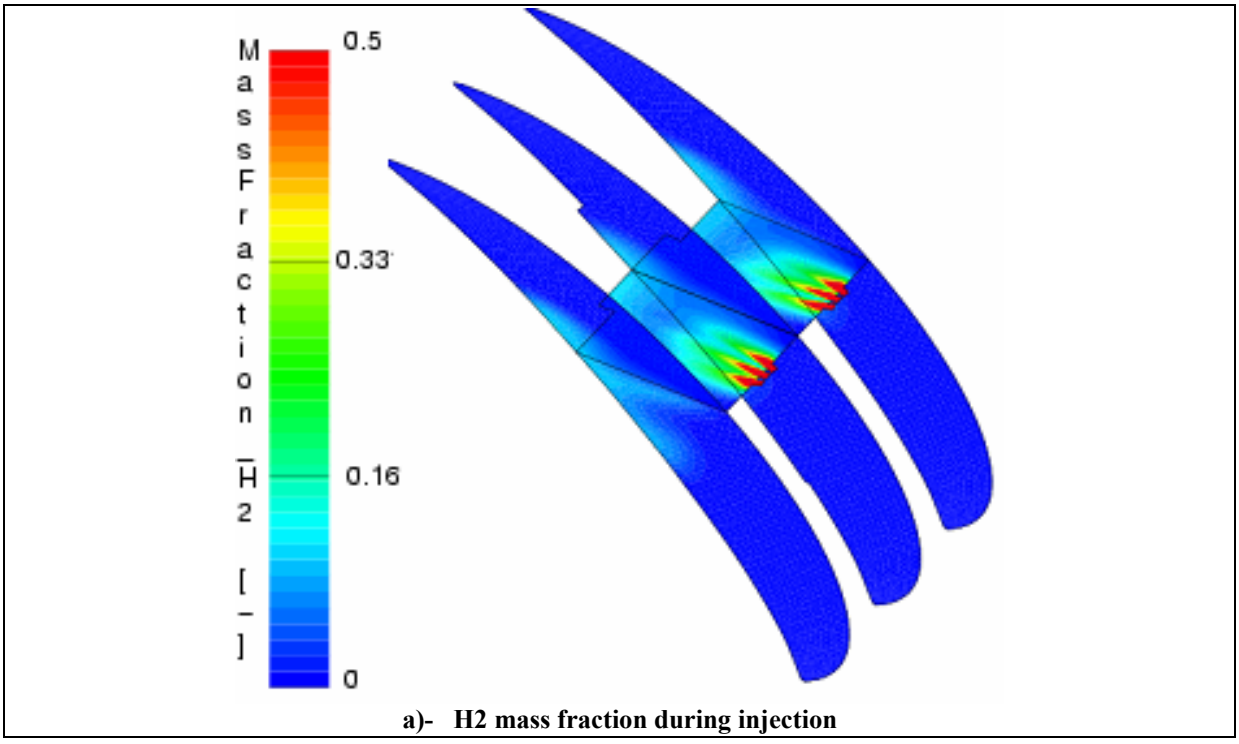

a)- H2 mass fraction during injection

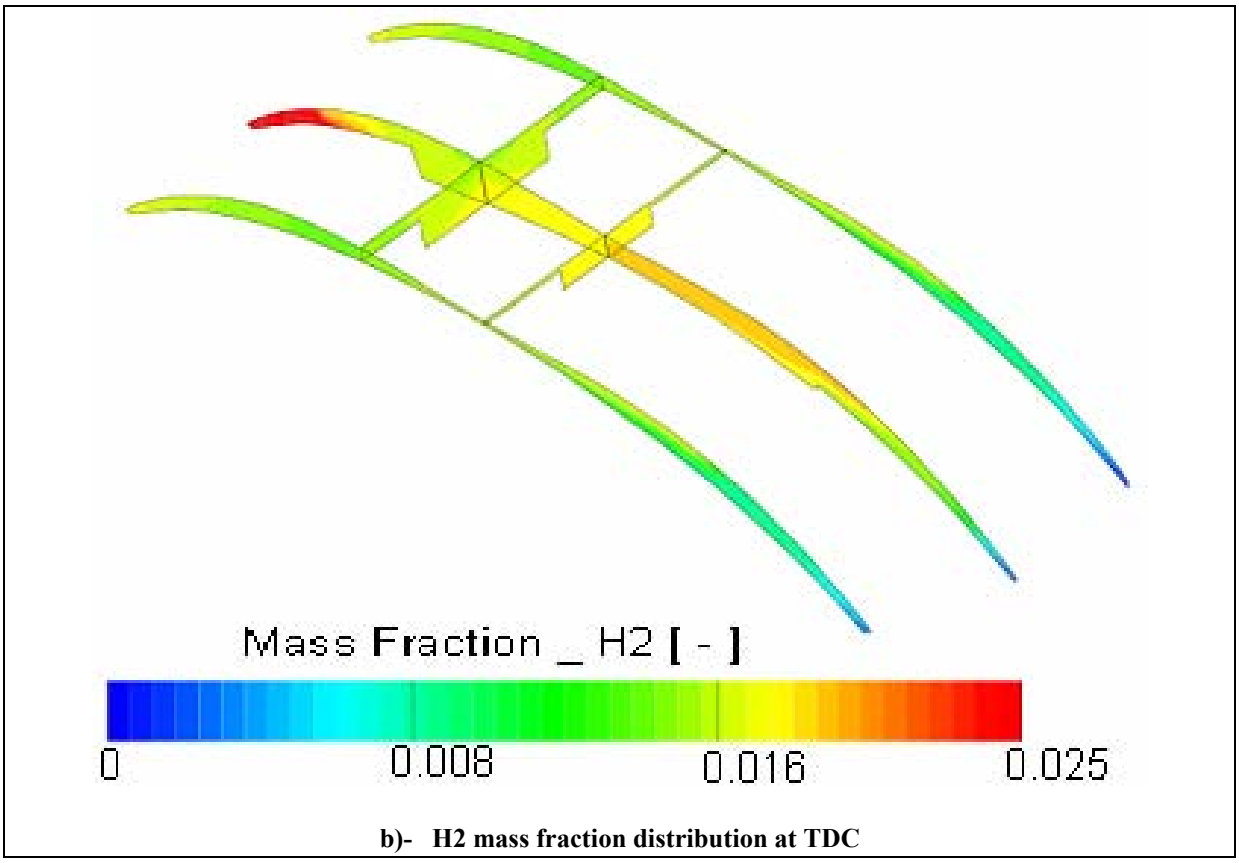

b)- H2 mass fraction distribution at TDC

Fig.7. 34 Injected hydrogen mass fraction

The pressure and temperature display were presented on figure 7.35 (a, b). The maximum total pressure during injection period is 4.8 Pascal. Figure 7.36 shows the equivalence ratio at the spark plug position against the engine rotation angle.

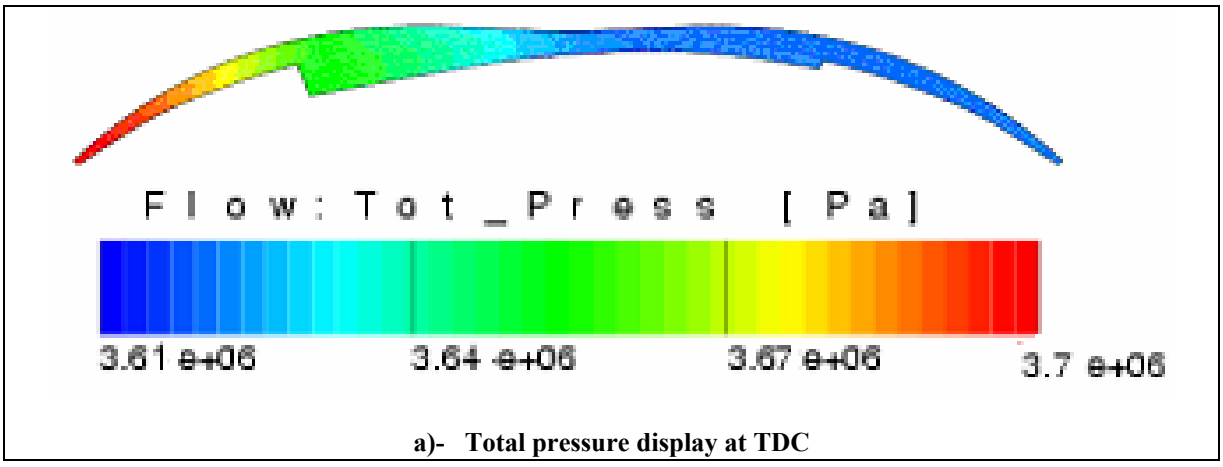

a)- Total pressure display at TDC

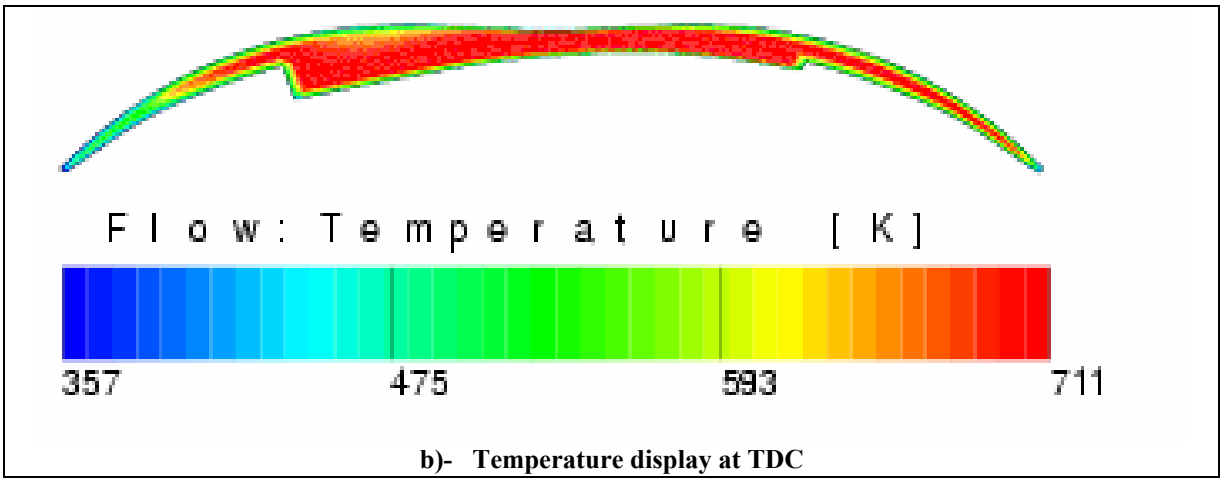

b)- Temperature display at TDC

Fig.7. 35 Pressure and temperature display at TDC

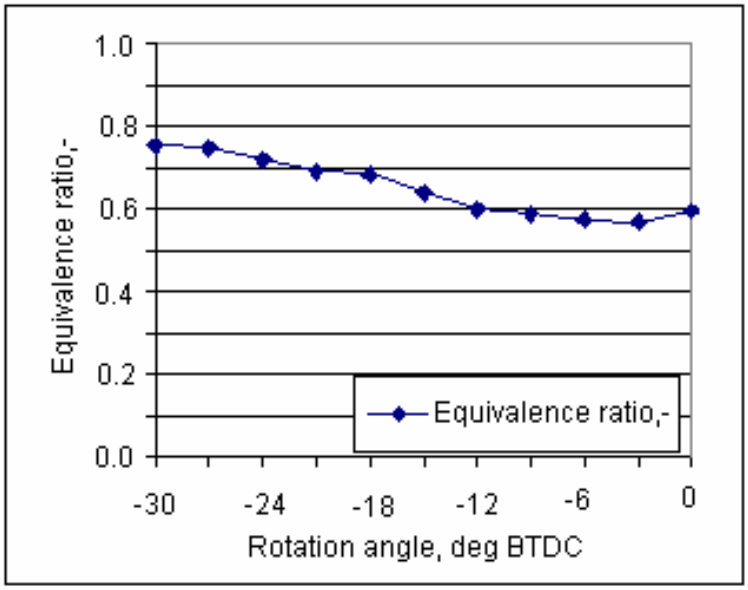

Fig.7. 36 Mixture equivalence ratio at spark plug position

7.5.3 High-pressure injection

The high-pressure hydrogen injection strategy is similar to diesel engine spray, where hydrogen is injected at engine high-pressure, just few degrees BTDC. The hydrogen is then ignited and burned in locally rich region, even if a very small amount of hydrogen was injected. This strategy lets the engine to be run very lean overall. Similar to the diesel injector

optimization of spray angle and angle between injection holes introduced in the previous chapter, several hydrogen injection models were tested and two optimized models were presented in the following example.

In the next model example, two injectors of one hole injector and three holes injector were tested and the results were presented. Figure 7.37 shows geometrical models of both injectors (a, b). In this example model, the angle between holes in three holes injector is set to be 15º and 12º the declination angle to horizontal, long axis. The moving mesh tool was used to rotate the rotor from 24º BTDC to 24º ATDC.

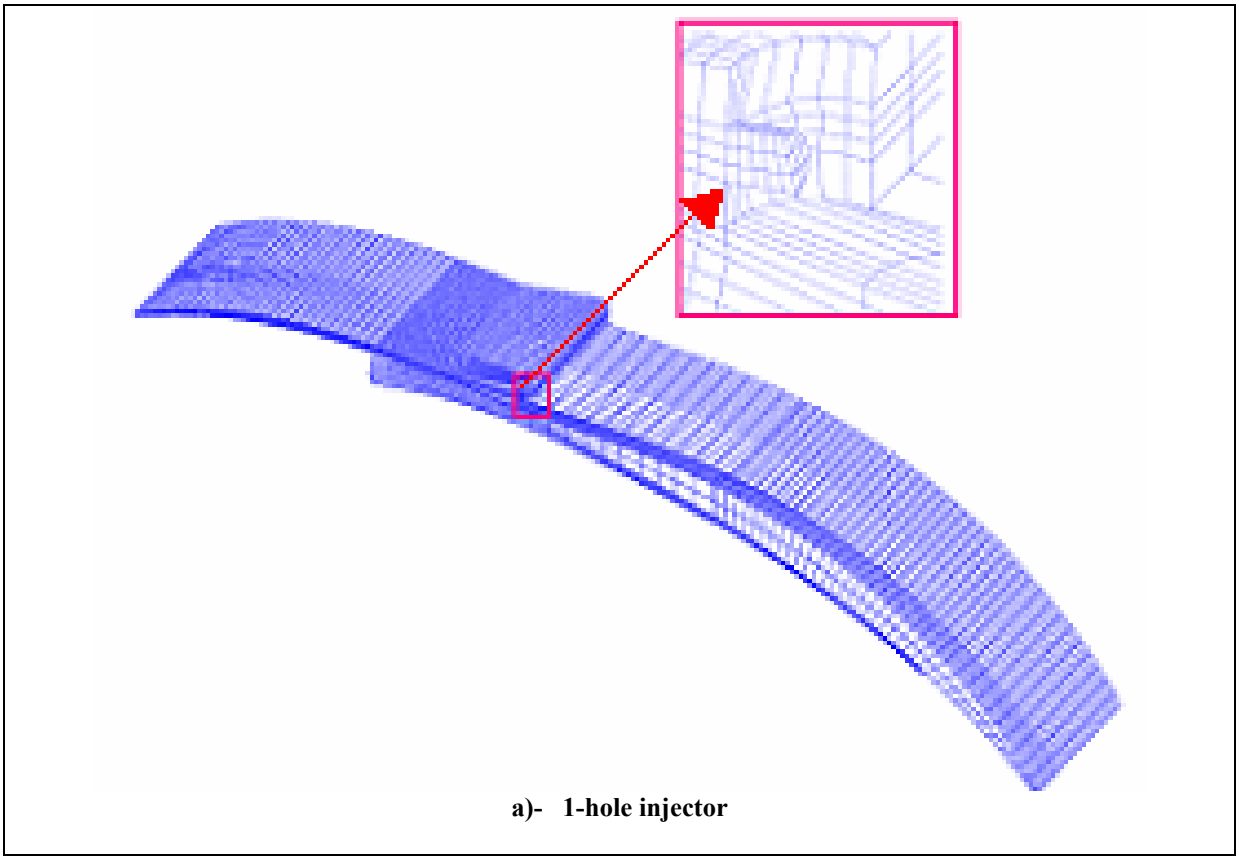

a)- 1-hole injector

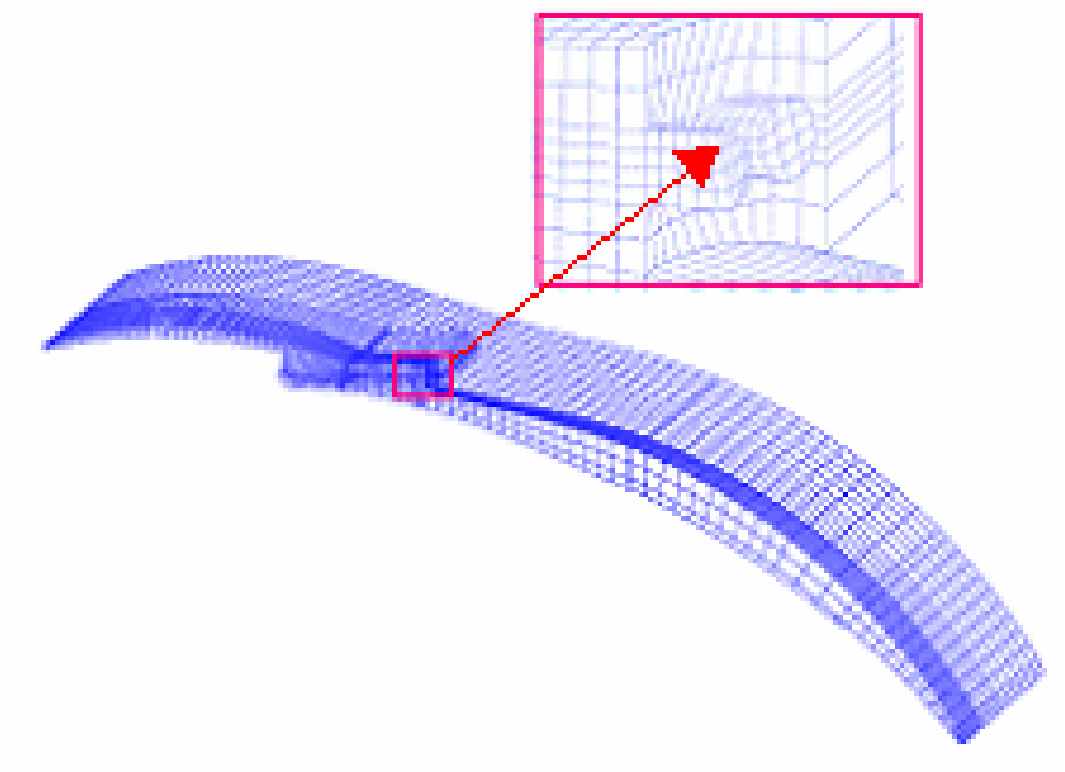

b)- 3-hole injector

Fig.7. 37 High-pressure hydrogen injection geometry

The hole diameter is 1.5mm for one hole injector and 1.2mm for three holes injector.
The boundary and initial conditions were to be as indicted table7.2.

Initial pressure, pa	Temperature, k	Turbulence model	Engine speed, rpm	Injection start angle, deg.
1.5e+6	550	Kε	2000	20º

Table-7. 2 Models initial conditions

7.5.4 Results

The results of high-pressure hydrogen injection were displayed and plotted on the following figures. The hydrogen mass fraction display for both models is presented on figures 7.38 (a, b). On this figure, it can be clearly seen that the hydrogen mass concentration covers more surface area when using multi-hole injector, and hence better mixture formation.

For one hole injector, the mixture equivalence ratio at the spark plug position (31mm) is presented on figure 7.40 (a), and the injector lift timing on figure 7.40 (b). Similar results for three holes injector are presented on figure 7.41 (a, b).

Immediately after the injection starts the mixture equivalence ratio can reach very high levels making hydrogen rich zone could reach up to (Φ =13).

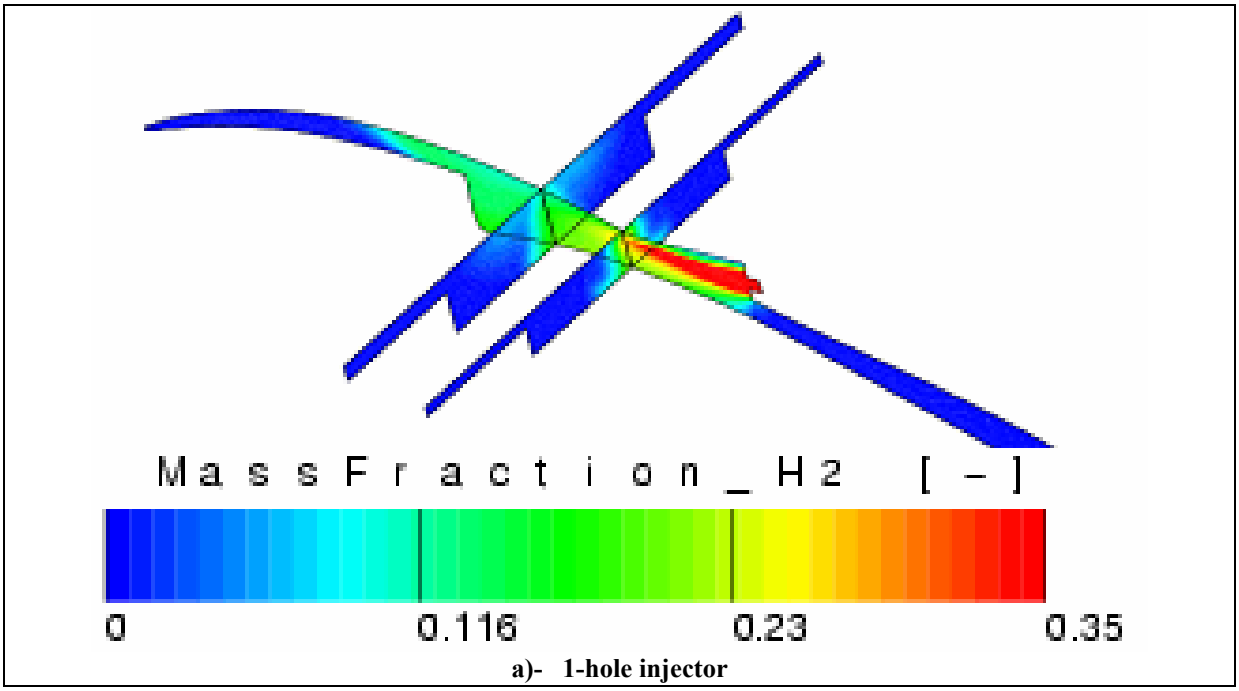

a)- 1-hole injector

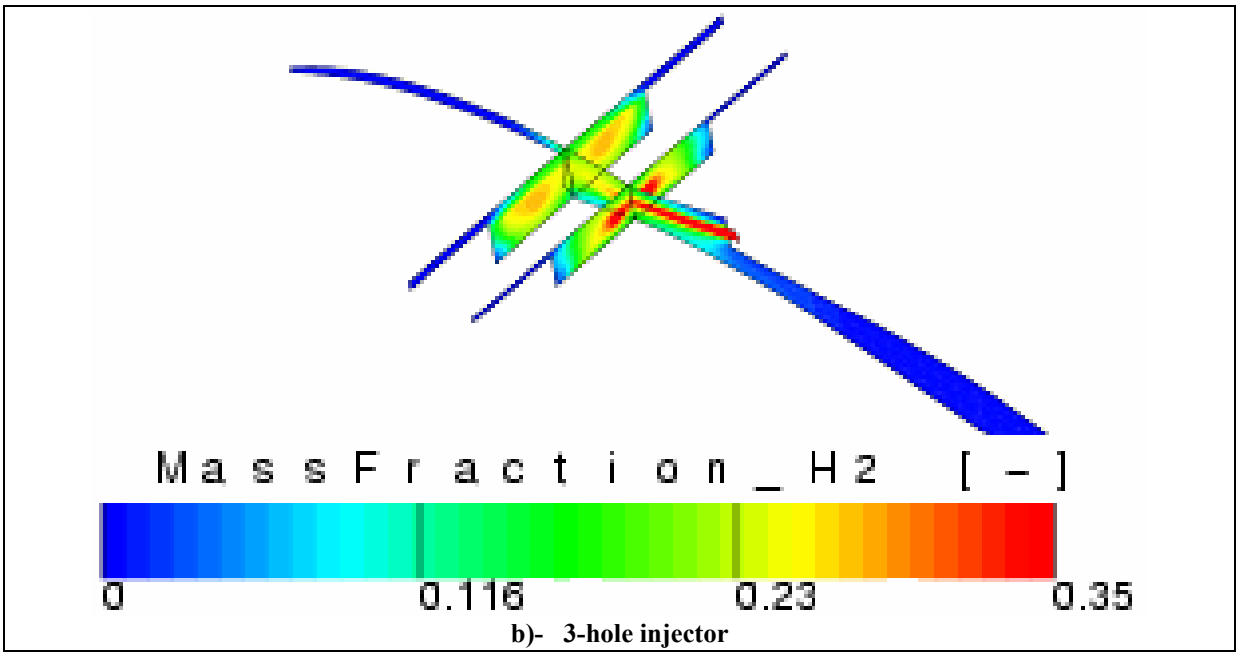

b)- 3-hole injector

Fig.7. 38 Injected hydrogen mass fraction

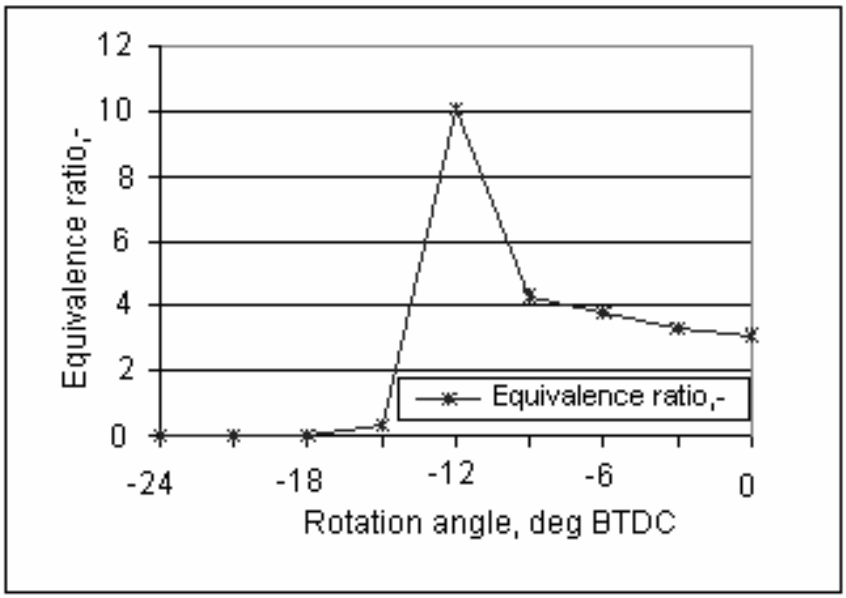

a)- Equivalence ratio

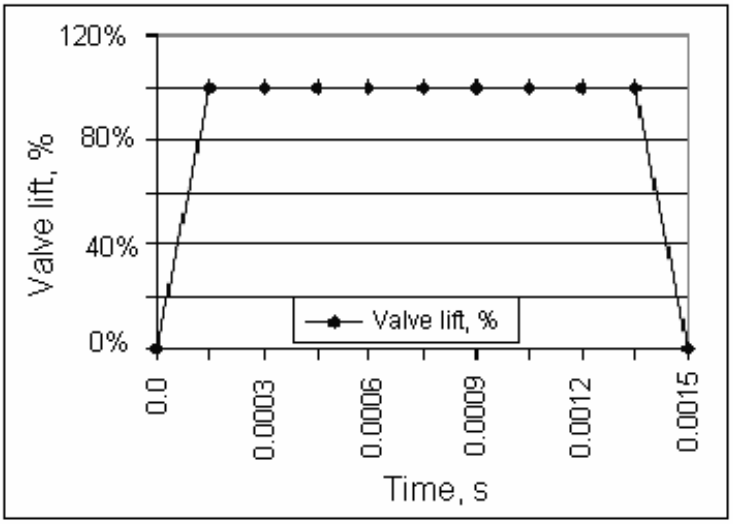

b)- injector valve lift

Fig.7. 39 1-hole injector equivalence ration at spark plug position

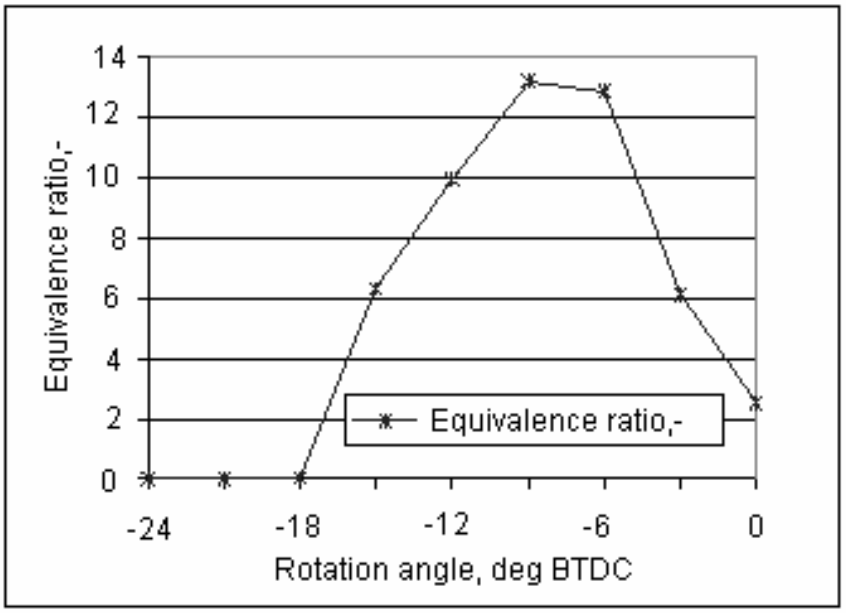

a)- Equivalence ratio

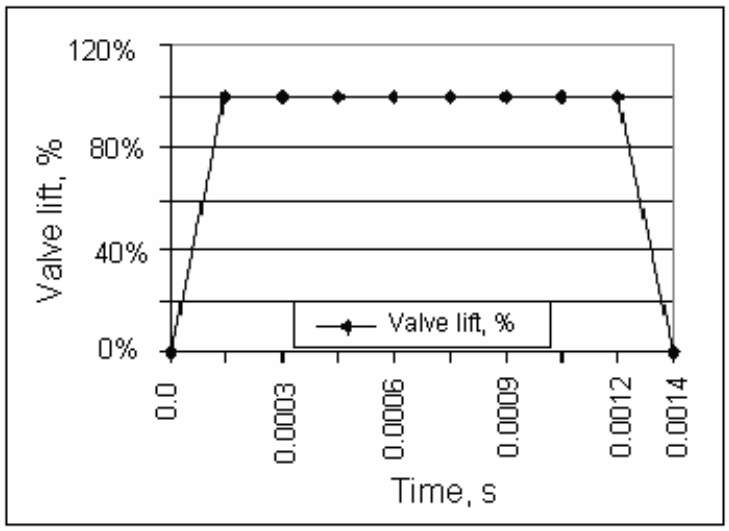

b)- injector valve lift

Fig.7. 40 3-hole injector equivalence ration at spark plug position

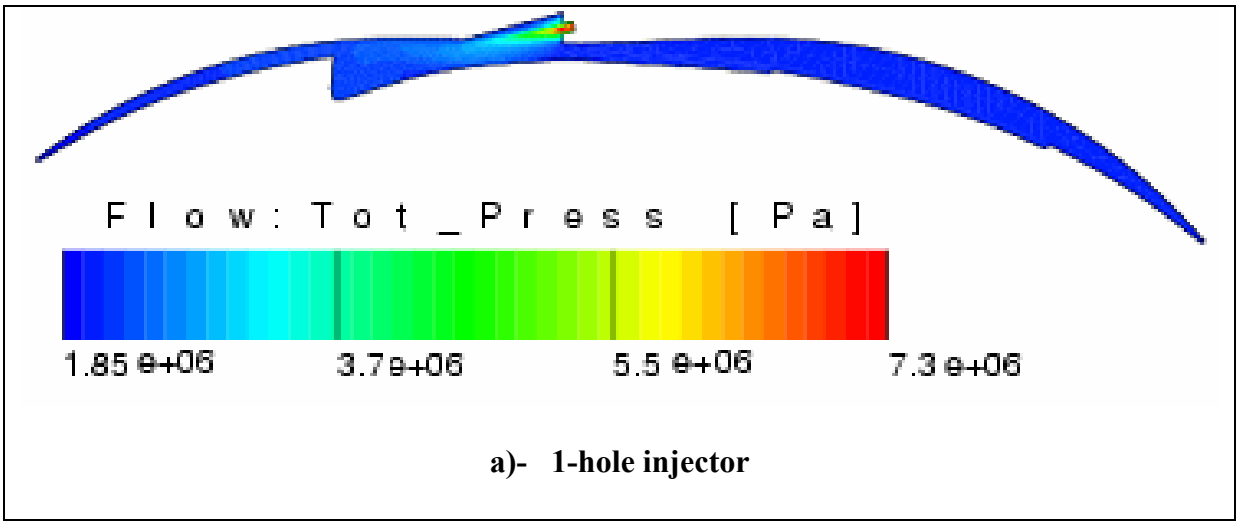

a)- 1-hole injector

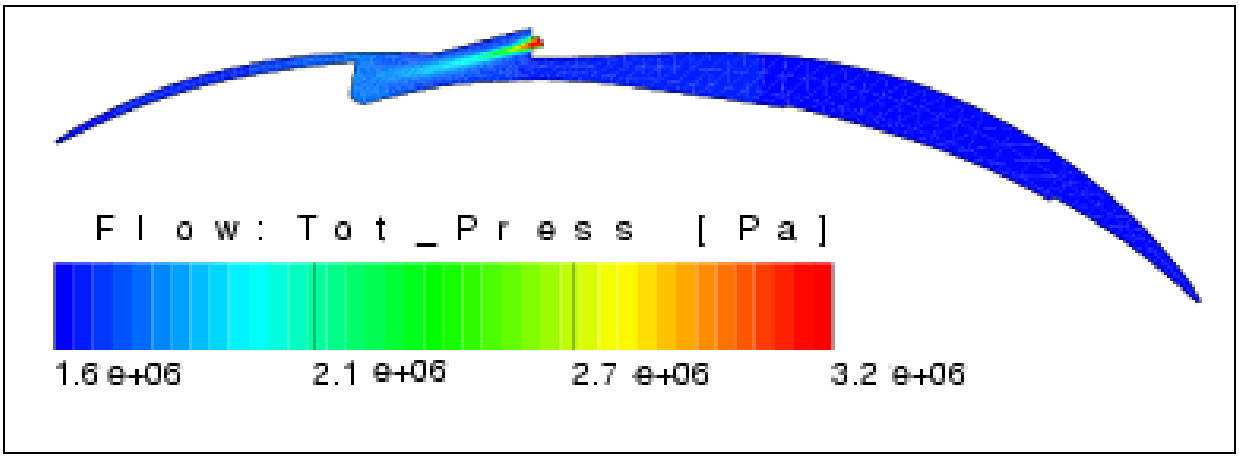

b)- 3-hole injector

Fig.7. 41 Maximum injection total pressure

The maximum injection pressure reaches 7.3e+6 pa for one hole injector and 3.2e+6 pa for three holes injector.

7.6 Hydrogen combustion

In this research thesis, the main objectives are concentrated on the 3-D complex fluid flow inside the combustion chamber of Wankel engine and liquid and hydrogen fuel mixture formation. In this part of this chapter, highlights on hydrogen combustion and different parameters affected hydrogen combustion have been studied and presented in this part.

In previous study by Liu [1] (has already been introduced), this study has concentrated combustion models available in AVL-Fire Code of both versions 7.3.1 and 8.3, and suitability for hydrogen combustion. The study proves that the TFSC Model (Turbulent Flame Speed Closure Model) is the best model suits the hydrogen combustion with its high burning velocity. Due to the model limitations, it is possible to study the hydrogen combustion with reasonable results between, Φ=0.5 to Φ =1.

According to this study, it is not necessary to repeat or to check all available models again to predict the suitable model for hydrogen combustion, and hence only the TFSC Model were used for hydrogen combustion. Unfortunately, this model is only available in AVL-Fire version 8.3, so only fixed mesh of full surface of Wankel engine model were used to study the different parameters affecting hydrogen combustion.

The Wankel engine mesh used for this study is presented on figure 7.42, where the position of this model was set to be 15º BTDC. The boundary and initial conditions were presented on table 7.3.

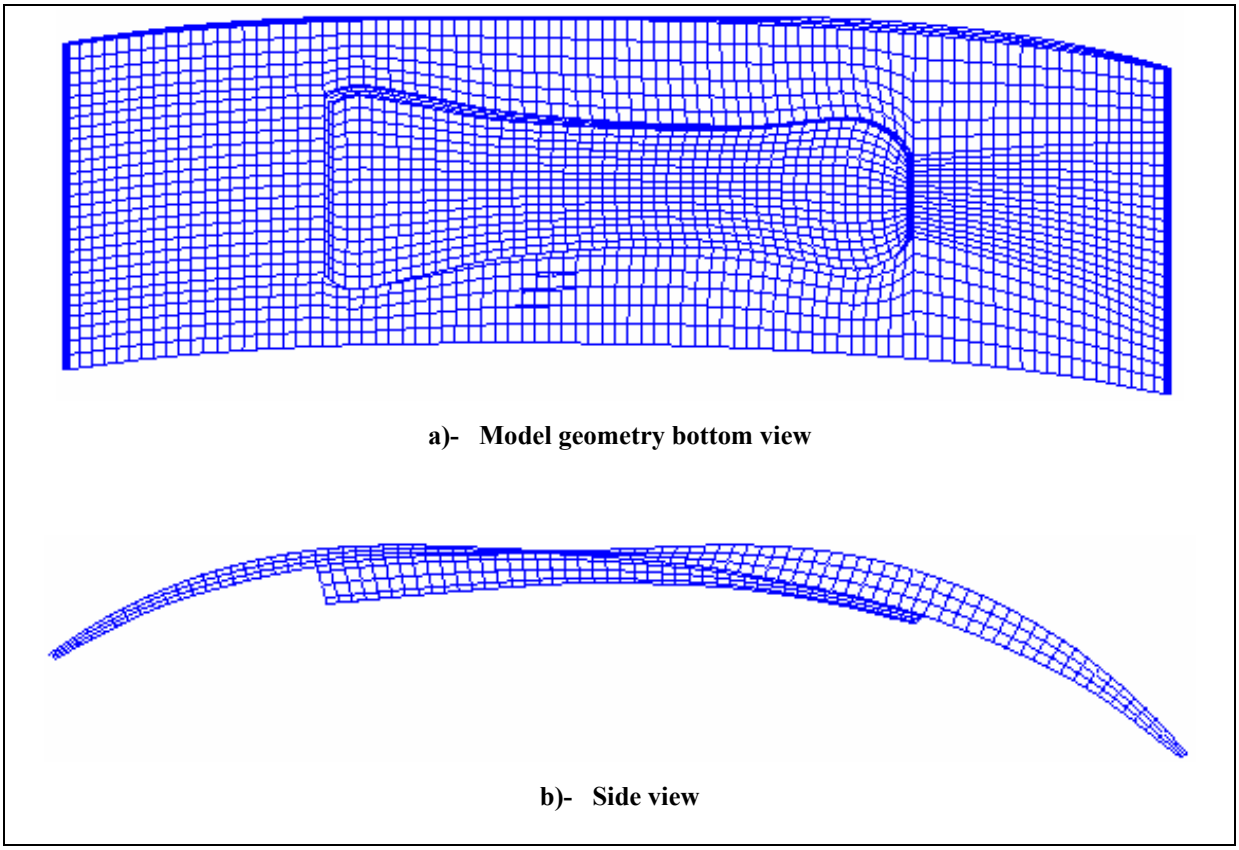

a)- Model geometry bottom view

b)- Side view

Fig.7. 42 Hydrogen combustion model

Initial pressure, pa	Temperature, k	Model Geo	Turbulence model	Combustion Model	Constant CFP
3.2e+6	750	Full Geo	kε	TFSC	3.4

Table-7. 3 Model initial conditions

7.6.1 Results

The results of homogeneous charge combustion were plotted and presented on the following figures, where the mixture concentration was set to be stoichiometric (Φ =1).

Figures 7.44 (a, b), show the pressure and temperature changes against time during combustion.

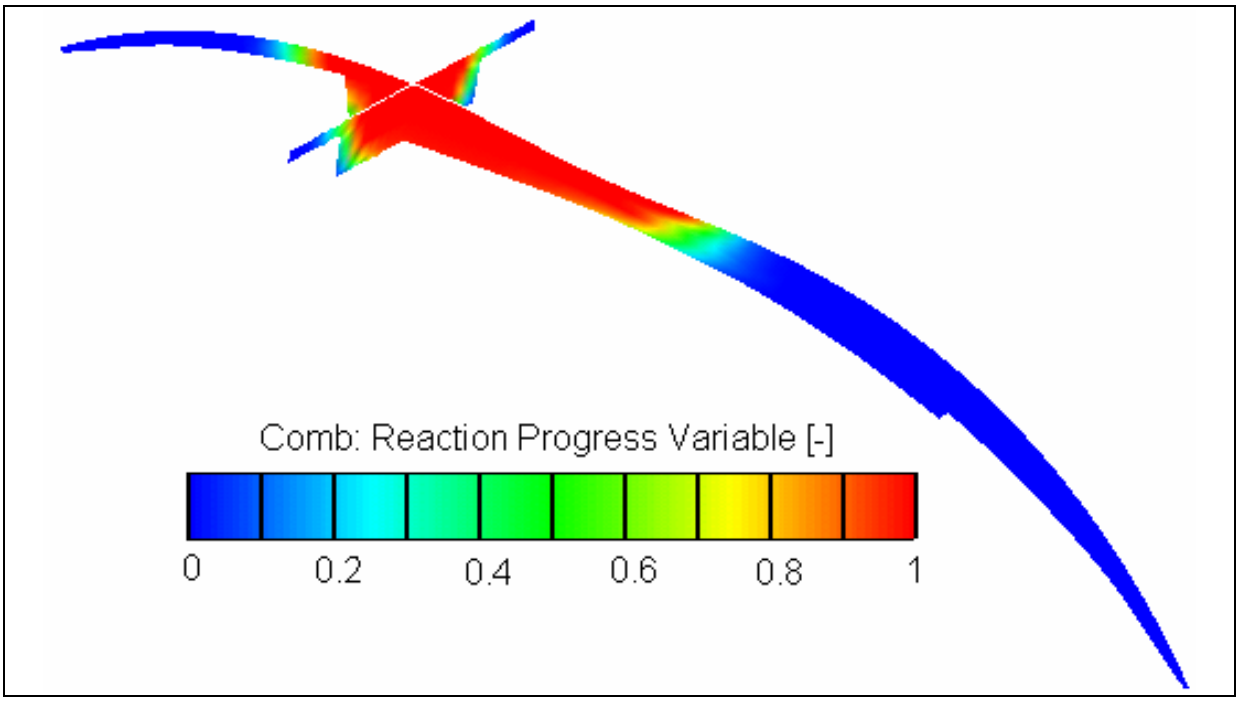

Fig.7. 43 combustion reaction progress variable at 2ms

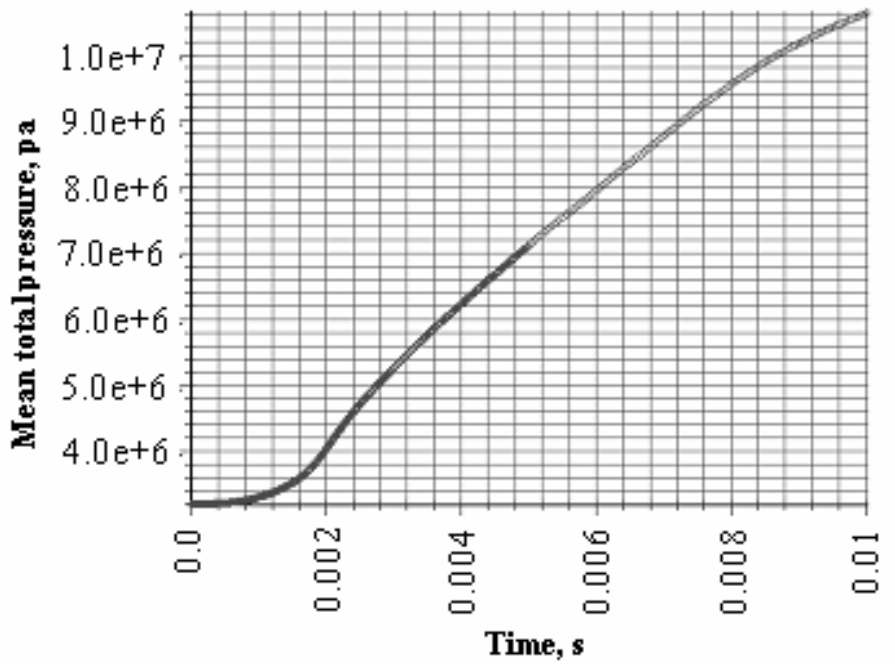

a)- Pressure changes

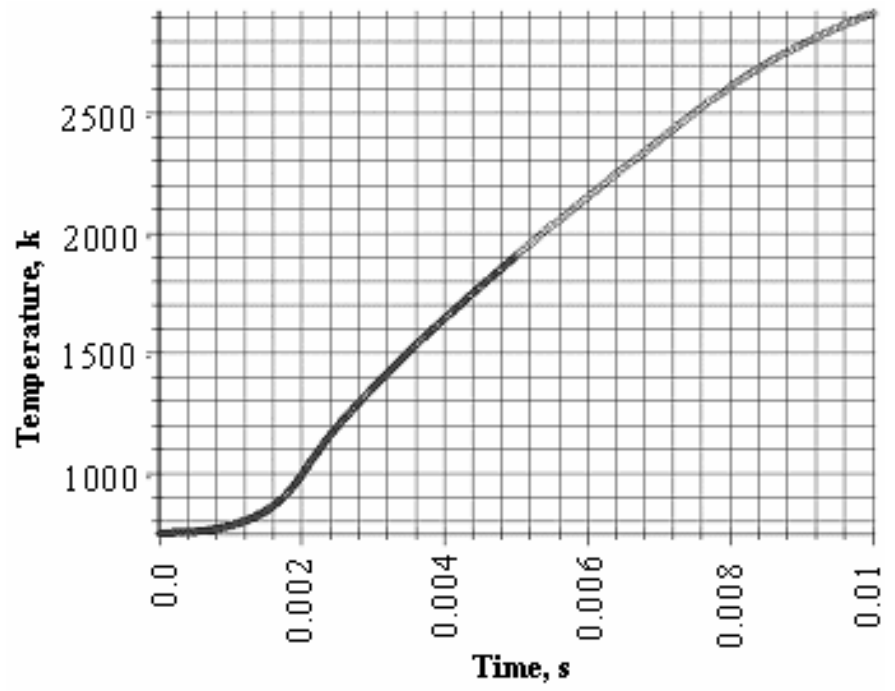

b)- Temperature changes

Fig.7. 44 Pressure and temperature changes

Figure 7.45 (a, b), shows the rate of heat release, turbulent kinetic energy and dissipation rate changes during hydrogen combustion. Figure 7.46 shows the mean NO_x mass fraction.

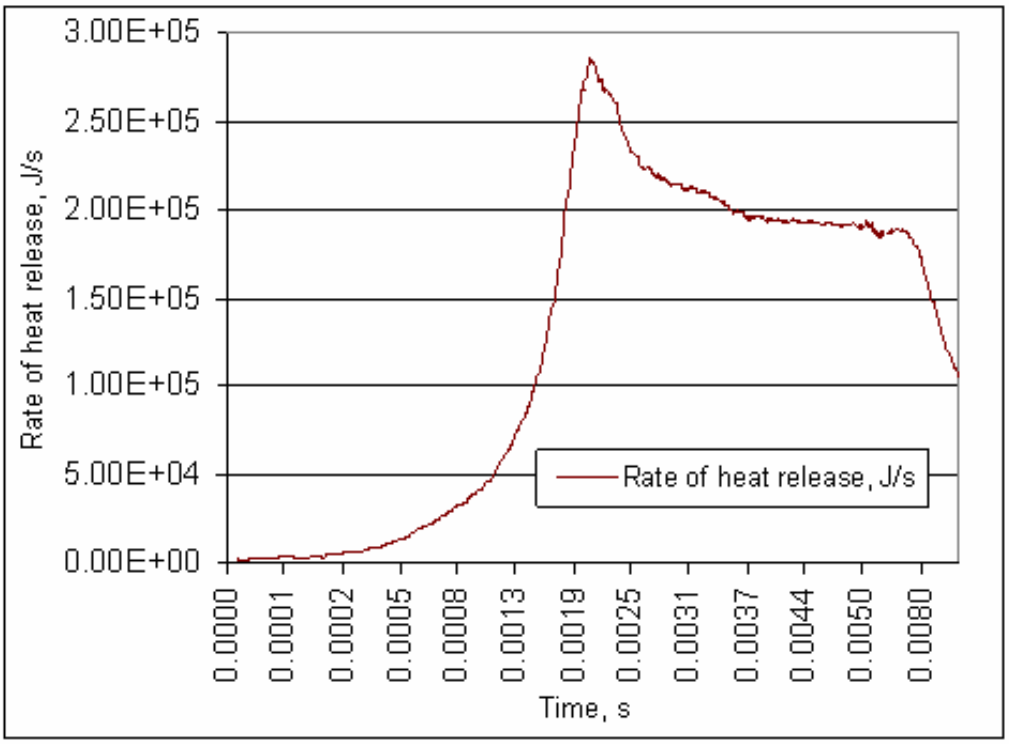

a)- Rate of heat release

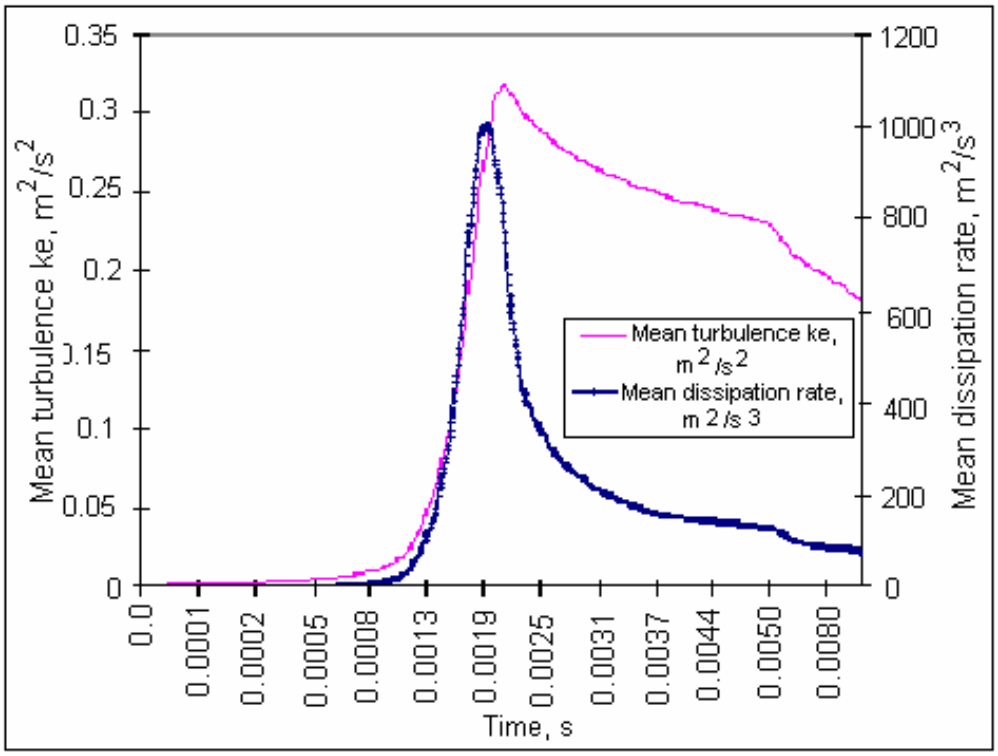

b)- Tke and dissipation rate changes

Fig.7. 45 Rate of heat release, Tke and dissipation rate changes

It can be seen that the NO_x mass fraction is increased more rapidly near the end of combustion, clearly because the temperature become higher and high temperature is the main reason that can produce more nitrogen oxides.

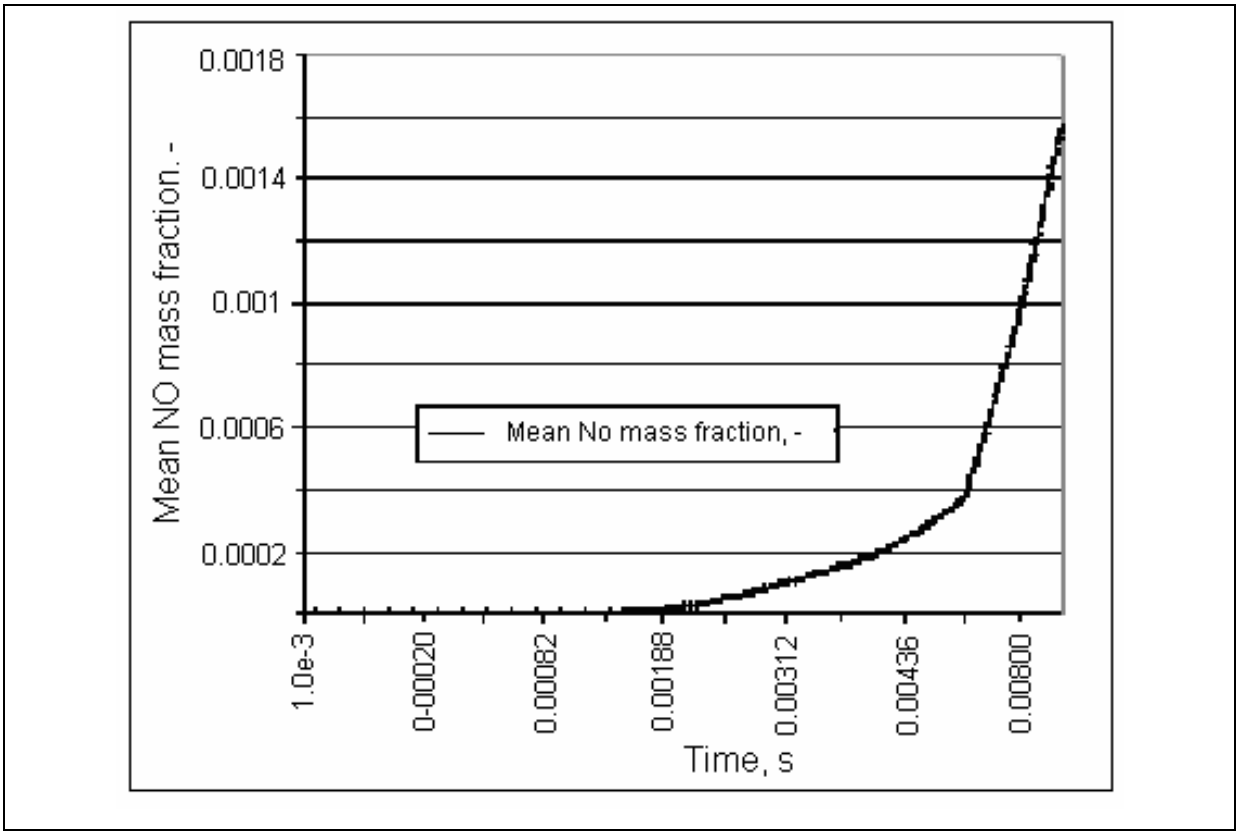

Fig.7. 46 Mean NO_x mass fraction

7.6.2 Effect of different initial parameters

The effects of different initial parameters, like initial temperature, pressure and mixture concentration on hydrogen combustion were tested and results were presented.

7.6.2.1 Initial temperature effect

The initial temperature was varied to be 600k, 650k, 700k and 750k to test its influence on the hydrogen combustion and on the NO_x formation. The results were presented on the following figures. Figure 7.47 (a), shows the effect of initial temperature on mean (average) pressure and temperature. The mean temperature at the end of combustion is increased

significantly (2200 k to 2900 k), as the initial temperature increased. The rate of heat release is also increased as the initial temperature increased that can be seen clearly on figure 7.47 (b).

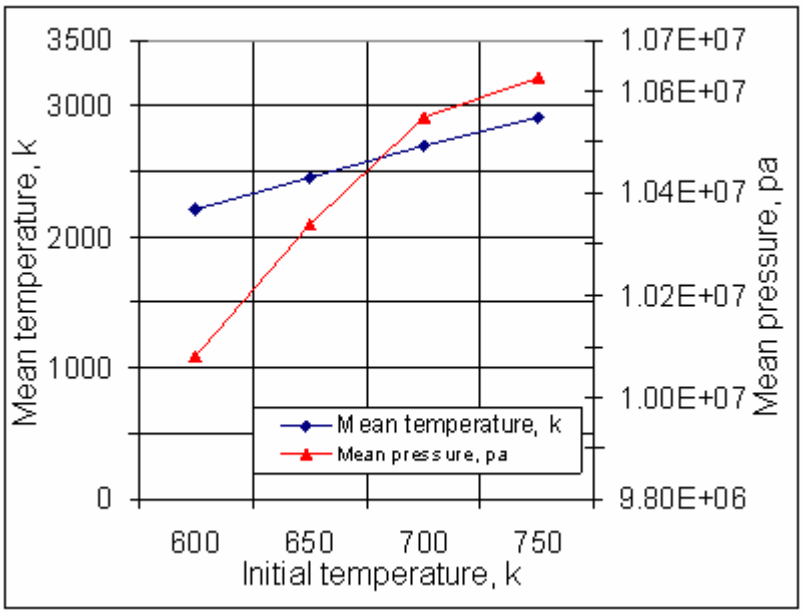

a)- Mean pressure & temperature changes

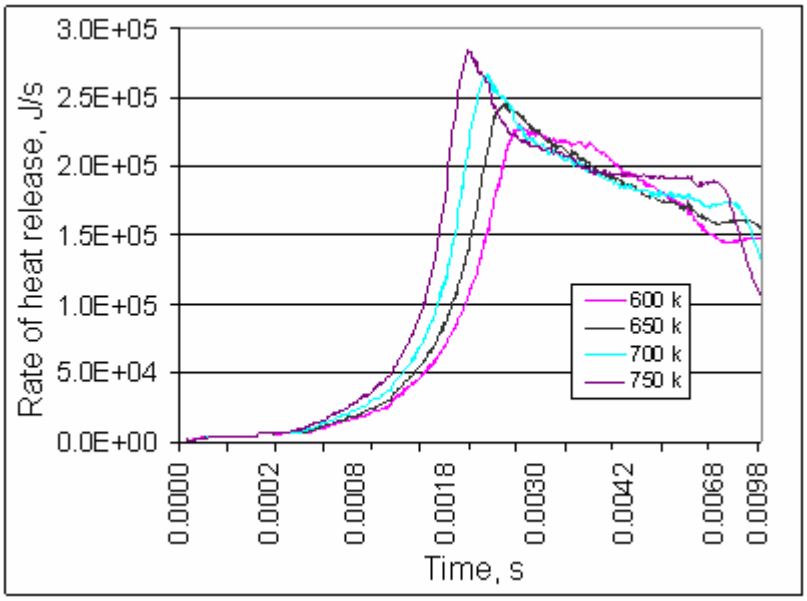

b)- Rate of heat release changes

Fig.7. 47 Effect of initial temperature on end mean pressure, temperature and rate of heat release

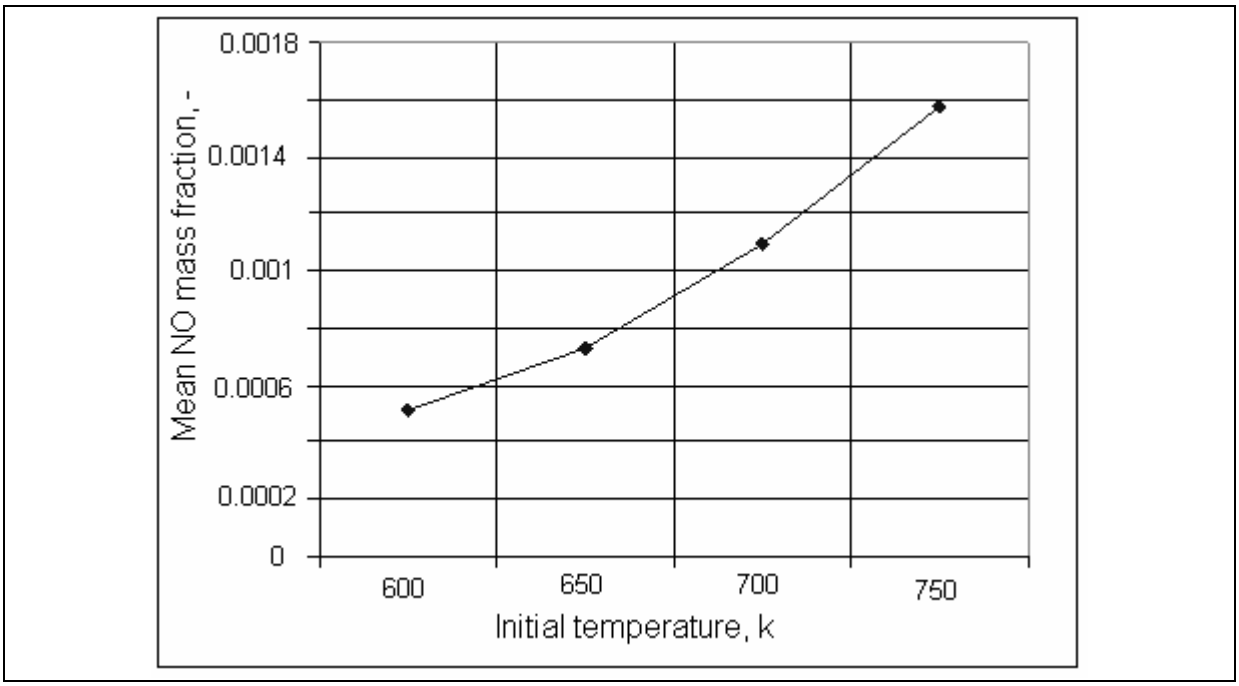

Fig.7. 48 Effect of initial temperature on NO_x mass fraction

The NO_x mass fraction on figure 7.48 is also increased, clearly because of higher temperatures accelerates the NO_x formation exponentially.

7.6.2.2 Initial pressure effect

The initial pressure was varied to be 2.0e+6pa, 2.5e+6pa and 3.2e+6pa to test its influence on the hydrogen combustion and on the NO_x formation. The results were presented on the following figures. It can be seen on figure 7.49 (a), that the initial pressure has a little inversely effect on the mean end temperature and a significant influence on the end average pressure. The rate of heat release is also increased as the initial pressure increased, as it can be seen on figure 7.49 (b).

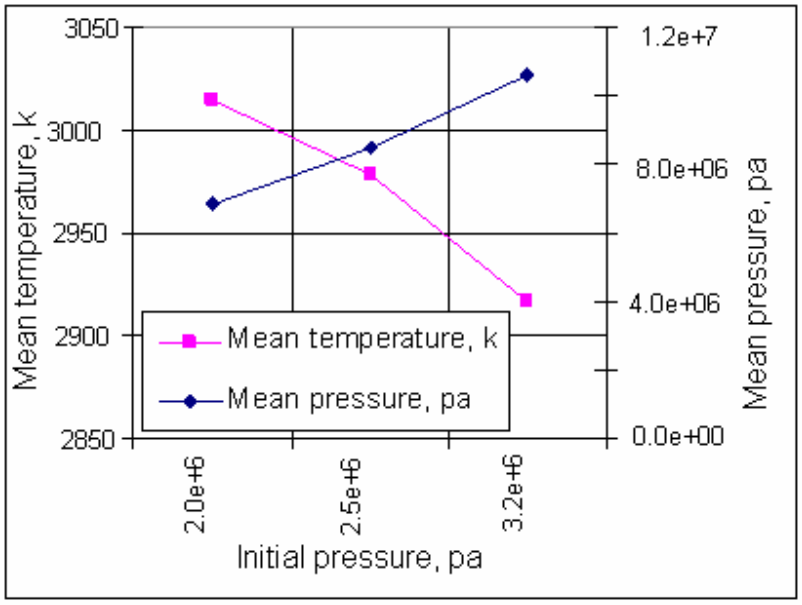

a)- Mean pressure & temperature changes

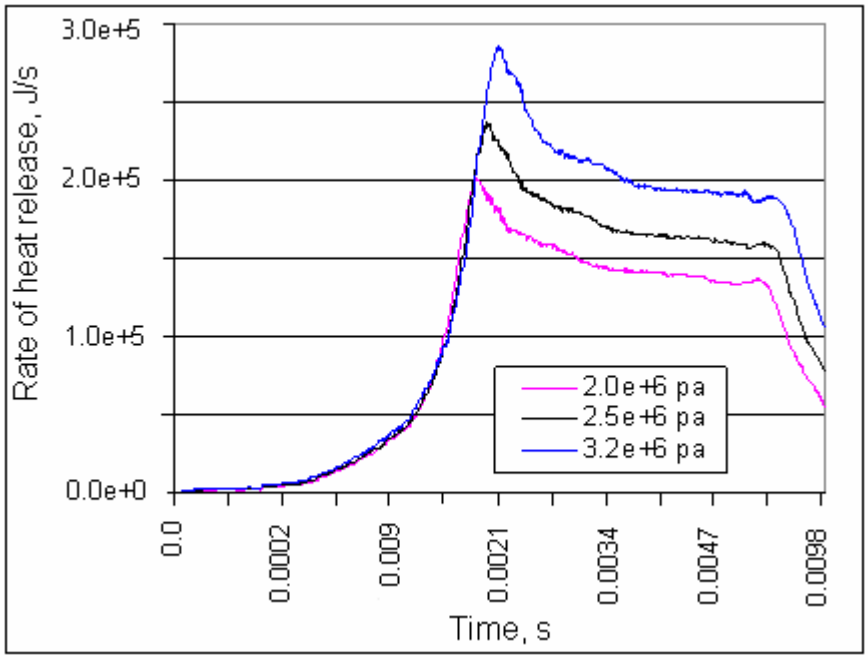

b)- Rate of heat release changes

Fig.7. 49 Effect of initial pressure on mean temperature, pressure and rate of heat release

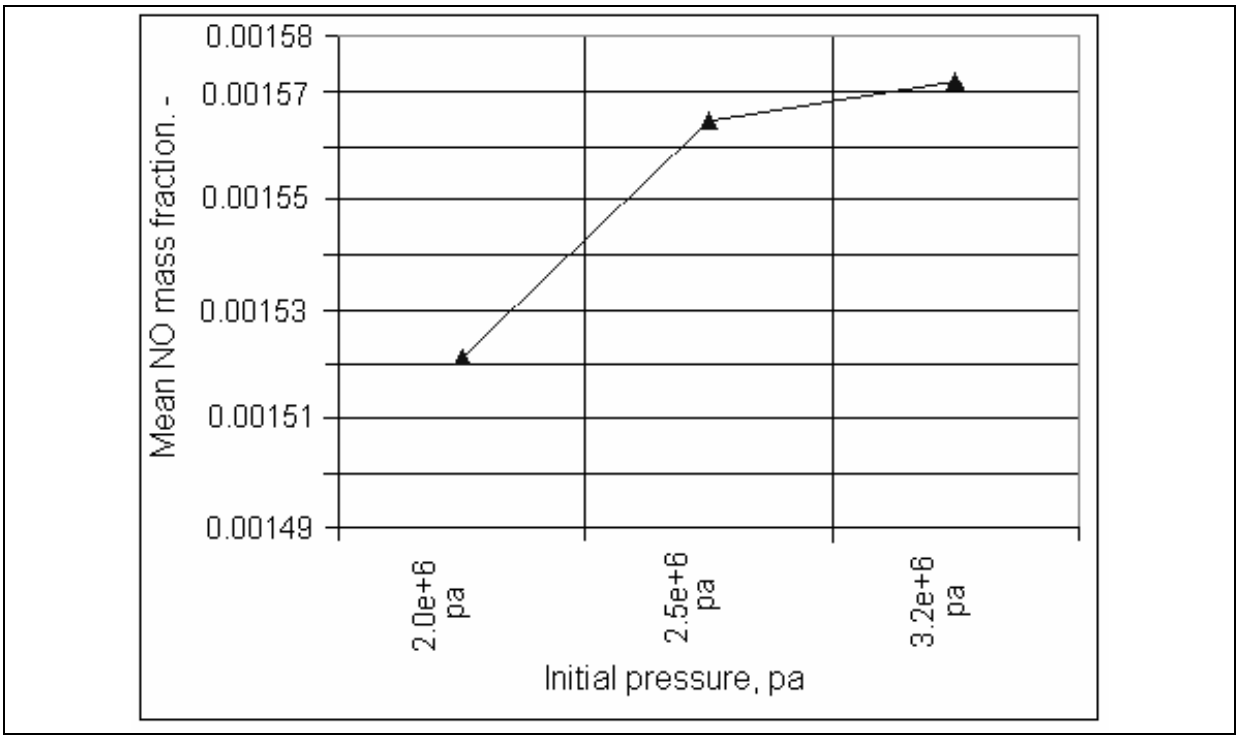

Fig.7. 50 Effect of initial Pressure on NO_x mass fraction

Figure 7.50 shows very little or almost no effect of the initial pressure on the NO_x mass fraction or NOx formation, clearly because it has very little effect on the final mean temperature.

7.6.2.3 Mixture concentration effect

Homogeneous mixture with concentration varied between (Φ=0.4 to Φ=1), the effect of mixture concentration was studied and comparison results were presented in the following figures.

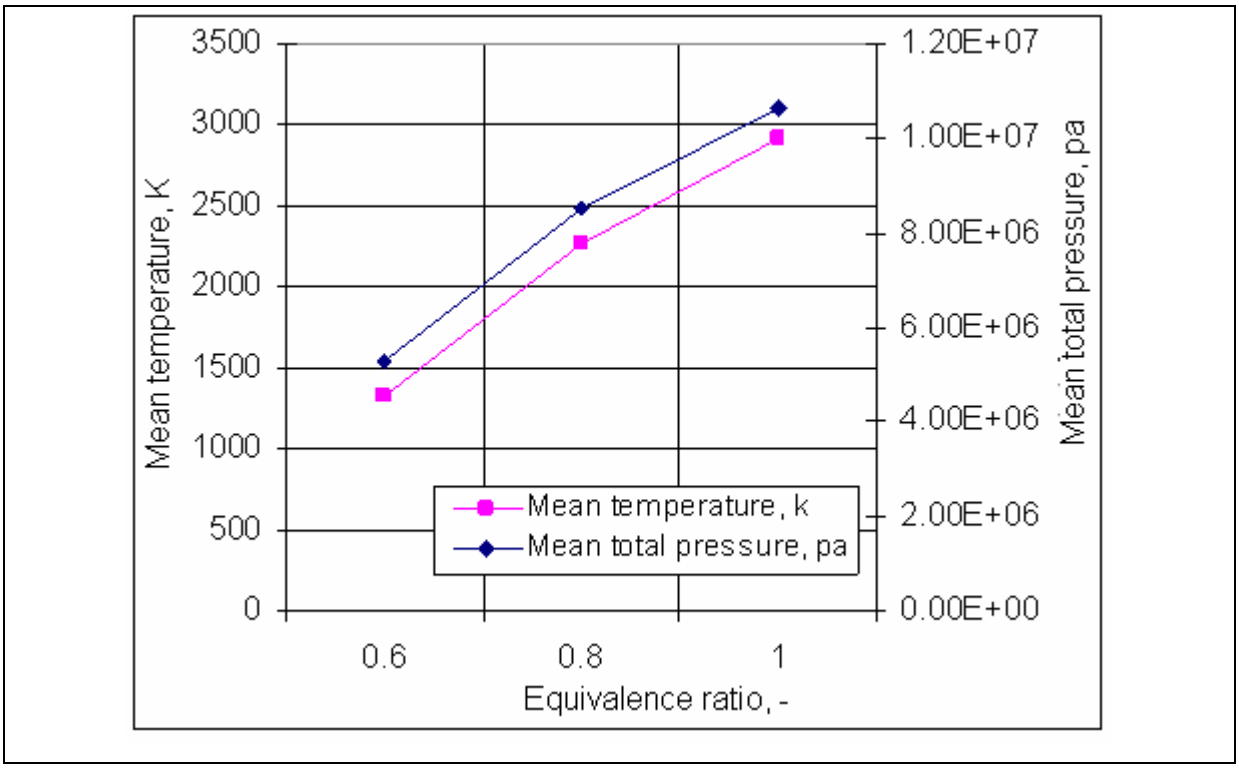

Fig.7. 51 Effect of mixture concentration on mean temperature and pressure

The end mean temperature and pressure are clearly dependent on the mixture concentration as shown on figure 7.51, that can be supported by figure 7.52 (a, b), where the heat release rate and accumulated heat are significantly increased causing higher over all mean pressure and temperature.

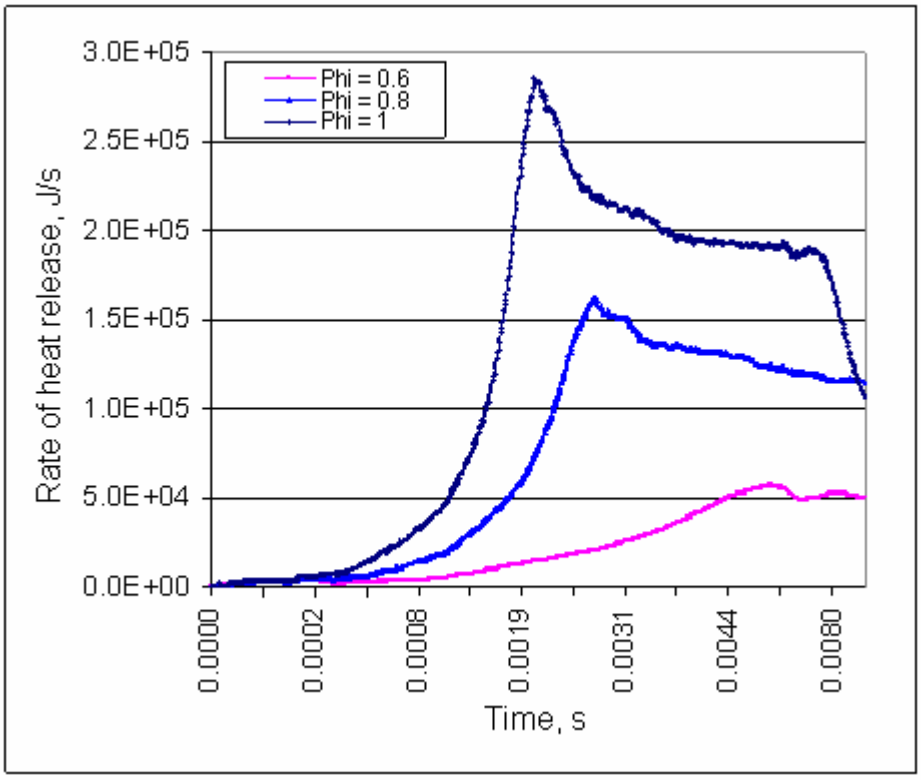

a)- Rate of heat release changes

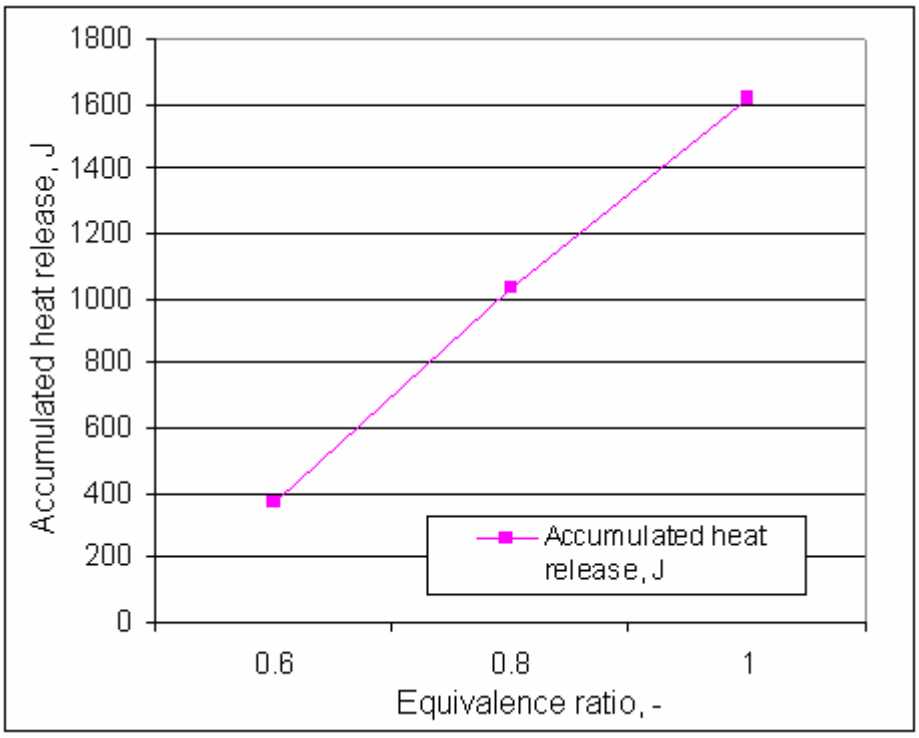

b)- Accumulated heat, J

Fig.7. 52 Effect of mixture concentration on rate of heat release and accumulated heat released

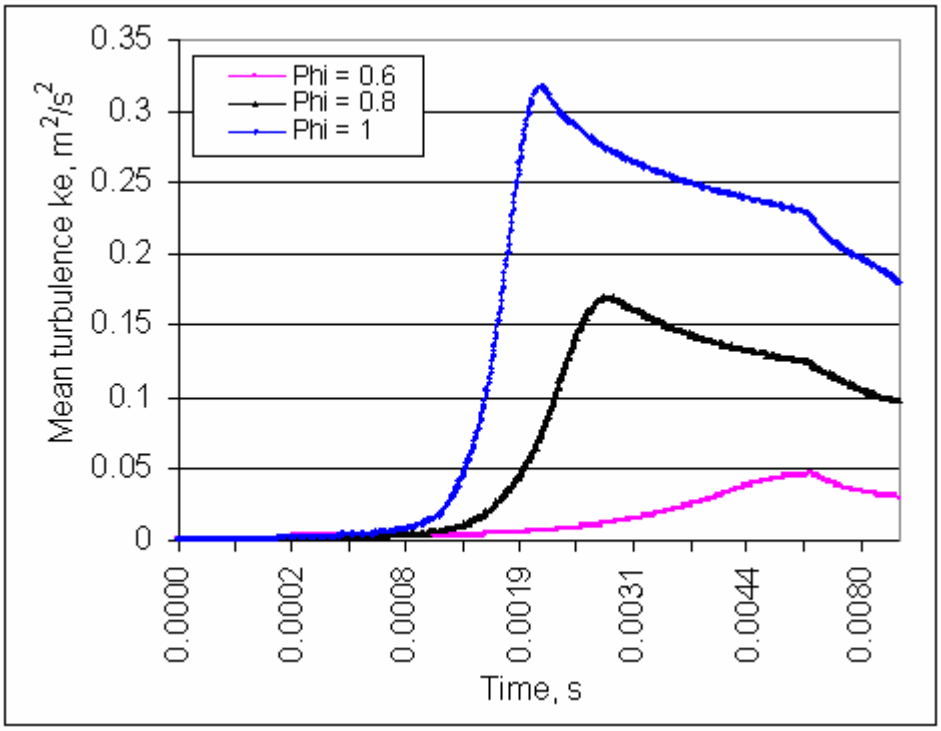

a)- Mean turbulence kinetic energy

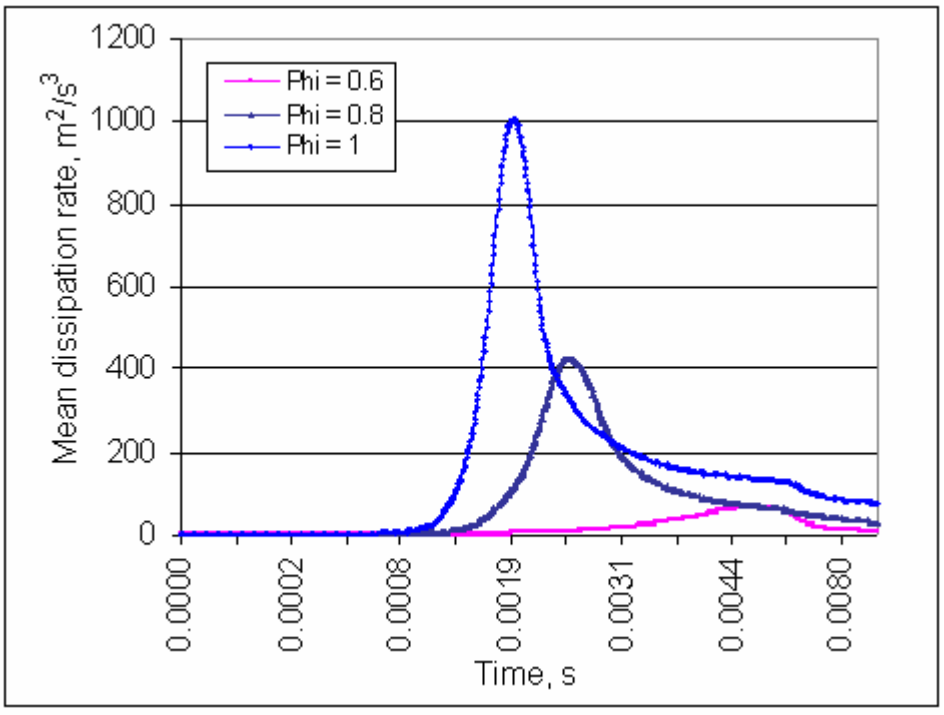

b)- Mean dissipation rate

Fig.7. 53 Mixture concentration effect on mean Tke and dissipation rate

The mean Tke and dissipation rate are greatly dependent on the mixture concentration, as shown on figure 7.53 (a, b).

The mixture concentration has major effect on NO_x production. At low concentration (lean, Φ=0.6) and (stoichiometric, Φ=1) mixtures, the mean NO_x mass fraction is very low (max. 0.0016) in comparison to relatively high concentration of (Φ=0.8), as it can be seen on figure 7.54, where the mixture concentration of (Φ=0.8) was plotted separately, because of big scale difference, (mean NO_x mass fraction reaches 0.073).

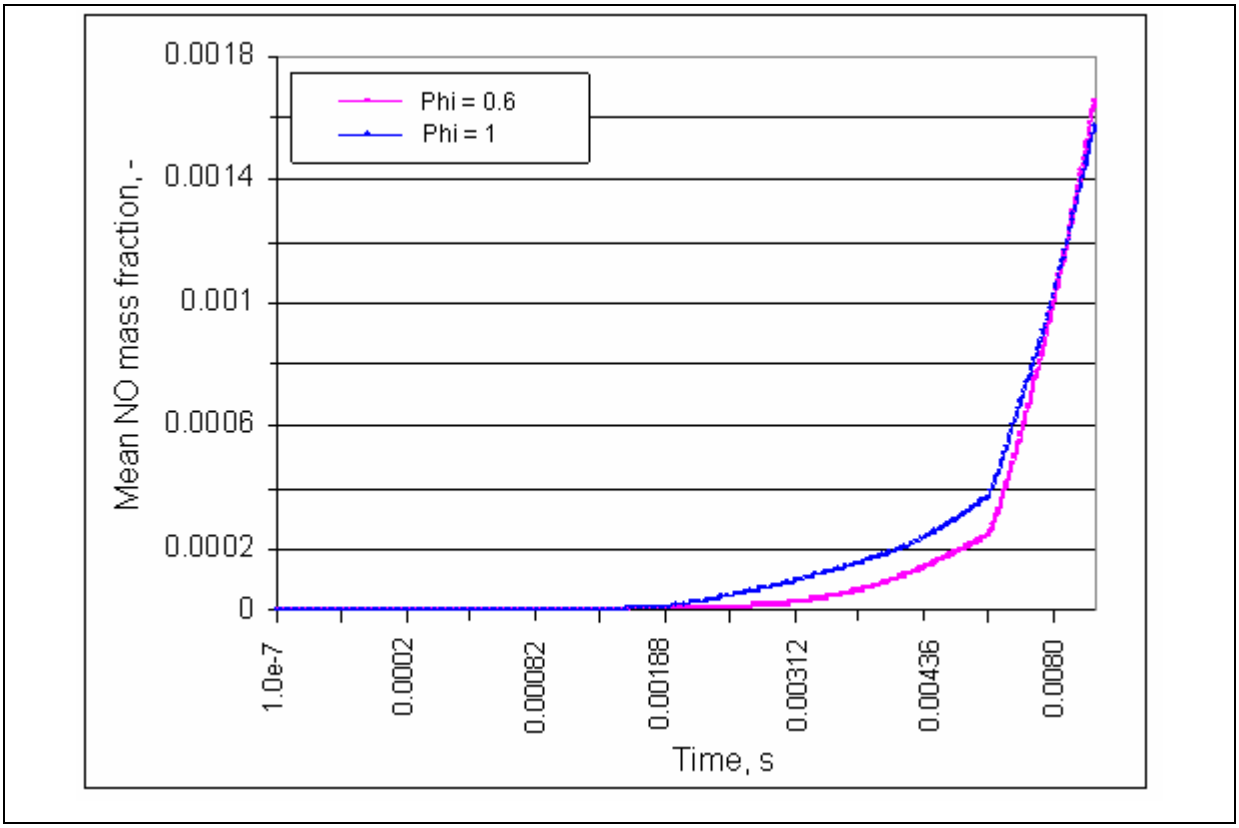

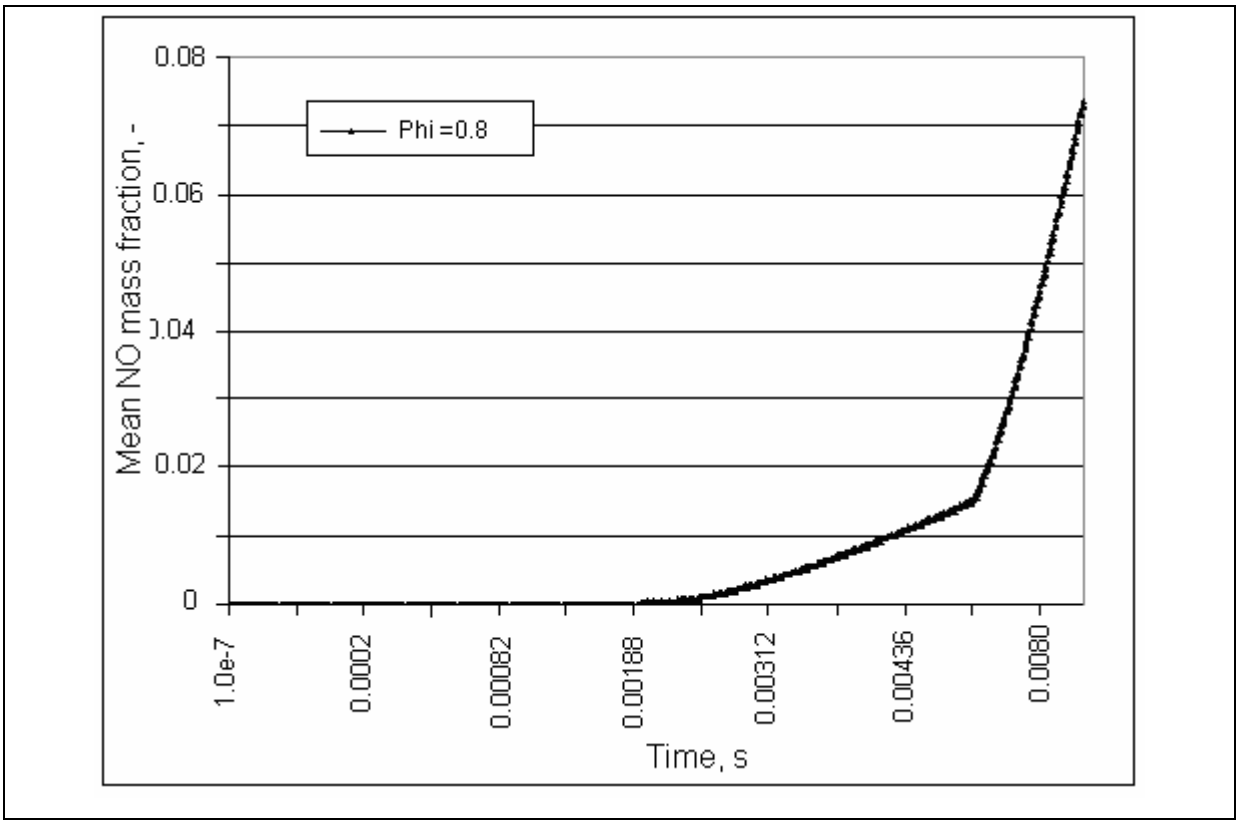

Fig.7. 54 Mixture concentration effect on mean NO_x mass fration

The hydrogen combustion is normally produced a very low NO_x when burns at lean concentrations, because of less heat produced. At stoichiometric homogeneous combustion, produces also very little amount of NO_x, clearly because of no oxygen will be left to produce nitrogen oxides. The production of nitrogen oxides is very high when hydrogen is burned at high or near stoichiometric concentrations, clearly because of high combustion temperature and access air available to produce more nitrogen oxides.

Figure7.55 shows the NO_x production at different mixture concentration. Figure 7.56 shows the effect of mixture concentration on flame speed at different temperatures.

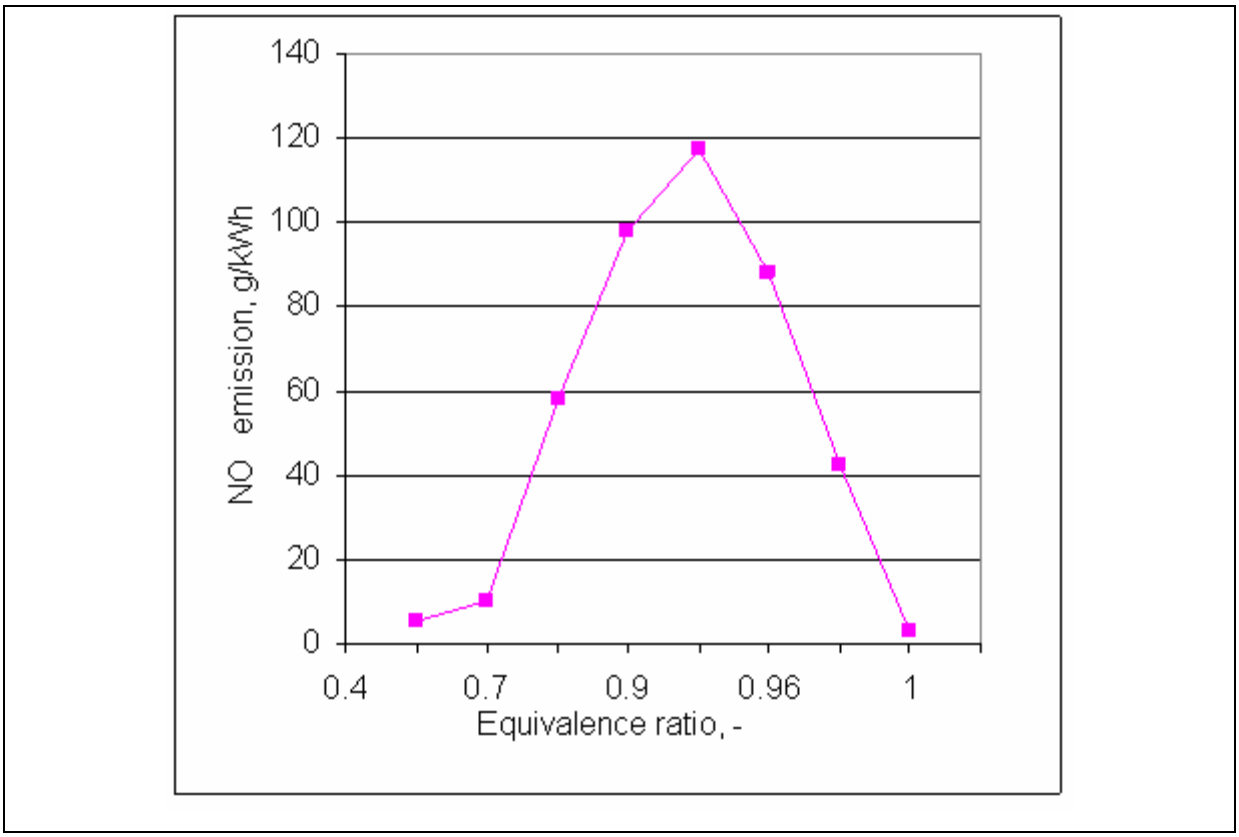

Fig.7. 55 NO_x as a function of mixture concentration

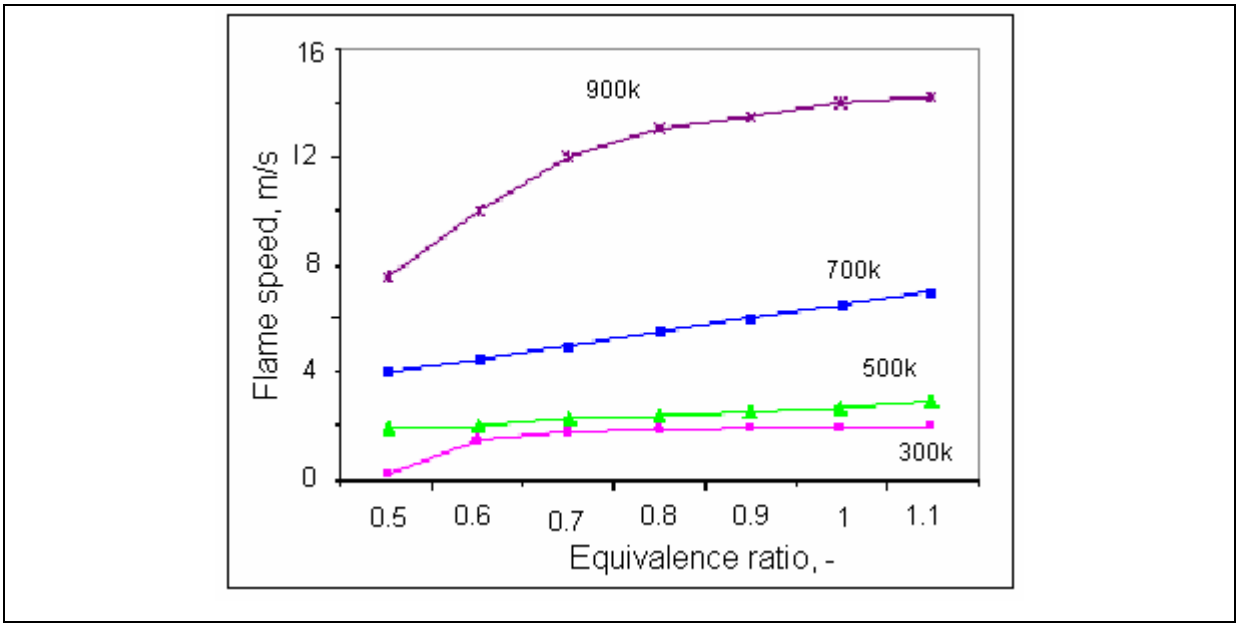

Fig.7. 56 Effect of concentration on flame speed at different initial temperature

7.7 Brief summary

In this chapter, the hydrogen mixture formation and combustion were studied; the results were presented and plotted in three parts. The first part concerns a general hydrogen injection to investigate the CFD capability of hydrogen injection and its validation and comparison to experimental hydrogen injection. Also, general investigation in the hole size that necessary to evaluate the right size suitable for certain hydrogen mass needs to be injected.

The second part concerns the hydrogen injection into real combustion chamber of Wankel engine, including low and high-pressure injection, using a single hole and three holes injector. The third part deals with hydrogen combustion and the different parameters that affecting combustion of hydrogen.

. The main conclusion of work in this chapter can be summarized as follows:

- According to this work and to previous work run by this chair, AVL-Fire code is capable of simulating hydrogen supersonic injection and proved a good agreement with experimental results.
- Multi-hole injector gives better fuel distribution and reduces the maximum rail pressure needed to inject the right amount of hydrogen in very limited short time.
- Low-pressure injection gives almost homogeneous mixture at the end of compression stroke and hence betters combustion.
- The use of two injectors in low-pressure injection, gives the choice of injecting the huge volume of hydrogen needed in very short time with lower rail pressure. To reduce the injection pressure, Mazda has used two injectors in its low-pressure direct injection engine.
- High-pressure hydrogen injection is more sophisticated system, needs a very high injection pressure and complicated pressure instruments installation. Also, the injector it self still under development and not yet available in market.
- According to the above, it is simpler to install low-pressure injectors and inject the hydrogen at low pressure after the inlet port closed to avoid any additional installations to raise the injection pressure.
- Hydrogen combustion produces high temperatures and hence high nitrogen oxides. Therefore, it is necessary to control NO_x formation by controlling the mixture

concentration. That means the engine should run on lean mode at low and medium loads with wide open throttle and at high loads runs at stoichiometric concentrations, throttle controlled.

- In normal piston engine, the high flame speed of hydrogen could cause power shock due to sudden heat release. But, when hydrogen is burned in long combustion chamber of Wankel engine that will be an advantage where the flame travels longer distance and hence smoother heat released. Also the use of one spark plug is possible.

In the next chapter, a general conclusion will summarize all parts of this thesis work, including, flow investigations, diesel spray and hydrogen injection.

8

Summary and Main Conclusion

In this research work, the main objectives were concentrated on Wankel engine and its air/Fuel mixture formation optimization, including diesel and hydrogen fuels. In other words, an engine that capable to run on multi-fuel, liquid and gas fuels. The tools available for such study were the CFD AVL-Fire in its versions V8.3.1 and V7.3.1. An experience has been gained in optimizing and validating models using these tools in previous work has been already done for BMW, at this chair by Fushui Liu [1].

To achieve such goal, it was necessary to study the engine it self, including the flow inside engine combustion chamber and its effect on the air/fuel mixture formation to improve engine combustion.

Since the mixture quality inside the engine chamber is the key point to improve the engine combustion and hence engine performance. So, the mixture formation has taken more attention in this thesis work with concentration on the different parameters that affects flow inside the combustion chamber and hence affects the mixture formation.

In this thesis, discussion and detailed assumption have been presented for each part separately. So, the main general conclusion of this work were summarized and presented in three parts as follows.

8.1 CFD Simulation

CFd simulation is an effective tool to study the different flow parameters including pressure, temperature, velocity…etc. AVL-Fire CFD tool is designed specially to study the different engine variable parameters, including flow, liquid fuel spray and gas injection, combustion and engine performance. It has been also proved to be an effective tool for supersonic flow of

hydrogen injection. All the relative aspects, such as grid and iterative convergence, should be carefully studied and adjusted before a reliable practical simulation can be done.

8.2 Wankel engine

The engine and mixture formation study can be summarized and concluded in three parts as follows.

8.2.1 Flow inside combustion chamber

Since the flow inside the engine chamber is important for the mixture formation especially when direct injection is applied. So, this complex 3-D flow has been studied and the following summarized conclusion can be made.

- The results show that two flow vortexes formed on both sides of the rotor during the early stage of the intake stroke continued until the tailing rotor apex become closer to inlet port.
- The rotor geometry and recess shape has a little effect on the flow patterns during intake and compression strokes, the flow affected mainly by the inlet geometry and position (peripheral or side intake)
- At the end of compression, the fluid flows along the rotor surface in direction of rotation without any sign of flow vortex.
- The flow velocity at the end of compression could reach high level at the housing tip (short axis), depending on the rotor recess size.
- The two simple fixed models and the experimental visualization presented can validate the 2D model prepared specially to be comparable to the 2D experimental results.

8.2.2 Diesel mixture formation

Diesel engine is normally running on high compression ratio and hence high pressure and temperature is reached. Diesel is then injected and any small amount of fuel injected will be self ignited due to high temperature inside the combustion chamber. So, it is an advantage for diesel engine to run very lean without any air throttling to control the engine stochiometry. In

Wankel engine it is important to use ignition assistant when the engine prepared to run on diesel fuel due to lower compression ratio and hence chamber temperature. The idea is to run the engine in lean concentration overall, but locally rich combustion. So, it is necessary to reach the ignitable charge, (0.6% - 7.5% by volume, diesel vapor) at the spark plug.

The study in this part was concentrated on the diesel mixture formation inside the combustion chamber of Wankel engine and the main conclusion can be summarized as follows.

- Injector angle between holes below 13º is to small and the spray cones interfaced and acts like one bore nozzle. 18º angle between injector holes show better penetration and cover most of the combustion chamber at spray angle of 32º.
- Early fuel spray (39º BTDC) gives more time for mixture formation, but the fuel concentration at the spark is lowered due to charge forward movement, when ignition time is on, (10º-15º BTDC). 29º BTDC spray start angle gives better results for engine speed less than 4000-rpm.
- The new suggested spark plug position (18mm from short axis) shows ignition difficulties due to low fuel concentration on this position, as the fuel evaporation rate is low near the nozzle.
- The new suggested injector position (31mm before short axis), shows better results and covers more area of combustion chamber, and shows more fuel penetration at spray angle 40º.

8.2.3 Hydrogen mixture formation and combustion

Oil limitations and oil crisis in addition to the environmental and air pollution of burning fossil fuels; have led several companies and scientists to search for alternative fuels. Hydrogen the most abundant element in the universe is an ideal energy carrier with its extra clean combustion property will be the fuel of future.

In this research part, it was concentrated on the hydrogen mixture formation inside the combustion chamber of a Wankel engine. The main conclusion can be summarized as follows.

- Since the injector is the main important part for mixture preparation, it has been proved that, multi-hole injector and/or multi-injector can give better hydrogen distribution and

hence better homogeneous mixture, especially for low-pressure injection. Also reduces the hydrogen injection pressure.

- Low-pressure injection gives almost homogeneous mixture at the end of compression stroke and hence betters combustion.
- High-pressure hydrogen injection is more sophisticated system, needs a very high injection pressure and complicated pressure instruments installation. Also, the injector it self still under development and not yet available in market.
- Hydrogen combustion produces high temperatures and hence high nitrogen oxides. Therefore, it is necessary to control NO_x formation by controlling the mixture concentration.

8.3 General conclusion

CFD AVL-Fire is a very good tool for engine research including hydrogen flow supersonic injection.

Wankel rotary engine is a promising engine for use in general aviation aircraft and suitable for various stationary and automotive applications. Wankel engine is the best suits multi-fuel installation; it gives more freedom of multi-injector installations, without any cylinder head complications.

Low-pressure hydrogen direct injection is simpler and suits better for a multi-fuel installation on wankel engines. Mazda RENESIS hydrogen rotary engine also proved this installation with multi-injector in each chamber.

The hydrogen engine is normally produces high amount of NO_x due to high combustion temperature. It has been found that the amount of NO_x can be controlled in acceptable range by running the engine on lean mode (up to Φ=0.7) for idle and medium loads. Heavy and full load is then kept at stoichiometric mixture (Φ=1), and throttling is applied. Figure 8.1 shows the hydrogen engine proposal of running control strategy.

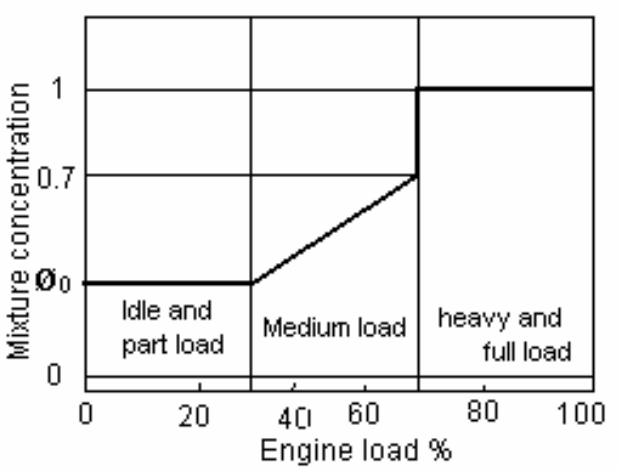

Fig.8. 1 Hydrogen engine load control proposal

8.4 Recommendations and future work

The engine investigated in this research work is still under development and test bench investigations with diesel fuel. A high-pressure common rail diesel spray system was applied and the improvement of diesel injector shows better results.

In future, the next step of work is to prepare the engine for hydrogen combustion with hydrogen injector installation to test the hydrogen engine experimentally.

The use of turbo chargers is always recommended to improve the engine performance.

Nomenclature

A_f: area of flame surface

ATDC: After Top Dead Center

BTDC: Before Top Dead Center

c: progress variable

CFM: Coherent Flame Model

CO: carbon monoxide

CO_2: carbon dioxide

C_{FP}: constant in TFSC model

$C_{fu,}$ C_{pr}: empirical coefficients

c_v: constant volume specific heat

D_b: mixture density in burnet zone

D_u: mixture density in unburned zone

EGR: Exhaust Gas Recycling

H_2: Hydrogen

H_2O: water

H_u : the lower calorific value of fuel

H_G : the lower calorific value of mixture

k: isentropic exponent

k_o: initial turbulence kinetic energy

k_a: turbulent Karlovitz number

l : characteristic length scale

l_t: turbulent length scale

l_{t0}: initial turbulent length scale

L_{st}: Stoichiometric air demand

m_f: total fuel mass

$m_{f,b}$: burnt fuel mass

m_{pr}: combustion product mass

$m_{pr,\infty}$: theoretical maximum mass of combustion products

m_T: total mixture mass

m_u: unburned mixture mass

u: engine speed

P: pressure

P_b: pressure in burnt zone

P_o: initial pressure

P_t: mean pressure at time t

P_u: pressure in unburned zone

PDF: Probability Density Function

r: flame radius

R: radius of spherical vessel

Re: Reynolds number

R_0: Rotation number

SI: Spark ignition

S_L: laminar flow velocity

S: stoichiometric air to fuel ratio

S_T: turbulent burning velocity

Sc_t: turbulent Schmidt number

S_h : heat release of chemical reaction

t_F: time scale of laminar flame

t_k: Kolmogorov time scale

T: temperature

T_0: initial temperature

TDC: Top Dead Center

TFSC: Turbulence Flame Speed Closure

TKE: Turbulence kinetic Energy

V_0: total volume of spherical vessel

X_{1D}: flame surface position in rectangle geometry

y_{fu}: fuel mass fraction

y_{ox}: oxygen mass fraction

y_{pr}: product mass fraction

$y_{fu,fr}$: fuel mass fraction in fresh

Φ: fuel equivalence ratio

$\rho_{fu,fr}$: partial fuel density of fresh charge

ρ_{fr}: density of fresh charge

ρ_G : density of stoichiometric mixture

ρ_a : air density

v: characteristic kinetic viscosity

τ_R: turbulent mixing time scale

∇y_{fuel} : fuel mass fraction gradient

$\boldsymbol{\omega_L}$: mean laminar fuel consumption rate per unit surface along flame front

$\boldsymbol{\omega}_{fuel}$: fuel reaction rate

$\boldsymbol{\omega}_{AI}$: auto-ignition reaction rate

$\boldsymbol{\omega}_{FP}$: reaction rate of flame propagation

g: gravity acceleration

g_f: residual gas mass fraction

ε: dissipation rate

δ_L: laminar flame thickness

u': turbulence intensity

u_0': initial turbulence velocity

λ: air excess, relative F/A ratio

$\overline{\rho r_{fu}}$: mean reaction rate

η_{th} : cycle theoretical thermal efficiency

u_i, u_j : velocity components

τ_{ij} : the stress tensor component

$\overline{\Phi}$: time averaged value

l_t : turbulence scale

C_μ : empirical coefficient

$\dot{r}_k$: species reaction rate

y_{fu}: fuel mass fraction

References

1. Fushui Liu, *CFD Study on Hydrogen Engine Mixture Formation and Combustion,* Doctor Thesis, BTU-Cottbus, December 1, 2003.

2. Raymond F., *The State of the Art and Future Perspectives of The Application Hydrogen I.C. Engines,* BMW Group Research and Technology, D-80788 Munchen.

3. Murat Ulutas, Evren O., *Investigation and Simulation of Hydrogen Blend Fuel Effects on Gasoline Engine*, Ford Otosan, Kocael, Turkey.

4. Danieli, G.A.,Keck, I.C. and Heywood, J.B.; *Experimental and Theoretical Analysis of Wankel Engine performance.* SAE Paper 780416, 1978.

5. Jong T. Lee, Y.Y. Kim, *The Development of Dual Injection Hydrogen Fueled Engine with High Power and High Efficiency,* School of Mechanical Engineering, Sungkywan University, Jangan, Suwon, 440-746,Korea.

6. Brahmadevan V.P., *Numerical Modelling and Simulation of Rotary Engine*, MSc Thesis, Cranfield University, 2004.

7. Heller, D.A., *International Strategic Alliance of Technology Strategy: The case of Rotary Engine Development at Mazda.* Shinshu University, Rev. Octobe 4, 2004.

8. Roberts, J.A., Norman, T.J., Ekchian, J.A., and Heywood, J.B.; *Computer Models for Evaluating Premixed and DISC Wankel engine Performance.* SAE Paper 860613, 1986.

9. Bracco,F.V., and Sirignano, W.A., *Theoretical Analysis of Wankel Engine Combustion.* Combustion Science and Technology. Vol. 7, no. 3, 1973, pp. 109-123.

10. Grasso, F.,Wey, M.J., Bracco, F.V., and Abraham, J.; *Three-Dimensional Computations of Flow in a Stratified-Charge Rotary Engine.* SAE Paper 870409, 1987.

11. Amsden, A.A., Ramshaw, J.D., et al, *KIVA: A Computer Program for Two and Three Dimensional Fluid Flows with Chemical reactions and Fuel Sprays*. LA-10245-MS, Los Alamos National Laboratory, Feb, 1985.

12. Abraham, J. and Bracco, F.V., *3-D Computations to Improve Combustion in a Stratified Charge Rotary Engine-Part III.* Improved Ignition Strategies, SAE International Congress and Exposition, Detroit, Mich., SAE Paper 920304, 1992.

13. Shih, T.I., Yang, S.L., and Schock, H.J., *A Two-Dimension Numerical Study of the Flow Inside the Combustion Chamber of a Motored Rotary Engine.* SAE Paper 860615, 1986.

14. Steinthorsson, E., Shih T.I., et al, *Calculations of the Unsteady Three-Dimensional Flow Field Inside a Motored Wankel Engine.* SAE Paper 880625, 1988.

15. Abraham, J. and Bracco, F.V.; *Pressure Non-Uniformity and Mixing Characteristics in Stratified Charge Rotary Engine Combustion. SAE Paper 880624, 1988.*

16. Abraham, J., and Bracco, F.V.; *Comparison of Computed and Measured Pressure in a Premixed-Charge Natural Gas-Fueld Rotary Engine.* Rotary Engine Design, Analysis and Development, SAE Paper SP-768, SAE, Warrendale, PA, 1989, PP. 117-131.

17. Li, Z., Steinthorsson, E., Shih T.I., and Nguyen, H.L., *Modelling and Simulation of Wankel Engine Flow Fields.* SAE Paper 900029, 1990.

18. Module 3: *Hydrogen Use in Internal Combustion Engines.* College of Desert, Hydrogen Fuel Cell Engines and Related Technology, Rev. 0, December 2001.

19. Sierens, R., Verhelst, S., *Experimental Study of a Hydrogen-Fueld Engine.* Journal of Engineering for Gas Turbines and Power, ASME, Jan. 2001, Vol. 123.

20. Sierens, R., Verhelst, S., *A Hydrogen Fueled V-8 Engine For City Bus Application.* International Journal of automotive Technology, Vol. 2, No.2, pp. 39-45, 2001.

21. Yamamoto, K., *Rotary Engine,* Sankaido, Tokyo, 1981.

22. Norbye, J.P., *The Rotary Engine, Design Development Applications.* Published by Bailey Bros & Swinfen Ltd, SBN 561-00137-5.

23. Bensinger, W.-D., *RotationsKolben-Verbrennunsmotoren*. Spriger-Verlag Berlin-Heidlberg-Newyork 1973.

24. Masaki Ohkubo, Seiji Tashima, Ritsuharu Shimizu, and Hiroshi Ebino, *Development Technologies of the New Rotary Engine (RENESIS).* Mazda Motor Corporation, SAE-2004-01-1790, SAE World Congress Detroit, Michigan, March 8-11, 2004.

25. Hamady, F., Schock, H., and Stueckon, T., *Air Flow Visualization and LDV Measurements in a Motored Rotary Engine Assemply-Part 1.* Flow Visualization, SAE Paper 900030, 1989.

26. Raju, M.S., Willis E.A., *Computational Experience With a Three- Dimensional Rotary Engine Combustion Model.* NASA Technical Memorandum 103104, New Jersey, April 11-12, 1990.

27. Tatschl, R., Gabriel, H.-P., Priesching, P., *FIRE – A Generic CFD Platform for DI Diesel Engine Mixture Formation and Combustion Simulation.* International Multidimensional Modelling User's Group Meeting at SAE Congress, March 4, 2001, Detroit, MI.

28. Herry Lehtiniemi, Yongzhe Zhang, and Rajesh Rawat, *Efficient 3-D CFD Combustion Modelling with Transient Flamelet Models.* SAE Paper offer 08PFL-689

29. Dr.-Ing. Rudolf Klotz, *DerWankelMotor Fur Wasserstoffanwendungen.* Wankel Rotary GmbH.

30. Kelvin, Fu., Aaron, K.J., Fabian, C.M., Walther, D.C., *Design and Experimental Results of Small-Scale Rotary Engines.* ASME International Mechanical Engineering Congress and Exposition, Nov. 11-16, 2001, New York, Ny. IMECE2001/MEM-23924.

31. Volchkov, E.P, Terekhov, V.V., and Terekhov, B.I., *Numerical Simulation of A Hydrogen Combustion in A Boundary Layer with Different Blowing Parameters.* S.S. Kutateladze Institute of Thermophysics SB RAS 630090 Novosibirsk, Russia.

32. Jaakko Jalmari Halmari, B.S., *Computer Simulation of A Hydrogen Fueled Internal Combustion Engine.* MSc Thesis, Texas Tech. University, May 2005.

33. Sierens, R., Verhelst, S., *Hydrogen Fueled Internal Combustion Engines.* Labiratory of Transport Technology, Ghent University, Sint Pietersnieuwstraat 41, B-9000 Gent, Belgium.

34. Raju, M.S., Willis, E.A., *Analysis of Rotary Engine Combustion Processes Based on Unsteady, Three-Dimensional Computation.* NASA Technical Memorandum 102469 AIAA-90-0643.

35. Subramanian, V., Mallikarjuna, J.M. and Ramesh, A., *Improvement of Combustion Stability and Thermal Efficiency of a Hydrogen Fueled Engine at Low Loads by*

Throttling. I.C. Engines Lab, Dept. of Mech. Eng., Indian Institute of Technology Madras, Chennai-600 036.

36. Lee, J.T., Kim, Y.Y., Lee, C-W. Caton, J.A., *An Investigation of Cause of Backfire and its Control Due to Crevice Volumes in a Hydrogen Fueled Engine.* Transaction of the ASME, Vol. 123, Jan. 2001 pp. 204-210.

37. Yasuaki, H., Kouichi, Y., *An Experimental Investigation on Air-Fuel Mixture Formation Inside a Low-Pressure Direct Injection Stratified Charge Rotary Engine.* SAE Paper 930678, March 1-5, 1993.

38. AVL Fire, *Theory.* Version 8, July 2003.

39. AVL Fire, *Combustion,* Version 8, Jan 2003.

40. AVL Fire, *Primer*. Version 8, June 2002.

41. http://experts.about.com/e/w/wa/Wankel_engine.htm**.**

42. http://www.anl.gov/Media_Center/News/2006/news060622.pdf

43. http://www.hydrogenassociation.org/newsletter/autumn06/bmw.pdf

44. http://www.technologyreview.com/Energy/17526/

45. http://avt.inl.gov/hydrogen.html

46. http://www.physorg.com/news70207345.html

47. http://www.hydrogenassociation.org/general/fleet_Module5.pdf

48. http://forms.gradsch.psu.edu/equity/sroppapers/2002/ParamoMelvin.pdf

49. http://www.hubbertpeak.com/2006.asp

50. http://www.planetforlife.com/oilcrisis/oilpeak.html

51. http://www.itepsa.com/samples/AFE199907_ES.PDF

52. http://www.der-wankelmotor.de/wasserstoff.pdf

53. Willis, E.A., McFaddaeb, J.J., *NASA's Rotary Engine Technology Enablement Program-1983 Through 1991.* NASA Technical Memorandum, 105562.

54. Bartrand, T.A.m., Willis, E.A., *Performance of a Supercharged Direct Injection Stratified-Charge Rotary Combustion Engine.* NASA Technical Memorandum 103105, New Jersey, April 11-12, 1990.

55. DeFilippis, M., Hamady, F., Novak, M., Schock, H., *Effects of Pocket Configuration on the Flow Field in a Rotary Engine Assembly.* SAE Technical Paper No. 920300.

56. Sierens, R., Verhelst, S., *Aspects Concerning the Optimisation of a Hydrogen Fueled Engine.* International Journal of Hydrogen Energy 26 (2001) 981-985. Published by Elsevier Science Ltd. PII: S0360-3199 (01) 00031-3.

57. Kenji Morita, *Automotive Power Sorce in 21st Century.* JSAE 20034001 Review 24 (2003) 3-7.

58. Blarigan, P.V., *Advanced Internal Combustion Engines Research.* Proceeding of the 2000 DOE Hydrogen Program Review NREL/CP-570-28890.

59. Aceves. S.M., Smith, J.R., *Hybrid and Conventional Hydrogen Vehicles that Meet EZEV Emissions.* This Paper prepared for submittal to the 1997 SAE International Congress and Exposition, Detroit, Michigan, Feb. 24-27, 1997, UCRL-JC125891.

60. Green, J.B., Domingo, N., Storey, J.M.E., Wagner, R.M., and Armfield, J.S., *Experimental Evaluation of SI Engine Operation Supplemented by Hydrogen Rich Gas from a Compact Plasma Boosted Reformer.* SAE Technical Paper No. 2000-01-2206, June 19-21, 2000.

61. Polasek M., Macek, J., *Hydrogen Fueled Engine –Properties of Working Cycle and Emission Potentials*. Czech Technical University, Prague Czech Republic, Paper Code: F02V102.

62. Kimitaka Y., Masakuni, O., Tomonori, K., Kouta, M., Takashi, K.,and Yasuo, T., *A Development of a High Pressure H2 Gas Injector with High Response by Using Common-Rail Injection System for Direct Injection H2 Fuelled Engines*. WHEC 16 / 13-16 June 2006 – Lyon France.

63. AVL LIST, 2000. User's Guide FIRE Version 7 and Swift Version 2. Graz, Austria.

64. AVL LIST, 2004. CFD SOLVER, v8.3. Graz, Austria.

65. Wankel Super-Tec GmbH, 2004. The New Generation of Wankel Rotary Engines. Cottbus, Germany**.**

66. Paul A. Salanki, and James S. Wallace, *Evaluation of Hydrogen-Fueled Rotary Engine for Hybrid Vehicle Applications*, SAE Technical Paper series, no. 960232**.**

67. Xiaolaihe, M.S.E.E., *Development and Validation of Hybrid Electric Vehicle with Hydrogen Internal Combustion Engine,* Doctor of Philosophy Thesis, Texas Tech University**.**

68. RWTH Aachen, Lehrstuhl für Wärme- und Stoffübertragung, Prof. Knerr, http://www.wsa.rwth-aachen.de/

69. Berg, H.P., H.T. Izweik, T. Poojitganont, O. Antoshkiv: *Anwendung fortschrittlicher Simulationswerkzeuge in der Wankelmotorenentwicklung*. ATZ / MTZ - Konferenz Virtual Powertrain Creation 2006.

70. Thanapol Poojitganont, Heinz Peter Berg, Husni Taher Izweik, Axel Himmelberg, Brandenburg University of Technology Cottbus, Germany, *Multi-fuel Wankel Engine for Small Aircrafts and UAVs Applications: Strategies of the Engine Development*, ISABE-2007-1128.

71. AVL Fire, *Species transport*, Version 8, July2003.

72. Loyd, R., Curtiss-Wright Corp., R.C. Engine Division. Wood-Ridge. N.J. 07075, *Curtiss-Wright Stratified Charge Rotary Engine Development*, Combustion Science and Technology 1976, Vol. 12, pp.47-61

73. Mount, Robert E., and LaBouff, Gary A., *Advanced Stratified-Charge Rotary Engine Design,* Society of Automotive Engineers Paper 890324, 1989

74. Jones et al., *Stratified Charge Rotary Engine with High and Low Pressure Fuel Supply*, United States Patent, 3923012, Dec. 2, 1975.

75. Ryoji Kagawa, Syunki Okazaki, Nobuhiro Somyo, and Yuji Akagi, Mazda Motor Corp., *Study of a Direct-Injection Stratified-Charge Rotary Engine for Motor Vehicle Application*

76. James W. Walker and Robert E. Mount, Rotary Engine Division, *The Stratified Charge Rotary Engine,* John Deere Technologies Int'l Inc. Woodridge, N.J.